Spatially Correlated Decoherence: Understanding and Exploiting Spatial Noise Correlations in Quantum Systems

by

Dipl.-Phys. Jan Jeske

Submitted in fulfilment of the requirements for the degree of

Doctor of Philosophy

Theoretical Chemical and Quantum Physics Group
School of Applied Science
RMIT University

March 2014

Declaration

I declare that the work is that of the me alone except where due acknowledgement has been made. The work has not been submitted previously, in whole or in part, to qualify for any other academic award. The content of the thesis is the result of work which has been carried out since the official commencement date of the approved research program. Any editorial work, paid or unpaid, carried out by a third party is acknowledged. Ethics procedures and guidelines have been followed.

Melbourne, 28 March 2014

.....

(**Jan Jeske**)

Acknowledgements

First of all I'd like to thank my senior supervisor Dr. Jared Cole, whom I have worked with since the start of my German 'Diplom' in 2010. He has been an outstanding supervisor who gave me great ideas and creative input, has always acted in my best interest and provided personal encouragement in the difficult times of this research project. He furthermore has provided detailed feedback and helped to improve the structure and language of this thesis. I'm also very grateful to my associate supervisors Prof. Andrew Greentree and Prof. Salvy Russo for their ongoing support throughout my PhD.

I'd like to thank Prof. Susana Huelga and her group in Ulm for being great hosts, who made my time there very enjoyable and for the fruitful collaborations and the great feedback on manuscripts that I received from Susana. Similarly I'd like to thank Prof. Schön and Dr. Michael Marthaler and their group for generously hosting me when I was in Germany and for the continuing collaborations and the valuable exchanges.

I'd like to thank Nico Vogt, Dr. Paolo Longo and Dr. Angel Rivas for great collaborations, valuable exchanges and for proof reading my thesis. Your input as experts was very helpful. I'd like to thank David Ing and Jesse Vaitkus who have provided feedback on large parts of this thesis early on and implemented work based on the formalism of chapter 2. For my work in chapter 6 David provided me with the position data of the 7 sites of the FMO complex since he implemented similar code.

To all of the RMIT physics department, particularly Ben, Tim, Chris, Nick, Masturina, Steph, Michael, Bogdan, Celine, Jackson, Daniel, Hamid, Kelly, Abi and Nico: Thanks for making RMIT such a sociable and awesome place.

I thank my parents Harald and Regina as well as my sisters Nele and Vera for their support from the other end of the planet. Finally I thank the most important person in my life, Maheshie for her love and support.

Publications

During the course of this PhD the following publications were written:

1. Jan Jeske, David Ing, Jared H Cole, "Bloch-Redfield equations for modeling light-harvesting complexes",
   Submitted to *J. Chem. Phys.*, ArXiv 1408.2726

2. Jan Jeske, Jared H Cole, Susana Huelga, "Quantum metrology in the presence of spatially correlated noise: Restoring Heisenberg Scaling",
   New J. Phys. **16**, 073039 (July 2014)

3. Jan Jeske, Nicolas Vogt, Jared H. Cole, "Excitation- and state-transfer through spin chains in the presence of spatially correlated noise",
   Phys. Rev. A **88**, 062333 (Dec 2013)

4. Nicolas Vogt, Jan Jeske, Jared H. Cole, "Stochastic Bloch-Redfield theory: Quantum jumps in a solid-state environment",
   Phys. Rev. B **88**, 174514 (Nov 2013)

5. Jan Jeske, Jared H Cole, "Derivation of Markovian master equations for spatially correlated decoherence",
   Phys. Rev. A **87** 052138 (May 2013)

6. Jan Jeske, Jared H Cole, Clemens Müller, Michael Marthaler, Gerd Schön, "Dual-probe decoherence microscopy: probing pockets of coherence in a decohering environment",
   New J. Phys. **14** 023013 (Feb 2012)

Chapters

Contents

Summary

The challenge of making nano-scale quantum systems experimentally accessible is being overcome for an increasing diversity of systems by improved fabrication techniques and experimental control. Despite rapid progress, one of the main hindrances in all experiments is the difficulty of isolating the quantum system from the surrounding environment and its fluctuations. This experimental "noise" perturbs the quantum system, a process that is generally referred to as decoherence: the system slowly loses its distinguishing quantum features. This makes all controlled quantum systems mesoscopic systems, which are close to the verge of quantum and classical physics.

With ever growing experimental and computational capabilities, larger systems at smaller spatial distances are being studied. Simple models of spatially uncorrelated noise are therefore becoming increasingly questionable. In this thesis the effects of spatial correlations in the noise environment with a finite correlation length are investigated. The consequences for the experimental design of controlled quantum systems as well as the dynamics of solid state systems are presented. We utilize the Bloch-Redfield formalism, a Markovian master equation approach, which gives a close connection to the underpinning system-environment model. We show how to use this formalism to model any spatial correlation function of the noise environment. Using microscopic environmental models, several correlation functions are derived and their properties connected to the environmental parameters. Several phenomenological correlation functions are also studied and a mapping to the Lindblad master equation is presented, which provides a test of positivity for phenomenological models.

The study of spatial noise correlations is a novel but essential field of research in quantum metrology. Noise correlations have been observed in experiments with trapped ions, in which they limit the use of such experiments for metrology. Quantum advantage, i.e. a better precision scaling than the standard quantum limit has been proven impossible in the presence of uncorrelated Markovian noise only. We

show that for certain optimized states the best possible quantum advantage, Heisenberg scaling, can be achieved in the presence of noise with a finite spatial decay of correlations. We furthermore identify how dephasing effects change in strength with increasing correlation length for entangled states in a general way. For finite correlation length a topology dependence of entangled quantum states emerges, such that the arrangement of the participating ions changes the decoherence properties.

For quantum transport through spin chains and networks, noise is generally detrimental. Spatial correlations however reduce the effect of dephasing noise and can reinstate the transport dynamics. The critical correlation length proves to be closely connected to the maximal packet width of one excitation in the transfer process. For dissipation noise, relaxation-free states emerge with spatial correlations. The decay of an excitation is therefore fundamentally modified into a fast decay towards an intermediate relaxation-reduced state and a subsequent decay to the ground state on a much longer time scale.

Biological photosynthetic complexes have recently been found to potentially include quantum coherent dynamics, particularly in the process of transmitting an exciton from the point of creation to the reaction centre. We show how the formalism of spatially correlated decoherence adapts to this significantly different energy regime. Typical effects of decoherence in this field are presented and we show how the light-harvesting efficiency is influenced by spatial correlations in the noise.

Finally we investigate the influence of spatial noise correlations in the Heisenberg model of a quantum ferromagnet. Here we focus on the calculation of macroscopic properties of the crystal, such as the magnetisation and its dynamics, from a microscopic master equation. We find that larger correlation length in the phonon noise of the ferromagnetic lattice prolongs the out-of-equilibrium time of the magnetisation and changes the shape of the decay to the equilibrium value.

This thesis highlights the fundamental relevance of noise correlations to several fields of quantum physics and the importance of the efficient and comprehensive modeling techniques presented.

Chapter 1

1 Introduction

The study of open quantum systems and the concept of a density matrix master equation is the basis for a variety of fields in modern physics, be it quantum optics, photonics, condensed matter physics, quantum computation or even medical imaging such as MRI and NMR. When deriving or assuming a particular form for the master equation via the usual system-bath model [1], it is common to assume each component of a system either couples to the same bath (*correlated* or *collective* decoherence channels) or individual baths (*uncorrelated* or *independent* decoherence channels), see e.g. [2–6]. We explore the regime between these two extremes, introducing the concept of a *correlation length* ξ and deriving a general master equation method for treating such partially correlated environments.

Decoherence induced by a correlated environment is a commonly observed effect. The early discovery of super- and sub-radiance in a radiating gas in 1954 [7, 8] was the first effect based on several subsystems coupled to the same environmental mode. More recently in the context of quantum computation, master equation modeling has become an intensively studied field of research. The mathematical equivalent of super- and sub-radiance was described for two qubits with dissipation to the same bath [5, 9]. Furthermore the concept of decoherence-free subspaces [10–15] relies on common environments. Even some of the foundational work on decoherence in quantum computation considered both fully correlated and uncorrelated environments [16–20]. A review discussing both methods is in [21]. Recently, the ramifications of correlated environments have been discussed in such diverse situations as scalable quantum error correction [2, 22–28], photosynthesis and biological chromophores [29–33] and multi-atom trapping experiments [34–37]. Especially in earlier work it was common to derive a master equation for a particular system in

a particular environment [16, 17, 20], leading to common models such as the largely employed spin-boson model [17, 38–41]. In this thesis we present the Bloch-Redfield equations in a more general way. Any environment can be reduced to its relevant parameters, the spatial-temporal correlations contained in the spectral function and the system-environment coupling operators. With this intermediate step the Bloch-Redfield equations can be applied to any system without the need to derive a new master equation each time.

The Lindblad equations [1, 42–44] are a common tool for open quantum systems due to their simple form and well behaved mathematical properties. Yet, deriving a general master equation of this form for (partially) correlated environments is non-trivial. Lindblad operators can be derived or assumed to act individually, pairwise or collectively, yet how does one choose these in a physically sensible manner? We use a general Bloch-Redfield approach, where environmental noise correlation functions appear naturally in the formalism. Given sufficiently well behaved environmental correlations, a closed form master equation can be obtained with the same form as the Lindblad equation but whose operators and rates are linked directly to the original physical system-bath Hamiltonian. Following this route we consider a generalisation of the environmental correlation function which includes spatial (as well as temporal) correlations and therefore derive a general master equation. This describes spatially correlated decoherence independent of the particular bath Hamiltonian and purely based on environmental correlation functions. Following this introduction (chapter 1) the master equation methodology is described in chapter 2.

We also consider several examples where such *spatial-temporal* correlation functions can be derived microscopically from an environmental model and derive the corresponding spectral functions. This is a major stepping stone as it facilitates writing down the Bloch-Redfield equations immediately for any system combined with the respective environmental model. Furthermore it links the features of the spectral functions to environmental parameters, which gives the intuition required to work with phenomenological spectral functions. We present our example environmental models in chapter 3.

Measuring the features and properties of environmental noise directly is difficult because the environment is by definition the part of the experiment which is not controlled and measured. Accordingly there are many experiments with little information about the nature and properties of environmental noise. Despite this, recent

experiments with trapped ions have shown evidence of strongly correlated environmental noise [35, 45]. This makes our work highly relevant to the ultrahigh-precision measurements carried out in ion traps. Particularly since a lot of theoretical work for these quantum metrology experiments has been based on the assumption of uncorrelated noise. For example there have been suggestions of experimental setups, which achieve quantum advantage, i.e. a better precision scaling with the number of measurements than can be achieved classically. Although quantum advantage has been proven impossible in the presence of uncorrelated Markovian noise [46] there have been first experiments confirming the existence of quantum advantage with two and three entangled ions [47, 48]. This shows the need for a rigorous experimental framework for spatially correlated noise. We extend the theoretical work to spatially correlated decoherence and describe in detail an experimental setup which achieves the best-possible quantum advantage in chapter 4.

Another field which involves coupled systems of many sites is the transport of excitations and quantum states through spin chains and networks. This large field of research is relevant to quantum information, quantum electronics and quantum communication and ranges from the study of existing structures to the search for ideal engineered spin networks [49–65]. Decoherence effects however are often either neglected or assumed as spatially uncorrelated. We describe the effects of spatially correlated noise for both state and excitation transfer generally in chapter 5.

A mathematically closely connected process in an very different class of systems is the transport of photon-induced excitons in biological photosynthetic systems. This originally biochemical field of research has recently been found likely to involve some level of quantum coherent processes [66, 67], causing an overlap with quantum transport and decoherence modeling. In particular, the possibility of spatially correlated noise has been discussed in several contexts [68–74]. Since the detailed knowledge about photosynthetic systems is in the biochemical community and the systems are on a largely different parameter scale than most controlled quantum systems, there has been a lot of confusion about which master equation approach to use. While some use very similar formalism to the one presented in this thesis [69, 75], others are led to believe that Bloch-Redfield and/or Lindblad equations are insufficient to describe transport in light-harvesting complexes [32, 68, 70, 73, 76]. This is fuelled by the common practice in the biochemical community to use Bloch-Redfield equations (which are there usually just referred to as 'Redfield equations') to describe purely incoherent transition processes. A variety of alternatives and extensions has been proposed [74, 77–81]. We describe how the Bloch-Redfield formalism adapts very

well to model Markovian noise in light-harvesting systems by a careful application of the secular approximation and we describe the typical noise effects which occur in the prototypical dimer system in chapter 6.

Using quantum master equations to calculate macroscopic properties of solid state systems can yield details about the material properties and dynamics. This is a distinctly different application from the calculation of expectation values in small quantum systems of only a few states. For certain systems such as the quantum ferromagnet, analytical solutions can be obtained from master equation approaches [82]. We show the influence of phonon noise and its spatial correlations onto the macroscopic properties of the quantum ferromagnet such as the magnetisation in chapter 7.

Finally chapter 8 summarizes the results and gives the conclusions of the thesis.

Throughout this thesis we assume natural units $\hbar = 1$ and only write $\hbar$ explicitly for clarity when we write down fundamental equations, i.e. only in chapter 2.

Chapter 2

2 Master equations

This chapter serves as ground work for the rest of the thesis. The Bloch-Redfield equations are derived in detail and the mapping to the Lindblad form is discussed. Then we explain how a model for spatially correlated noise arises naturally from the formalism, how to implement and test spatial correlation functions and explain the fundamental effects of spatial correlations in qubit systems. Finally we discuss numerical methods to solve master equations. The material in this chapter has appeared in references [83, 84] and has contributed to all of the other publications listed on page vii.

Introduction

The Schrödinger equation is the equation of motion for the state vector of any quantum system. For a statistical ensemble of quantum systems, described by a density matrix, the equation of motion is called a quantum master equation. A quantum master equation is used to describe open quantum systems which experience random statistical perturbations from their environment.

For a closed quantum system the equation of motion for a density matrix derives directly from the Schrödinger equation and is called the von-Neumann equation:

$$i\hbar\,\partial_t\,|\Psi\rangle = H\,|\Psi\rangle \qquad \text{Schrödinger equation} \qquad (2.1)$$

$$-i\hbar\,\partial_t\,\langle\Psi| = \langle\Psi|\,H$$

$$\Rightarrow i\hbar\,\partial_t\rho = [H,\rho] \qquad \text{von-Neumann equation} \qquad (2.2)$$

where the density matrix $\rho = \sum_j p_j |\Psi_j\rangle \langle\Psi_j|$ for a statistical ensemble which is in state $|\Psi_j\rangle$ with probability p_j. All master equations for open quantum systems are derived from the assumption that the closed combination of system and environment are governed by the von-Neumann equation. The derivation then always aims to trace out the environment, such that the master equation describes the evolution for the reduced density matrix of the system alone and the environment is a perturbation incorporated in the form of the equation. There are several approaches to simplify the process of deriving a new master equation for each system-environment combination. We present the Bloch-Redfield equations here and discuss the mapping to a second common form of the master equation, the Lindblad equations.

2.1 Theoretical background

2.1.1 The Bloch-Redfield equations

2.1.1.1 Derivation

The techniques used to set up what is now widely called the Bloch-Redfield equations were developed in the 1950s by Felix Bloch's student R. K. Wangsness [85], Bloch himself [86, 87] and A. G. Redfield [88]. As these techniques have been generalised since then, equations of a similar form are sometimes called Bloch-Redfield equations [21, 89], sometimes Bloch-Wangsness-Redfield theory [90], or at other times they are just referred to as "the master equation in the Born-Markov approximation" [1, 5, 44]. This refers to the fact that in the derivation a Born-type approximation of the integral is used and a second approximation (also called the Redfield-approximation) which is based on the assumption that the system dynamics is a Markov-process. Here we derive a general and compact notation based on [91–93].

To derive the Bloch-Redfield equations we start with the usual approach of tracing out the environment of the von-Neumann equations for system and environment with the help of the Born-Markov approximation [1, 44]. The Hamiltonian is divided into:

$$H = H_S + H_B + H_{int}$$

where H_S describes the system, H_B describes the bath and H_{int} the interaction

between the two. The interaction is assumed to be of the form:

$$H_{int} = \sum_j s_j B_j \tag{2.3}$$

where each s_j is an operator acting on the system and each B_j an operator acting on the bath. We denote the combined density matrix for both system and environment by χ. The density matrix follows the von-Neumann equation:

$$i\hbar\, \partial_t \chi(t) = [H, \chi(t)] \tag{2.4}$$

We change to the interaction picture with respect to H_{int} (see appendix F):

$$i\hbar\, \partial_t \tilde{\chi}(t) = \left[\tilde{H}_{int}(t), \tilde{\chi}(t)\right] \tag{2.5}$$

We denote all transformed operators by a tilde and note that $\tilde{H}_{int}(t)$ can again be divided into products of system and environment operators since operators acting on different subspaces commute:

$$\tilde{H}_{int}(t) = e^{\frac{i}{\hbar}(H_S+H_B)t} H_{int} e^{-\frac{i}{\hbar}(H_S+H_B)t} = \sum_j \; e^{\frac{i}{\hbar}H_S t} s_j e^{-\frac{i}{\hbar}H_S} \;\; e^{\frac{i}{\hbar}H_B} B_j e^{-\frac{i}{\hbar}H_B} = \sum_j \tilde{s}_j \tilde{B}_j \tag{2.6}$$

Integrating eq. 2.5 gives:

$$\tilde{\chi}(t) = \chi(0) + \frac{1}{i\hbar}\int_0^t dt' \left[\tilde{H}_{int}(t'), \tilde{\chi}(t')\right] \tag{2.7}$$

Putting this back into eq. 2.5 yields its integro-differential form:

$$i\hbar\, \partial_t \tilde{\chi} = \left[\tilde{H}_{int}, \tilde{\chi}(0)\right] + \frac{1}{i\hbar}\int_0^t dt' \left[\tilde{H}_{int}(t), \left[\tilde{H}_{int}(t'), \tilde{\chi}(t')\right]\right] \tag{2.8}$$

It is then assumed that at $t = 0$, system and environment are uncorrelated $\chi(0) = \rho(0) \otimes \rho_B(0)$. The environment is then traced out, the first term assumed to be zero[1]

[1] If the first term is not zero $\mathrm{Tr}_B[\tilde{H}_{int}, \tilde{\chi}(0)] = \sum_j s_j \langle B_j(0)\rangle \neq 0$ then this average expectation value can be included into the system Hamiltonian $H_S \to H_S + \sum_j s_j \langle B_j(0)\rangle$ and the corresponding bath operators can be renormalised such that they only fluctuate around zero: $B_j \to B_j - \langle B_j(0)\rangle$.

and we denote the density matrix for the system as $\rho(t) = \mathrm{Tr}_B\, \chi(t)$.

$$\partial_t \tilde{\rho}(t) = \mathrm{Tr}_B \frac{-1}{\hbar^2} \int_0^t dt' \left[\tilde{H}_{int}(t), \left[\tilde{H}_{int}(t'), \tilde{\chi}(t')\right]\right] \tag{2.9}$$

Based on the assumption that the environment is not influenced by the system since it is much larger, the Born-approximation simplifies $\chi(t') \approx \rho(t') \otimes \rho_B(t')$, which lets us divide all terms into system and bath operators respectively:

$$\begin{aligned}\partial_t \tilde{\rho}(t) = \frac{-1}{\hbar^2} \sum_{j,k} \int_0^t dt' \; \Big\{ &[\tilde{s}_j(t)\tilde{s}_k(t')\tilde{\rho}(t') - \tilde{s}_k(t')\tilde{\rho}(t')\tilde{s}_j(t)] \;\; \mathrm{Tr}[\tilde{B}_j(t)\tilde{B}_k(t')\tilde{\rho}_B] \\ &+ [\tilde{\rho}(t')\tilde{s}_k(t')\tilde{s}_j(t) - \tilde{s}_j(t)\tilde{\rho}(t')\tilde{s}_k(t')] \;\; \mathrm{Tr}[\tilde{B}_k(t')B_j(t)\tilde{\rho}_B] \Big\}\end{aligned} \tag{2.10}$$

Assuming that correlations $\mathrm{Tr}[\tilde{B}_j(t)\tilde{B}_k(t')\tilde{\rho}_B]$ in the bath decay to zero with increasing $\tau = t - t'$ much faster than the typical scale of the system dynamics the Markov-approximation furthermore simplifies $\chi(t') \approx \rho(t) \otimes \rho_B(t')$ and $\int_0^t dt' \approx \int_0^\infty dt'$. The Markov approximation simplifies the differential equations enormously. At the same time it limits the possible choices of environments because it assumes that any correlations in the bath decay almost immediately on the time scale of any dynamics in the system. In other words there is no coherent dynamics in the bath. Any system-environment interaction where a particular excitation leaves the system to the environment and then reoccurs in the system at a later point would therefore break the Markov approximation[2]. Applying the Markov approximation one finds:

$$\begin{aligned}\dot{\tilde{\rho}} = &\frac{-1}{\hbar^2} \sum_{jk} \int_0^\infty dt' \, [\tilde{s}_j(t)\tilde{s}_k(t')\tilde{\rho}(t) - \tilde{s}_k(t')\tilde{\rho}(t)\tilde{s}_j(t)] \, \langle \tilde{B}_j(t)\tilde{B}_k(t') \rangle \\ &+ \frac{-1}{\hbar^2} \sum_{jk} \int_0^\infty dt' \, [\tilde{\rho}(t)\tilde{s}_k(t')\tilde{s}_j(t) - \tilde{s}_j(t)\tilde{\rho}(t)\tilde{s}_k(t')] \, \langle \tilde{B}_k(t')\tilde{B}_j(t) \rangle\end{aligned} \tag{2.11}$$

Eq. 2.11 is the typical form of the master equation in the Born-Markov-approximation (see e.g. Carmichael [44] eq. 1.34).

The bath expectation values are assumed to only depend on the time difference $\tau = t - t'$, i.e. they can be written $\langle \tilde{B}_j(t)\tilde{B}_k(t') \rangle = \langle \tilde{B}_j(\tau)\tilde{B}_k(0) \rangle$. These are the time correlation functions of the bath and can be written in the common form of a

[2] To consider non-Markovian environments one either needs to find a solution to the particular non-Markovian integral kernel. Another way of considering non-Markovian dynamics is to include certain environmental pockets of coherence into what is formally labelled the "system" and solve the master equation with the new system-environment threshold which then can be assumed to be Markovian.

correlation function $\langle \tilde{B}_j(t)\tilde{B}_k(t')\rangle - \langle \tilde{B}_j(t)\rangle \cdot \langle \tilde{B}_k(t')\rangle$ because the expectation values $\langle B_j(t)\rangle = 0$ are assumed to be zero[3] in all noise-environments.

We then transform back to the Schrödinger picture (appendix F). We start with the left-hand side of eq. 2.11:

$$\begin{aligned}\partial_t \left(e^{\frac{i}{\hbar}H_S t}\rho e^{-\frac{i}{\hbar}H_S t}\right) &= e^{\frac{i}{\hbar}H_S t}\frac{i}{\hbar}H_S\rho e^{-\frac{i}{\hbar}H_S t} + e^{\frac{i}{\hbar}H_S t}\dot{\rho}e^{-\frac{i}{\hbar}H_S t} + e^{\frac{i}{\hbar}H_S t}\rho\left(-\frac{i}{\hbar}H_S\right)e^{-\frac{i}{\hbar}H_S t} \\ &= e^{\frac{i}{\hbar}H_S t}\left(\rho - \frac{1}{i\hbar}\left[H_S,\rho\right]\right)e^{-\frac{i}{\hbar}H_S t} \end{aligned} \tag{2.12}$$

We then multiply the whole eq. 2.11 from the left with $e^{-\frac{i}{\hbar}H_S t}\cdot$ and from the right with $\cdot e^{\frac{i}{\hbar}H_S t}$,

$$\begin{aligned}\rho - \frac{1}{i\hbar}\left[H_S,\rho\right] &= \frac{-1}{\hbar^2}\sum_{jk}\int_0^\infty dt' \left[s_j Q(\tau)\rho(t) - Q(\tau)\rho(t)s_j\right]\langle \tilde{B}_j(\tau)\tilde{B}_k(0)\rangle \\ &\quad + \frac{-1}{\hbar^2}\sum_{jk}\int_0^\infty dt' \left[\rho(t)Q(\tau)s_j - s_j\rho(t)Q(\tau)\right]\langle \tilde{B}_k(-\tau)\tilde{B}_j(0)\rangle \\ Q &:= e^{-\frac{i}{\hbar}H_S\tau}s_k e^{\frac{i}{\hbar}H_S\tau}\end{aligned} \tag{2.13}$$

where $\tau = t - t'$. We then change the integration variable $\int_0^t dt' = \int_t^0(-d\tau) = \int_0^t d\tau \approx \int_0^\infty d\tau$.

To simplify the matrix-exponentials in Q in an arbitrary basis $\{|a_n\rangle\}$ we introduce the transformation matrix $V = \sum_n |\omega_n\rangle\langle a_n|$ to the system Hamiltonian's eigenstates $H_S|\omega_n\rangle = \hbar\omega_n|\omega_n\rangle$. In other words:

- V is the matrix which contains the eigenvectors of H_S in its columns.
- $\hbar\omega_n$ is the eigenvalue of H_S which corresponds to the nth column of V

We insert unity operators $VV^\dagger$ into the equations and find:

$$\begin{aligned}\rho - \frac{1}{i\hbar}\left[H_S,\rho\right] &= \frac{-1}{\hbar^2}\sum_{jk}\int_0^\infty d\tau \left[s_j V\hat{Q}(\tau)V^\dagger\rho(t) - V\hat{Q}(\tau)V^\dagger\rho(t)s_j\right]\langle \tilde{B}_j(\tau)\tilde{B}_k(0)\rangle \\ &\quad + \frac{-1}{\hbar^2}\sum_{jk}\int_0^\infty d\tau \left[\rho(t)V\hat{Q}(\tau)V^\dagger s_j - s_j\rho(t)V\hat{Q}(\tau)V^\dagger\right]\langle \tilde{B}_k(-\tau)\tilde{B}_j(0)\rangle \\ \hat{Q} &:= V^\dagger e^{-\frac{i}{\hbar}H_S\tau}VV^\dagger s_k VV^\dagger e^{\frac{i}{\hbar}H_S\tau}V\end{aligned} \tag{2.14}$$

[3] This assumption becomes clearer when we remember that in a real physical system all expectation values can be time-dependent but are then averaged over the whole ensemble of systems. The assumption $\langle B_j(t)\rangle = 0$ then simply means a fluctuation around zero as the only time evolution, i.e. a static bath.

Since V transforms into the H_S-eigenbasis we can see that $\hat{Q}$ is simply given by s_k multiplied with two diagonal matrices. We formally simplify $\hat{Q}$ by inserting unity operators $\sum_n |\omega_n\rangle \langle\omega_n|$:

$$\hat{Q} = \sum_{lmnp} |a_l\rangle \underbrace{\langle\omega_l| e^{-\frac{i}{\hbar}H_S\tau} |\omega_m\rangle}_{=e^{-i\omega_l\tau}\delta_{lm}} \langle\omega_m| s_k |\omega_n\rangle \underbrace{\langle\omega_n| e^{\frac{i}{\hbar}H_S\tau} |\omega_p\rangle}_{=e^{i\omega_n\tau}\delta_{np}} \langle a_p| \tag{2.15}$$

$$= \sum_{mn} |a_m\rangle \langle\omega_m| s_k |\omega_n\rangle \langle a_n| e^{i(\omega_n-\omega_m)\tau} \tag{2.16}$$

$$\langle a_m| \hat{Q} |a_n\rangle = \langle\omega_m| s_k |\omega_n\rangle e^{i(\omega_n-\omega_m)\tau} = \langle a_m| V^\dagger s_k V |a_n\rangle e^{i(\omega_n-\omega_m)\tau} \tag{2.17}$$

The τ-dependency in each element is now just a scalar. The τ-integration can then be performed element-wise and we find:

$$\dot{\rho} = \frac{i}{\hbar}[\rho, H_s] + \frac{1}{\hbar^2}\sum_{j,k}\left(-s_j V q_{jk} V^\dagger \rho + V q_{jk} V^\dagger \rho s_j - \rho V \hat{q}_{jk} V^\dagger s_j + s_j \rho V \hat{q}_{jk} V^\dagger\right) \tag{2.18}$$

$$\text{with} \quad \langle a_m|q_{jk}|a_n\rangle = \langle a_n| V^\dagger s_k V |a_m\rangle \int_0^\infty d\tau\, e^{i(\omega_n-\omega_m)\tau} \langle\tilde{B}_j(\tau)\tilde{B}_k(0)\rangle \tag{2.19}$$

$$\langle a_m|\hat{q}_{jk}|a_n\rangle = \langle a_n| V^\dagger s_k V |a_m\rangle \int_0^\infty d\tau\, e^{i(\omega_n-\omega_m)\tau} \langle\tilde{B}_k(-\tau)\tilde{B}_j(0)\rangle \tag{2.20}$$

If the one-sided Fourier transforms in eq. 2.19 and 2.20 contain an imaginary part, this imaginary part purely leads to additional coherent dynamics (which in the secular approximation can even be written as a correction of the system Hamiltonian, see section 2.1.4).

Only the real part causes decoherence. Assuming the property $\left(\langle\tilde{B}_j(\tau)\tilde{B}_k(0)\rangle\right)^* = \langle\tilde{B}_j(-\tau)\tilde{B}_k(0)\rangle$ this real part can be rewritten in terms of the two-sided Fourier transform:

$$\mathrm{Re}\left[\int_0^\infty d\tau\, e^{i\omega\tau} \langle\tilde{B}_j(\tau)\tilde{B}_k(0)\rangle\right] = \tag{2.21}$$

$$= \frac{1}{2}\int_0^\infty d\tau\, e^{i\omega\tau} \langle\tilde{B}_j(\tau)\tilde{B}_k(0)\rangle + \frac{1}{2}\int_0^\infty d\tau\, e^{-i\omega\tau} \left(\langle\tilde{B}_j(\tau)\tilde{B}_k(0)\rangle\right)^* \tag{2.22}$$

$$= \frac{1}{2}\int_0^\infty d\tau\, e^{i\omega\tau} \langle\tilde{B}_j(\tau)\tilde{B}_k(0)\rangle + \frac{1}{2}\int_0^\infty d\tau\, e^{-i\omega\tau} \langle\tilde{B}_j(-\tau)\tilde{B}_k(0)\rangle \tag{2.23}$$

$$= \frac{1}{2}\int_0^\infty d\tau\, e^{i\omega\tau} \langle\tilde{B}_j(\tau)\tilde{B}_k(0)\rangle + \frac{1}{2}\int_{-\infty}^0 d\hat{\tau}\, e^{i\omega\hat{\tau}} \langle\tilde{B}_j(\hat{\tau})\tilde{B}_k(0)\rangle \tag{2.24}$$

$$= \frac{1}{2}\int_{-\infty}^\infty d\tau\, e^{i\omega\tau} \langle\tilde{B}_j(\tau)\tilde{B}_k(0)\rangle \tag{2.25}$$

For the transform in eq. 2.20 we furthermore substitute the integration variable $\hat{\tau} = -\tau$ a second time and assign the resulting minus sign to the frequency:

$$\frac{1}{2}\int_{-\infty}^{\infty} d\tau\; e^{i\omega\tau}\,\langle \tilde{B}_j(-\tau)\tilde{B}_k(0)\rangle = \frac{1}{2}\int_{-\infty}^{\infty} d\hat{\tau}\; e^{i(-\omega)\hat{\tau}}\,\langle \tilde{B}_j(\hat{\tau})\tilde{B}_k(0)\rangle \tag{2.26}$$

Note that the limits need to be adapted and then swapped, which cancels the minus sign from $d\hat{\tau} = -d\tau$.

2.1.1.2 The equations

We then find a compact and general form of **the Bloch-Redfield equations**:

$$\dot{\rho} = \frac{i}{\hbar}[\rho, H_s] + \frac{1}{\hbar^2}\sum_{j,k}\left(-s_j V q_{jk} V^\dagger \rho + V q_{jk} V^\dagger \rho s_j - \rho V \hat{q}_{jk} V^\dagger s_j + s_j \rho V \hat{q}_{jk} V^\dagger\right) \tag{2.27}$$

$$\text{with} \quad \langle a_n|q_{jk}|a_m\rangle = \langle a_n|\, V^\dagger s_k V\, |a_m\rangle\, \frac{1}{2}C_{jk}(\omega_m - \omega_n) \tag{2.28}$$

$$\langle a_n|\hat{q}_{jk}|a_m\rangle = \langle a_n|\, V^\dagger s_k V\, |a_m\rangle\, \frac{1}{2}C_{kj}(\omega_n - \omega_m) \tag{2.29}$$

$$C_{jk}(\omega) = \int_{-\infty}^{\infty} d\tau\; e^{i\omega\tau}\,\langle \tilde{B}_j(\tau)\tilde{B}_k(0)\rangle \tag{2.30}$$

These equations are true for any basis $|a_n\rangle$. If the eigenbasis of the Hamiltonian H_S is chosen $|a_n\rangle = |\omega_n\rangle$ then the matrix V becomes the identity matrix. Note that the matrix q_{jk} (or $\hat{q}_{jk}$) is simply given by an element-wise multiplication of s_k in the eigenbasis of H_s and the matrix of $C_{jk}(\omega_m - \omega_n)$ (or $C_{kj}(\omega_n - \omega_m)$), where n is the row and m the column of the matrix.

2.1.1.3 Superoperator Form

The Bloch-Redfield equations can be written in *superoperator form*, such that:

$$\dot{\vec{\rho}} = \mathfrak{R}\vec{\rho}$$

where $\vec{\rho} = vec(\rho)$ is the vector representation of ρ and $\mathfrak{R}$ is the Redfield tensor written as one large matrix of dimensions (d^2, d^2) where d is the number of states in the system. In our notation the Redfield tensor $\mathfrak{R}$ includes both the coherent dynamics due to the system Hamiltonian H_S and the decoherent dynamics due to the coupling to the bath.

Note that a matrix can be formed into a vector in two non-equivalent ways (column- or row-ordered), resulting in different superoperators. We use the column-ordered convention here, that is:

$$M := \begin{pmatrix} 1 & 3 \\ 2 & 4 \end{pmatrix} \qquad \Rightarrow \qquad vec(M) = \begin{pmatrix} 1 \\ 2 \\ 3 \\ 4 \end{pmatrix}$$

Column-ordered form is the default for the Matlab function *reshape*. Note that the Mathematica functions *Partition* and *Flatten* use row-ordered form by default (speaking in rows and columns of the display produced by *MatrixForm*).

Using the mathematical relation for column-ordered vector representation [94, 95]

$$vec(AXB) = (B^T \otimes A)vec(X)$$

we can write the Bloch-Redfield equations in superoperator form:

$$\dot{\vec{\rho}} = \mathfrak{R}\vec{\rho} \tag{2.31}$$

$$= \frac{i}{\hbar}\left(H^T \otimes \mathbb{1} - \mathbb{1} \otimes H\right)\vec{\rho} \tag{2.32}$$

$$+ \frac{1}{\hbar^2}\sum_{jk}\left(-\mathbb{1} \otimes s_j V q_{jk} V^\dagger + s_j^T \otimes V q_{jk} V^\dagger - s_j^T V^* \hat{q}_{jk}^T V^T \otimes \mathbb{1} + V^* \hat{q}_{jk}^T V^T \otimes s_j\right)\vec{\rho}$$

where $\mathbb{1}$ is the unity matrix of the dimension of H.

2.1.2 Bloch-Redfield approach to spatial correlations

Spectral function In the Bloch-Redfield equations the spectral functions (eq. 2.30) define the environment. The only restriction on the spectral functions in the formalism is placed by the Markov approximation.

For the Markov approximation the correlation functions of the bath operators $\tilde{B}_j$ at different times $\langle \tilde{B}_j(\tau)\tilde{B}_k(0)\rangle$ were assumed to decay with increasing time difference τ to zero. This decay of the correlation function was assumed to occur over a faster time scale than the system-environment interaction. For the Fourier transform of the correlation function $C_{jk}(\omega)$ the Markov approximation means that $C_{jk}(\omega)$ cannot vary on the scale of the frequency of the system dynamics (i.e. be "smooth" on that

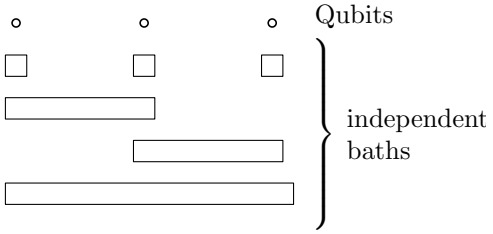

Figure 2.1: Illustration of the independent baths approach for three qubits. Each box symbolises a bath which couples to the qubits above it. Two different boxes are uncorrelated.

scale) because a restriction on the signal width in the time domain is a restriction on the resolution in the frequency domain (and vice versa).

That does not mean that *spatial* correlations break the Markov approximation. A Markovian noise environment can have a long *spatial* correlation length, such that several qubits "feel" a correlated noise, as long as the *temporal* correlations are short-lived.

Independent baths One approach to describing spatially correlated decoherence is to introduce a series of independent baths. The bath operators B_j (see eq. 2.3) can be grouped such that

$$C_{jk}(\omega) = \begin{cases} C_{jk}(\omega) & \text{if } j \text{ and } k \text{ are in the same group} \\ 0 & \text{if } j \text{ and } k \text{ are in different groups} \end{cases}$$

We call each group an independent bath since they are not correlated with the other baths. Independent baths may be due to either groups of different types of coupling operators (see appendix C) or the assumption of a certain structure in the environment.

Such a structure could for example be given in the case where very different, i.e. uncorrelated, sources of decoherence are present. In a system consisting of several subsystems (e.g. qubits, spins) the different sources might affect different subsystems, i.e. we can differentiate independent noise, which affects each subsystem separately, and collective noise. Figure 2.1 illustrates this approach where each individual bath is drawn as a box underneath the qubits which couple to it.

Individual coupling strengths for each qubit and each bath can easily be used in this model if necessary. The simplest method of implementing correlated decoherence is

using independent baths and assuming all spectral functions within one bath to be equal. The amount of correlation is then governed by the relative coupling strength of the common and the independent baths.

Spatial-temporal correlation functions An alternative approach is to regard the environment as a continuum in which the spatial correlations in the noise decay over a certain correlation length. A more flexible model in this case is to generalise the concept of a bath correlation function $\langle B_j(\tau)B_k(0)\rangle$ and its Fourier transform $C_{jk}(\omega)$ to the case of a spatial-temporal correlation function $\langle B_j(\tau,\mathbf{r}_1)B_k(0,\mathbf{r}_2)\rangle$ and the corresponding spectral function:

$$C_{jk}(\omega,\mathbf{r}_j,\mathbf{r}_k) := \int_{-\infty}^{\infty} d\tau\; e^{i\omega\tau}\,\langle \tilde{B}_j(\tau,\mathbf{r}_j)\tilde{B}_k(0,\mathbf{r}_k)\rangle$$

where the components of the system couple to the environment at positions $\mathbf{r}_j, \mathbf{r}_k$.

These 'spectral functions' in time can also be regarded as 'correlation functions' in space and the latter name is also used, particularly when speaking about the spatial aspect for a given frequency. The functions are similar but distinct from the van-Hove functions [96] as we do not transform into k-space to define the spectral function. As in conventional Bloch-Redfield theory, this spectral function can be derived from a more fundamental microscopic model or its form can be phenomenologically assumed based on the physical nature of the environment in question.

Often one considers a homogeneous environment in which the spatial correlations depend only on the distance between the spatially localised subsystems. In that case one can simplify the spectral function to:

$$C_{jk}(\omega,\mathbf{r}_j,\mathbf{r}_k) = C(\omega,|\mathbf{r}_j-\mathbf{r}_k|) \tag{2.33}$$

When both transversal and longitudinal coupling at the same spatial position are considered then one needs to work with two independent homogeneous spectral functions $C_\perp(\omega,|\mathbf{r}_j-\mathbf{r}_k|)$ and $C_\parallel(\omega,|\mathbf{r}_j-\mathbf{r}_k|)$ respectively. See appendices B and C for details. When considering a system spatially localised at one point (e.g. a single qubit), the spatial aspect disappears $C(\omega,|\mathbf{r}_j-\mathbf{r}_j|) = C(\omega,0) = C(\omega)$. For a pair of subsystems with some spatial separation $\mathbf{r}_1-\mathbf{r}_2$, we now have contributions from both the individual self-correlations ($|\mathbf{r}_j-\mathbf{r}_j|=0$) and collective decoherence terms ($|\mathbf{r}_j-\mathbf{r}_k|>0$).

As is usual with Bloch-Redfield theory, we can define a correlation decay time τ over which the correlation function decays to zero. We now also have a correlation length ξ over which the correlations decay in space. If the two qubits are separated such that $|\mathbf{r}_1 - \mathbf{r}_2| \gg \xi$ then the qubits' noise is uncorrelated, whereas $|\mathbf{r}_1 - \mathbf{r}_2| \ll \xi$ implies fully correlated decoherence.

As a basic example we could choose the following form for the spectral function:

$$C(\omega, x) = exp\left(-\frac{\omega^2}{\omega_0^2}\right) exp\left(-\frac{x}{\xi}\right)$$

This spectral function is a Gaussian peaked around zero in frequency, which means it will mainly lead to dephasing. Spatially it decays exponentially with the decay rate $1/\xi$, i.e. the correlation length ξ.

2.1.3 Secular approximation of the Bloch-Redfield equations

We show now that the secular approximation largely simplifies the mathematical form of the Bloch-Redfield equations (to eq. 2.51) in all generality. This is important for mapping the Bloch-Redfield equations to Lindblad form and helps to understand the effect of complex correlation functions. The secular approximation is based on assumptions about separated (secular) time scales of the dynamics of system and environmental coupling. To clearly link assumptions about certain system parameters to the corresponding approximations it is more useful to apply the secular approximation by the technique outlined in the appendix of [6] than in the general formal way presented here.

First we separate the system operators s_j into several operators by multiplication with projection operators onto the Hamiltonian eigenstates $|\omega_n\rangle$.

$$s_j(\epsilon) = \sum_{\omega_m - \omega_n = \epsilon} |\omega_n\rangle \langle\omega_n| s_j |\omega_m\rangle \langle\omega_m| \tag{2.34}$$

The sum extends over all Hamiltonian eigenvalues ω_n and ω_m with a fixed difference ϵ. In other words we split up the matrices $q_{jk}, \hat{q}_{jk}$ in the Bloch-Redfield equations (eq. 2.27) by collecting all elements with the same frequency dependence.

Assuming all s_j to be Hermitian [4] we find:

$$s_j(-\epsilon) = s_j(\epsilon)^\dagger \tag{2.35}$$

Using Eq. 2.34, we write:

$$s_j = \sum_\epsilon s_j(\epsilon) \tag{2.36}$$

$$q_{jk} = V^\dagger \sum_\epsilon s_j(\epsilon) \frac{1}{2} C_{jk}(\epsilon) V \tag{2.37}$$

$$\hat{q}_{jk} = V^\dagger \sum_\epsilon s_j(\epsilon) \frac{1}{2} C_{kj}(-\epsilon) V \tag{2.38}$$

Replacing eq. 2.36 to 2.38 in the Bloch-Redfield equations (eq. 2.27) and changing to the interaction picture (appendix F)

$$e^{iH_S t} s_j(\epsilon) e^{-iH_S t} = e^{-i\epsilon t} s_j(\epsilon) \tag{2.39}$$

One then finds:

$$\begin{aligned}\dot{\tilde{\rho}} = &\sum_{jk\epsilon\epsilon'} e^{-i(\epsilon+\epsilon')t} C_{jk}(\epsilon) \left(-s_j(\epsilon')s_k(\epsilon)\tilde{\rho} + s_k(\epsilon)\tilde{\rho}s_j(\epsilon')\right) \\ &+ \sum_{jk\epsilon\epsilon'} e^{-i(\epsilon+\epsilon')t} C_{kj}(-\epsilon) \left(-\tilde{\rho}s_k(\epsilon)s_j(\epsilon') + s_j(\epsilon')\tilde{\rho}s_k(\epsilon)\right)\end{aligned}$$

Since ϵ includes negative frequencies the only non-oscillating terms are for $\epsilon' = -\epsilon$. In the secular approximation, the oscillating terms which are neglected are fast oscillating on the time scale of the dynamics in the interaction picture. This time scale of the oscillations $\tau_o = 1/|\epsilon - \epsilon'|$ for $\epsilon \neq \epsilon'$ must be much shorter than the decoherence time scale set by the terms C_{jk} and the magnitudes of the s_j. Roughly this can be restated as $H_S \gg H_{int}$. More precisely the condition is that $|\epsilon - \epsilon'|$ must be large (for all $\epsilon \neq \epsilon'$) compared to the relevant system times, which are set by the magnitude of the elements of $C_{jk}(\omega)s_j s_k$, i.e. H_{int}. Since zero is a possible value for ϵ the condition means that the differences ϵ of the energy levels of the system must

[4] In systems where non-Hermitian ladder operators are chosen for the s_j their transform to the interaction picture turns out to oscillate at plus and minus the same frequency, i.e. they also are a pair, which complies with $s_j(-\epsilon) = s_j(\epsilon)^\dagger$. In systems where more complicated non-Hermitian operators are chosen, one could derive the Bloch-Redfield equations by replacing one occurrence of $H_{int} = \sum_j s_j B_j = \sum_j s_j^\dagger B_j^\dagger$ in eqs. 2.9 and 2.10 and continuing analogously otherwise. Note that this means that the correlation functions take the form $\langle \tilde{B}_j^\dagger(\tau) B_k(0) \rangle$.

be large as well as the differences of the differences $\epsilon - \epsilon'$. For cases where this is not fulfilled for certain pairs $\epsilon - \epsilon'$ the secular approximation is usually applied by assuming $\epsilon \approx \epsilon'$ for those differences. Applying the secular approximation one finds:

$$\begin{aligned}\dot{\tilde{\rho}} = \sum_{jk\epsilon} [&C_{jk}(\epsilon)\left(-s_j(-\epsilon)s_k(\epsilon)\tilde{\rho} + s_k(\epsilon)\tilde{\rho}s_j(-\epsilon)\right) \\ &+ C_{kj}(-\epsilon)\left(-\tilde{\rho}s_k(\epsilon)s_j(-\epsilon) + s_j(-\epsilon)\tilde{\rho}s_k(\epsilon)\right)]\end{aligned} \tag{2.40}$$

Since the sum over ϵ extends over all positive and negative energy differences we can replace $-\epsilon \to \epsilon$ in the second line of eq. 2.40. Note that this makes the last two terms the Hermitian conjugate of the first two terms. Furthermore we swap the equivalent indices j and k in the last two terms. This together with eq. 2.35 yields the **Bloch-Redfield equations in the secular approximation**:

$$\dot{\tilde{\rho}} = \sum_{\epsilon} \sum_{jk} C_{jk}(\epsilon) \left(s_k(\epsilon)\tilde{\rho}s_j(\epsilon)^\dagger - \frac{1}{2}\left\{ s_j(\epsilon)^\dagger s_k(\epsilon), \tilde{\rho} \right\} \right) \tag{2.41}$$

In several cases one finds only one frequency in the elements of q_{jk} and $\hat{q}_{jk}$ in which case the summation over ϵ contains only one summand and can be omitted, simplifying eq. 2.41 (back in the Schrödinger picture) to:

$$\dot{\rho} = \frac{i}{\hbar}[\rho, H_s] + \frac{1}{\hbar^2} \sum_{j,k} C_{jk} \left(s_k \rho s_j^\dagger - \frac{1}{2}\{ s_j^\dagger s_k, \rho \} \right) \tag{2.42}$$

For ease of notation, the form of Eq. (2.42) is used in section 2.1.5 without loss of generality. For cases where the summation over ϵ in eq. 2.41 is relevant, each frequency component is added independently and all further results apply analogously. The general arguments above are analogous to the derivation of the Lindblad form on page 128 ff. in Breuer [1].

We rewrite eq. 2.41 in column-ordered superoperator form (sec. 2.1.1.3) again by using

$$vec(AXB) = (B^T \otimes A)vec(X)$$

and convert back to the Schrödinger picture by adding the coherent part:

$$\dot{\vec{\rho}} = \frac{i}{\hbar}\left(H^T \otimes \mathbb{1} - \mathbb{1} \otimes H\right)\vec{\rho} + \frac{1}{\hbar^2}\sum_{jk} C_{jk}(\epsilon)\left(s_j^*(\epsilon) \otimes s_k(\epsilon) - \frac{1}{2}\mathbb{1} \otimes s_j^\dagger(\epsilon)s_k(\epsilon) - \frac{1}{2}s_k^T(\epsilon)s_j^*(\epsilon) \otimes \mathbb{1}\right)\vec{\rho} \quad (2.43)$$

This is the master equation in the secular approximation in superoperator form.

In superoperator form, when the density matrix is written as a vector and the Redfield tensor $\mathfrak{R}$ as a matrix, the secular approximation can be illustrated with this matrix. First the density matrix elements in the vector should be ordered by putting the diagonal elements first and the off-diagonal elements after. The secular approximation then sets all off-diagonal elements in the Redfield tensor matrix to zero except for the upper left submatrix which links the diagonal elements of the density matrix. More details about this are published in appendix A of reference [97].

Eq. 2.41 gives enormous insight into the decoherent dynamics of quantum systems because it shows that no mixed terms between operators which belong to different energy splittings ϵ_1 and ϵ_2 exist. We demonstrate this with an example. For a single qubit in its eigenbasis $H_s = \omega_q\sigma_z$ the most general form of an environmental interaction is given by

$$H_{int} = \sum_{j=1}^{3} s_j B_j = \sigma_x B_1 + \sigma_y B_2 + \sigma_z B_3 \quad (2.44)$$

since the Pauli matrices, together with the unity operator $\mathbb{1}$ form a complete basis of the operator space. In the interaction picture (appendix F) the system operators $\tilde{s}_1, \tilde{s}_2, \tilde{s}_3$ become:

$$\tilde{\sigma}_x = \begin{pmatrix} 0 & e^{2i\omega_q} \\ e^{-2i\omega_q} & 0 \end{pmatrix}; \quad \tilde{\sigma}_y = \begin{pmatrix} 0 & -ie^{2i\omega_q} \\ ie^{-2i\omega_q} & 0 \end{pmatrix}; \quad \tilde{\sigma}_z = \begin{pmatrix} 1 & 0 \\ 0 & -1 \end{pmatrix}$$

According to eq. 2.34 and 2.39 we break the system operators up into the $s_j(\epsilon)$ with three values for $\epsilon \in \{2\omega_q, -2\omega_q, 0\}$. We find only three relevant operators[5], which

[5]Note that $s_2(2\omega_q)$ and $s_2(-2\omega_q)$ are neglected because they are linearly dependent $s_2(2\omega_q) \propto s_1(2\omega_q)$ and $s_2(-2\omega_q) \propto s_1(-2\omega_q)$. Any complex coefficient in eq. 2.41 can be absorbed into the spectral function assuming a complex spectral function (see section 2.1.4).

turn out to be $\sigma_-, \sigma_+, \sigma_z$:

$$s_1(2\omega_q) = \begin{pmatrix} 0 & 0 \\ 1 & 0 \end{pmatrix}; \quad s_1(-2\omega_q) = \begin{pmatrix} 0 & 1 \\ 0 & 0 \end{pmatrix}; \quad s_3(0) = \begin{pmatrix} 1 & 0 \\ 0 & -1 \end{pmatrix} \tag{2.45}$$

Eq. 2.41 tells us that no mixed terms between these three operators occur because they each belong to a different energy ϵ. The operators cause relaxation, excitation gain and dephasing respectively.

Furthermore for a system of N qubits we find N operators corresponding to each of the three values[6] of ϵ. Again operators corresponding to different values of ϵ are not combined in eq. 2.41. Therefore dephasing, relaxation and excitation gain can always be regarded as coupling to different independent baths. In other words, the indices j and k are purely spatial indices and in all generality there are three independent baths for qubit systems, each with its own spatial correlation function: $C(2\omega_q, \mathbf{r}_j, \mathbf{r}_k)$ for relaxation (energy loss), $C(-2\omega_q, \mathbf{r}_j, \mathbf{r}_k)$ for excitation gain (energy gain) from the environment and $C(0, \mathbf{r}_j, \mathbf{r}_k)$ for dephasing. The master equation 2.41 takes the form:

$$\begin{aligned} \dot{\rho} = \frac{i}{\hbar}[\rho, H_s] &+ \frac{1}{\hbar^2}\sum_{j,k} C(2\omega_q, \mathbf{r}_j, \mathbf{r}_k)\left(\sigma_-^{(k)}\rho\sigma_+^{(j)} - \frac{1}{2}\{\sigma_+^{(j)}\sigma_-^{(k)}, \rho\}\right) \\ &+ \frac{1}{\hbar^2}\sum_{j,k} C(-2\omega_q, \mathbf{r}_j, \mathbf{r}_k)\left(\sigma_+^{(k)}\rho\sigma_-^{(j)} - \frac{1}{2}\{\sigma_-^{(j)}\sigma_+^{(k)}, \rho\}\right) \\ &+ \frac{1}{\hbar^2}\sum_{j,k} C(0, \mathbf{r}_j, \mathbf{r}_k)\left(\sigma_z^{(k)}\rho\sigma_z^{(j)} - \frac{1}{2}\{\sigma_z^{(j)}\sigma_z^{(k)}, \rho\}\right) \end{aligned} \tag{2.46}$$

The same observation of different independent baths is made more explicitly in appendix C. The secular approximation is mathematically analogous to the rotating-wave approximation, typically made for a fast-oscillating external driving field [98].

[6] For N qubits the coupling energies between qubits need to be considered. However, the Markov approximation forces us to regard the spectral function as smooth on the scale of all coupling energies. Energy splittings which differ only by these coupling energies are therefore approximated as the same value for ϵ.

2.1.4 Complex spectral functions and correlated decoherence lead to environment-induced couplings

Strictly speaking the spectral function $C_{jk}(\omega)$ is only the real part of a one-sided Fourier transform $D_{jk}(\omega_n - \omega_m) := \int_0^\infty d\tau \; e^{i(\omega_n-\omega_m)\tau} \langle \tilde{B}_j(\tau)\tilde{B}_k(0)\rangle$ (see eq. 2.19) which can in general be complex. Taking that into account eq. 2.40 becomes[7]:

$$\begin{aligned}\dot{\tilde{\rho}} = &\sum_{jk\epsilon} D_{jk}(\epsilon)\left(-s_j(-\epsilon)s_k(\epsilon)\tilde{\rho} + s_k(\epsilon)\tilde{\rho}s_j(-\epsilon)\right) \\ &+ \sum_{jk\epsilon} (D_{jk}(\epsilon))^*\left(-\tilde{\rho}s_k(-\epsilon)s_j(\epsilon) + s_j(\epsilon)\tilde{\rho}s_k(-\epsilon)\right)\end{aligned} \tag{2.47}$$

Dividing the expression into its real and imaginary components $D_{jk}(\epsilon) = C_{jk}(\epsilon) + iF_{jk}(\epsilon)$, one finds additional terms to eq. 2.41:

$$\dot{\tilde{\rho}} = \sum_\epsilon \sum_{jk} \frac{1}{2} C_{jk}(\epsilon)\left(2s_k(\epsilon)\tilde{\rho}s_j(\epsilon)^\dagger - \left\{s_j(\epsilon)^\dagger s_k(\epsilon), \tilde{\rho}\right\}\right) \tag{2.48}$$

$$+ \sum_\epsilon \sum_{jk} iF_{jk}(\epsilon)\left(\rho s_j(\epsilon)^\dagger s_k(\epsilon) - s_j(\epsilon)^\dagger s_k(\epsilon)\rho\right) \tag{2.49}$$

which (back in the Schrödinger picture) can be regarded as a correction to the system Hamiltonian.

$$\begin{aligned}\dot{\rho} &= \frac{i}{\hbar}[\rho, H_s + H_{cor}] + \frac{1}{\hbar^2}\sum_\epsilon \sum_{jk} \frac{1}{2} C_{jk}(\epsilon)\left(2s_k(\epsilon)\tilde{\rho}s_j(\epsilon)^\dagger - \left\{s_j(\epsilon)^\dagger s_k(\epsilon), \tilde{\rho}\right\}\right) \\ H_{cor} &= \frac{1}{\hbar}\sum_\epsilon \sum_{jk} F_{jk}(\epsilon) s_j(\epsilon)^\dagger s_k(\epsilon)\end{aligned} \tag{2.50}$$

A correction Hamiltonian of this form is sometimes called a "Lamb shift term" [1]. In cases of uncorrelated decoherence (all terms for which $j \neq k$ are zero) this correction of the system Hamiltonian is generally neglected since the terms $s_j^\dagger s_j$ in qubit systems are diagonal in the system eigenbasis. In cases of correlated decoherence however the correction Hamiltonian H_{cor} for qubit systems can lead to interaction terms between the qubits, i.e. oscillations due to environmentally induced interactions.

[7] The fact that the spectral function in the second term becomes simply the complex conjugate of the first can either be derived assuming $B_j^\dagger = B_j$ or following the procedure mentioned in the footnote on page 18 and noting that $\langle \tilde{B}_j^\dagger(\tau)B_k(0)\rangle^* = \langle \tilde{B}_k^\dagger(0)B_j(\tau)\rangle$.

2.1.5 Mapping the master equation to the Lindblad form

Our model is based on the Bloch-Redfield equations. Their core strength is the underpinning physical model, which is set by the system operators which couple to the environment and by environmental correlation functions. A different master equation, which is equally if not more commonly used is the Lindblad master equation. It was independently published by Göran Lindblad [42] and Gorini, Kossakowski, Sudarshan [43]. Contrary to the Bloch-Redfield equation they do not necessarily connect directly to a physical model of the environment, but are often used with phenomenologically assumed decoherence rates for the system. However, the Lindblad form of a master equation is known to be "the most general form of the generator of a quantum dynamical semigroup" [1, 42, 43]. This means that the evolution due to a certain master equation preserves complete positivity of the density matrix if and only if there exists a basis in which the master equation takes on Lindblad form. The Bloch-Redfield equations do not guarantee complete positivity by their mathematical form but depend on a consistent model of the environment's temporal and spatial correlation functions. When assuming a phenomenological spatial-temporal correlation function $C_{jk}(\omega, \mathbf{r}_j, \mathbf{r}_k)$, highly non-trivial physical conditions apply for multipartite correlations.

We will therefore now present a method to test whether or not our master equations can be mapped to Lindblad form and then prove for chains of equidistant two-level systems that this mapping is possible and straight-forward for all master equations which are based on either any Gaussian spatial correlation function or any exponentially decaying spatial correlation function. This proof will be true for an arbitrary number of two-level systems (TLSs) with an arbitrary (but equal for all nearest neighbours) distance between them. Furthermore we will show that a master equation based on a step correlation function cannot in general be mapped to Lindblad form, which reflects the physical contradiction arising from a step correlation function.

2.1.5.1 General conditions for the mapping

To map our master equations to the Lindblad form [1, 42, 43] we take the Bloch-Redfield equations in the secular approximation[8] (eq. 2.42):

$$\dot{\rho} = \frac{i}{\hbar}[\rho, H_s] + \frac{1}{\hbar^2}\sum_{j,k} C_{jk}\left(s_k \rho s_j^\dagger - \frac{1}{2}\left\{s_j^\dagger s_k, \rho\right\}\right) \tag{2.51}$$

Equation 2.51 can be mapped to the Lindblad form if the coefficient matrix C_{jk} is positive semi-definite, i.e. can be diagonalised with non-negative eigenvalues. The coefficient matrix is real and symmetric, i.e. Hermitian. The matrix of its eigenvectors u (if it exists) is therefore unitary. If the coefficient matrix C_{jk} is furthermore positive semi-definite then u exists and

$$u^\dagger C_{jk} u = \begin{pmatrix} \gamma_1 & 0 & 0 & \dots \\ 0 & \gamma_2 & 0 & \\ 0 & 0 & \gamma_3 & \\ \vdots & & & \ddots \end{pmatrix} \tag{2.52}$$

with only positive semi-definite $\gamma_j \geq 0$. In that case eq. 2.51 is finally brought into Lindblad form by defining a new set of operators:

$$L_k := \sum_j u_{jk} s_j \qquad \Rightarrow \qquad s_j = \sum_k (u^\dagger)_{kj} L_k = \sum_k u_{jk}^* L_k \tag{2.53}$$

$$\text{because } \sum_k (u^\dagger)_{kl} L_k = \sum_{jk} (u^{-1})_{kl} u_{jk} s_j = \sum_j \delta_{lj} s_j = s_l$$

Expressing all s_j and s_k in eq. 2.51 with L_k we find terms of the form:

$$\sum_{jk} C_{jk} s_j s_k^\dagger \rho = \sum_{jklm} C_{jk} (u^\dagger)_{lj} L_l u_{km} L_m^\dagger \rho = \sum_{lm} \gamma_l \delta_{lm} L_l L_m^\dagger \rho = \sum_l \gamma_l L_l L_l^\dagger \rho$$

Analogous simplification for all terms finally yields the usual Lindblad form:

$$\dot{\rho} = \frac{i}{\hbar}[\rho, H_s] + \frac{1}{\hbar^2}\sum_j \gamma_j \left(L_j \rho L_j^\dagger - \frac{1}{2}\left\{L_j^\dagger L_j, \rho\right\}\right)$$

[8] Note that instead of taking the secular approximation one can also assume an immediate decay of the correlation function $\langle \tilde{B}_j(\tau)\tilde{B}_k(0)\rangle = \delta(\tau)$, which makes the spectral function frequency independent and also simplifies the Bloch-Redfield equations to the form of eq. 2.51

The Lindblad rates γ_j are non-negative if the coefficient matrix is positive semi-definite (eq. 2.52). If one or more eigenvalues of the coefficient matrix are negative then according to Sylvester's law of inertia [99] [9] all diagonalising transforms $u^\dagger C_{jk} u$ (including non-unitary matrices u) will have the same number of negative values on the diagonal, i.e. there is no mapping to Lindblad form.

2.1.5.2 Exponentially decaying, Gaussian and step-function spatial correlations

System sites which are far apart are likely to be exposed to uncorrelated noise, but when sites are situated close enough the noise sources will inevitably overlap. In this section we investigate valid functional forms for this transition and find exponential as well as Gaussian decay generally physically valid for Markovian noise by mapping to Lindblad form. Furthermore we find that a step-function cutoff of spatial noise correlations cannot be used as a homogeneous correlation function for Markovian noise.

To map our master equations to Lindblad form the coefficient matrix in equation 2.51 must be positive semi-definite. This coefficient matrix is given by the spatial correlation function C_{jk}, where j and k are the indices of two different bath operators. Assuming a one-dimensional system of equidistant TLS simplifies the expression for C_{jk} to be only dependent on the magnitude of the difference $C_{jk} = C(d * |j - k|)$ with j and k natural numbers and d the distance between neighbouring subsystems. Absorbing d into the functional form of $C(|j - k|)$ the coefficient matrix takes the

[9] To facilitate the understanding of Sylvester's law of inertia: many algebra books give Sylvester's law of inertia in terms of bilinear forms. Reference [99] states it for the more general case (needed here) of a sesquilinear form $\Phi(x, y)$ and an orthogonal basis x_j with respect to Φ. Note that any Hermitian matrix A defines a sesquilinear form for two vectors x, y by $\Phi(x, y) = y^* A x$. An orthogonal basis with respect to Φ means $\Phi(x_j, x_k) = 0$ for $j \neq k$. This is equivalent to eq. 2.52 using the x_j as the columns of a matrix u. This matrix (different to eq. 2.52) is potentially non-unitary but invertible (since x_j form a basis). Sylvester's law of inertia states that the number of positive and negative $\Phi(x_j, x_j)$ is independent of the choice of the basis. In terms of matrices that means that the number of positive and negative diagonal elements γ_j in eq. 2.52 is independent of the choice of any invertible matrix u. This is non-trivial because non-unitary transformations are included which are not basis transformations in the usual sense. In other words, if the matrix is diagonalised and one or more negative diagonal elements are found than all diagonalising invertible matrices u will lead to a negative diagonal element.

form:

$$(C_{jk}) = \begin{pmatrix} C(0) & C(1) & C(2) & C(3) & \dots \\ C(1) & C(0) & C(1) & C(2) & \ddots \\ C(2) & C(1) & C(0) & C(1) & \ddots \\ C(3) & C(2) & C(1) & C(0) & \ddots \\ \vdots & \ddots & \ddots & \ddots & \ddots \end{pmatrix}$$

In this matrix all elements on a line parallel to the diagonal are equal. This type of matrix is called Toeplitz matrix. A short notation of a Toeplitz matrix is defined by

$$T_n = [t_k; k = -n, -n+1, ..., n-1, n]$$

with the convention:

$$\begin{pmatrix} t_0 & t_{-1} & t_{-2} & t_{-3} & \dots & t_{-n+1} \\ t_1 & t_0 & t_{-1} & t_{-2} & \ddots & \\ t_2 & t_1 & t_0 & t_{-1} & \ddots & \\ t_3 & t_2 & t_1 & t_0 & \ddots & \\ \vdots & \ddots & \ddots & \ddots & \ddots & \vdots \\ t_{n-1} & & & & \dots & t_0 \end{pmatrix}$$

For increasing size n a sequence of Toeplitz matrices is defined by the same t_k. In this notation all possible coefficient matrices are given by the sequence defined by $t_k = C(|k|)$. A helpful tool to determine whether Toeplitz matrices are positive semi-definite is given by Gray [100] in Chapter 4.2, Lemma 6:

The eigenvalues of a Hermitian Toeplitz matrix with absolutely summable elements t_k,

$$\sum_{k=-\infty}^{\infty} |t_k| < \infty$$

are not smaller than the minimum and not greater than the maximum of the Fourier series (appendix G) $f(\lambda)$ *defined by*

$$f(\lambda) = \sum_{k=-\infty}^{\infty} t_k e^{-ik\lambda}.$$

Using this Lemma it can be shown that exponentially decaying spatial correlations as well as Gaussian spatial correlations lead to coefficient matrices with positive semi-definite eigenvalues and the corresponding master equations can therefore always be mapped to Lindblad form.

Exponentially decaying spatial correlations

Assume a sequence of Toeplitz matrices given by the elements:

$$u_k = e^{-a|k|} \qquad \text{with } a > 0$$

The elements are absolutely summable:

$$\sum_{k=-\infty}^{\infty} |u_k| = \sum_{k=0}^{\infty} e^{-ak} + \sum_{k=1}^{\infty} e^{-ak} = \frac{1}{1-e^{-a}} + \sum_{k=0}^{\infty} e^{-ak} - 1 = \frac{2}{1-e^{-a}} - 1 < \infty$$

The Fourier series could be proven to be greater than zero easily with Mathematica by evaluating the code:

$$\text{Simplify[FullSimplify[Sum[Exp[}Ik\lambda\text{]Exp[}-a\text{Abs[}k\text{]], }\{k, -\infty, \infty\}\text{]] > 0, }a > 0\text{]}$$

This evaluates to $\cos[\lambda] < \text{Cosh}[a]$, which is true since $a > 0$.

However without the help of Mathematica, the Fourier series can be evaluated:

$$\begin{aligned}
g(\lambda) &= \sum_{k=-\infty}^{\infty} u_k \exp(-ik\lambda) = \sum_{k=-\infty}^{\infty} \exp(-ik\lambda - a|k|) \\
&= \sum_{k=0}^{\infty} \exp[k(-a - i\lambda)] + \sum_{k=-\infty}^{-1} \exp[k(a - i\lambda)] \\
&= \frac{1}{1-\exp(-a-i\lambda)} + \sum_{k=0}^{\infty} \exp[k(-a+i\lambda)] - 1 \\
&= \frac{1}{1-\exp(-a-i\lambda)} + \frac{1}{1-\exp(-a+i\lambda)} - 1 \\
&= \frac{1}{1-\exp(-a-i\lambda)} + c.c. - 1 \\
&= 2\,\text{Re}\left(\frac{1}{1-e^{-a}(\cos\lambda - i\sin\lambda)} \frac{(1-e^{-a}\cos\lambda - i\,e^{-a}\sin\lambda)}{(1-e^{-a}\cos\lambda - i\,e^{-a}\sin\lambda)}\right) - 1 \\
&= -1 + \frac{2(1-e^{-a}\cos\lambda)}{1-2e^{-a}\cos\lambda + e^{-2a}}
\end{aligned}$$

The extrema of this function are at $\sin\lambda = 0$. Defining $u := e^{-a}$ leads to $0 < u < 1$ and the extrema then give the values:

$$g_{max} = -1 + \frac{2(1-u)}{1-2u+u^2}$$
$$g_{min} = -1 + \frac{2(1+u)}{1+2u+u^2} > -1 + \frac{2(1+u)}{1+2u+1} = 0$$

Since the Fourier series $g(\lambda)$ is greater than zero, the eigenvalues of the corresponding Toeplitz matrices are greater zero. Any master equation based on an exponentially decaying spatial correlation function $C_{jk} = \exp(-a|j-k|)$ can therefore be mapped to Lindblad form.

Gaussian spatial correlations

Assume a sequence of Toeplitz matrices given by the elements:

$$v_k = e^{-ak^2}$$

The elements are absolutely summable:

$$\sum_{k=-\infty}^{\infty} v_k = \sum_{k=-\infty}^{\infty} e^{-ak^2} = 2\sum_{k=0}^{\infty} e^{-ak^2} - 1 \leq 2\sum_{k=0}^{\infty} e^{-ak} - 1 = 2\frac{1}{1-e^{-a}} - 1 < \infty$$

The Fourier series is:

$$h(\lambda) = \sum_{k=-\infty}^{\infty} v_k e^{ik\lambda} = \sum_{k=-\infty}^{\infty} e^{-ak^2+ik\lambda} = \sum_{k=1}^{\infty} e^{-ak^2+ik\lambda} + 1 + \sum_{k=1}^{\infty} e^{-ak^2-ik\lambda}$$
$$= 1 + 2\sum_{k=1}^{\infty} e^{-ak^2}\cos(k\lambda)$$

This can be written in terms of the third Jacobian theta-function. Its definition and a helpful formula can be found in Whittaker and Watson [101], chapter 21, p.463f, p.475:

$$\vartheta_3(z,q) := 1 + 2\sum_{n=1}^{\infty} q^{n^2}\cos(2nz)$$
$$\vartheta_3(z|\tau) := \vartheta_3(z, e^{i\pi\tau})$$
$$\vartheta_3(z|\tau) = (-i\tau)^{-\frac{1}{2}} \exp\left(\frac{z^2}{\pi i\tau}\right) \vartheta_3\left(\frac{z}{\tau}\middle| -\frac{1}{\tau}\right)$$

The last formula can be applied to $h(\lambda)$:

$$\begin{aligned}
h(\lambda) &= \vartheta_3\left(\frac{\lambda}{2}, q = e^{-a}\right) = \vartheta_3\left(\frac{\lambda}{2}\middle|\, \tau = i\frac{a}{\pi}\right) \\
&= \left(-ii\frac{a}{\pi}\right)^{-\frac{1}{2}} \exp\left(\frac{\lambda^2\pi}{4\pi iia}\right) \vartheta_3\left(\frac{\lambda\pi}{2ia}\middle|\, \frac{-\pi}{ia}\right) \\
&= \sqrt{\frac{\pi}{a}} \exp\left(\frac{-\lambda^2}{4a}\right) \vartheta_3\left(\frac{\lambda\pi}{2ia}\middle|\, \frac{-\pi}{ia}\right) \\
&= \sqrt{\frac{\pi}{a}} \exp\left(\frac{-\lambda^2}{4a}\right) \left(1 + 2\sum_{k=1}^{\infty} \exp\left(\frac{-\pi^2k^2}{a}\right) \cos\left(\frac{k\lambda\pi}{ia}\right)\right) \\
&= \underbrace{\sqrt{\frac{\pi}{a}} \exp\left(\frac{-\lambda^2}{4a}\right)}_{>0} \left(1 + 2\sum_{k=1}^{\infty} \underbrace{\exp\left(\frac{-\pi^2k^2}{a}\right)}_{>0} \underbrace{\cosh\left(\frac{k\lambda\pi}{a}\right)}_{>0}\right) \\
&> 0
\end{aligned}$$

The Fourier series $h(\lambda)$ consists of a positive coefficient multiplied with a sum over only positive summands and is therefore positive itself. The eigenvalues of the corresponding Toeplitz matrices must therefore be greater zero. This means that any master equation based on a Gaussian correlation function $C_{jk} = e^{-a(j-k)^2}$ can be mapped to Lindblad form.

Step-function spatial correlations

Assume a sequence of Toeplitz matrices given by the elements:

$$w_k = \begin{cases} 1 & \text{for } |k| < 2 \\ 0 & \text{otherwise} \end{cases}$$

The elements are absolutely summable since there are only three, $k \in \{-1, 0, 1\}$. The Fourier series however has negative values:

$$\sum_{k=-\infty}^{\infty} w_k e^{ik\lambda} = e^{i\lambda} + e^{-i\lambda} + 1 = 1 + 2\cos\lambda$$

In fact one finds

$$\det\begin{pmatrix} 1 & 1 & 0 \\ 1 & 1 & 1 \\ 0 & 1 & 1 \end{pmatrix} = -1,$$

which proves that the matrix is not positive semi-definite. This matrix is a principal submatrix to all larger Toeplitz matrices based on w_k or on a similar step function with the step at $k = k_0 > 2$. All of these matrices are therefore not positive semi-definite either. This can be proven with the help of Pemberton/Rau [102], p.239, statement b), which reads:

An $n \times n$ symmetric matrix is positive semi-definite if and only if the determinant of its principal submatrices are all non-negative.

This means that master equations based on a spatial correlation function with a non-trivial step (i.e. other than the step below $k_0 = 1$) cannot be mapped to Lindblad form. This reflects the physical contradiction induced by step-function spatial correlations: Suppose three subsequent TLS A, B and C with the correlation function $C(k) = w_k$, which means perfect correlation with nearest neighbours, no correlation to further neighbours. That means that the noise of A and B is perfectly correlated, the noise of B and C is perfectly correlated, however the noise of A and C is not correlated at all, which is contradictory. Similarly any step function induces a contradiction, which is reflected in the negative eigenvalues of the corresponding coefficient matrix.

In conclusion we find that for partially correlated environments a spatial decay of correlations in exponential or Gaussian shape is a realistic phenomenological model, while a step function is not.

2.2 Spatially correlated effects in qubit systems

After discussing the derivation and intricate details of the Bloch-Redfield equations we will now give a practical, general approach for spatially correlated decoherence. We will then point out very generally the new dynamics and effects that emerge from spatial noise correlations in systems of several TLSs (qubits, spin-1/2 etc.), without defining the system parameters such as interqubit coupling or dimensionality more closely. These results give an intuition and form a starting point for the analysis of any particular system. As we pointed out in the previous section dephasing and relaxation generally couple to separate baths and we will discuss them separately.

2.2.1 The quick users' guide to Bloch-Redfield equations

Our approach is applicable to systems of any number of spatially located sites. We will use the language of qubits here, however it is equally applicable for systems with any number of sites (e.g. harmonic oscillators, spins, photonic modes, molecules, pigments in light-harvesting complexes etc.) as long as these states have large on-site energies compared to the couplings between sites.

Consistent with the majority of controllable quantum systems we work with the secular approximation based on large on-site energies (i.e. qubit level splittings) compared to the couplings between sites. This removes any couplings other than longitudinal and transversal coupling (appendix B). The secular approximation furthermore guarantees independent baths for dephasing, relaxation and excitation gain (eq. 2.46 and appendix C) even for spatially correlated noise. Note that this is a very common parameter regime, however the secular approximation can be applied to any regime where parameters of different orders of magnitude appear. To generalize, it decouples the subspaces, which differ in the number of excitations in the large order of magnitude and guarantees independent (i.e. uncorrelated) baths for the groups of operators which belong (in the sense of eq. 2.39) to different energies ϵ (on that large scale).

Without loss of generality (w.l.o.g.) we choose the uncoupled qubits' eigenbasis, i.e. the system Hamiltonian reads $H_s = \sum_j (\omega_q + \delta^{(j)})\sigma_z^{(j)} + couplings$. For the secular approximation it is necessary, that the differences $\delta^{(j)}$ between the qubits' eigenenergies are small compared to ω_q, i.e. only of the order of the interqubit couplings. The master equation can then immediately be written as (eq. 2.46):

$$\begin{aligned}\dot{\rho} = \frac{i}{\hbar}[\rho, H_s] &+ \frac{1}{\hbar^2}\sum_{j,k} C(2\omega_q, \mathbf{r}_j, \mathbf{r}_k)\left(\sigma_-^{(k)}\rho\sigma_+^{(j)} - \frac{1}{2}\{\sigma_+^{(j)}\sigma_-^{(k)}, \rho\}\right) \\ &+ \frac{1}{\hbar^2}\sum_{j,k} C(-2\omega_q, \mathbf{r}_j, \mathbf{r}_k)\left(\sigma_+^{(k)}\rho\sigma_-^{(j)} - \frac{1}{2}\{\sigma_-^{(j)}\sigma_+^{(k)}, \rho\}\right) \\ &+ \frac{1}{\hbar^2}\sum_{j,k} C(0, \mathbf{r}_j, \mathbf{r}_k)\left(\sigma_z^{(k)}\rho\sigma_z^{(j)} - \frac{1}{2}\{\sigma_z^{(j)}\sigma_z^{(k)}, \rho\}\right) \quad (2.54)\end{aligned}$$

The spectral function of positive frequency $C(2\omega_q, \mathbf{r}_j, \mathbf{r}_k)$ determines the strength of the relaxation (energy loss), while negative frequency $C(-2\omega_q, \mathbf{r}_j, \mathbf{r}_k)$ determines the strength of excitation gain from the environment. The zero frequency noise $C(0, \mathbf{r}_j, \mathbf{r}_k)$ determines the dephasing strength. The spectral function at these three

frequencies forms three independent spatial correlation functions.

The indices j, k are spatial indices and run over all qubits in the system. The three spatial correlation functions can be derived from a particular microscopic model of the environment or simply set to phenomenologically reasonable functions. Phenomenological spatial correlation functions are usually assumed to be homogeneous $C(\omega, |\mathbf{r}_j - \mathbf{r}_k|)$ and normalised such that self-correlations $C(\omega, 0) = 1$ and any magnitude is defined by an additional system-environment coupling strength. For spatially uncorrelated noise they turn into Kronecker-deltas $C(\omega, r_j, r_k) = \delta_{jk}\, C(\omega)$. For perfect spatial correlations one sets $C(\omega, |\mathbf{r}_j - \mathbf{r}_k|) = C(\omega)$. For anything in between these extremes one needs to assume a functional form, e.g. exponential decay or Gaussian decay on a correlation length ξ. Not all functional forms are necessarily physically possible, so one needs to choose carefully. Section 2.1.5.1 gives a method to test any assumed spatial correlation function and section 2.1.5.2 proves exponential and Gaussian decay as valid forms. Examples of microscopic models for the environment and respective derivations of the spatial correlation functions can be found in chapter 3.

2.2.2 Spatially correlated dephasing

For n qubits in an uncorrelated environment the dephasing rate between two states is proportional to the number n_f of flipped qubits between the two states. In a perfectly correlated environment however the dephasing rate between two states with a difference of n_e excitations is proportional to n_e^2 and n_f is irrelevant. This is shown in detail in appendix D. Therefore the dephasing rate between states with equal excitation number is reduced to zero when the noise correlation length increases well beyond the qubits' separation. In other words each subspace of states with equal numbers of excitations becomes a decoherence-free subspace. On the other hand for states such as the GHZ state $|111...\rangle + |000...\rangle)/\sqrt{2}$ which have $n_f = n_e$ the dephasing rate increases enormously in spatially correlated environments. These effects of spatially correlated dephasing have also been mentioned in references [16, 48, 75, 103].

Taking four qubits as an example, an off-diagonal density matrix element of the form $|0011\rangle\langle 1100|$ will decay with rate $\Gamma = n_f\gamma = 4\gamma$ for correlation length $\xi \to 0$ and as $\Gamma = n_e^2\gamma = 0$ for $\xi \to \infty$, where γ is the corresponding single qubit dephasing rate. In contrast, the coherence $|0000\rangle\langle 1111|$ also decays as $\Gamma = n_f\gamma = 4\gamma$ for $\xi \to 0$, but will decay as $\Gamma = n_e^2\gamma = 16\gamma$ for $\xi \to \infty$, i.e. the rate increases immensely for long

correlation length (compare figure 2.2).

two states	$\|0000\rangle$, $\|1111\rangle$	$\|0011\rangle$, $\|1100\rangle$	$\|0000\rangle$, $\|0001\rangle$
dephasing rate for $\xi \to 0$	4γ	4γ	γ
dephasing rate for $\xi \to \infty$	16γ	0	γ

Figure 2.2: With increasing correlation length the change of the dephasing rate is strongly dependent on the pair of states.

2.2.3 Spatially correlated relaxation

We will now regard qubit systems with only the relaxation (energy loss) part of eq. 2.46, which is proportional to $C(2\omega_q, \mathbf{r}_j, \mathbf{r}_k)$.

In an uncorrelated environment relaxation is easily understood. A state with m_{exc} qubits in the excited state and m_{gr} qubits in the ground state will have m_{exc} transition rates[10] into lower energy states and m_{gr} rates from higher energy states. In other words the time-derivative of its corresponding diagonal density matrix element will depend on m_{exc} other diagonal elements with a negative coefficient and on m_{gr} other diagonal elements with a positive one.

In a fully correlated environment the dynamics is much harder to grasp. For two qubits [5] one finds the state $(|\uparrow\downarrow\rangle - |\downarrow\uparrow\rangle)/\sqrt{2}$ to be relaxation-free, i.e. stationary. The state $(|\uparrow\downarrow\rangle + |\downarrow\uparrow\rangle)/\sqrt{2}$ on the other hand decays twice as fast to the ground state as for uncorrelated decoherence. Furthermore the state $|\uparrow\uparrow\rangle$ has only one decay rate (instead of two) into the state $|\uparrow\downarrow\rangle + |\downarrow\uparrow\rangle$. This effect was mentioned in [9] and is completely analogous to Dicke's model of super- and sub-radiance in an atomic gas [7].

Regarding the part of eq. 2.46 which determines the excitation gain from the environment and is proportional to $C(-2\omega_q, \mathbf{r}_j, \mathbf{r}_k)$ we find qualitatively the same effects with the inverse rates for two qubits in a fully correlated environment.

This result for two qubits however does not generalize to more qubits easily. The analogy to the Dicke model can be used to understand the dynamics for more qubits via the Clebsch-Gordan coefficients. Regarding the qubits as spin-1/2 particles one can for example always find a relaxation-free state. It is the eigenstate $|\Psi\rangle$ with

[10] A transition rate or relaxation rate from state $|a\rangle$ to state $|b\rangle$ means that $\frac{d}{dt}\rho_{aa} = -\gamma\rho_{aa} + ...$ and $\frac{d}{dt}\rho_{bb} = \gamma\rho_{aa} + ...$

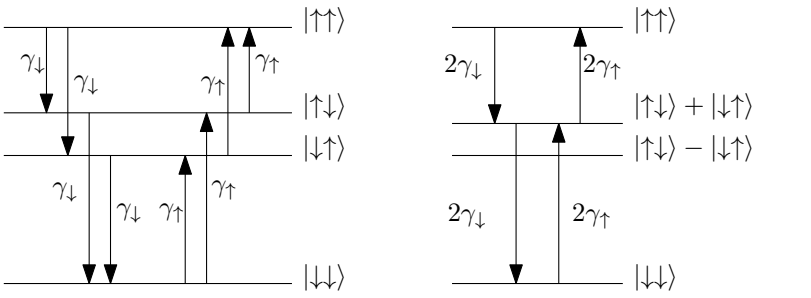

Figure 2.3: Relaxation rates and excitation rates for a qubit pair in uncorrelated (left) and fully correlated (right) environments. For uncorrelated decoherence all states in the subspace $\{|\uparrow\downarrow\rangle, |\downarrow\uparrow\rangle\}$ decay at the same rate. For fully correlated noise there is one stationary (i.e. decoherence-free) state and one that decays twice as fast. The rates are $\gamma_\downarrow = C(2\omega_q, 0)$ and $\gamma_\uparrow = C(-2\omega_q, 0)$.

$S_z |\Psi\rangle = \sum_j \sigma_z^{(j)} |\Psi\rangle = 0$ and zero total spin $S^2 |\Psi\rangle = S_x^2 + S_y^2 + S_z^2 |\Psi\rangle = 0$ (see ref. [7]).

Single excitation subspace In low-temperature systems the equilibrium state is very close to the ground state and the dynamics of a single excitation in a system of n qubits is often of interest. For this subspace of states with only one excitation the two qubit example gives us a good understanding of the dynamics. The subspace is spanned by the n states:

$$\begin{aligned} &|\uparrow\downarrow\downarrow \ldots \downarrow\rangle \\ &|\downarrow\uparrow\downarrow \ldots \downarrow\rangle \\ &|\downarrow\downarrow\uparrow \ldots \downarrow\rangle \\ &\ldots \\ &|\downarrow\downarrow\downarrow \ldots \uparrow\rangle \end{aligned} \tag{2.55}$$

Since all but one qubit are in the ground state we can immediately identify $n-1$ decoherence-free, i.e. stationary states:

$$|s_1\rangle = v_2 |\uparrow\downarrow\downarrow \ldots \downarrow\rangle - v_1 |\downarrow\uparrow\downarrow \ldots \downarrow\rangle \tag{2.56}$$

$$|s_2\rangle = v_3 |\uparrow\downarrow\downarrow \ldots \downarrow\rangle - v_1 |\downarrow\downarrow\uparrow \ldots \downarrow\rangle \tag{2.57}$$

$$\ldots \tag{2.58}$$

$$|s_{n-1}\rangle = v_{n-1} |\uparrow\downarrow\downarrow \ldots \downarrow\rangle - v_1 |\downarrow\downarrow\downarrow \ldots \uparrow\rangle \tag{2.59}$$

where v_j is the coupling strength of the jth spin to the environment. Of course we could also choose any other pair, however with the given set of states we have chosen $n-1$ linearly independent (but not orthogonal) states. Further pairs would only be superpositions of the given set of stationary states. The linear independence becomes clear when we note that each stationary state is a superposition of $|\uparrow\downarrow\downarrow\ldots\downarrow\rangle$ with respectively one other state of the orthogonal set 2.55.

The master equation is linear for the density matrix (see superoperator form, section 2.1.1.3). This means that for two density matrices which are stationary, a linear combination of them is also stationary. Such a linear combination however is *not a pure state* but a statistical mixture of the two states. The density matrix corresponding to a superposition of stationary states has additional coherences (i.e. off-diagonal elements). Since we do not regard dephasing here these superpositions are in fact decoherence-free (or more precisely relaxation-free). In other words the stationary states span a decoherence-free subspace.

To find the one last state that is required to make the stationary states a basis (of the single excitation subspace) we first orthonormalise the stationary states via Gram-Schmidt orthogonalisation, then start with $|\uparrow\downarrow\downarrow\ldots\downarrow\rangle$, again subtract the existing orthonormal states weighted with their overlap and find the one decaying state for four qubits:

$$|d\rangle = v_1|\uparrow\downarrow\downarrow\downarrow\rangle + v_2|\downarrow\uparrow\downarrow\downarrow\rangle + v_3|\downarrow\downarrow\uparrow\downarrow\rangle + v_4|\downarrow\downarrow\downarrow\uparrow\rangle \tag{2.60}$$

This pattern can be generalised to n qubits:

$$|d\rangle = v_1|\uparrow\downarrow\downarrow\ldots\downarrow\rangle + v_2|\downarrow\uparrow\downarrow\ldots\downarrow\rangle + v_3|\downarrow\downarrow\uparrow\ldots\downarrow\rangle + \cdots + v_n|\downarrow\downarrow\downarrow\ldots\uparrow\rangle \tag{2.61}$$

We have now found an orthogonal basis that describes the single excitation subspace by $n-1$ stationary states and only 1 state decays to the ground state. In other words there is a relaxation-free subspace of $n-1$ states within the single-excitation subspace.

Relaxation blocking by uncoupled spins The combination of many relaxation-free states and one decaying state leads to a paradoxical effect. Uncoupled spins in their ground state reduce the relaxation of one spin in its excited state if they are all coupled to the same bath (i.e. their noise is perfectly correlated). We investigate this phenomenon numerically by measuring the $\langle\sigma_z\rangle$ expectation value of the excited

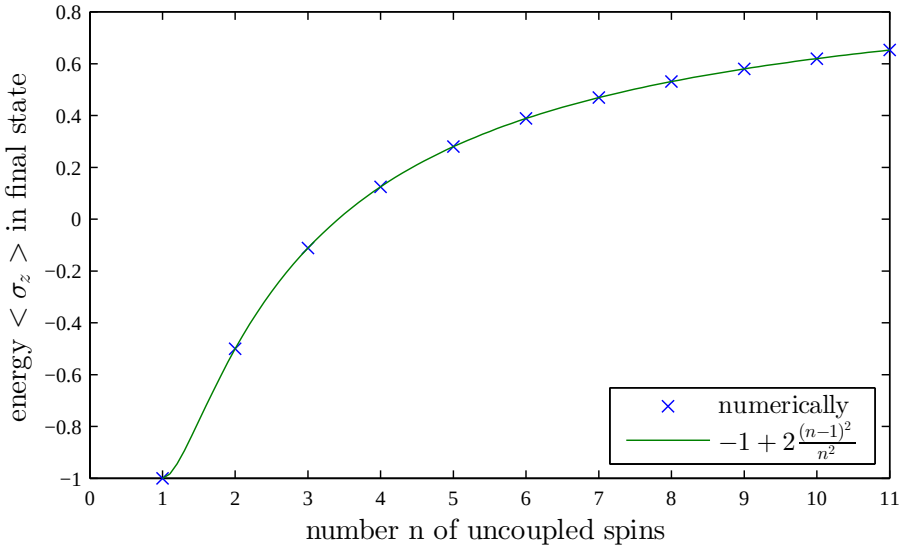

Figure 2.4: Relaxation of a single spin, which is initially in its excited state $\langle\sigma_z\rangle = 1$. Other spins in their ground state are coupled to the same environment. Plotted is $\langle\sigma_z\rangle$ of the excited spin in the final state of the system dependent on the total number of spins. The relaxation of the spin is partially blocked because a relaxation-free subspace is formed, which overlaps more and more with the initial state.

spin for very large times. We do so with an increasing number of spins in their ground state which are not coupled to the excited spin but coupled to the same environmental noise. Figure 2.4 shows that the uncoupled spins block the relaxation of the one excited spin.

For four qubits we calculate the final state analytically by dividing the initial state $|\uparrow\downarrow\downarrow\downarrow\rangle$ into a stationary part and a decaying part. The stationary part is found by projection onto the orthonormalised basis of the relaxation-free subspace, the decaying part by projection onto the normalised decaying state. The final state is then found by replacing the decaying part with the ground state. We then find $\langle\sigma_z\rangle$ (i.e. the energy in the qubit) in that final state:

$$\langle\sigma_z(t\to\infty)\rangle = -1 + \frac{2\left(v_2^2+v_3^2+v_4^2\right)^2}{\left(v_1^2+v_2^2+v_3^2+v_4^2\right)^2} \tag{2.62}$$

where again v_j is the coupling of the jth spin to the environment. The pattern can

be easily generalised to n spins:

$$\langle \sigma_z(t \to \infty) \rangle = -1 + \frac{2\left(\sum_{j=2}^{n} v_j^2\right)^2}{\left(\sum_{k=1}^{n} v_k^2\right)^2} \quad \overset{\text{all } v_j \text{ equal}}{\longrightarrow} \quad -1 + 2\frac{(n-1)^2}{n^2} \tag{2.63}$$

The second expression is obtained when the coupling of all spins to the environment is equally strong (as assumed in our numerics). This generalisation for n spins describes the numerical calculations quite well as can be seen in figure 2.4. In collaboration with Nicolas Vogt it has been analytically proven to be correct, which can be found in our publication, reference [104].

2.3 Solving master equations numerically

The quantum master equation, just as any other first order, linear, homogeneous differential equation, can always be written as a constant matrix multiplied with the vector of variables, i.e. superoperator form:

$$\frac{d}{dt}\vec{\rho} = \mathcal{L}\vec{\rho} \tag{2.64}$$

where $\vec{\rho}$ is a vector containing all elements of the density matrix and $\mathcal{L}$ is a matrix, which is often called a Liouvillean operator since this is the quantum equivalent of the classical Liouville equation. It can also be called a "superoperator" which purely names the mathematical object. To obtain an analytical solution the superoperator matrix needs to be diagonalised, which decouples the equations yielding complex exponential solutions. Imaginary eigenvalues lead to oscillations and real eigenvalues to exponential decay. The diagonalisation however can quickly become analytically infeasible with increasing system size, even with simplifications from the secular approximation, because the superoperator matrix has d^4 elements, where d is the number of system states.

In cases where the analytical diagonalisation is infeasible the equations can always be solved with *numerical diagonalisation*. This means to assign values to all system parameters and then diagonalise the resulting matrix $\mathcal{L}$ in eq. 2.64. This is an exact calculation to the precision to which numbers are stored during the calculation (e.g. double precision with approx. fifteen significant numbers in Matlab). When the matrix is diagonalised, any point in time can easily be calculated. Additionally the eigenvalues can help to identify frequencies and transition rates between

states and effective decay rates can be calculated because the individual exponential rates (eigenvalues) and corresponding coefficients (eigenvectors) are calculated. For small system sizes this can even be a faster calculation than a numerical integration of the differential equation (see below). However the diagonalisation process is computationally highly time-consuming for large systems.

An alternative method is a step-by-step *numerical integration* with for example the trapezoidal rule, a Runge-Kutta algorithm or a Krylov subspace algorithm [105,106]. The computation time for these algorithms scale better with increasing system size, measured in number of states, resulting in enormous efficiency for large systems. These algorithm need to be calculated step-by-step from the initial state and bear a numerical error in each time step. However the precision can be set to a necessary minimum to further increase computation speed.

In computational science different solution methods to differential equations are often compared by the scaling of error with the step size h. For example the fifth-order Runge-Kutta method used here has an error that scales as $\mathcal{O}(h^5)$ [107]. We take a more applied measure here and regard scaling of the computation time for a given error.

2.3.1 Comparing computation times in Matlab

The computation times for both methods are compared for a system of coupled two-level systems (spin chain) in the single excitation subspace, where the number of spins equals the number of states. This system is well suited for computation time measurements as it is easily scalable and highly relevant to this thesis.

All calculations were performed in Matlab 7.13(Release 2011b). The "tic" and "toc" functions were used to measure the computation times displayed in figure 2.5. We ran all calculations on one core of our quad-core machine "Fenchurch" with an Intel Xeon W3550 chip @3.07 GHz with 16 GB RAM.

The diagonalisation method consists of the construction of the superoperator matrix $\mathcal{L}$, the actual diagonalisation and the calculation of the density matrix for each time step which is of interest. In our computation time measurements the last step was not performed as it is dependent on the number of points to be obtained (and typically takes up a negligible amount of time anyway). Matlab's "eig"-function was used for the diagonalisation.

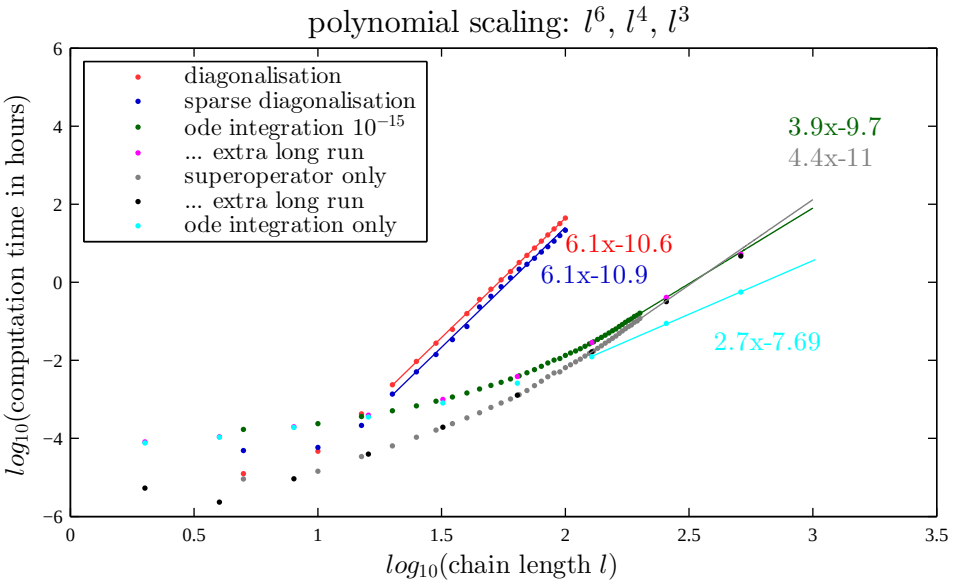

Figure 2.5: Scaling of computation times with increasing chain length (i.e. number of states in the system) for different computation methods. Additional to the actual measurements (marked by dots) a linear fit is obtained and plotted in the range where the dots scale linearly for each method. For the numerical integration this fit is extrapolated for longer chain lengths and can be compared to a second run (pink/ black) with logarithmically equidistant and longer chain lengths. We find that diagonalisation method scales as l^6, while the ode-integration method scales as l^4. Splitting up the calculation into the construction of the superoperator only and the ode-integration only we see that the ode-integration actually scales as l^3. The construction of the superoperator causes the l^4 scaling and takes up larger part of the computation time.

The numerical integration method consists of the construction of the superoperator matrix and the numerical integration of the density matrix. The time for this integration was chosen as the time for one perfect state transfer through the chain in this set up (see section 5.1). The multiplication with the constructed superoperator matrix was defined as a function and given to the Matlab "ode45"-solver for the integration which uses an explicit Runge-Kutta(4,5) formula [108].

Figure 2.5 shows the computation time over the chain length l both in logarithmic scaling which is ideal to determine scaling behaviour as polynomial scaling converts to the gradient of linear scaling and exponential scaling stays exponential:

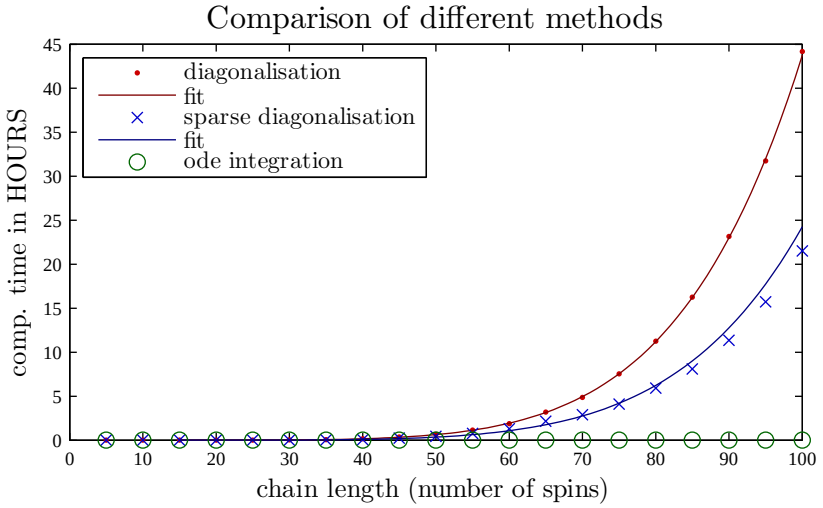

Figure 2.6: Computation times with normal scaling. Here the enormous advantage of numerical integration for large systems becomes apparent.

$$
\begin{aligned}
y &= c_1 x^a \\
\tilde{y} :&= \log y = \log(c_1 x^a) = a \log x + \log c_1 \\
&= a\tilde{x} + \log c_1
\end{aligned}
\qquad\qquad
\begin{aligned}
y_2 &= e^{a x_2} \\
\tilde{y}_2 :&= \log y_2 = a x_2 = a e^{\log x_2} \\
&= a e^{\tilde{x}_2}
\end{aligned}
$$

The diagonalisation method (red / dark blue in figure 2.5) is faster than the numerical integration for a chain length of up to 15 spins. For longer chain lengths it scales with approximately l^6. The use of the sparse matrix format[11] (dark blue) for the superoperator matrix decreases the computation time considerably but does not change the scaling. The numerical integration method (green) scales approximately with l^4 and enables calculations well above $l = 100$. Splitting up the computation time into the time for the construction of the superoperator matrix (grey/ black) and the time for the numerical "ode45"-integration (light blue) we find that the former becomes the limiting factor as the "ode45"-integration scales with approximately l^3.

The computation times with normal scaling are plotted in figure 2.6 and 2.7. Although these curves look similar to an exponential increase exponential scaling can be clearly ruled out in figure 2.8.

To summarize, numerical integration is enormously faster than numerical diagonalisation for large systems. Numerical diagonalisation bears an advantage for special

[11] In the sparse matrix format only non-zero elements and their positions are stored.

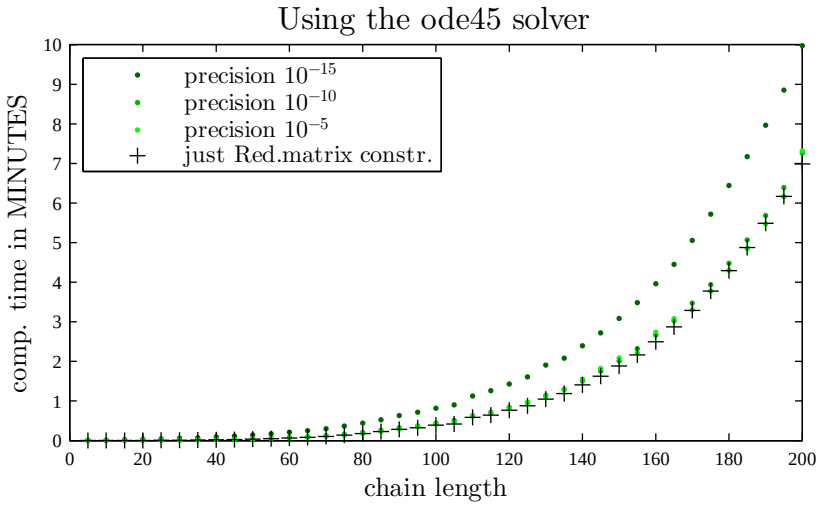

Figure 2.7: Computation times (including the superoperator construction time) for different numerical errors per time step. The time for the construction of the superoperator matrix takes up the largest amount of time. The "ode45"-integration to a precision of 5 and 10 significant numbers adds hardly any distinguishable computation time. Only a precision of 15 significant figures adds a visible amount of computation time.

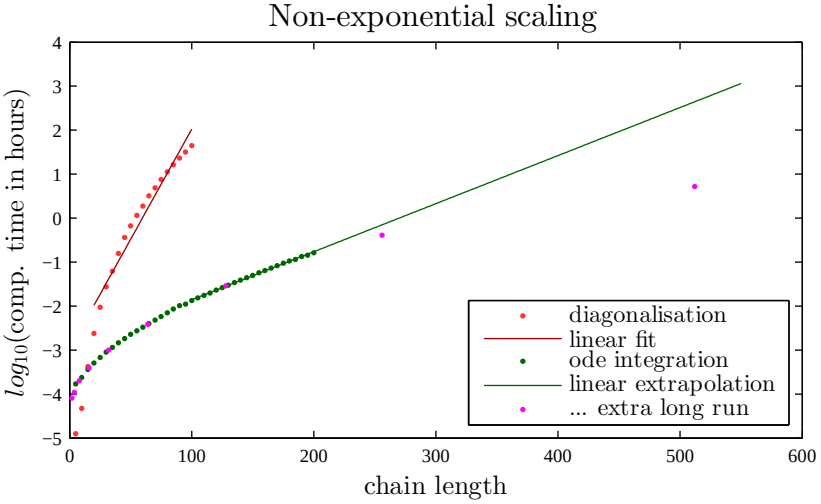

Figure 2.8: We can see that for both methods the points do not form a linear curve but a logarithmic curve. Although the numerical integration (green) might be misinterpreted as linear in the end an extrapolation does not match the two points of the extra-long run (pink). Therefore the computation time definitely does not scale exponentially but polynomial.

cases: when the time of interest is unusually long after the initial state or when further information about the rates and frequencies of the system is wanted e.g. effective rates need to be calculated.

2.4 Chapter summary

In section 2.1 we found a general form for the Bloch-Redfield equations, a Markovian master equation with efficient but comprehensive modeling options. A core strength is the direct link back to the interaction and bath Hamiltonian, which give an underpinning physical model. The relevant environmental properties are contained in the spectral functions, which define temporal and spatial correlations of the environment. The derived form eq. 2.27 facilitates a faster and more clearly laid out calculation than the common element-wise notation. We laid out an efficient, consistent method of investigating spatial correlations with this formalism, which is particularly useful for large systems. This straightforward approach offers more flexibility than the 'several baths' approach since any correlation function can be used.

The secular approximation has been shown generally to simplify the mathematical form of the equations. This approximation is based on the existence of two different time scales in the system dynamics, which is a common occurrence in controlled quantum systems. Applying the secular approximation for spatially uncorrelated decoherence directly yields the Lindblad form of a master equation. For spatially correlated decoherence we presented the required additional step: the diagonalisation of the coefficient matrix. This step also provides a test of physicality for phenomenological spatial correlation functions in the Markovian regime and we showed that exponential and Gaussian decay with arbitrary correlation length proves to be a physical model for spatial noise correlations. The secular approximation is furthermore a great tool in finding analytical solutions to the Bloch-Redfield equations as it helps identify elements of the superoperator which can be approximated by zero. It is important to point out that while it is common to apply the full secular approximation, which bears the danger of neglecting physical features, we present a more detailed general approach by which we only neglect justified elements based on the respective system at hand.

In section 2.2 we first gave a rather instructive summary on how to model spatially correlated noise in systems of several qubits/spins. This also forms the basis of chap-

ter 5. We then investigated very generally the effects of spatial noise correlations. These results are essential to this thesis as they provide a fundamental understanding of correlated noise effects, which can be applied to several different systems in following chapters: While for short correlation lengths the dephasing rate between two states is proportional to the number n_f of flipped spins one finds that for long correlation lengths it becomes proportional to n_e^2, where n_e is the difference in the number of excitations. This leads to much stronger dephasing between certain states with large n_e but also to the creation of dephasing-free subspaces for $n_e = 0$.

For relaxation the dynamics becomes rather complex for long correlation lengths. Characteristic is the fact that a pair of spins in the state $(|\uparrow\downarrow\rangle + |\downarrow\uparrow\rangle)/\sqrt{2}$ contributes a decay rate, which is twice as high as the relaxation rate in uncorrelated noise. In contrast, a pair in the state $(|\uparrow\downarrow\rangle - |\downarrow\uparrow\rangle)/\sqrt{2}$ does not contribute a decay rate from that state. In the single excitation subspaces all of these $n-1$ states are therefore relaxation-free, meaning that the whole subspace only contains one decaying state. This leads to the paradoxical effect that a qubit's relaxation can be blocked by other qubits in their ground state, which are not coupled to the excited qubit but only to the same environmental noise.

In section 2.3 we presented two numerical solution methods for master equations: Numerical diagonalisation yields more information such as steady states, eigenfrequencies, decay rates and the ability to calculate any time point in the evolution without a step-wise integration. However with increasing number of states l the computation time for the diagonalisation scales as l^6. For large systems numerical integration is therefore enormously faster, scaling as l^3. With this method the construction of the superoperator actually becomes the computationally most expensive process as it scales as l^4.

Chapter 3

3 Microscopic models of the environment

In this chapter the correlation function $C_{jk}(\tau) = \langle \tilde{B}_j(\tau)\tilde{B}_k(0)\rangle$, which characterizes the environment in the Bloch-Redfield formalism (eq. 2.27) is calculated for certain simplified microscopic models of the environment. These examples help to connect the properties of the correlation function to a physical picture. This chapter is in contrast to the rest of this thesis where the environment is only characterised by the correlation function and the system is modelled in detail. The material in this chapter has appeared in reference [83]. Other interesting work on large dissipative systems can be found in references [20, 109, 110].

3.1 Coupled quantum harmonic oscillators

We begin by considering a chain of coupled quantum harmonic oscillators as a model for the environmental bath of one-dimensional systems. This can be seen as an extension of the well known spin-boson model [17,38–41], which describes a system of spins coupled to an environmental bath of uncoupled harmonic oscillators. We consider a nearest-neighbour coupling and derive the spectral function for this environment. Once the spectral function is calculated it can be inserted in the Bloch-Redfield equations and can be combined with any system, that is placed in this environmental model. Furthermore obtaining the spectral function from an environmental model shows us which environmental parameters determine which features of the spectral function. We are particularly interested in the spatial correlations of the bath and

we will show that the strength of spatial correlations is determined by the coupling of the environmental sites. The environmental bath Hamiltonian for a linear chain of harmonic oscillators with nearest-neighbour coupling is given by:

$$H_B = \sum_{x=1}^{N} \omega_q a_x^\dagger a_x + \sum_{x=1}^{N-1} g \left(a_x^\dagger a_{x+1} + a_{x+1}^\dagger a_x \right) \tag{3.1}$$

a_x is the annihilation operator of the harmonic oscillator at position x, satisfying the bosonic commutation relation $[a_x, a_{x'}^\dagger] = \delta_{xx'}$ with $\delta_{xx'}$ the Kronecker-Delta. Furthermore ω_q is the level splitting and g is the coupling strength.

Hamiltonians of coupled bosons are uncoupled (i.e. "diagonal") in Fourier space when the coupling depends only on the relative distance. Therefore a Fourier lattice transformation is employed changing the description to travelling modes rather than localized excitations:

$$\begin{aligned} a_k &= \frac{1}{\sqrt{N}} \sum_x e^{-ikxd} a_x \quad a_x = \frac{1}{\sqrt{N}} \sum_k e^{ikxd} a_k \\ a_k^\dagger &= \frac{1}{\sqrt{N}} \sum_x e^{ikxd} a_x^\dagger \quad a_x^\dagger = \frac{1}{\sqrt{N}} \sum_k e^{-ikxd} a_k^\dagger \end{aligned} \tag{3.2}$$

where d is the lattice constant of the chain and the position $x \in \mathbb{N}$ is dimensionless. For simplicity of notation the wave number k is not dimensionless here. In a more detailed discretization the inverse transformation in eq. 3.2 is $a_x^\dagger = \frac{1}{\sqrt{N}} \sum_{n=-N/2}^{N/2} \exp(-ik_n xd) a_k^\dagger$ with $k_n = \frac{2\pi}{Nd} n$ and dimensionless $n \in \mathbb{N}$.

Since we assume a finite chain with large N the Fourier lattice transform for operators is analogous to a discrete Fourier transform. Further details can be found in [111,112] and appendix G. Note the commutation relations for the transformed operators are

preserved for bosons and fermions but not for spins:

$$\text{bosons: } [a_x, a_{x'}^\dagger] = \delta_{xx'} \tag{3.3}$$

$$[a_k, a_{k'}^\dagger] = \frac{1}{N}\left[\sum_x e^{-ikxd} a_x, \sum_{x'} e^{ik'x'd} a_{x'}^\dagger\right] = \frac{1}{N}\sum_{x,x'} e^{id(k'x'-kx)}[a_x, a_{x'}^\dagger] = \delta_{kk'} \tag{3.4}$$

$$\text{fermions: } \{c_x, c_{x'}^\dagger\} = \delta_{xx'} \tag{3.5}$$

$$\{c_k, c_{k'}^\dagger\} = \frac{1}{N}\sum_{xx'} e^{id(k'x'-kx)}\{a_x, a_{x'}^\dagger\} = \delta_{kk'} \tag{3.6}$$

$$\text{spins: } [s_x^+, s_{x'}^-] = \delta_{xx'} s_x^z \tag{3.7}$$

$$[s_k^+, s_{k'}^-] = \frac{1}{N}\sum_{xx'} e^{id(k'x'-kx)}[s_x^+, s_{x'}^-] = \frac{1}{N}\sum_x e^{idx(k'-k)} s_x^z = s_{k'-k}^z \tag{3.8}$$

It can be seen here that making the chain infinitely long and changing to a Fourier series (appendix G) does not make a significant difference. The chain length only sets how closely spaced the k-values are in the Brillouin zone.

Replacing a_x and $a_x^\dagger$ with their transforms in the Hamiltonian (eq. 3.1) one finds:

$$H_B = \omega_q \sum_{k,k'} \underbrace{\frac{1}{N}\sum_x e^{i(k'-k)xd}}_{\delta_{kk'}} a_k^\dagger a_{k'} + g\sum_{kk'} \underbrace{\frac{1}{N}\sum_x e^{i(k'-k)xd}}_{\delta_{kk'}} e^{ikd} a_k^\dagger a_{k'} \tag{3.9}$$

$$+ g \underbrace{\frac{1}{N}\sum_x e^{i(k'-k)xd}}_{\delta_{kk'}} e^{-ikd} a_k^\dagger a_{k'}$$

$$= \omega_q \sum_k a_k^\dagger a_k + g\sum_k a_k^\dagger a_k (e^{ikd} + e^{-ikd}) \tag{3.10}$$

$$= \sum_k (\omega_q + 2g\cos kd) a_k^\dagger a_k \tag{3.11}$$

$$= \sum_k \omega_k a_k^\dagger a_k \tag{3.12}$$

The Hamiltonian is diagonal in Fourier space with the dispersion relation $\omega_k = \omega_q + 2g\cos kd$.

Note that an arbitrary dispersion relation represents the Fourier lattice transform of the coupling coefficients in space. This is seen by insertion of the inverse transforms

(eq. 3.2) into:

$$H_B = \omega_k \sum_k a_k^\dagger a_k = \sum_{xx'} \underbrace{\sum_k \frac{1}{N} \omega_k e^{ikd(x-x')}}_{=:g_{x-x'}} a_x^\dagger a_{x'} \tag{3.13}$$

The coupling constant $g_{x-x'}$ is the Fourier lattice transform (appendix G) of the dispersion relation and vice versa[1].

$$\omega_k = \sum_u g_u e^{ikud} \quad \text{with} \quad u := x - x' \tag{3.14}$$

By choosing nearest-neighbour coupling $g_{x-x'} = g\delta_{x,x'+1} + g\delta_{x+1,x'}$ we obtain in x-space the Hamiltonian (eq. 3.1) and in k-space a cosine dispersion relation (eq. 3.12).

If we assume the correlations in the chain are dominated by propagating (i.e. dispersion-free) excitations, we may also linearise the dispersion relation ($\cos kd \approx -|kd| + \pi/2$) and find the simpler:

$$\omega_k \approx \omega_q + 2g\left(-|kd| + \frac{\pi}{2}\right) \qquad \text{with } k \in \left[-\frac{\pi}{d}, \frac{\pi}{d}\right] \tag{3.15}$$

3.1.1 Space-time correlation function

In order to understand the decohering influence of a chain of coupled harmonic oscillators in general, we calculate the space-time correlation function of typical coupling operators. They contain all information which is relevant for the Bloch-Redfield equations; their Fourier transform is the spectral function.

The bath operators whose correlation functions are typically of interest are $B_{1x} = a_x^\dagger, B_{2x} = a_x$ and $B_{3x} = a_x + a_x^\dagger$ because they are typically involved in the interaction Hamiltonian of a system coupling to particular spatially located parts of the bath. Using the inverse Fourier transforms (eq. 3.2) the calculation can be carried out

[1] Note that in this general notation the function $g_{x-x'}$ also has negative arguments $x - x' < 0$ and therefore the Fourier transform needs to run over the entire interval: $\omega_k = \sum_{u=-N+1}^{N-1} g_u e^{ikud}$. For the dispersion relation ω_k the larger interval makes a difference and must be considered. Generally a symmetric $g_u = g_{-u}$ guarantees a real dispersion relation. The fact that the interval is twice as long in x-space means in k-space a resolution which is better by a factor of two (cf. eq. 3.13):
$x - x' = 0, \ldots, N \quad \longleftrightarrow \quad k_n = \frac{2\pi}{Nd} n \qquad \text{with } n = -N/2, \ldots, N/2$
$x - x' = -N, \ldots, N \quad \longleftrightarrow \quad k_n = \frac{2\pi}{2Nd} n \qquad \text{with } n = -N, \ldots, N$

completely in Fourier space.

$$B_{1x} = a_x^\dagger = \frac{1}{\sqrt{N}} \sum_k e^{-ikxd} a_k^\dagger =: \sum_k g_{kx} a_k^\dagger \tag{3.16}$$

$$B_{2x} = a_x = \frac{1}{\sqrt{N}} \sum_k e^{ikxd} a_k =: \sum_k g_{kx}^* a_k \tag{3.17}$$

Changing to the Heisenberg picture (appendix F) the time-dependent bath operator reads:

$$\tilde{B}_{1x}(t) = e^{\left(i \sum_k \omega_k a_k^\dagger a_k t\right)} \sum_{k'} g_{k'x} a_{k'}^\dagger \; e^{\left(-i \sum_{k''} \omega_{k''} a_{k''}^\dagger a_{k''} t\right)} \tag{3.18}$$

$$= \prod_k e^{\left(i\omega_k a_k^\dagger a_k t\right)} \sum_{k'} g_{k'x} a_{k'}^\dagger \prod_{k''} e^{\left(-i\omega_{k''} a_{k''}^\dagger a_{k''} t\right)} \tag{3.19}$$

$$= \sum_k e^{\left(i\omega_k a_k^\dagger a_k t\right)} g_{kx} a_k^\dagger e^{\left(-i\omega_k a_k^\dagger a_k t\right)} \tag{3.20}$$

$$= \sum_k \sum_n \frac{1}{n!} (i\omega_k t)^n g_{kx} \; (a_k^\dagger a_k)^n a_k^\dagger e^{\left(-i\omega_k a_k^\dagger a_k t\right)} \tag{3.21}$$

$$= \sum_k \sum_n \frac{1}{n!} (i\omega_k t)^n g_{kx} \; a_k^\dagger (a_k a_k^\dagger)^n e^{\left(-i\omega_k a_k^\dagger a_k t\right)} \tag{3.22}$$

$$= \sum_k g_{kx} a_k^\dagger \underbrace{e^{i\omega_k a_k a_k^\dagger}}_{= e^{i\omega_k (1 + a_k^\dagger a_k) t}} e^{\left(-i\omega_k a_k^\dagger a_k t\right)} \tag{3.23}$$

$$= \sum_k g_{kx} a_k^\dagger e^{i\omega_k t} \tag{3.24}$$

We rewrote the first exponential as a power series and combined it with $a_k^\dagger$. The operator $\tilde{B}_{2x}(t)$ is found similarly, by rewriting the second exponential as a power series, combining it with a_k and writing $a_k (a_k^\dagger a_k)^n = (a_k a_k^\dagger)^n a_k$. This leads to:

$$\tilde{B}_{2x}(t) = \sum_k g_{kx}^* a_k e^{-i\omega_k t} = \tilde{B}_{1x}^\dagger(t) \tag{3.25}$$

The four different correlation functions involving $\tilde{B}_{1x}$ and $\tilde{B}_{2x}$ can now be calculated

using the quantum regression theorem [44, 113, 114].

$$\langle \tilde{B}_{1x}(t)\tilde{B}_{1x'}(t')\rangle = \mathrm{Tr}\left(\tilde{B}_{1x}(t)\tilde{B}_{1x'}(t')\rho_B\right) \tag{3.26}$$

$$= \mathrm{Tr}\left(\sum_{kk'} g_{kx}g_{k'x'}a_k^\dagger a_{k'}^\dagger e^{i(\omega_k t+\omega_{k'}t')}\rho_B\right) \tag{3.27}$$

$$= \sum_{kk'} g_{kx}g_{k'x'}e^{i(\omega_k t+\omega_{k'}t')}Tr(a_k^\dagger a_{k'}^\dagger \rho_B) \tag{3.28}$$

$$= 0 \tag{3.29}$$

The last step requires the assumption that the environment is in a steady state which is the fully mixed state with no non-zero off-diagonal elements in ρ_B (using the Fock basis of the k-modes). This seems reasonable for an equilibrium state of bath modes with a diagonal Hamiltonian (eq. 3.12). Then follows analogously:

$$\langle \tilde{B}_{2x}(t)\tilde{B}_{2x'}(t')\rangle = \sum_{kk'} g_{kx}^* g_{k'x'}^* e^{-i(\omega_k t+\omega_{k'}t')}Tr(a_k a_{k'}\rho_B) \tag{3.30}$$

$$= 0 \tag{3.31}$$

The mixed correlation functions however are given by:

$$\langle \tilde{B}_{1x}(t)\tilde{B}_{2x'}(t')\rangle = \sum_{kk'} g_{kx}g_{k'x'}^* e^{-i(\omega_{k'}t'-\omega_k t)} \underbrace{\mathrm{Tr}(a_k^\dagger a_{k'}\rho_B)}_{=\delta_{kk'}\langle n_k\rangle} \tag{3.32}$$

$$= \sum_{k} g_{kx}g_{kx'}^* e^{i\omega_k(t-t')}\langle n_k\rangle \tag{3.33}$$

$$\langle \tilde{B}_{2x}(t)\tilde{B}_{1x'}(t')\rangle = \sum_{kk'} g_{kx}^* g_{k'x'} e^{-i(\omega_k t-\omega_{k'}t')}\,\mathrm{Tr}(a_k a_k^\dagger \rho_B) \tag{3.34}$$

$$= \sum_{k} g_{kx}^* g_{kx'} e^{-i\omega_k(t-t')}(1+\langle n_k\rangle) \tag{3.35}$$

where $\langle n_k\rangle$ is the expectation value of the occupation number of mode k given by the Bose-Einstein distribution $\langle n_k\rangle = 1/(exp(\frac{\hbar\omega_k}{kT})-1)$. For large energies this can be approximated by the Boltzmann distribution $exp(-\frac{\hbar\omega_k}{kT})$. The calculation from eq. 3.16 to eq. 3.35 is similar to [20]. It is done more generally and with more detail in appendix A.

Replacing g_{kx} with its definition (eq. 3.16) we find the two space-time correlation

functions for a coupled chain of harmonic oscillators:

$$\langle \tilde{B}_{1x}(\tau)\tilde{B}_{2x'}(0)\rangle = \sum_k \frac{1}{N} e^{-ik(x-x')d} e^{i\omega_k \tau}\langle n_k\rangle \tag{3.36}$$

$$\langle \tilde{B}_{2x}(\tau)\tilde{B}_{1x'}(0)\rangle = \sum_k \frac{1}{N} e^{ik(x-x')d} e^{-i\omega_k \tau}(1+\langle n_k\rangle) \tag{3.37}$$

Markovianity For Markovian system dynamics the correlation functions of the bath have to decay faster than the relevant system dynamics. To check whether the correlation functions (eq. 3.36) decay we calculate the sum explicitly. For simplicity linear dispersion $\omega_k = \omega_q + 2g\left(-|kd| + \frac{\pi}{2}\right)$ and the Boltzmann distribution are assumed here$\langle n_k\rangle = exp(-\beta\omega_k)$ with $\beta = 1/(k_B T)$ is the inverse of Boltzmann constant k_B and temperature T. Furthermore the sum is changed to an integration assuming closely spaced k-values, i.e. a long chain:

$$\frac{1}{N}\sum_{n=-N/2}^{N/2} f(k_n) = \frac{1}{N}\frac{Nd}{2\pi}\int_{-\pi/d}^{\pi/d} dk f(k) \qquad \text{with } k_n = \frac{2\pi}{Nd}n \tag{3.38}$$

Then eq. 3.36 can be evaluated:

$$\langle \tilde{B}_{1x}(\tau)\tilde{B}_{2x'}(0)\rangle = \tag{3.39}$$

$$= \frac{d}{2\pi}\int_{-\pi/d}^{\pi/d} dk\; e^{-ik(x-x')d} e^{(i\tau-\beta)(\omega_q+\pi g)} e^{-u|k|} \qquad \text{with } u := (i\tau-\beta)2gd \tag{3.40}$$

$$= \frac{d}{2\pi} e^{(i\tau-\beta)(\omega_q+\pi g)}\left(\int_0^{\pi/d} dk\; e^{(-ixd+ix'd-u)k} + \int_{-\pi/d}^{0} dk\; e^{(-ixd+ix'd+u)k}\right) \tag{3.41}$$

$$= \underbrace{\frac{d}{\pi}\frac{u}{u^2+(x-x')^2d^2}}_{\text{decay } \propto \frac{1}{2\pi g\tau} \text{ for large } \tau} \underbrace{e^{(i\tau-\beta)\omega_q}\left[(-1)^{x-x'}e^{-(i\tau-\beta)\pi g} - e^{(i\tau-\beta)\pi g}\right]}_{\text{oscillating with } \tau} \tag{3.42}$$

$$\propto \frac{1}{2\pi g\tau} \tag{3.43}$$

For the last step it was used that $\exp(i(x-x')\pi) = (-1)^{x-x'}$ as $(x-x') \in \mathbb{Z}$ is an integer.

The correlation function decays in time with an algebraic decay. The same is found for the correlation function 3.37 analogously. While an algebraic decay by definition has no decay scale (unlike an exponential decay), it will be further away from zero than an exponential decay for large enough time. The fact that the correlation

function in time is not a delta function but an algebraic decay indicates the potential for non-Markovian memory effects of this environment. The coefficient of the $1/\tau$ decay is given by the coupling strength g, which is an environmental parameter and in the limit where g is orders of magnitude larger than the relevant system energies, this model of the environment can be used in Markovian master equations.

spatial decay for $\tau = 0$ Looking at one moment in time $t = t' \Leftrightarrow \tau = 0$ the spatial correlation function (eq. 3.43) takes the form of a Lorentzian:

$$\langle \tilde{B}_{1x}(t)\tilde{B}_{2x'}(t)\rangle = \frac{1}{\pi}e^{-\beta\omega_q}\frac{-2\beta g}{(2\beta g)^2 + (x-x')^2}\left(e^{-\beta\pi g} - (-1)^{x-x'}e^{\beta\pi g}\right) \tag{3.44}$$

The coefficient is a Lorentzian with width $g\beta = \frac{g}{k_B T}$ i.e. the correlation length is given by $\frac{g}{k_B T}$. For strong environmental coupling g compared to the temperature $k_B T$ the correlation length is long and one of the two exponentials $exp(\pm\pi g\beta) \to 0$ depending on the sign of g, i.e. nearest neighbours are correlated (anticorrelated) for attractive (repulsive) coupling with strongly negative (positive) coupling strength g. For weak environmental coupling βg (which is only possible for large $\beta\omega_q$ since the Bose-Einstein distribution was approximated as the Boltzmann distribution) the Lorentzian has a short width and $exp(2\pi g\beta) \to 1$ i.e. every second neighbour is uncorrelated. Note that for $x = x'$ one finds a non-zero $\lim_{g\to 0}\langle \tilde{B}_{1x}(t)\tilde{B}_{2x}(t)\rangle = e^{-\beta\omega_q}$.

Dividing eq. 3.44 by its value for $x = x'$ we find the relative spatial correlation function:

$$\frac{\langle \tilde{B}_{1x}(t)\tilde{B}_{2x'}(t)\rangle}{\langle \tilde{B}_{1x}(t)\tilde{B}_{2x}(t)\rangle} = \frac{(2\beta g)^2}{(2\beta g)^2 + (x-x')^2} \cdot \begin{cases} 1 & \text{for } x-x' \text{ even} \\ \coth(-\pi g\beta) & \text{for } x-x' \text{ odd} \end{cases} \tag{3.45}$$

This function is shown in figure 3.1 and demonstrates clearly the decay of correlations due to the interplay of correlation hopping along the chain and thermal noise.

The second correlation function (eq. 3.37) (with the Boltzmann distribution $\langle n_k\rangle = e^{-\beta\omega_k}$) can be expressed in terms of the first:

$$\langle \tilde{B}_{2x}(\tau)\tilde{B}_{1x'}(0)\rangle = \left(\langle \tilde{B}_{2x}(\tau)\tilde{B}_{1x'}(0)\rangle\right)^\dagger + \lim_{\beta\to 0}\left(\langle \tilde{B}_{2x}(\tau)\tilde{B}_{1x'}(0)\rangle\right)^\dagger \tag{3.46}$$

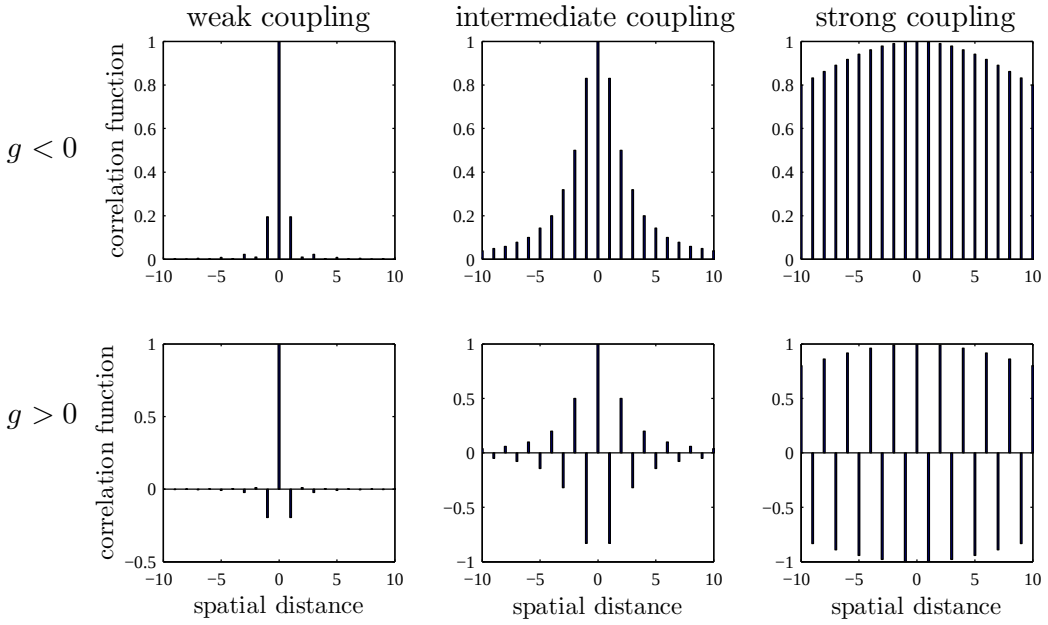

Figure 3.1: Correlation function $\langle \tilde{B}_{1x}(t)\tilde{B}_{2x'}(t)\rangle$ (eq. 3.45) normalised by its value at $x = x'$ over spatial distance $|x - x'|$. These plots are for weak coupling ($g\beta = \pm 0.1$), intermediate coupling ($g\beta = \pm 1$) and strong coupling ($g\beta = \pm 10$).

Combining 3.46 and 3.44 leads to:

$$\langle \tilde{B}_{2x}(t)\tilde{B}_{1x'}(t)\rangle = \begin{cases} 1 + e^{-\beta\omega_q} & \text{for } x = x' \\ \langle \tilde{B}_{1x}(t)\tilde{B}_{2x'}(t)\rangle & \text{for } x \neq x' \end{cases} \tag{3.47}$$

3.1.2 Spectral function

In the Bloch-Redfield equations the spectral function (defined in eq. 2.30) is used, i.e. the Fourier transform of the time correlation function. For the bosonic chain (eq. 3.36) the spectral function can be written in terms of Dirac delta functions:

$$C_{1x2x'}(\omega) = \int_{-\infty}^{\infty} d\tau e^{i\omega\tau}\langle \tilde{B}_{1x}(\tau)\tilde{B}_{2x'}(0)\rangle \tag{3.48}$$

$$= \sum_k \delta(\omega + \omega_k)\frac{2\pi}{N}e^{-ik(x-x')d}\langle n(|\omega|)\rangle \tag{3.49}$$

$$C_{2x1x'}(\omega) = \int_{-\infty}^{\infty} d\tau e^{i\omega\tau}\langle \tilde{B}_{2x}(\tau)\tilde{B}_{1x'}(0)\rangle \tag{3.50}$$

$$= \sum_k \delta(\omega - \omega_k)\frac{2\pi}{N}e^{ik(x-x')d}(1 + \langle n(|\omega|)\rangle) \tag{3.51}$$

since the inverse Fourier transform of these expressions yield back eq. 3.36 and 3.37.

The spectral function can then be calculated for specific dispersion relations ω_k, changing from summation to integration (eq. 3.38) and using for the Delta-functions [115]:

$$\delta\left(f(x)\right) = \sum_j \frac{\delta(x - x_j)}{|f'(x_j)|} \qquad \text{with } \forall_j : f(x_j) = 0 \tag{3.52}$$

As examples we calculate the spectral function for linearised dispersion (eq. 3.15) and cosine dispersion (eq. 3.10).

Linear dispersion With linearised dispersion for propagating excitations $\omega_k = \omega_q + 2g\left(-|kd| + \frac{\pi}{2}\right)$ with $k \in \left[-\frac{\pi}{d}, \frac{\pi}{d}\right]$ the corresponding spectral function (eq. 3.49) is obtained (using eq. 3.38 and 3.52):

$$C_{1x2x'}(\omega) = d\int_{-\pi/d}^{\pi/d} dk \;\; \delta(\omega + \omega_q + \pi g - 2g|k|d) e^{-ikd(x-x')} \langle n(|\omega|)\rangle \tag{3.53}$$

$$k_0 = \pm\frac{\omega + \omega_q + \pi g}{2gd} \tag{3.54}$$

$$f_2(k) = \omega + \omega_q + \pi g - 2g|k|d \tag{3.55}$$

$$|f_2'(k_0)| = 2|g|d \tag{3.56}$$

$$C_{1x2x'}(\omega) = d\frac{1}{2|g|d}\left(e^{i\frac{\omega+\omega_q+\pi g}{2g}(x-x')} + e^{-i\frac{\omega+\omega_q+\pi g}{2g}(x-x')}\right)\langle n(|\omega|)\rangle\Theta(-|\omega+\omega_q| + \pi|g|) \tag{3.57}$$

$$= \frac{1}{|g|}\cos\left(\frac{\omega+\omega_q+\pi g}{2g}(x-x')\right)\langle n(|\omega|)\rangle\Theta(-|\omega+\omega_q| + \pi|g|) \tag{3.58}$$

Analogously one finds:

$$C_{2x1x'}(\omega) = d\int_{-\pi/d}^{\pi/d} dk \;\; \delta(\omega - \omega_q - \pi g + 2g|k|d) e^{ikd(x-x')}\left(1 + \langle n(|\omega|)\rangle\right) \tag{3.59}$$

$$= \frac{1}{|g|}\cos\left(\frac{\omega-\omega_q-\pi g}{2g}(x-x')\right)\left(1 + \langle n(|\omega|)\rangle\right)\Theta(-|\omega-\omega_q| + \pi|g|) \tag{3.60}$$

Cosine dispersion For a cosine dispersion relation (see eq. 3.12) the corresponding spectral function (eq. 3.49) is obtained using 3.38:

$$C_{1x2x'}(\omega) = d\int_{-\pi/d}^{\pi/d} dk \;\; \delta(\omega+\omega_q+2g\cos kd)e^{-ikd(x-x')}\langle n(\omega)\rangle \tag{3.61}$$

$$k_0 = \pm\arccos\left(-\frac{\omega+\omega_q}{2g}\right)\frac{1}{d} \quad \Leftrightarrow \quad \omega+\omega_{k_0}=0 \tag{3.62}$$

$$f(k) = \omega+\omega_q+2g\cos kd \tag{3.63}$$

$$|f'(k_0)| = |2gd\sin k_0 d| = \left|2gd\sin\left(\pm\arccos\frac{-\omega-\omega_q}{2g}\right)\right| \tag{3.64}$$

$$= \left|\pm 2gd\sqrt{1-\frac{(\omega+\omega_q)^2}{4g^2}}\right| = d\sqrt{4g^2-(\omega+\omega_q)^2} \tag{3.65}$$

$$C_{1x2x'}(\omega) = \frac{1}{\sqrt{4g^2-(\omega+\omega_q)^2}}\left(e^{i(x-x')\arccos(\dots)}+e^{-i(x-x')\arccos(\dots)}\right)\langle n(\omega)\rangle \cdot\Theta\left(-|\omega+\omega_q|+2|g|\right) \tag{3.66}$$

$$C_{1x2x'}(\omega) = \Theta\left(-|\omega+\omega_q|+2|g|\right)\frac{2}{\sqrt{4g^2-(\omega+\omega_q)^2}} \cdot\cos\left[(x-x')\arccos\left(-\frac{\omega+\omega_q}{2g}\right)\right]\langle n(\omega)\rangle \tag{3.67}$$

Analogously one finds:

$$C_{2x1x'}(\omega) = \Theta\left(-|\omega-\omega_q|+2|g|\right)\frac{2}{\sqrt{4g^2-(\omega-\omega_q)^2}} \cdot\cos\left[(x-x')\arccos\left(\frac{\omega-\omega_q}{2g}\right)\right](1+\langle n(\omega)\rangle) \tag{3.68}$$

The spectral function shows that the noise consists of frequencies around the oscillators eigenenergies ω_q. The Heaviside Θ-functions mark the noise cut-off at $2g$ left and right of this frequency due to the band gap of the chain.

For any fixed frequency ω the spatial correlation is a cosine oscillation with increasing distance $|x-x'|$, allowing points of negative correlations. This is quite different to the time-correlation function (eq. 3.43 and 3.44) because the spatial and temporal part of the correlation function are not separable into a product in this example.

Taking for example two qubits and placing them at different relative distances in this environment one will find points, where the cosine is zero, and the decoherence will appear completely uncorrelated. At points where the cosine is 1 the noise is fully correlated and correlated decoherence effects will be the strongest. At the points where cosine is -1 the noise is fully anticorrelated and some effects of correlated decoherence will be reversed. See section 4.4.1 for an example.

3.1.3 Decoherent environmental evolution

We now introduce decoherence into the evolution of the environment and show how this changes the mixed correlation functions and the conditions for Markovianity. We regard the same coupled bosonic chain given by the Hamiltonian in eq. 3.1 or Fourier lattice transformed in eq. 3.12:

$$H_B = \omega_k \sum_k a_k^\dagger a_k \qquad \text{with} \qquad \omega_k = \omega_q + 2g\cos kd \tag{3.69}$$

However contrary to section 3.1 the time evolution is not assumed to be coherent. Instead we assume a Lindblad equation with two Lindblad operators $a_x, a_x^\dagger$ on each site in space:

$$\dot{\rho} = -i[H_B, \rho] + \sum_x \Gamma_\downarrow \left(a_x \rho a_x^\dagger - \frac{1}{2}\{a_x^\dagger a_x, \rho\} \right) + \sum_x \Gamma_\uparrow \left(a_x^\dagger \rho a_x - \frac{1}{2}\{a_x a_x^\dagger, \rho\} \right) \tag{3.70}$$

Replacing the spatial ladder operators with their Fourier lattice transform (eq. 3.2) we find that the Lindblad equation transforms easily to k-space. Explicitly for the first decoherent term:

$$\sum_x a_x \rho a_x^\dagger = \frac{1}{N} \sum_{kk'} \underbrace{\sum_x e^{ixd(k-k')}}_{=N\delta_{kk'}} a_k \rho a_{k'}^\dagger = \sum_k a_k \rho a_k^\dagger \tag{3.71}$$

Analogous for all other terms we find:

$$\dot{\rho} = -i[H_B, \rho] + \sum_k \Gamma_\downarrow \left(a_k \rho a_k^\dagger - \frac{1}{2}\{a_k^\dagger a_k, \rho\} \right) + \sum_k \Gamma_\uparrow \left(a_k^\dagger \rho a_k - \frac{1}{2}\{a_k a_k^\dagger, \rho\} \right) \tag{3.72}$$

$$= \mathcal{L}\rho \tag{3.73}$$

where we have defined the superoperator $\mathcal{L}$. Again our aim is to find correlation functions of the bath operators

$$B_{1x} = a_x^\dagger = \frac{1}{\sqrt{N}} \sum_k e^{-ikxd} a_k^\dagger =: \sum_k g_{kx} a_k^\dagger \tag{3.74}$$

$$B_{2x} = a_x = \frac{1}{\sqrt{N}} \sum_k e^{ikxd} a_k =: \sum_k g_{kx}^* a_k \tag{3.75}$$

Contrary to the coherent case (eq. 3.18) we calculate the Heisenberg picture time evolution of these operators by solving the adjoint master equation (see chapter 3.2.3 in [1]) which for an arbitrary Heisenberg operator $A_H(t)$ reads:

$$\frac{d}{dt} A_H(t) = \mathcal{L}^\dagger A_H(t) \tag{3.76}$$

where $\mathcal{L}$ is the Lindblad superoperator that defines the differential equation for the density matrix. For this system it is given by eq. 3.73. First we solve the time evolution of $\tilde{a}_k(t)$ which is the time-dependent Heisenberg-picture operator of Schrödinger picture operator a_k:

$$\begin{aligned} \frac{d}{dt}\tilde{a}_{k'}(t) = i \left[\sum_k \omega_k a_k^\dagger a_k, \tilde{a}_{k'}(t) \right] + \sum_k \Gamma_\downarrow \left(a_k^\dagger \tilde{a}_{k'}(t) a_k - \frac{1}{2} \left\{ a_k^\dagger a_k, \tilde{a}_{k'}(t) \right\} \right) \\ + \sum_k \Gamma_\uparrow \left(a_k \tilde{a}_{k'}(t) a_k^\dagger - \frac{1}{2} \left\{ a_k a_k^\dagger, \tilde{a}_{k'}(t) \right\} \right) \end{aligned} \tag{3.77}$$

To solve this differential equation we calculate $\mathcal{L}^\dagger a_k$. Keeping the bosonic commutation relation in mind $[a_k, a_{k'}^\dagger] = \delta_{kk'}$ we find that all terms for $k \neq k'$ vanish:

$$\mathcal{L}^\dagger a_k = i\left[\omega_k a_k^\dagger a_k, a_k\right] + \Gamma_\downarrow\left(a_k^\dagger a_k a_k - \frac{1}{2}\left\{a_k^\dagger a_k, a_k\right\}\right) \tag{3.78}$$

$$+ \Gamma_\uparrow\left(a_k a_k a_k^\dagger - \frac{1}{2}\left\{a_k a_k^\dagger, a_k\right\}\right) \tag{3.79}$$

$$= i\omega_k(a_k^\dagger a_k a_k - \underbrace{a_k a_k^\dagger}_{=a_k^\dagger a_k + 1}\ a_k) + \Gamma_\downarrow\left(a_k^\dagger a_k a_k - \frac{1}{2}a_k^\dagger a_k a_k - \frac{1}{2}\ \underbrace{a_k a_k^\dagger}_{=a_k a_k^\dagger + 1}\ a_k\right) \tag{3.80}$$

$$+ \Gamma_\uparrow\left(a_k a_k a_k^\dagger - \frac{1}{2}a_k\ \underbrace{a_k^\dagger a_k}_{=a_k a_k^\dagger - 1}\ - \frac{1}{2}a_k a_k a_k^\dagger\right) \tag{3.81}$$

$$= \left(-i\omega_k - \frac{1}{2}\Gamma_\downarrow + \frac{1}{2}\Gamma_\uparrow\right)a_k \tag{3.82}$$

This result motivates our ansatz for the time-dependent Heisenberg-picture operator:

$$\tilde{a}_k(t) = e^{\left(-i\omega_k - \frac{\Gamma_\downarrow - \Gamma_\uparrow}{2}\right)(t-t_0)}a_k \tag{3.83}$$

which is easily confirmed to be correct by insertion into eq. 3.77. Analogously we find for $a_k^\dagger$:

$$i\omega_k[a_k^\dagger a_k, a_k^\dagger] = i\omega_k\left(a_k^\dagger\ \underbrace{a_k a_k^\dagger}_{=a_k^\dagger a_k + 1}\ - a_k^\dagger a_k a_k^\dagger\right) = i\omega_k a_k^\dagger \tag{3.84}$$

$$\Gamma_\downarrow\left(a_k^\dagger a_k^\dagger a_k - \frac{1}{2}a_k^\dagger\ \underbrace{a_k a_k^\dagger}_{=a_k^\dagger a_k + 1}\ - \frac{1}{2}a_k^\dagger a_k^\dagger a_k\right) = -\frac{1}{2}\Gamma_\downarrow a_k^\dagger \tag{3.85}$$

$$\Gamma_\uparrow\left(a_k a_k^\dagger a_k^\dagger - \frac{1}{2}a_k a_k^\dagger a_k^\dagger - \frac{1}{2}\ \underbrace{a_k^\dagger a_k}_{=a_k a_k^\dagger - 1}\ a_k^\dagger\right) = \frac{1}{2}\Gamma_\uparrow a_k^\dagger \tag{3.86}$$

which confirms that the two Heisenberg-picture operators are the Hermitian conjugate of each other:

$$\tilde{a}_k = e^{\left(-i\omega_k - \frac{\Gamma_\downarrow - \Gamma_\uparrow}{2}\right)(t-t_0)} a_k \tag{3.87}$$

$$\tilde{a}_k^\dagger = e^{\left(i\omega_k - \frac{\Gamma_\downarrow - \Gamma_\uparrow}{2}\right)(t-t_0)} a_k^\dagger \tag{3.88}$$

To find the Heisenberg-picture bath operators $\tilde{B}_{1x}(t), \tilde{B}_{2x}(t)$ we note that the adjoint master equation is a linear differential equation and can be solved for each summand in eq. 3.75 individually, leading to:

$$\tilde{B}_{1x}(t) = \frac{1}{\sqrt{N}} \sum_k g_{kx} e^{\left(i\omega_k - \frac{\Gamma_\downarrow - \Gamma_\uparrow}{2}\right)(t-t_0)} a_k^\dagger \tag{3.89}$$

$$\tilde{B}_{2x'}(t') = \frac{1}{\sqrt{N}} \sum_{k'} g_{k'x'}^* e^{\left(-i\omega_{k'} - \frac{\Gamma_\downarrow - \Gamma_\uparrow}{2}\right)(t'-t_0')} a_k^\dagger \tag{3.90}$$

We can then calculate all four correlation functions. Analogous to eq. 3.29 two of these are zero

$$\langle \tilde{B}_{1x}(t) \tilde{B}_{1x'}(t') \rangle \propto \langle a_k^\dagger a_{k'}^\dagger \rho_0 \rangle = 0 \tag{3.91}$$

$$\langle \tilde{B}_{2x}(t) \tilde{B}_{2x'}(t') \rangle \propto \langle a_k a_{k'} \rho_0 \rangle = 0 \tag{3.92}$$

The mixed correlations follow from eq. 3.90 as [2]:

$$\langle \tilde{B}_{1x}(t) \tilde{B}_{2x'}(t') \rangle = \frac{1}{N} \sum_{kk'} g_{kx} g_{k'x'}^* e^{i\omega_k (t-t')} e^{-\frac{\Gamma_\downarrow - \Gamma_\uparrow}{2}|t-t'|} \underbrace{\langle a_k^\dagger a_{k'} \rangle}_{=\delta_{kk'}\langle n_k \rangle} \tag{3.93}$$

$$= \frac{1}{N} \sum_k g_{kx} g_{kx'}^* e^{i\omega_k (t-t')} e^{-\frac{\Gamma_\downarrow - \Gamma_\uparrow}{2}|t-t'|} \langle n_k \rangle \tag{3.94}$$

$$\langle \tilde{B}_{2x}(t) \tilde{B}_{1x'}(t') \rangle = \frac{1}{N} \sum_k g_{kx}^* g_{kx'} e^{i\omega_k (t'-t)} e^{-\frac{\Gamma_\downarrow - \Gamma_\uparrow}{2}|t-t'|} (\langle n_k \rangle + 1) \tag{3.95}$$

[2] The initial times t_0, t_0' in eq. 3.90 are both given by the time at which the initial condition $\rho(t) = \rho_0$ is fulfilled because at this time the Heisenberg operators have to equal the time-independent Schrödinger operators ,i.e. $t_0 = t_0'$. For the calculation of correlation functions of the form $\mathrm{Tr}(B_{1x}(t) B_{2x'}(t') \rho_0)$ the initial condition (a diagonal ρ_0) is fulfilled for the earlier of the two times t or t'. Note that these two cases lead to different oscillating exponentials but the same decaying exponential in eq. 3.90. This is the reason for a magnitude sign around the relative time $\tau = t - t'$ only in the decaying exponential.

Replacing g_{kx} with its definition (eq. 3.75) we find:

$$\langle \tilde{B}_{1x}(t)\tilde{B}_{2x'}(t')\rangle = \frac{1}{N}\sum_k e^{ikd(x-x')}e^{i\omega_k(t-t')}e^{-\frac{\Gamma_\downarrow-\Gamma_\uparrow}{2}|t-t'|}\langle n_k\rangle \tag{3.96}$$

$$\langle \tilde{B}_{2x}(t)\tilde{B}_{1x'}(t')\rangle = \frac{1}{N}\sum_k e^{-ikd(x-x')}e^{-i\omega_k(t-t')}e^{-\frac{\Gamma_\downarrow-\Gamma_\uparrow}{2}|t-t'|}(\langle n_k\rangle + 1) \tag{3.97}$$

The introduced decoherence leads to an additional factor which is a decaying exponential in time (cf. eq. 3.36 and 3.37). This can potentially lead to a much faster temporal decay of the correlation function since this decaying exponential is just a coefficient in the k integration of eq. 3.43, i.e. remains unchanged in the spectral function. This can make the noise Markovian even when the coupling strength g between the environmental harmonic oscillators is not large.

3.2 One-Dimensional Ising model

As a second example of an environmental model we consider a linear chain of N spins without external field, i.e. a one-dimensional Ising model [116]. While the two-dimensional Ising model has a ferromagnetic phase transition [117], the one-dimensional model always stays in a single phase. In contrast to the previous model of quantum harmonic oscillators this model is purely classical. Each spin is assigned a stochastic variable which can only take on the values $S_j = \pm 1$ with $j = 1, 2, ..., N$. The Hamiltonian reads:

$$H_B = -J\sum_{j=1}^{N-1} S_j S_{j+1} \tag{3.98}$$

The thermal equilibrium steady state correlation is (eq. 6.19 in [118])

$$\langle S_j S_{j+k}\rangle = \tanh^k(\beta J) = \exp\left\{\frac{\ln[\tanh(\beta J)]}{d}\,(x-x')\right\} \tag{3.99}$$

where β is the inverse Boltzmann constant and temperature $\beta = 1/(k_B T)$. The distance $k = (x - x')/d$ was rewritten as the spatial distance over the spacing between spins d to exhibit an exponentially decaying spatial correlation function (at one point in time).

This was extended to a space-time-correlation function in [109] by making each spin switch between the two states $S_j = \pm 1$ (due to a heat bath) at random intervals but

with a known rate per unit time $\alpha/2$. This leads to (eq. 76 in [109])

$$\langle S_j(0)S_{j+k}(\tau)\rangle = e^{-\alpha|\tau|}\sum_{l=-\infty}^{\infty}\eta^{|k+l|}I_l(\gamma\alpha|\tau|) \tag{3.100}$$

where $\eta := \tanh(\beta J)$; $\gamma := \tanh(\beta 2J)$ and the modified Bessel functions of the first kind $I_n(x) = i^{-n}J_n(ix)$ with the Bessel functions of first kind $J_n(x)$. Note that setting $\tau \to 0$ in eq. 3.100 yields back eq. 3.99.

The spin operators S_j typically couple longitudinally to a system, causing dephasing noise. We are therefore interested in the corresponding spectral function, i.e. the Fourier transform of eq. 3.100. Since eq. 3.100 is an even function of τ the Fourier transform is simply given by 2 times the one-sided Fourier transform.

Since dephasing noise is caused by the zero-frequency component of the spectral function, we simplify the calculation by settting $\omega \approx 0$. The one-sided Fourier transform then simplifies to an integral:

$$\int_0^\infty d\tau e^{i\omega\tau}\langle S_j(0)S_{j+k}(\tau)\rangle \to \int_0^\infty d\tau\langle S_j(0)S_{j+k}(\tau)\rangle \tag{3.101}$$

This integral of one summand in eq. 3.100 can be calculated with conditions:

$$\int_0^\infty d\tau e^{-\alpha|\tau|}I_l(\gamma\alpha|\tau|) = \frac{\left(\frac{\gamma}{1+\sqrt{1-\gamma^2}}\right)^l}{\alpha\sqrt{1-\gamma^2}} = \frac{\zeta\eta^l}{\alpha} \qquad \text{for } \gamma > 0, \alpha > 0 \text{ and } l \geq 0 \tag{3.102}$$

where $\zeta = \cosh(2J\beta)$. The rate $\alpha > 0$ is always true. The condition $\gamma > 0$ is true for positive coupling $J > 0$. We will now rearrange eq. 3.100 to formally fulfil the integration criterion $l \geq 0$. First we note properties of the Bessel functions for integer l [119]:

$$J_l(\tau) = \sum_{m=0}^{\infty}\frac{(-1)^m}{2^{2m+l}m!(l+m)!}\tau^{2m+l} \qquad I_l(\tau) = i^{-l}J_l(i\tau) \tag{3.103}$$

$$J_{-l}(\tau) = (-1)^l J_l(\tau) \quad \Rightarrow \quad I_{-l}(\tau) = i^{-l+2l}J_{-l}(i\tau) = I_l(\tau) \tag{3.104}$$

$$J_l(-\tau) = (-1)^l J_l(\tau) \quad \Rightarrow \quad I_l(-\tau) = (-1)^l I_l(\tau) \tag{3.105}$$

Using these relations we make $l \geq 0$ as follows:

$$\sum_{l=-\infty}^{\infty} \eta^{|k+l|} I_l(\gamma\alpha|\tau|) = \sum_{l=-\infty}^{-1} \eta^{|k+l|} I_l(\gamma\alpha|\tau|) + \eta^{|k|} I_0(\gamma\alpha|\tau|) + \sum_{l=1}^{\infty} \eta^{|k+l|} I_l(\gamma\alpha|\tau|) \tag{3.106}$$

$$= \sum_{l=1}^{\infty} \eta^{|k-l|} I_l(\gamma\alpha|\tau|) + \eta^{|k|} I_0(\gamma\alpha|\tau|) + \sum_{l=1}^{\infty} \eta^{|k+l|} I_l(\gamma\alpha|\tau|) \tag{3.107}$$

In this form we can perform the integration on each summand using eq. 3.102.

$$\int_0^{\infty} d\tau \langle S_j(0) S_{j+k}(\tau)\rangle = \frac{\mathrm{Cosh}[2J\beta]\mathrm{Tanh}[J\beta]^{|k|}}{\alpha} + \sum_{l=1}^{\infty} \frac{\mathrm{Cosh}[2J\beta]\mathrm{Tanh}[J\beta]^{l+|k-l|}}{\alpha} + \sum_{l=1}^{\infty} \frac{\mathrm{Cosh}[2J\beta]\mathrm{Tanh}[J\beta]^{l+|k+l|}}{\alpha} \tag{3.108}$$

Since this expression is invariant to the operation $k \to -k$ we can assume w.l.o.g. $k > 0$. We then remove the magnitude sign accordingly:

$$\int_0^{\infty} d\tau \langle S_j(0) S_{j+k}(\tau)\rangle = \frac{\mathrm{Cosh}[2J\beta]\mathrm{Tanh}[J\beta]^{k}}{\alpha} + \sum_{l=1}^{k} \frac{\mathrm{Cosh}[2J\beta]\mathrm{Tanh}[J\beta]^{l+k-l}}{\alpha} + \sum_{l=k+1}^{\infty} \frac{\mathrm{Cosh}[2J\beta]\mathrm{Tanh}[J\beta]^{l+l-k}}{\alpha} + \sum_{l=1}^{\infty} \frac{\mathrm{Cosh}[2J\beta]\mathrm{Tanh}[J\beta]^{l+k+l}}{\alpha} \tag{3.109}$$

The first sum is independent of l and simply yields a factor k. The other two can be calculated with the geometric series:

$$\int_0^{\infty} d\tau \langle S_j(0) S_{j+k}(\tau)\rangle = \frac{\mathrm{Cosh}[2J\beta]\mathrm{Tanh}[J\beta]^{|k|}(\mathrm{Cosh}[2J\beta] + |k|)}{\alpha} \tag{3.110}$$

$$= \frac{\zeta \eta^{\frac{|x-x'|}{d}} \left(\zeta + \frac{|x-x'|}{d}\right)}{\alpha} \tag{3.111}$$

where we have replaced some substitutions again. The magnitude sign for $|k|$ is put in to allow for negative k again. Note that this is the integral from 0 to ∞. For the standard spectral function we add a factor of 2 (see eq. 2.25 and 2.30):

$$C(\omega = 0, |x - x'|) = \frac{2}{\alpha} \zeta \eta^{\frac{|x-x'|}{d}} \left(\zeta + \frac{|x-x'|}{d}\right) \tag{3.112}$$

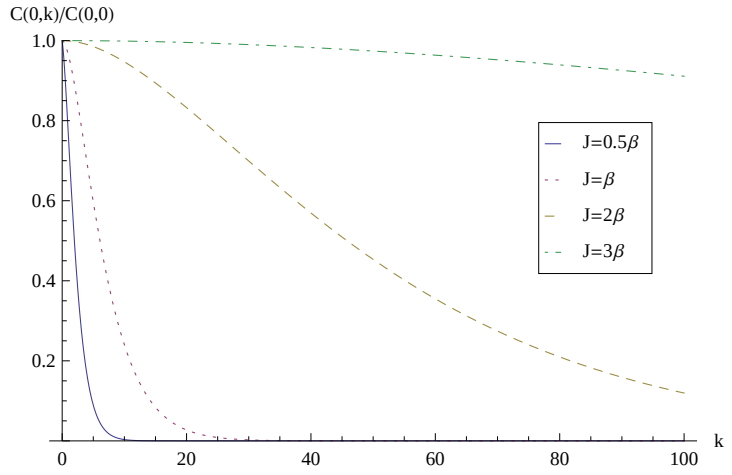

Figure 3.2: The spectral function $C(\omega = 0, |x - x'|)$ from eq. 3.112 normalised by its value for $|x - x'| = 0$. The coupling strength J determines the width and is set to the values $J = \{0.5\beta, \beta, 2\beta, 3\beta\}$.

with $\zeta = \cosh(2J\beta)$ and $\eta = \tanh(J\beta)$. The spectral function decays with distance as $|x| \exp(-|x|)$. The effective correlation length in this example increases with the coupling J of the environmental spins and decreases with temperature $k_B T$. Strongly coupled environmental spins lead to spatially correlated noise, while thermal effects can destroy the spatial correlations of the noise. The spectral function is plotted in figure 3.2.

3.3 Two qubits placed in these environmental models

We have now calculated spectral functions for two classes of models for the environmental noise: an ensemble of coupled quantum harmonic oscillators and a spin ensemble in a classical Ising model. From both model classes we have obtained the spectral function which characterises the environment entirely as required for the Bloch-Redfield equations. To illustrate how these spectral functions can now be used as an environmental model for any system and to illustrate the physical properties of these spectral functions we now assume a system of two uncoupled qubits, which are placed in these environments.

The two qubits $H_S = \sum_{j=1}^{2} \omega_q \sigma_z^{(j)}$ are each interacting longitudinally with the environment $H_{int} = \sum_{j=1}^{2} \sigma_z^{(j)} B_j$. With the four states $|1,1\rangle$,$|1,0\rangle$,$|0,1\rangle$,$|0,0\rangle$ we find a

reduced dephasing rate γ_- for the single excitation subspace $\{|1,0\rangle, |0,1\rangle\}$ and an enhanced dephasing rate γ_+ between the states $|1,1\rangle$ and $|0,0\rangle$ while all other pairs dephase at a rate γ_0. These rates are obtained in terms of $C(\omega, |\mathbf{r}_j - \mathbf{r}_k|)$ as,

$$\gamma_- = C(0,0) - C(0,l) \tag{3.113}$$

$$\gamma_+ = C(0,0) + C(0,l) \tag{3.114}$$

$$\gamma_0 = C(0,0)/2 \tag{3.115}$$

where $l = |\mathbf{r}_1 - \mathbf{r}_2|$ is the distance between the qubits. For uncorrelated decoherence only the self-correlations are non-zero, i.e. $C(0,l) = 0$, and all coherences decay at the rate γ_0 or $2\gamma_0$. With increasing noise correlation length and fixed qubit distance the single excitation subspace's dephasing rate γ_- is reduced by $C(0,l)$ while γ_+ is increased by $C(0,l)$. This reduction of γ_- is the basis of a decoherence-free subspace [10].

If the two qubits are placed in an Ising model environment as discussed in section 3.2, we simply use the respective spectral function eq. 3.112 and find the rates:

$$\gamma_- = \frac{2\zeta}{\alpha}\left[\zeta - \eta^{l/d}(\frac{l}{d} + \zeta)\right] \tag{3.116}$$

$$\gamma_+ = \frac{2\zeta}{\alpha}\left[\zeta + \eta^{l/d}(\frac{l}{d} + \zeta)\right] \tag{3.117}$$

$$\gamma_0 = \zeta^2/\alpha \tag{3.118}$$

where $\zeta = \cosh(2J\beta)$ and $\eta = \tanh(J\beta)$; and the qubit distance l is given in units of the environmental Ising spins' nearest-neighbour distance d. For close distances $d \ll J\beta$ the correlated decoherence effects are the strongest and the reduced dephasing rate γ_- is close to zero. As the qubits are put increasingly further apart the correlated decoherence terms vanish and $\gamma_- \approx \gamma_+$.

If the two qubits are placed in the environment of coupled harmonic oscillators as discussed in section 3.1 we use the respective spectral function eq. 3.67 and find:

$$\gamma_- = [1 - \cos(l\pi/2d)]\langle n(0)\rangle/(2\pi g) \tag{3.119}$$

$$\gamma_+ = [1 + \cos(l\pi/2d)]\langle n(0)\rangle/(2\pi g) \tag{3.120}$$

$$\gamma_0 = \langle n(0)\rangle/(\pi g) \tag{3.121}$$

where the qubit distance l is given in units of the environmental nearest-neighbour

distance of the harmonic oscillators d and we assume $\omega_0 \approx 0$ on the scale of the system energies making their energy spectrum approximately continuous. There are now three types of system dynamics: For $\cos(l\pi/2d) = 1$ one finds the qubits fully (positively) correlated and $\gamma_- \to 0$, similar to the previous Ising model for short distances. At the points where $\cos(l\pi/2d) = 0$ the collective terms are zero and all correlated decoherence effects vanish. For $\cos(l\pi/2d) = -1$ the collective terms are negative and $\gamma_+ \to 0$, i.e. the reduced and enhanced rates swap roles. This means the subspace $\{|1,1\rangle, |0,0\rangle\}$ becomes decoherence-free and the subspace $\{|1,0\rangle, |0,1\rangle\}$ has an enhanced dephasing rate. This rare case only occurs at points where the environmental noise of the two qubits is negatively correlated.

This unusual behaviour, where the roles of decoherence-reduced and decoherence-enhanced subspaces are swapped plays an important role in section 4.4. A similar effect was described in reference [103] for entangled states of two different transitions with anticorrelated noise.

3.4 Chapter summary

We investigated two environmental models and derived their respective spectral functions. In section 3.1 we modeled the environments with a large number of quantum harmonic oscillators with nearest-neighbour coupling. This can be regarded as an extension of the common spin-boson model, which assumes an environment of uncoupled quantum harmonic oscillators.

We found that the space-time correlation function does not necessarily reflect the spatial correlation of the spectral functions (frequency domain), which enter the Bloch-Redfield equations. The spatial correlations are only the same if the space-time correlation function is a product of a spatial and a temporal part, i.e. they are separable.

Markovianity of the environment is guaranteed when the time correlations decay fast. For this environment the time-decay is polynomial with the inverse coupling strength $1/g$ of environmental harmonic oscillators, i.e. the environment is only Markovian if it is very strongly coupled relative to the system energies of interest. However, the assumption of an intrinsic decoherence in the environment can be used to reinforce Markovianity regardless of g.

Spatial correlations at any single point in time are given by a Lorentzian spatial decay

with a correlation length given by the environmental coupling strength $g/(k_BT)$ and nearest neighbours are correlated or anticorrelated depending on the sign of g. Since space-time correlations are non-separable the spectral function shows a very different, cosine-shaped spatial correlation. The noise frequencies are centred around the oscillators eigenenergies with a noise cut-off at 2g left and right of this frequency due to the band gap of the chain.

In section 3.2 the environment was regarded as a one-dimensional Ising model. The spectral function at zero frequency was purely positive and showed monotonically decaying spatial correlations in the functional form $|x|\exp(-|x|)$. The correlation length is determined by the coupling strength $J/(k_BT)$ of the environmental Ising spins. The environmental correlation length increases with stronger coupling between the environmental spins. It decreases with thermal effects, which grow stronger with temperature.

In section 3.3 we showed how two qubits, coupled longitudinally to each of these environmental models respectively would be affected by them. When the qubits are close together we find that in both environments there emerges a decoherence-free subspace and decoherence-enhanced subspace. Increasing the distance between the qubits in the Ising model environment weakens these correlated decoherence effects and reverts back to uncorrelated decoherence. In the environment of coupled harmonic oscillators the spatial correlations oscillate with increasing distance of the qubits, leading to certain distances for the qubits where the correlated decoherence effects are zero, but also some distances where the noise is anticorrelated and the correlated decoherence effects are inverted, i.e. the decoherence-free and decoherence-enhanced subspaces are swapped. This has important implications in quantum metrology (see section 4.4).

Chapter 4

4 Quantum metrology with correlated decoherence

We investigate how spatially correlated decoherence affects quantum metrology with entangled states. We find that for suitable n-entangled states the precision scales with the best-possible, Heisenberg-limited scaling. This is in contrast to a large body of work which is concerned with uncorrelated decoherence and has found this type of noise to fundamentally limit the scaling by the standard quantum limit. We find that this limit can be overcome in spatially correlated noise environments and the Heisenberg-limited setup is robust even for finite spatial correlations. With finite correlations the dephasing rate becomes dependent on the order in which the ions are arranged and how the array is scaled up relative to the correlation length.

Introduction

Quantum metrology deals with high precision measurements of quantum mechanical parameters [120]. A particular focus is the measurement of time and frequency with accuracies of the order 1 part in $10^{14} - 10^{18}$. The standard experiment is Ramsey spectroscopy [46,121], where the frequency of the relative phase of a superposition of two quantum states is measured. Statistics are obtained by measuring n times (either repeatedly on one atom/ion or on an array of n identical atoms/ions). The frequency uncertainty is found to be $1/(\sqrt{n}t)$ where t is the time for one measurement. This scaling is called the *standard quantum limit* [120] or sometimes *shot noise limit* [122].

The standard quantum limit can be overcome with maximally entangled initial states

yielding an improved frequency uncertainty of $1/(nt)$ [123–125], which coincides with the best possible scaling allowed by the energy/time uncertainty relation, the Heisenberg limit [125]. First experimental precision measurements with entangled input states have been performed [47, 48]. However, in the presence of uncorrelated Markovian noise both entangled states and product states were found to have an uncertainty of $1/(\sqrt{n}t)$, i.e. the standard quantum limit [46]. These findings were recently reinforced by a rigorous mathematical framework [126, 127].

Investigations of precision scalings are generally made assuming an uncorrelated decoherence source even though some noise sources, for example in ion traps, have been found to be correlated [35, 48]. We investigate here the scaling behaviour of both initial product states and initial entangled states in the presence of *correlated* decoherence and point out advantages and disadvantages in comparison to uncorrelated decoherence.

First we will discuss a setup in which correlated decoherence is advantageous: electric quadrupole measurements for which maximally entangled states are used, which are of relevance for the calibration of optical frequency standards [128]. In this setup correlated decoherence restores the Heisenberg limit in certain circumstances, which is discussed in sections 4.2 and 4.3. In section 4.4 we will show that correlated decoherence is disadvantageous in Ramsey spectroscopy setups with Greenberger-Horne-Zeilinger (GHZ) states.

4.1 Measurement of the electric quadrupole moment of hydrogen-like ions

We consider a system of n hydrogen-like ions with a Zeeman splitting term of the sublevels J_z of the total angular moment and a small correction term due to the interaction of the atomic electric quadrupole moment with the external electric field gradient. These correction terms are quadratic in J_z [48, 129].

$$H_s = \omega_0 \sum_{j=1}^{n} J_z^{(j)} + \alpha \sum_{j=1}^{n} (J_z^{(j)})^2 \tag{4.1}$$

The electric quadrupole moment can be measured by entangling two states which have the same expectation value for the first term in eq. 4.1 but different expectation values for the second. The relative phase of the two states then oscillates at the

quadrupole frequency. This has been done experimentally by C. Roos [48] for two $D_{5/2}$ systems with $J_z |m_j\rangle = m_j |m_j\rangle$ and $m_j \in [\frac{-5}{2}, \frac{-3}{2}, \frac{-1}{2}, \frac{1}{2}, \frac{3}{2}, \frac{5}{2}]$. Out of the six states only three were occupied however. They initialised an entangled state of the form $\frac{1}{\sqrt{2}}(|m_1, m_2\rangle + |m_3, m_4\rangle)$ where $m_1 + m_2 = m_3 + m_4$. Particularly their state is:

$$\frac{1}{\sqrt{2}} (|-5/2, 3/2\rangle + |-1/2, -1/2\rangle)$$

We generalise this quadrupole measurement scheme for two ions to an even number n of ions but reduce each ion to an effective three state system (because only three states are relevant) and generalise the J_z operator for these three states to be

$$J_z = \begin{pmatrix} m_+ & 0 & 0 \\ 0 & m_0 & 0 \\ 0 & 0 & m_- \end{pmatrix} \tag{4.2}$$

with $m_+ = m_0 + m_\Delta$ and $m_- = m_0 - m_\Delta$. In other words m_+ and m_- differ from m_0 by the same arbitrary natural number m_Δ. We investigate two entangled states, each composed of two components which have the same expectation value for the first term in eq. 4.1, i.e. $\frac{n}{2}m_- + \frac{n}{2}m_+ = nm_0$ and different expectation values for the second term in eq. 4.1. In particular we will look at the two initial states:

$$\left|\Psi_0^{(1)}\right\rangle = \frac{1}{\sqrt{2}}(|\underbrace{m_-, m_-, ..., m_-}_{n/2}, \underbrace{m_+, m_+, ..., m_+}_{n/2}\rangle + |m_0, m_0, m_0, ..., m_0\rangle) \tag{4.3}$$

$$\left|\Psi_0^{(2)}\right\rangle = \frac{1}{\sqrt{2}}(|m_-, m_+, m_-, m_+, m_-..., m_+\rangle + |m_0, m_0, m_0, ..., m_0\rangle) \tag{4.4}$$

These states look equivalent since the ions are simply in a different order. However for partially correlated decoherence we will find a difference in their dephasing rates. For the coherent time evolution $\partial_t |\Psi\rangle = -iH_s |\Psi\rangle$ of the relative phase of our initial states the Zeeman shift cancels and the quadrupole moment gives the only

contribution. We demonstrate this explicitly for $\left|\Psi_0^{(1)}\right\rangle$:

$$\omega_0 \sum_{j=1}^{n} J_z^{(j)} \left|m_-, m_-, ..., m_-, m_+, m_+, ..., m_+\right\rangle = \omega_0 \sum_{j=1}^{n} J_z^{(j)} \left|m_0, m_0, m_0, ..., m_0\right\rangle \tag{4.5}$$

$$\alpha \sum_{j=1}^{n} (J_z^{(j)})^2 \left|m_-, m_-, ..., m_-, m_+, m_+, ..., m_+\right\rangle = \alpha \frac{n}{2}(m_0 + m_\Delta)^2 + \alpha \frac{n}{2}(m_0 - m_\Delta)^2$$

$$= n\alpha(m_0^2 + m_\Delta^2) \tag{4.6}$$

$$\alpha \sum_{j=1}^{n} (J_z^{(j)})^2 \left|m_0, m_0, m_0, ..., m_0\right\rangle = n\alpha m_0^2 \tag{4.7}$$

Omitting the global phase, the coherent time evolution is given by:

$$\left|\Psi^{(1)}(t)\right\rangle = \left|m_-, m_-, ..., m_-, m_+, m_+, ..., m_+\right\rangle + e^{i\omega t} \left|m_0, m_0, m_0, ..., m_0\right\rangle \tag{4.8}$$

$$\text{with } \omega = n\alpha m_\Delta^2 \tag{4.9}$$

This frequency is the same for $\left|\Psi_0^{(2)}\right\rangle$. These states provide a means of measuring the electric quadrupole moment via a Ramsey-like measurement of the relative frequency. Note that it scales linearly with the number of ions n which contribute to the entangled state. These states are two examples of many entangled states which show Heisenberg precision scaling for purely unitary evolution, i.e. when all decoherence is neglected [123, 124]. The precision scalings for all entangled states collapse to the standard quantum limit in the presence of spatially uncorrelated dephasing [46, 126, 127]. In the next two sections we will investigate the precision scalings of the two states considering spatially correlated dephasing.

4.2 Fully correlated dephasing for quadrupole measurements

To study the effects of spatial correlations we begin with the mathematically simple case of a perfectly correlated noise environment throughout the entire ion array. The system-environment coupling is of the form

$$H_{int} = \sum_j J_z^{(j)} B_j \tag{4.10}$$

and the spectral function for a perfectly correlated environment is:

$$\forall j,k: \quad C_{jk}(\omega) = C(\omega) \tag{4.11}$$

4.2.1 Decoherence-free subspace

Using the spectral function above we set up the Bloch-Redfield equations (eq. 2.27). Since both the Hamiltonian and the system operators which couple to the bath are diagonal operators (pure dephasing) these equations simplify to

$$\dot{\rho} = \frac{i}{\hbar}[\rho, H_s] + \frac{1}{\hbar^2}\frac{C(\omega=0)}{2}\sum_{j,k}(-s_j s_k \rho + s_k \rho s_j - \rho s_k s_j + s_j \rho s_k) \tag{4.12}$$

where the system operators $s_j = J_z^{(j)}$. Taking the sums into each term we define a new Hermitian operator $S = \sum_j s_j$ with $S^\dagger = S$. We therefore find the equations to be of the simple Lindblad form:

$$\dot{\rho} = \frac{i}{\hbar}[\rho, H_s] + \frac{1}{\hbar^2}\frac{C(\omega=0)}{2}\left(2S\rho S - \{S^2, \rho\}\right) \tag{4.13}$$

We are interested in the coherence of the two states which make the constituents of our initial state (eq. 4.3). For these two states we find:

$$S\left|m_-, m_-, ..., m_-, m_+, m_+, ..., m_+\right\rangle = S\left|m_0, m_0, m_0, ..., m_0\right\rangle \tag{4.14}$$

In other words for their subspace $S \propto \mathbb{1}$ and the master equation becomes:

$$\dot{\rho} = \frac{i}{\hbar}[\rho, H_s] + \frac{1}{\hbar^2}\frac{C(\omega=0)}{2}\left(2\mathbb{1}\rho\mathbb{1} - \{\mathbb{1}^2, \rho\}\right) \tag{4.15}$$

$$= \frac{i}{\hbar}[\rho, H_s] + 0 \tag{4.16}$$

This means our entangled initial state is in a decoherence-free subspace (for a perfectly correlated bath). For a perfectly correlated bath this result applies to the second initial state $\left|\Psi_0^{(2)}\right\rangle$ equally, which is not surprising since it is the same state with simply a different order of the ions. Note that in the next section the two initial states will show different dephasing rates.

The time evolution of our initial state is coherent and simply given by the relative

phase which equals the energy difference of the two states (see eq. 4.9):

$$|\Psi(t)\rangle = |m_-, m_-, ..., m_-, m_+, m_+, ..., m_+\rangle + e^{i\omega t} |m_0, m_0, m_0, ..., m_0\rangle \tag{4.17}$$

$$\text{with } \omega = n\alpha m_\Delta^2 \tag{4.18}$$

The precision scaling with increasing number n of ions used in the entangled state is given by the coherent Heisenberg scaling since fully correlated dephasing does not affect the subspace of the entangled state. This is the first theoretical analysis where Heisenberg scaling is found in the presence of environmental noise and in stark contrast to spatially uncorrelated noise. However fully (i.e. perfectly) correlated noise will only persist to a certain number of ions. In the next section we investigate the realistic case of partially correlated dephasing with finite correlation length and find the Heisenberg scaling to persist under certain conditions.

4.3 Partially correlated dephasing in quadrupole measurements

We now regard the ions as a linear, equidistant (uncoupled) chain and assume homogeneous correlations in the bath, which decay exponentially with increasing relative distance:

$$C_{jk}(\omega = 0) = C(\omega = 0, |j-k|) = \exp\left(-\frac{|j-k|d}{\xi}\right) \tag{4.19}$$

where ξ gives the correlation length and d is the nearest-neighbour distance between ions. Putting this into the Bloch-Redfield equations (eq. 2.27) we find:

$$\dot{\rho} = \frac{i}{\hbar}[\rho, H_s] + \frac{1}{\hbar^2}\frac{1}{2}\sum_{j,k} \exp\left(-\frac{|j-k|d}{\xi}\right)(-s_j s_k \rho + s_k \rho s_j - \rho s_k s_j + s_j \rho s_k) \tag{4.20}$$

where again the system operators $s_j = J_z^{(j)}$ and the indices j and k run from 1 to n. In this dephasing environment the time-derivative of off-diagonal ρ-elements depends only on themselves. We therefore investigate only two elements of ρ, namely the ones associated with the coherence of our two initial states (eq. 4.3 and 4.4).

The elements are:

$$r = |m_-, m_-, ..., m_-, m_+, m_+, ..., m_+\rangle \langle m_0, m_0, m_0, ..., m_0| \tag{4.21}$$

$$r_2 = |m_-, m_+, m_-, m_+, ...\rangle \langle m_0, m_0, m_0, ..., m_0| \tag{4.22}$$

We will now continue the calculations for r and only point out the different results for r_2. To calculate eq. 4.20 for r we note how $s_j = J_z^{(j)}$ acts from the left and from the right onto this element

$$J_z^{(j)} r = \begin{cases} (m_0 - m_\Delta) r & \text{if } j \leq n/2 \\ (m_0 + m_\Delta) r & \text{if } j > n/2 \end{cases} \tag{4.23}$$

$$r J_z^{(j)} = m_0 r \tag{4.24}$$

We now calculate the time derivative of our first element of interest with the help of equation 4.20 and find for all n an equation of the form:

$$\dot{r} = (-in\alpha m_\Delta^2 + \Gamma(n, \xi)) r \tag{4.25}$$

We calculate this function $\Gamma(n, \xi)$ for increasing numbers of ions and also calculate the Taylor series of $\Gamma(n, \xi)$ for large ξ/d to first order of each function, replacing $e^x \approx 1 + x$. We present our results in the following table:

n	$\Gamma(n, \xi)$ (analytic)	$\Gamma(n, \xi)$ (Taylor series)
2	$\left(-1 + e^{-d/\xi}\right) m_\Delta^2$	$-m_\Delta^2 d/\xi + O\left[d/\xi\right]^2$
4	$\left(-2 + e^{-3d/\xi} + 2e^{-2d/\xi} - e^{-d/\xi}\right) m_\Delta^2$	$-6m_\Delta^2 d/\xi + O\left[d/\xi\right]^2$
6	$\left(-3 + e^{-5d/\xi} + 2e^{-4d/\xi} + 3e^{-3d/\xi} - 3e^{-d/\xi}\right) m_\Delta^2$	$-19m_\Delta^2 d/\xi + O\left[d/\xi\right]^2$

We find for n (details of the calculation in the appendix E):

n	$\dfrac{6e^{\frac{d}{\xi}} + 2e^{\frac{(1-n)d}{\xi}} - 8e^{\frac{(2-n)d}{2\xi}} + n - e^{\frac{2d}{\xi}} n}{2\left(-1 + e^{\frac{d}{\xi}}\right)^2} m_\Delta^2$	$-\dfrac{n(2+n^2)d}{12\xi} m_\Delta^2 + O\left[\frac{d}{\xi}\right]^2$

Note that to zero order in d/ξ the decay rate $\Gamma(n, \xi)$ vanishes, corresponding to our result of a decoherence-free subspace for a fully correlated bath.

The analytic decay rate $\Gamma(n,\xi)$ was calculated from the sum (appendix E)

$$\Gamma(n,\xi) = \left(-\frac{n}{2} + \sum_{x=1}^{n/2} -(n-3x)e^{-xd/\xi} + \sum_{x=n/2+1}^{n} (n-x)e^{-xd/\xi} \right) m_\Delta^2 \tag{4.26}$$

$$= \frac{6e^{\frac{d}{\xi}} + 2e^{\frac{(1-n)d}{\xi}} - 8e^{\frac{(2-n)d}{2\xi}} + n - e^{\frac{2d}{\xi}} n}{2\left(-1+e^{\frac{d}{\xi}}\right)^2} m_\Delta^2 \tag{4.27}$$

Similarly we find for the element r_2 the decay rate (appendix E):

$$\Gamma_2(n,\xi) = \left(-\frac{n}{2} + \sum_{x_c=1}^{n/2} (n-2x_c+1)e^{(2x_c-1)d/\xi} + \sum_{x_c=1}^{n/2} (2x_c-n)e^{2x_c d/\xi} \right) m_\Delta^2 \tag{4.28}$$

$$= \frac{-2e^{\frac{d}{\xi}} + 2e^{\frac{(1-n)d}{\xi}} + n - e^{2d/\xi} n}{2\left(1+e^{\frac{d}{\xi}}\right)^2} m_\Delta^2 \tag{4.29}$$

Here it becomes clear that ordering the ions in a different way makes a significant difference for partially correlated environments. For perfect correlations all the terms in each of the two rates add to zero. As the correlation length decreases this cancellation is not perfect any more. In the case of $\Gamma(n,\xi)$ all positive terms involve large distances x and all negative terms involve short distances. In the case of $\Gamma_2(n,\xi)$ positive and negative terms alternate with increasing distance x. Since the correlations for long distances are weaker than for short distances, the second rate $\Gamma_2(n,\xi)$ is more robust against partial correlations and the initial state $|\Psi_0^{(2)}\rangle$ is better protected against dephasing. This corresponds to the fact that pairs of ions with one ion in m_+ and one ion in m_- are generally further apart in $|\Psi_0^{(1)}\rangle$ and closer together in $|\Psi_0^{(2)}\rangle$. Compare eq. 4.3 and 4.4.

Note that we can calculate both dephasing rates for other functional forms than exponential decay (eq. 4.19) by replacing $\exp(xd/\xi) \to C_{|j-k|=x}(\omega=0)$ in the respective sum (eq. 4.26 or 4.28).

The master equation 4.25 is now solved

$$r(t) = r_0 \exp\left(-i\omega t + \Gamma(n,\xi)t\right) \tag{4.30}$$

$$\tag{4.31}$$

with $\omega = n\alpha m_\Delta^2$ and $\Gamma(n,\xi)$ given in eq. 4.27. For the two-state subspace of the initial state (eq. 4.3) the density matrix follows as:

$$\rho(t) = \begin{pmatrix} 1/2 & \frac{1}{2}e^{-i\omega t+\Gamma(n,\xi)t} \\ \frac{1}{2}e^{i\omega t+\Gamma(n,\xi)t} & 1/2 \end{pmatrix} \tag{4.32}$$

Performing a parity measurement on the ion array results in the two probabilities for an even or odd parity:

$$P_{even} = \mathrm{Tr}\left[\frac{1}{2}\begin{pmatrix} 1 & 1 \\ 1 & 1 \end{pmatrix}\rho(t)\right] = \frac{1}{4} + \frac{1}{4}e^{i\omega t+\Gamma(n,\xi)t} + \frac{1}{4}e^{-i\omega t+\Gamma(n,\xi)t} + \frac{1}{4} \tag{4.33}$$

$$= \frac{1}{2} + \frac{1}{2}\cos(\omega t)e^{\Gamma(n,\xi)t} \tag{4.34}$$

$$P_{odd} = \mathrm{Tr}\left[\frac{1}{2}\begin{pmatrix} 1 & -1 \\ -1 & 1 \end{pmatrix}\rho(t)\right] \tag{4.35}$$

$$= \frac{1}{2} - \frac{1}{2}\cos(\omega t)e^{\Gamma(n,\xi)t} \tag{4.36}$$

again with $\omega = n\omega_{meas} = n\alpha m_\Delta^2$ and $\Gamma(n,\xi)$ given in eq. 4.27.

Using these two probabilities we calculate the Fisher information (see [130] or eq. 5 in [131]) as:

$$F(\omega_{meas}) = \sum_{j=even,odd} \frac{1}{P_j}\left(\frac{\partial P_j}{\partial \omega_{meas}}\right)^2 \tag{4.37}$$

$$= \frac{e^{2t\Gamma}n^2t^2\sin\left[nt\omega_{\mathrm{meas}}\right]^2}{4\left(\frac{1}{2} - \frac{1}{2}e^{t\Gamma}\cos\left[nt\omega_{\mathrm{meas}}\right]\right)} + \frac{e^{2t\Gamma}n^2t^2\sin\left[nt\omega_{\mathrm{meas}}\right]^2}{4\left(\frac{1}{2} + \frac{1}{2}e^{t\Gamma}\cos\left[nt\omega_{\mathrm{meas}}\right]\right)} \tag{4.38}$$

$$= \frac{n^2t^2\sin\left[nt\omega_{\mathrm{meas}}\right]^2}{e^{-2t\Gamma} - \cos\left[nt\omega_{\mathrm{meas}}\right]^2} \tag{4.39}$$

From that we calculate the uncertainty[1] (see eq. 4 in [131])

$$\Delta\omega_{meas} = \sqrt{\frac{1}{NF(\omega_{meas})}} = \sqrt{\frac{1}{\frac{T}{t}F(\omega_{meas})}} \tag{4.40}$$

$$= \sqrt{\frac{e^{-2t\Gamma} - \cos\left[nt\omega_{\mathrm{meas}}\right]^2}{n^2tT\sin\left[nt\omega_{\mathrm{meas}}\right]^2}} \tag{4.41}$$

[1] Note that this calculation of the uncertainty via the Fisher information (eq. 4.37 and 4.40) is equivalent to the following simple considerations: In a binary (two outcomes only) process the expectation value is the probability. The standard deviation for it is $\Delta P = \sqrt{P(1-P)/N}$. Propagation of error then yields the standard deviation of the frequency $\Delta\omega_{\mathrm{meas}} = \frac{\sqrt{P(1-P)/N}}{|dP/d\omega_{\mathrm{meas}}|}$.

where the total number of measurements $N = T/t$ is given by total time of all repeated measurements T divided by the time for one measurement t.

4.3.1 Time-optimisation of the uncertainty

The uncertainty (eq. 4.41) is a function of the time at which the system is measured. This raises the question of what is the optimal time to reduce the uncertainty to a minimum. We rewrite the uncertainty in the form:

$$\Delta\omega_{meas} = \sqrt{\frac{e^{-2t\Gamma} - \cos\left[nt\omega_{\text{meas}}\right]^2}{n^2 tT \sin\left[nt\omega_{\text{meas}}\right]^2}} = \sqrt{\frac{e^{-2t\Gamma} - 1 + \sin\left[nt\omega_{\text{meas}}\right]^2}{n^2 tT \sin\left[nt\omega_{\text{meas}}\right]^2}} \tag{4.42}$$

$$= \sqrt{\frac{\frac{\exp(-2\Gamma t)-1}{\sin^2(n\omega_{\text{meas}}t)} + 1}{n^2 tT}} \tag{4.43}$$

To minimize this uncertainty we want the $\sin^2$-term to be 1 by choosing a measuring time:

$$n\omega_{\text{meas}}t = m\pi/2 \qquad (m \text{ odd}) \tag{4.44}$$

This yields the expression

$$\Delta\omega_{meas} \to \sqrt{\frac{\exp(2\Gamma t)}{n^2 tT}} \tag{4.45}$$

with the minimum

$$\Delta\omega_{meas}^{opt} = \sqrt{\frac{2e|\Gamma(n,\xi)|}{n^2 T}} \tag{4.46}$$

$$\text{at } t = \frac{1}{2|\Gamma(n,\xi)|} \tag{4.47}$$

We then find the total optimum by choosing that value for t (out of the options given by eq. 4.44) which is closest to $1/(2|\Gamma|)$. An example is given in figure 4.1.

This time-optimised uncertainty is general for all entangled frequency measurements (eq. 4.36) with $\omega = n\omega_{\text{meas}}$ and any dephasing rate $\Gamma(n,\xi)$. For Ramsey spectroscopy one finds this analogously (cf. eq. 14 in [46] or section 4.4 in this thesis).

Eq. 4.46 shows how the precision scaling with the number of ions n is determined by the fundamental interplay between faster dynamics through entanglement (reducing

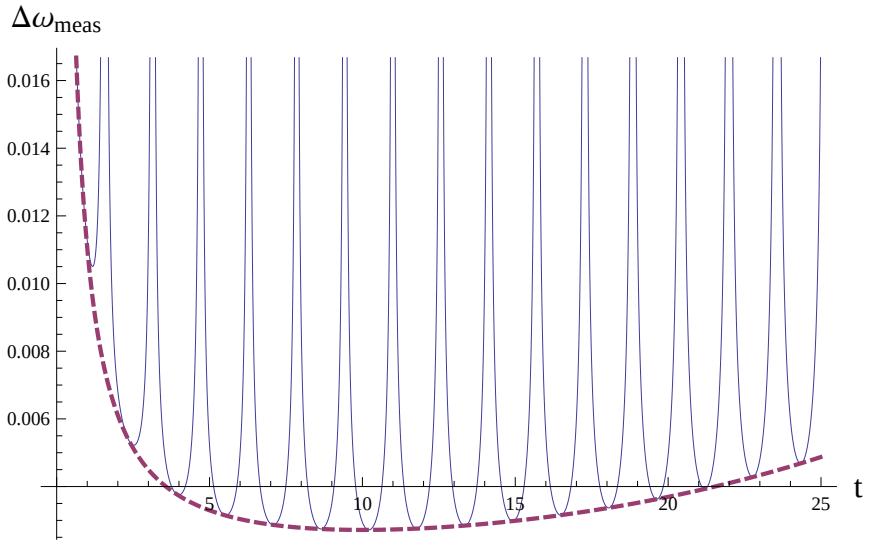

Figure 4.1: Time evolution of the uncertainty in eq. 4.43 (solid) and eq. 4.45 (dashed) for the parameters: $\Gamma = -0.1; n = 10; T = 100t; \omega_{\text{meas}} = 0.2$

the uncertainty) on the one hand and stronger dephasing on the other. An entangled state of n ions oscillates n times faster than each ion by itself in an independent measurement. This gives a scaling advantage of $1/\sqrt{n}$. However, for many states the dephasing rate also increases as more particles are entangled. If the rate scales linearly $\Gamma(n, \xi) \propto n$ then the scaling advantage is entirely cancelled and the experiment shows the standard quantum limit. This is true for uncorrelated Markovian dephasing in all generality. For other types of noise the precision scaling is determined by the scaling of the dephasing rate. A constant dephasing rate (independent of n) leads to Heisenberg scaling, a dephasing rate that scales linearly leads to the standard quantum limit.

4.3.2 Scaling of the optimal uncertainty with n

We found before that the rate $\Gamma_2(n, \xi)$ for the second initial state (eq.4.4) is advantageous over $\Gamma(n, \xi)$. We therefore continue using $\Gamma_2(n, \xi)$ from here on. To judge whether entangled states give an advantage over the standard quantum limit ($\propto 1/\sqrt{n}$) for quantum metrology in the presence of (exponentially decaying) correlated noise we need to find out whether the dephasing rate $\Gamma(n, \xi)$ scales faster or

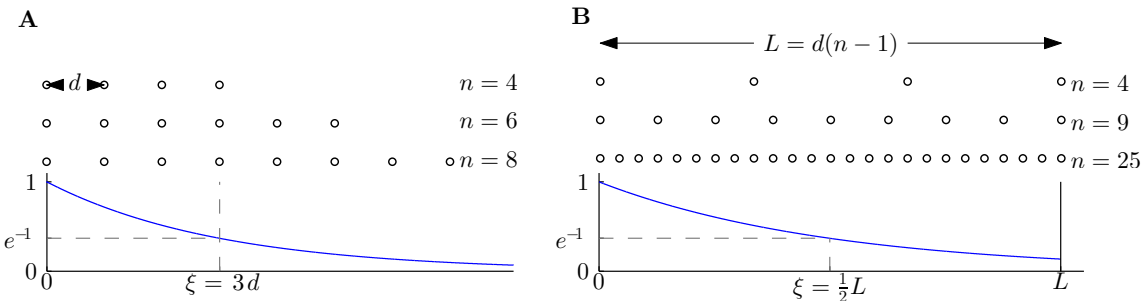

Figure 4.2: Three arrays with increasing numbers n of ions with two ways of scaling them relative to the spatial correlation function $C(0,x) = \exp(-x/\xi)$: **A** The distance d between ions is fixed and the array becomes longer with increasing n. **B** The array length L is fixed and ions become more dense with increasing number n.

slower than n (compare eq. 4.46). The rate is given by (eq. 4.29):

$$\Gamma_2(n,\xi) = \frac{-2e^{\frac{d}{\xi}} + 2e^{\frac{(1-n)d}{\xi}} + n - e^{\frac{2d}{\xi}} n}{2\left(1+e^{\frac{d}{\xi}}\right)^2} m_\Delta^2 \tag{4.48}$$

From the derivation in appendix E it follows clearly[2] that for uncorrelated decoherence the dephasing rate is given by:

$$\Gamma_u = -\frac{n}{2} m_\Delta^2 \tag{4.49}$$

We can compare these two rates in two different ways (figure 4.2). On the one hand we can scale the correlation length $\xi = cL$ as a certain fraction of the whole array length L which means that the correlations between the first ion and the last ion in the array have a fixed value $C(\omega = 0, n) = \exp(-1/c)$. On the other hand we can set the correlation length $\xi = cd$ to a fixed number of ions which means that the array gets longer relative to the correlation length as we increase n. This will ultimately restore the scaling of uncorrelated decoherence when $n \gg \xi$. We discuss both types of scaling below and compare both with Γ_u in figure 4.3. In experiments both types of scaling are possible, depending on whether the density or the array length is kept fixed with increasing numbers; equidistant spacing between ions can be achieved in segmented ion traps [132].

[2]For uncorrelated decoherence all mixed terms $j \neq k$ are zero in eq. 9.21. Therefore only case 3 exists and all terms from case 1 and 2 are zero.

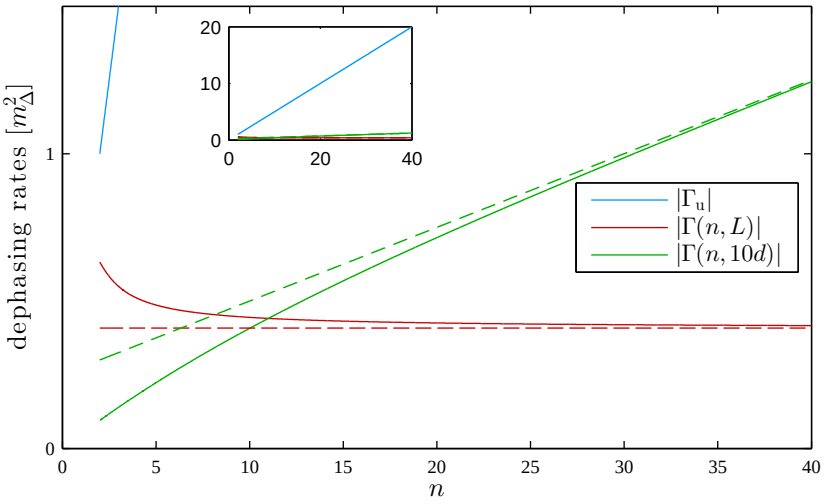

Figure 4.3: Dephasing rates in units of m_Δ^2 and their scaling with n. Dashed lines are the approximations for large n. Fixing the correlation length in terms of the array length (here: $\xi = L$) the correlated dephasing rate $\Gamma_2(n, L)$ (red) approaches a constant. Fixing the correlation length in terms of the nearest-neighbour distance (here: $\xi = 10d$) the correlated dephasing rate $\Gamma_2(n, \xi = 10d)$ (green) approaches linear scaling. Note the smaller slope compared to the uncorrelated dephasing rate Γ_u (blue). This plot shows that even partially correlated decoherence is strongly advantageous for the chosen initial states.

4.3.2.1 Correlation length as a fraction of the whole array

Using $d = L/(n-1)$ (see figure 4.2**B**) in eq. 4.48 we find an expression where the noise correlation length ξ is given relative to the array length L. We can see that the correlated dephasing rate quickly approaches a constant (see figure 4.3):

$$\lim_{n\to\infty} \frac{-2e^{\frac{L}{(n-1)\xi}} + 2e^{-\frac{L}{\xi}} + n - e^{\frac{2L}{(n-1)\xi}} n}{2\left(1 + e^{\frac{L}{(n-1)\xi}}\right)^2} = -\frac{m_\Delta^2}{4} + \frac{m_\Delta^2}{4} e^{-\frac{L}{\xi}} - \frac{m_\Delta^2 L}{4\xi} \tag{4.50}$$

For $\xi/L > 1 \Leftrightarrow \exp(-L/\xi) > 1/e$ this constant is always closer to zero than $m_\Delta^2/2$. For long correlation lengths $\xi \gg L$ this constant can be approximated as $m_\Delta^2 L/(2\xi)$, i.e. for almost fully correlated noise the dephasing rate approaches zero with the inverse correlation length.

The constant dephasing rate for large n results in a Heisenberg precision scaling. Inserting the constant rate eq. 4.50 into eq. 4.46 yields the uncertainty for state

$\left|\Psi_0^{(2)}\right\rangle$, which scales as $1/n$:

$$\Delta\omega_{meas}^{opt} = \sqrt{\frac{e^1[1-\exp(-L/\xi)+L/\xi]m_\Delta^2}{2T}}\,\frac{1}{n} \tag{4.51}$$

This is Heisenberg scaling with n, i.e. the best possible which obeys the Heisenberg uncertainty relation [125]. It is better by a factor of $1/\sqrt{n}$ than the standard quantum limit. This scaling is in stark contrast to all quantum metrology experiments in the presence of Markovian *uncorrelated* noise, which are fundamentally limited by the standard quantum limit [46]. The $1/n$ scaling found here is also superior to all quantum metrology experiments with uncorrelated non-Markovian noise as this type of noise has a best-possible scaling of $1/n^{3/4}$ [131, 133]. Quantum metrology experiments are currently strongly limited in the number of qubits which can be entangled (maximum experimentally achieved is 14 qubits [35]). However, for the next generation of high-precision quantum metrology experiments our results show the best scaling behaviour of the uncertainty with n.

The $1/n$ scaling of the uncertainty equals the scaling of an experiment with coherent evolution of the entangled state, i.e. when decoherence is entirely neglected. Quadrupole measurements in a partially correlated environment could therefore potentially explore the full quantum advantage over the standard quantum limit. To quantify and plot quantum advantage we want to compare to a quadrupole measurement, which is in the standard quantum limit (SQL). The quadrupole frequency αm_Δ^2 in Hamiltonian 4.1 cannot be measured with a single ion; one needs at least an entangled state of two ions to realise it. To obtain a meaningful comparison for the scaling of the frequency uncertainty this must be taken into account. We therefore define two entangled ions as the minimum entanglement resource for measuring a quadrupole moment. We then compare the scaling of the n–entangled state with a product state of $n/2$ entangled pairs which contribute $n/2$ more measurements to the statistics. For this minimal entangled array of ion pairs, we find an uncertainty that scales with the SQL as we increase the number $n/2$ of pairs.

$$\Delta\omega_{meas,p}^{opt} = \sqrt{e\Gamma(2,\xi)/(nT)} \tag{4.52}$$

We then introduce the relative frequency resolution:

$$r = \frac{\Delta\omega_{meas,p}^{opt}}{\Delta\omega_{meas}^{opt}} \tag{4.53}$$

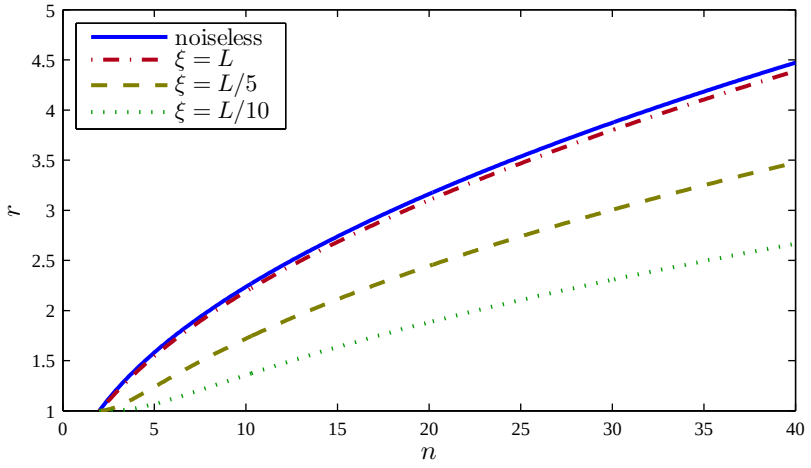

Figure 4.4: Relative frequency resolution r of a partially correlated environment with $\xi = L/10$ (dot-dashed), $\xi = L/5$ (dashed), $\xi = L$ (dotted) and a noiseless environment (solid). An n–entangled state scales better by a factor of $\sqrt{n}$ than a pair-wise entangled state and approaches noiseless scaling for increasing correlation length ξ.

where the full expression for r is given by equations 4.46, 4.48 and 4.53. We find that with increasing correlation length ξ the uncertainty approaches the noiseless Heisenberg scaling (figure 4.4). Even for partial correlations, which decay on the length scale of the array, the Heisenberg scaling of the uncertainty is robust.

4.3.2.2 Correlation length as a certain number of ions

Since the number of ions which can be placed within the correlation length of the environment might be limited we now regard the correlation length $\xi = cd$ as given in terms of a certain number of ions. Increasing the number of ions n now makes the array longer compared to the fixed correlation length (figure 4.2 **A**). For this situation we compare $\Gamma_2(n, 10d)$ from eq. 4.48 with Γ_u from eq. 4.49 in figure 4.3. We can see that this situation quickly restores linear scaling with n, i.e. the standard quantum limit:

$$\lim_{n\to\infty} \frac{-2e^{\frac{d}{\xi}} + 2e^{\frac{(1-n)d}{\xi}} + n - e^{2d/\xi}n}{2\left(1+e^{\frac{d}{\xi}}\right)^2} m_\Delta^2 = -\frac{m_\Delta^2 e^{\frac{d}{\xi}}}{\left(1+e^{\frac{d}{\xi}}\right)^2} + \frac{m_\Delta^2\left(1-e^{\frac{d}{\xi}}\right)n}{2+2e^{\frac{d}{\xi}}} \qquad (4.54)$$

The standard quantum limit is restored because with this scaling the correlation length, regardless how long, will ultimately be much smaller than the array length. The proportionality factor for Γ_2 however is always smaller than $m_\Delta^2/2$ (compare Γ_u) and approaches $m_\Delta^2 d/(4\xi)$ for large ξ/d. The different gradients can be clearly seen in figure 4.3. This is because even for $nd \gg \xi$ the non-zero correlation length reduces the dephasing-rate contribution of each ion slightly. So even though the scaling follows the standard quantum limit, one finds a better coefficient than for uncorrelated dephasing.

4.4 Ramsey spectroscopy of GHZ states with correlated decoherence

In standard Ramsey spectroscopy [46, 121] an ion trap is filled with n ions. After initialisation in the ground state $|0\rangle$ a $\pi/2$ pulse brings all ions in the superposition state $(|0\rangle + |1\rangle)/\sqrt{2}$. After a free evolution time t a second $\pi/2$ pulse is applied and the probability to find state $|0\rangle$ is measured. The probability oscillates at the frequency ω_0 of the transition $|1\rangle \leftrightarrow |0\rangle$. To gain more statistics the experiment is repeated leading to a total time T for all repetitions. The measurement uncertainty is $\Delta\omega_0 = 1/\sqrt{nTt}$. Instead of acting independently on the ions one can start from the GHZ state $(|111...\rangle + |000...\rangle)/\sqrt{2}$. The relative frequency is then given by $n\omega_0$ and the uncertainty is given by $1/(n\sqrt{Tt})$ (see [46]).

This scaling behaviour changes once decoherence is considered. We quickly review the situation for uncorrelated decoherence [46] and then regard correlated decoherence. Regarding the ions as pseudo-spins $|0\rangle$, $|1\rangle$ and coupling each ion to the environment with $\sigma_z = |1\rangle\langle 1| - |0\rangle\langle 0|$,

$$H_{int} = \sum_j \sigma_z^{(j)} B_j \tag{4.55}$$

we simplify the master equations analogous to eq. 4.20. We regard the time evolution of the coherence $r_3 = |111...\rangle\langle 000...|$.

Uncorrelated dephasing For uncorrelated dephasing the master equation (eq. 4.20 with $\xi \to 0$) for the element r_3 is:

$$\dot{r}_3 = i[r_3, H] + C(\omega = 0) \sum_j \left[-\left(\sigma_z^{(j)}\right)^2 r_3 - r_3 \left(\sigma_z^{(j)}\right)^2 + 2\sigma_z^{(j)} r_3 \sigma_z^{(j)} \right] \tag{4.56}$$

$$= -in\omega_0 r_3 + C(\omega = 0)\left(-2nr_3 + 2(-1)r_3\right) \tag{4.57}$$

$$= (-in\omega_0 - C(\omega = 0)4n)r_3 \tag{4.58}$$

Both the frequency $n\omega_0$ and the dephasing rate $n\gamma = C(\omega = 0)4n$ are proportional to the number of ions n and analogous to eq. 4.46 the time optimised uncertainty's n-scaling is equivalent to the standard quantum limit [46], i.e. $\Delta\omega_0 = \sqrt{2en\gamma/(n^2T)} = \sqrt{2e\gamma/(nT)}$.

Correlated dephasing For fully correlated dephasing the master equation (eq. 4.20 with $\xi \to \infty$) for the element r_3 is:

$$\dot{r}_3 = i[r_3, H] + C(\omega = 0) \sum_{jk} \left(-\sigma_z^{(j)} \sigma_z^{(k)} r_3 - r_3 \sigma_z^{(j)} \sigma_z^{(k)} + \sigma_z^{(j)} r_3 \sigma_z^{(k)} + \sigma_z^{(k)} r_3 \sigma_z^{(j)} \right) \tag{4.59}$$

$$= -in\omega_0 r_3 + C(\omega = 0)\left(-n^2 2r_3 + n^2(-1)2r_3\right) \tag{4.60}$$

$$= (-in\omega_0 - C(\omega = 0)4n^2)r_3 \tag{4.61}$$

The frequency scales with n but the dephasing rate scales with n^2, which means the dephasing increases strongly. This scaling has been observed experimentally in ion traps [35] and our analysis here shows that this scaling is clear indicator of strongly spatially correlated noise in ion traps. The uncertainty becomes $\Delta\omega_0 = \sqrt{2e\gamma/T}$ and an increase of ions in the GHZ state does not decrease the uncertainty any more. The only way to decrease the uncertainty is by repetition of the measurement, in which case the standard quantum limit scaling $(1/\sqrt{T})$ applies. To reduce experimental efforts it is therefore best to work on individual ions, i.e. product states in the ion array. Ultimately the result is that GHZ states are strongly disadvantageous to work with in spatially correlated environments. This result has also been found in reference [103].

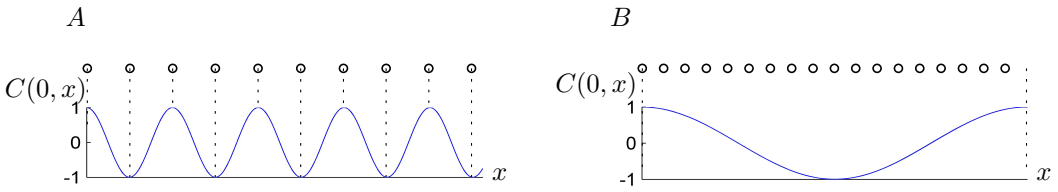

Figure 4.5: Two arrangements of ions in oscillating spatial correlations. Both arrangements achieve Heisenberg scaling of the GHZ state: A) For small oscillation length the ions are arranged to meet half the oscillation length. B) For long oscillation length the whole array is arranged to match up one oscillation length.

4.4.1 Oscillating spatial correlations

Until now we have considered perfect spatial correlations $C(0,x) = 1$ and decaying spatial correlations $C(0,x) = \exp(-x/\xi)$. Both are positive functions for all x and the n^2 scaling of the dephasing rates found experimentally [35] for GHZ states indicates that in ion traps these two functional forms are good approximations for the noise correlations. However, it is also physically possible for the spatial correlations to take the homogeneous form $C(0,x) = \cos(k_s x)$, where points of certain distances have noise with negative correlations. The environmental model discussed in section 3.1 is an example that yields cosine shaped spatial correlations in eq. 3.67 and 3.68. In such an environment GHZ states can be engineered to be within a decoherence-free subspace in two ways assuming the spatial oscillation length is known. One way is to place the ions at half the oscillation length of the environmental spatial correlations (figure 4.5A); the other way is to match the array length L with the oscillation length $L = 2\pi/k_s$ (figure 4.5B).

For the GHZ state's relevant coherence $r_3 = |111...\rangle\langle 000...|$ all operator pairings j,k in the master equation have the same effect. The only difference comes from the cosine shaped correlation function:

$$\dot{r}_3 = i[r_3, H_s] + \sum_{jk} \cos(k_s|j-k|d)\left(-\sigma_z^{(j)}\sigma_z^{(k)} r_3 - r_3\sigma_z^{(j)}\sigma_z^{(k)} + \sigma_z^{(j)} r_3 \sigma_z^{(k)} + \sigma_z^{(k)} r_3 \sigma_z^{(j)}\right) \tag{4.62}$$

where d is the distance between ions.

In the arrangement of figure 4.5A the correlation function becomes effectively $\cos(k_s\ |j-k|\ d) = (-1)^{|j-k|}$, i.e. alternates the sign with increasing distance. This recreates the effect of the coherence $r_2 = |m_-, m_+, m_-, m_+, ...\rangle\langle m_0, m_0, m_0, ..., m_0|$, cor-

responding to the initial state 4.4. In fact the decoherent part of eq. 4.62 is mathematically equivalent to eq. 9.51 in appendix E. In the arrangement of figure 4.5A the alternating sign comes from the correlation function and the operators produce the same term for all pairs of j and k. In the case of the coherence r_2 the alternating sign comes from the operators and the correlation function is always the same for $\xi \to \infty$. From this equivalence one finds that the arrangement of figure 4.5A leads to Heisenberg scaling for the GHZ state, even if the cosine correlation function has an additional exponentially decaying envelop.

In the arrangement of figure 4.5B the length of the array matches the spatial oscillation length of the environmental correlations. Regarding eq. 4.62 we group the pairs of the first ion $j = 1$ with all the other ions (including the self-correlation $j = k = 1$). We find that for each positive contribution $C(0, (1-k)d) > 0$ there is an equal negative contribution from the k-value $n/2$ further down the chain. The sum of all contributions of $j = 1$ therefore cancels (assuming an even number n of ions). The same argument applies for the sum of all contributions for $j = 2$ or any other value of j. For large numbers n of ions these summations for one value of j approach an integration over one oscillation length of a cosine, which illustrates the summation to zero even better.

In both arrangements of figure 4.5 the GHZ state $(|111...\rangle + |000...\rangle)/\sqrt{2}$ turns out to be a decoherence-free state or dark state for all n and frequency measurements with it will therefore show Heisenberg scaling. The difficulty of an experimental implementation of this is to find and map out a noise environment with cosine spatial correlations.

After discussing purely positive and oscillating spatial correlations we would like to point out that purely negative correlation functions, i.e. perfect anti-correlations are impossible due to the necessity of positive self-correlations $j = k$ and multipartite correlation rules. Particularly negative noise correlations between any positions a and b combined with negative correlations between positions b and c require positive correlations between positions a and c.

4.5 Chapter summary

We have investigated quantum metrological measurements with n-entangled states and their precision scaling with the number of ions n in a spatially correlated noise

environment. We chose particular states, suitable for the measurement of the atomic electric quadrupole frequency of trapped ions, a quantity relevant in frequency standard applications. We found these states to be protected against dephasing with increasing correlation length of the noise.

For two ions this dephasing-free subspace has been experimentally observed [48]. This shows that the noise environment in ion traps must be in fact strongly spatially correlated. Furthermore n-entangled GHZ-states have been reported to show a dephasing rate with a quadratic dependence on the number of ions n [35]. We found that this as well can only be caused by strongly correlated noise, which thus seems to be the norm in ion trap experiments.

For fully correlated noise the entangled quadrupole states are dephasing-free and the frequency uncertainty is therefore proportional to $1/n$. This is the Heisenberg limit, i.e. the best possible scaling allowed by the time-energy uncertainty relation [125]. The emergence of dephasing-free subspaces in the correlated noise environment enables a scaling, which outperforms all experiments with spatially uncorrelated noise, which is fundamentally bound by the standard quantum limit [46, 126, 127], i.e. an uncertainty which scales as $1/\sqrt{n}$. The $1/n$ scaling found here is also superior than any experiments in uncorrelated *non-Markovian* noise, which can have a best-possible scaling of $1/n^{3/4}$ [131].

With increasing number of ions the correlations in the noise are likely to show imperfections. We therefore investigated finite noise correlation length in depth. In this case the *topology* of the state, i.e. the order in which ions are arranged in the array becomes highly important for the dephasing properties of the state. Furthermore there are two ways to increase n relative to the noise correlation length: fixed array length and fixed density of the ions. Choosing an optimal topology and keeping the array length fixed we find that Heisenberg scaling persists for finite correlation length. With fixed ion density the uncertainty goes towards the standard quantum limit for large n but compared to uncorrelated noise is better by a factor of approximately $d/(2\xi)$.

Spatially correlated, Markovian noise is the only type of noise so far, which has been found to allow for Heisenberg-limited measurements with optimised states such as the electric quadrupole measurement. It also seems to be the most realistic noise model for ion traps. For GHZ states this noise environment is disadvantageous as it increases the dephasing rate relative to uncorrelated noise [103]. However, if the environmental correlation function shows oscillations, such that certain distances have

correlated and others anticorrelated noise, then GHZ states can also be engineered to show Heisenberg scaling. Such environments are physically possible and were found in the models of chapter 3 but are not yet found in the standard implementations of quantum metrology.

Chapter 5

5 Excitation and state transfer via spin chains with correlated decoherence

We investigate the effects of spatially correlated decoherence on quantum transport. A spin chain with perfect state transfer serves as a model system and the transport fidelity is calculated for both dephasing and relaxation with different correlation lengths. Long correlation lengths are found to be advantageous to transport but in the case of dephasing the state transfer turns into a classical bit transfer. New dynamics is found to emerge for spatially correlated relaxation. The material in this chapter has appeared in reference [104].

Introduction

The transfer of a quantum state is an important component for quantum technology. While transfer via photons in optic fibres enables high-speed communication for long-range communication and cryptography there has also been a large interest in short-distance transfer via (pseudo-) spin chains [49–65]. Many promising quantum technologies, such as optical lattices [134] and arrays of quantum dots [135,136], rely on such transport. Furthermore, a quantum mechanically very similar mechanism is the transfer of excitation energy in light-harvesting complexes in the context of photosynthesis [137–140].

Within the many configurations for transport in spin networks, a linear spin chain transversely coupled with a particular spatially varying coupling strength has been found to provide perfect state transfer from one end to the other [53]. We will focus on the case of perfect-state-transfer as this provides well defined analytical solutions. However, our results are more general and apply to other spin-network problems and spin-wave theory in general.

While the effects of correlated decoherence in photosynthetic systems have been studied repeatedly [137–140], studies of environmental noise on perfect state transfer are limited to spatially uncorrelated noise [141–144] or noise correlations between repeated transfers through the same chain [145–149]. Here we investigate comprehensively the effects of decoherence on excitation and state transfer. Particularly we assign a characteristic spatial correlation length ξ to the environmental noise and display our results as continuous functions of $\xi \in [0, \infty)$.

5.1 The model system

We investigate the influence of decoherence in a linear chain of N transversely coupled spins:

$$H_s = \sum_{j=1}^{N} \omega_q \sigma_z^{(j)} + \sum_{j=1}^{N-1} \frac{g_j}{2} \left(\sigma_x^{(j)} \sigma_x^{(j+1)} + \sigma_y^{(j)} \sigma_y^{(j+1)} \right) \tag{5.1}$$

where ω_q is the level splitting of the spins and g_j is the coupling strength of spin j to its right neighbour. To guarantee perfect state transfer [53] the coupling strength is chosen $g_j = g\sqrt{j(N-j)}$. Note that the coupling strength plotted as a function of the position j describes a half circle (figure 5.1). Initially we choose the spin at the start of the chain to be excited and all other spins in the ground state, i.e. $|\uparrow\downarrow\downarrow\downarrow \dots\rangle$. The coherent dynamics of this system is shown in figure 5.2. The excitation, initially at one end of the chain spreads out, travels through the chain and, due to the particular profile of the coupling strength, refocuses at the other end. Due to the symmetry of the system, the process then reverses. The time it takes for the excitation to pass through the chain once is $\pi/(2g)$. This system is an ideal model system to test the influence of environmental noise with different correlation lengths on excitation transfer because it has a clearly defined end point of the transfer, while the transfer process depends on the coherence of the spins.

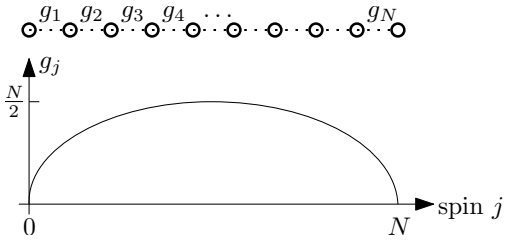

Figure 5.1: The coupling strength $g_j = g\sqrt{j(N-j)}$ between spins describes a half circle, i.e. is strongest in the middle of the chain, to guarantee perfect state transfer. For all numerical simulations we used the following parameters: $\omega_q = 100,\ g_j = \sqrt{j(N-j)},\ v_j = 0$ or $1,\ \nu_j = 0$ or 1.

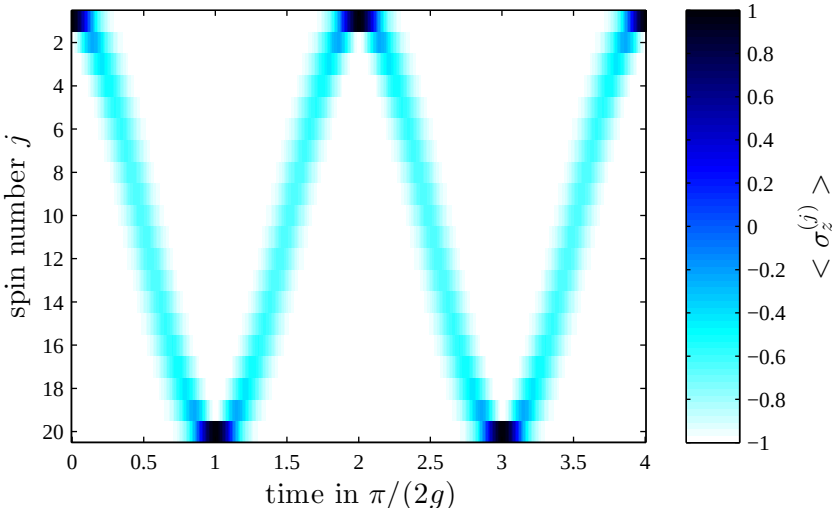

Figure 5.2: Coherent dynamics of the given spin chain (eq. 5.1). The excitation is transferred from one end of the spin chain to the other and back. This mechanism depends on the coherence of the spins because the excitation spreads out before it refocuses at the other end. This is an ideal model system to test the influence of decoherence with different spatial correlation lengths on the excitation transfer.

As pointed out in section 2.2.1 longitudinal and transversal couplings to the environment couple to independent baths (i.e. are not correlated). We therefore discuss them separately.

5.2 Dephasing

First we regard longitudinal coupling to the environment:

$$H_{int} = v_{\parallel} \sum_{j=1}^{N} \sigma_z^{(j)} B_{\parallel}^{(j)} \tag{5.2}$$

with the coupling strength $v_{\parallel}$. We assume a Gaussian shape of the corresponding spatial correlation function:

$$C_{\parallel}(\omega = 0, |x_j - x_k|) = 2^{-\frac{(x_j - x_k)^2}{\xi^2}} \tag{5.3}$$

which makes the correlation length ξ the half width at half maximum (HWHM).

As the dynamics of the excitation transfer depends on the coherence of the spins we find that uncorrelated dephasing destroys the refocusing at the other end and spreads the excitation out over the whole chain (figure 5.3, top). With increasing correlation length ξ the detrimental influence of the environment is reduced and the excitation transfer is restored without a change in the noise strength $v_{\parallel}$ (figure 5.3). For long correlations $\xi \to \infty$ the restored excitation transfer can be understood via the analytical result in section 2.2.2, i.e. *states with equal numbers of excitations become dephasing-free in a perfectly correlated noise environment.*

To quantify the excitation transfer and its dependence on noise correlation length, we measure $\langle \sigma_z \rangle$ of the end spin after one passing through the chain at $t = \pi/2$. We plot this result dependent on a logarithmically scaled correlation length ξ in figure 5.4 and find a clear step in the transfer quality, which means there is a particular critical correlation length ξ_c. Noise with a correlation length below ξ_c destroys the transfer, while above ξ_c the quality of the transfer is high. Numerical results show that the critical correlation length does not depend on the noise intensity $v_{\parallel}$ in the weak coupling regime $v_{\parallel} < \min(g_j)$.

Instead, the major determining influence is the chain length (figure 5.4). For the perfect state-transfer protocol an increasing chain length also increases the maximum

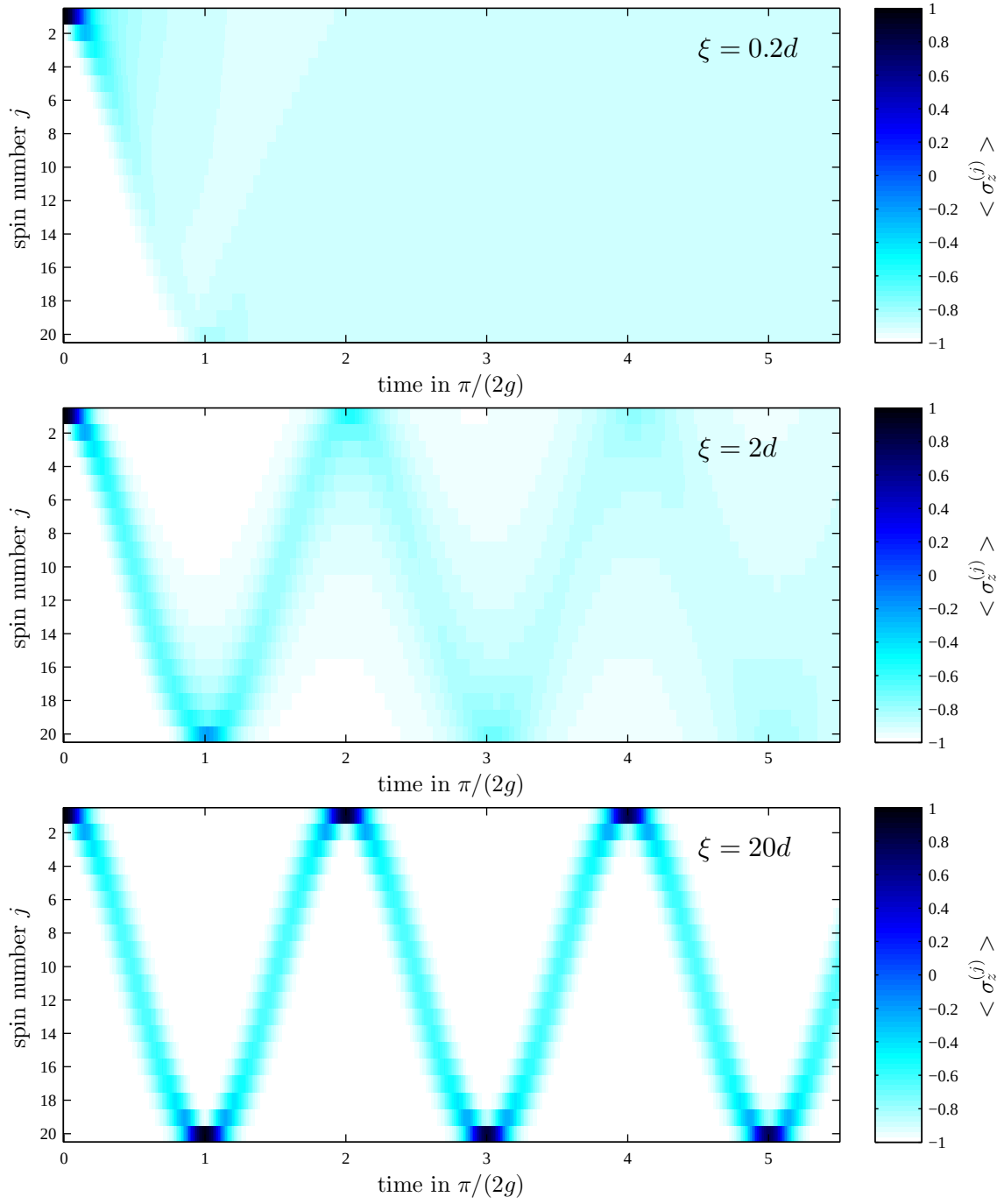

Figure 5.3: Dynamics of the spin chain with longitudinal bath coupling and different correlation lengths, **top**: $\xi = 0.2d$, **middle**: $\xi = 2d$, **bottom**: $\xi = 20d$ where d is the distance between spins. The relatively strong environmental coupling leads to dephasing, which for uncorrelated decoherence (top) makes the excitation spread out over the chain and destroys the transfer. With increasing correlation length of the environment the coherent dynamics (cf. figure 5.2) is restored even though the system-bath coupling is not decreased. In all simulations the following numerical values are chosen: $\omega_q = 100, g = 1, v_{\parallel} = 1$.

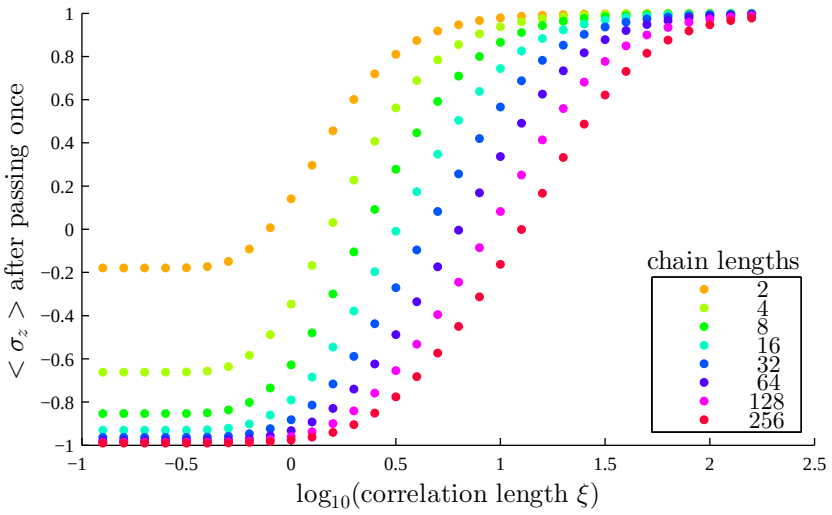

Figure 5.4: Transfer quality of an excitation through the spin chain dependent on logarithmically scaled correlation length for different chain lengths (see legend). The characteristic "step" in the transfer quality defines a critical correlation length ξ_c, which only changes with chain length and is independent of other parameters.

spread (or packet width) of one excitation in the transfer, which occurs at half the passing time $t = \pi/4$ (cf. fig. 5.2). In other words the critical noise correlation length ξ_c depends on the maximal packet width in the chain, which is an intuitive result since the transfer depends on the refocusing of that excitation packet. To quantify this statement we determined both quantities numerically for the nine different chain lengths given in figure 5.4. We determined the maximal packet width as the HWHM of the excitation packet after $t = \pi/4$. We determined the position of the step ξ_c in figure 5.4 by that correlation length (in number of spins) which corresponds to the maximal gradient using interpolation in both cases to increase precision. We then plotted both quantities in figure 5.5, which indeed shows linear dependence.

The linear dependence of ξ_c on the chain length suggests, that excitation transfer is not impaired by noise as long as the noise is correlated on a length scale that goes beyond the maximal packet width of the excitation. Similarly, the dynamics of a single excitation in a spin network in general is not impaired by noise that is correlated on a larger scale than the spread of the excitation.

Note that the long chain lengths in this case were numerically achievable by a reduction to the single-excitation subspace and numerical integration instead of diagonalisation (section 2.3).

The phase coherence to the ground state decays, regardless of the correlation length

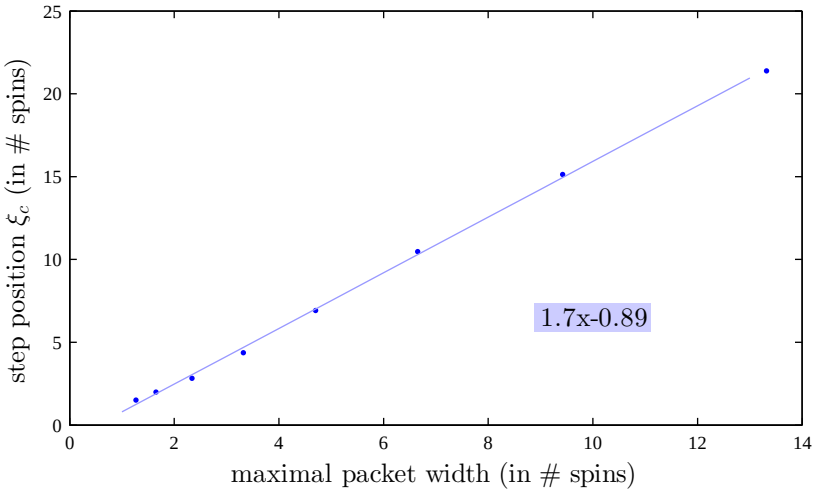

Figure 5.5: Critical correlation length ξ_c over maximal packet width for 9 different chain lengths $2^1, 2^2, \ldots, 2^9$. The data suggests a linear dependence. Excitation preserving dynamics seems to be immune to noise with a spatial correlation length longer than the maximal packet width of the excitation.

ξ, even when the excitation transfer is restored because the ground state has a difference of one excitation to the single-excitation subspace. This can be seen when $\langle\sigma_x\rangle$ (figure 5.6) or the purity (figure 5.7) is plotted. This loss of the phase information in the given setup means that for spatially correlated noise the excitation transfer is no longer a *state* transfer in the sense of quantum information but has become a classical bit transfer. One way that this problem might be overcome is via a Hahn echo technique, where a $\pi/2$ bit flip to the entire chain is incorporated after half of the transfer time. However, this would be a more technologically challenging setup. Outside quantum information there are applications in which the excitation transfer with "classical information" is equally desirable. An example is the energy transfer in light-harvesting complexes, which is discussed in chapter 6. In these situations correlated dephasing enables the transfer at high qualities even for relatively strong noise.

5.3 Relaxation

After the effects of longitudinal bath coupling in the previous section we will discuss only transversal bath coupling in this section. Note that a combined appearance of both couplings does not alter any of the effects described in this section but merely

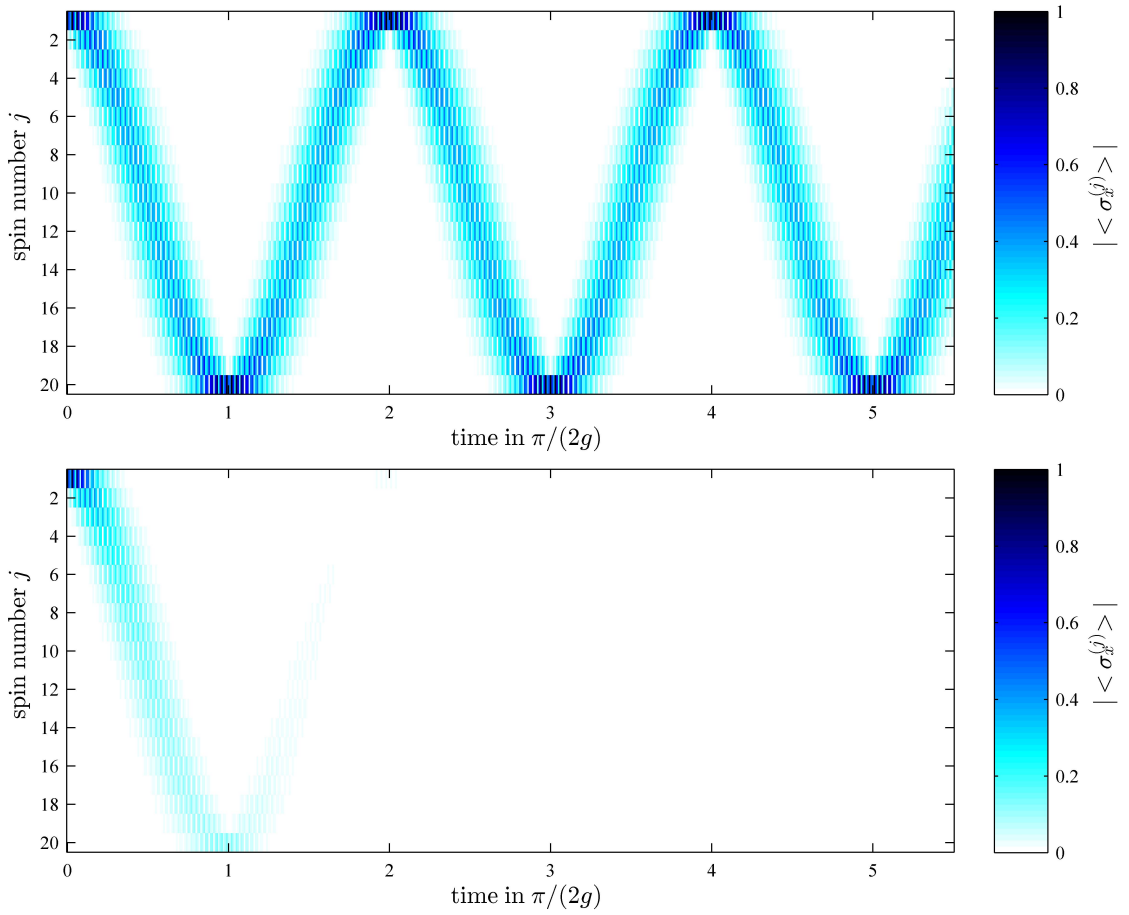

Figure 5.6: **Top**: Coherent evolution of the system where $|\langle\sigma_x\rangle|$ is plotted. The $\langle\sigma_x\rangle$ expectation value has a high frequency harmonic ($\propto 2\omega_q$) but here we plot $|\langle\sigma_x\rangle|$ to focus on the slow dynamics. The other spins in their ground state have zero expectation value. **Bottom**: In decoherent evolution, the phase information is lost very quickly even for widely correlated noise (here: $\xi = 20d$). Note that the bottom plot is the *same* evolution as the bottom plot of figure 5.3, i.e. the excitation is transferred very well, but the phase coherence to the ground state is lost very quickly at the same time.

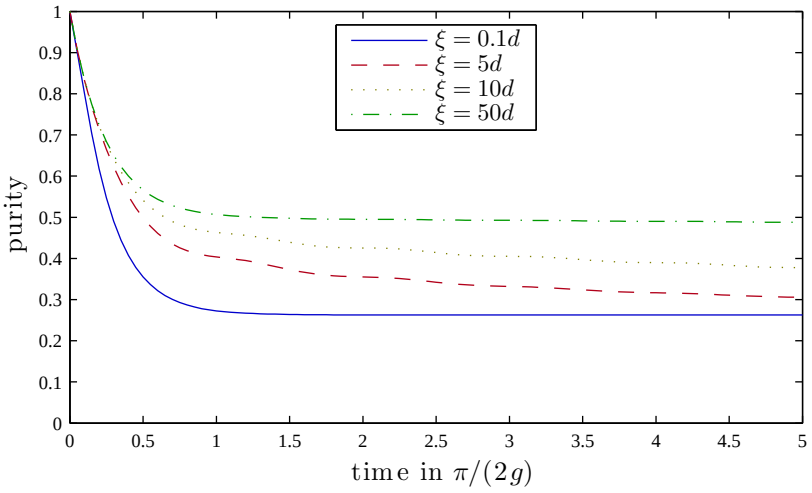

Figure 5.7: Purity $\mathrm{Tr}(\rho\rho)$ as a function of time with dephasing noise for different correlation lengths. The purity is partially restored for longer correlation lengths, however there is a residual decay because the phase coherence to the ground state is lost, despite the fact that excitation transfer is fully restored for long correlation lengths (cf. fig. 5.3).

adds dephasing as discussed above.

The spin chain with Hamiltonian 5.1 is now coupled transversely to the environment:

$$H_{int} = v_\perp \sum_{j=1}^{N} \sigma_x^{(j)} B_\perp^{(j)} \tag{5.4}$$

with the coupling strength $v_\perp$. We assume a vacuum or low temperature environment, i.e. the spectral function at negative frequency $-\omega_q$ is approximately zero. For positive frequency ω_q we again assume Gaussian shaped spatial correlations:

$$C(-\omega_q, |x_j - x_k|) = 0 \tag{5.5}$$

$$C(\omega_q, |x_j - x_k|) = 2^{-\frac{(x_j - x_k)^2}{\xi^2}} \tag{5.6}$$

This means we will only find energy loss out of the spin chain and no excitation gain from the environment will occur.

In the time evolution we find that longer correlation lengths ξ are advantageous for the transfer quality (Figure 5.8). This is similar to dephasing. However, contrary to dephasing the phase information is also preserved for longer correlation lengths ξ (figure 5.9). This means long correlation lengths actually reinstate the perfect state

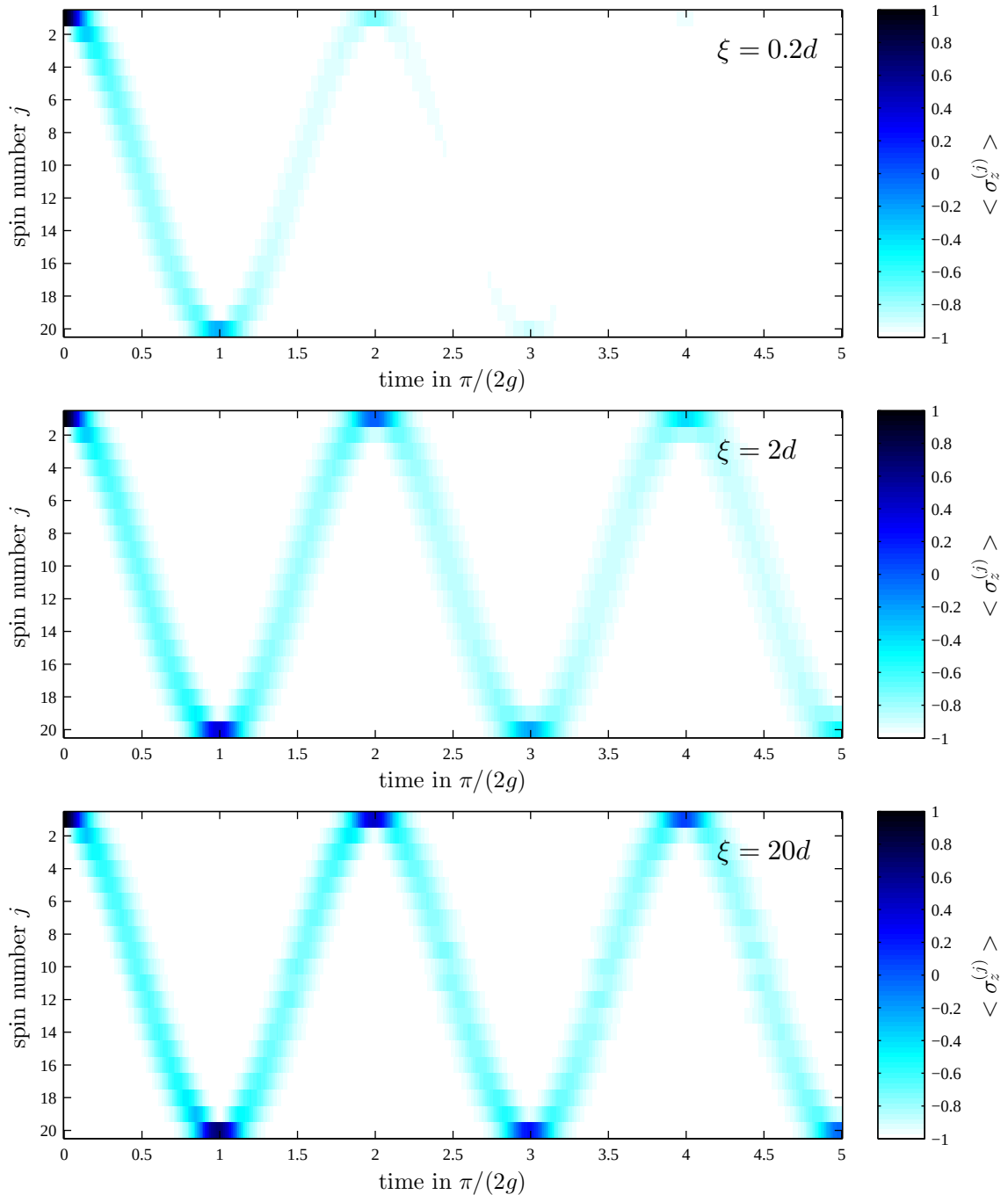

Figure 5.8: Relaxation (due to transversal coupling $v_\perp = 1$) with different correlation lengths: **top**: $\xi = 0.2d$, **middle**: $\xi = 2d$, **bottom**: $\xi = 20d$ where d is the distance between spins. Similar to dephasing (figure 5.3) long correlation lengths are advantageous for the transfer quality. The following numerical parameters were used: $\omega_q = 100, g = 1, v_\perp = 1$.

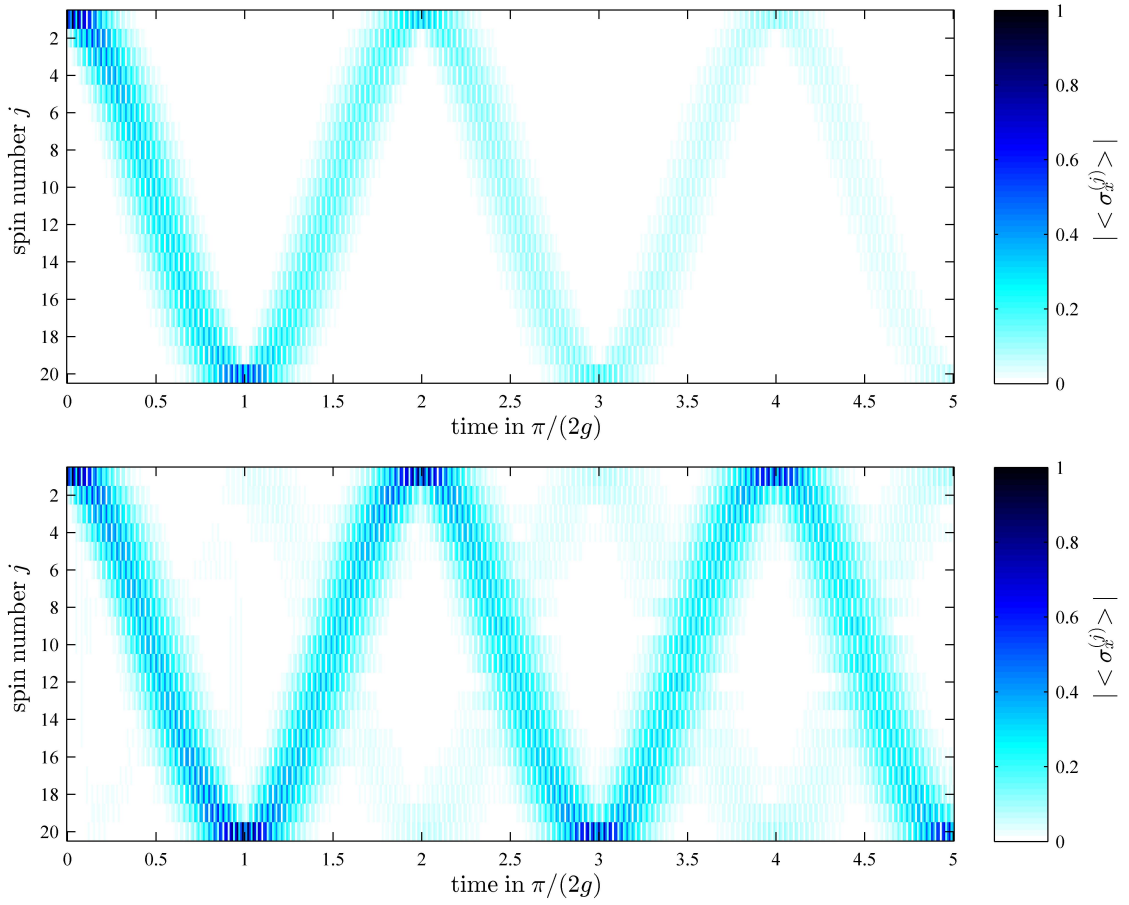

Figure 5.9: Evolution of the system undergoing pure relaxation, where $|\langle\sigma_x\rangle|$ is plotted. **top**: $\xi = 0.2d$; **bottom**: $\xi = 20d$. For long correlation lengths the phase information is also preserved and transferred through the spin chain.

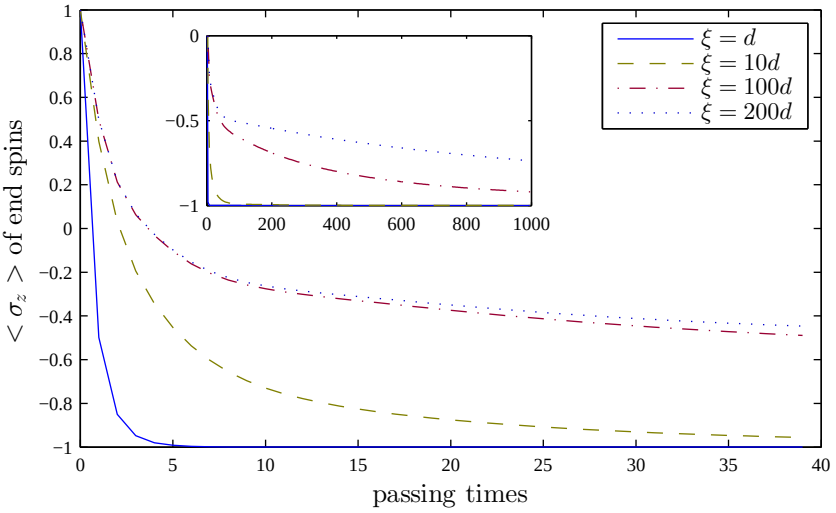

Figure 5.10: Transfer quality for continuing evolution with several different correlation lengths. For long correlation lengths two separate decay time scales arise.

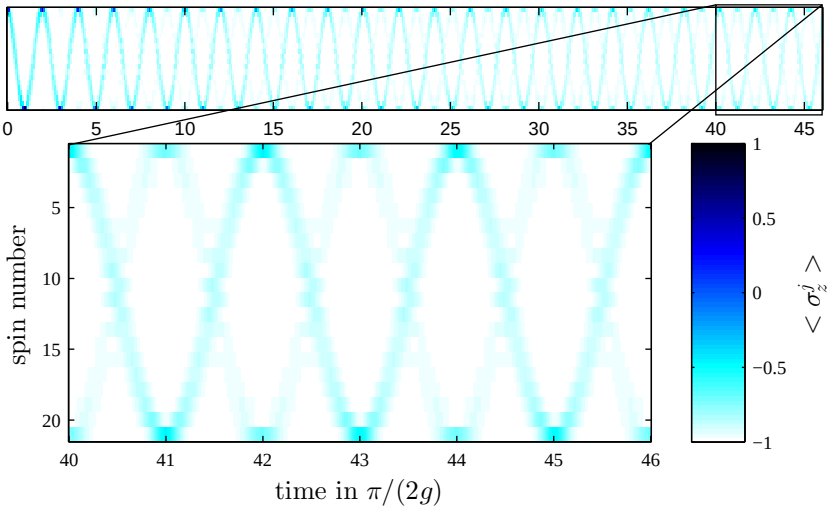

Figure 5.11: $\langle \sigma_z^{(j)} \rangle$ expectation value after 40 passings through the chain with relaxation $v_\perp = 1$ and long correlation length $\xi = 100d$. The dynamics shows the intermediate state (eq. 5.7) which occurs after the fast decay and before the slow decay in figure 5.10.

transfer in the absence of dephasing noise. Furthermore the relaxation is not entirely slowed down for long correlations. Two relaxation time scales emerge, a fast one and a slow one. This can be visualised by taking only the time points which are multiples of $\pi/2$, where in the coherent dynamics the state should be refocused at the ends of the chain. Plotting the expectation value of the respective spin displays a continuous decay with two distinct regimes. Figure 5.10 shows this decay and the two separate time scales are clearly visible. If we consider the dynamics of the spin chain at the time after the fast decay has finished, and the slow decay is just starting, we find that the excitation, which started initially at one end, is now split up and refocuses at both ends simultaneously (figure 5.11). The corresponding density matrix at these points in time is given by a statistical mixture of two states:

$$|\Psi_1\rangle = (|\uparrow\downarrow\downarrow \ldots \downarrow\rangle + |\downarrow\downarrow\downarrow \ldots \downarrow\uparrow\rangle)/\sqrt{2} \qquad p_1 = 0.5 \tag{5.7}$$

$$|\Psi_2\rangle = |\downarrow\downarrow\downarrow \ldots \downarrow\rangle \qquad p_2 = 0.5 \tag{5.8}$$

In other words the relaxation has entangled the first spin and the end spin with an efficiency of 50%. This entangled state then decays on a much slower time scale.

Again we can explain the behaviour with the analytical results for perfectly correlated environments from section 2.2.3. The coherent dynamics is entirely in the single-excitation subspace, which consists of n states. For perfect correlations $\xi \to \infty$ the single-excitation subspace contains only one decaying state and a relaxation-free (or subradiant) subspace of $n-1$ states. The coherent dynamics of the chain moves the excitation around and transfers probability between the relaxation-free states and the decaying state. All population in the decaying state however relaxes into the ground state on the short time scale. The only exception is the state $|\Psi_1\rangle$, which has a measurement probability in the initial state of $|\langle\Psi_1 \mid \uparrow\downarrow\downarrow \ldots\rangle|^2 = 1/2$. Figure 5.11 shows that in this state the excitations on both ends travel through the chain simultaneously. In other words the state $|\Psi_1\rangle$ evolves almost entirely in the relaxation-free subspace into itself, resulting in a much slower decay rate.

5.4 Chapter summary

For excitation transfer spatially correlated noise is strongly advantageous compared to uncorrelated noise. The detrimental effects of dephasing on the transfer dynamics

vanish as the noise correlation length is greater than the maximal packet width of the excitation in the transfer. The excitation can then be transferred with very high fidelity even for strong noise. While the dynamics of the transfer is restored with long correlation length the phase coherence to the ground state is still lost in the transfer and the high-fidelity excitation transfer is no longer a perfect *state* transfer. With relaxation the transfer also improves with increasing spatial correlation length of the noise. The relaxation time increases and two separate time scales arise. Initially the state $|\uparrow\downarrow\downarrow\ldots\downarrow\rangle$ relaxes into the entangled state $(|\uparrow\downarrow\downarrow\ldots\downarrow\rangle - |\downarrow\downarrow\ldots\downarrow\uparrow\rangle)/\sqrt{2}$. This intermediate state is very robust and decays on a longer time scale. It can be concluded that spatially correlated noise displays significantly different dynamics to spatially uncorrelated noise. Longer correlation lengths are generally advantageous to quantum transport as they reduce dephasing effects and produce an intermediate entangled state with reduced relaxation rates.

Chapter 6

6 Photosynthetic complexes with correlated decoherence

Photosynthetic systems have recently been found likely to include a certain amount of quantum coherent processes. In this chapter we show, that Bloch-Redfield equations are a good tool for modeling these systems. This is particularly timely because the misconception that Bloch-Redfield equations are a less powerful tool than Lindblad equations for modeling exciton transport in photosynthetic complexes has been published and cited several times [32]. We analyze a prototypical dimer system as well as a 7-site FMO complex in regards to temperature, dephasing rate and spatial correlation length of the noise and go beyond the capabilities of an ad-hoc Lindblad approach.

6.1 Introduction

The chemical processes of photosynthesis are carried out in the reaction centre of photosynthetic cells. The energy for it is provided by incoming photons, which create excitons. These excitons are collected via light-harvesting complexes (LHCs), which are much larger than the reaction centre. The function of an LHC is to cover larger areas of incoming photons and to transfer the excitons towards the reaction centres. Following experimental evidence of long-lived coherences in LHCs [66, 67], there have been many studies on quantum coherence in LHCs and the effects of decoherence [71, 137–139, 150, 151]. However, there is still some debate concerning the correct formalism for modeling the dynamics of such systems.

As explained in section 2.1.5 Lindblad equations guarantee complete positivity of the density matrix, i.e. a physical time evolution, by their mathematical form. This made Lindblad equations a popular tool for investigating light-harvesting complexes, as it enables one to get physical results for an open quantum system without the necessity of deriving a master equation from a microscopic model. While Lindblad equations are the mathematically simplest tool, a Bloch-Redfield approach allows a closer connection to the microscopic parameters and the causes of decoherence.

Quantum coherence in light-harvesting complexes combines the research fields of open quantum systems and biochemistry. While researchers with an open quantum systems background are typically more familiar with the capabilities of modeling quantum coherent evolution with Bloch-Redfield equations, researchers with a biochemistry background typically use simplified versions of the Bloch-Redfield equations (sometimes labelled 'Redfield equations') to only model decoherent transitions between states. In the context of light-harvesting complexes these simplified versions have previously been applied in a way that caused issues like non-positivity or the inability to model coherent oscillations. This has lead to the misconception that Bloch-Redfield equations are insufficient to model light-harvesting systems or are a simplified case of Lindblad equations, which has explicitly been published [32] and repeatedly been cited [68, 70, 73]. In this chapter we present how our Bloch-Redfield approach adapts to model LHCs with none of the issues mentioned. It enables more detailed models than Lindblad equations. As a simple example, we apply our formalism to a dimer system and show how coherent oscillations and decay arise from the system and noise environment parameters.

One important advantage of the Bloch-Redfield approach is that both temporal and spatial correlations in the environment can be modelled, assuming that the effect of the environment is approximately Markovian. Using other models, the relevance of spatial correlations in LHCs was pointed out in [70, 71], correlations were found to enhance coherence [72, 73, 75], which is consistent with the more general result that a decoherence-free subspace emerges in the single-excitation subspace for strongly correlated environments (section 2.2.2). Some models found noise correlations to slow transport down [73], others to speed up transport up to a certain optimal value depending on the strength of the reorganisation energy [69]. The latter is in agreement with our findings in this paper using Bloch-Redfield equations. We show that the Fenna-Matthews-Olsen (FMO) complex, one example of a intesively studied LHC, achieves maximum efficiency for a parameter regime with finite spatial noise correlations.

6.2 Lindblad vs. Bloch-Redfield equations for LHCs

In light-harvesting complexes the system Hamiltonian H_s describes the system and all its quantum coherent features. It is typically of the form $H_s = \sum_j \epsilon_j |j\rangle \langle j| + \sum_{j \neq k} g_{jk}(|j\rangle \langle k| + |k\rangle \langle j|$, where the first term describes the sites at energy ϵ_j and the second term the couplings between sites g_{jk}. To then model the noise influence and incoherent dynamics a master equation approach is often used. The Lindblad equations [1,42,43] are a popular tool for this because their mathematical form guarantees that the populations, i.e. the diagonal density matrix elements, are positive at all times (see section 2.1.5). This is physically necessary since they represent the probabilities of measuring the corresponding state. However modeling beyond Lindblad equations opens up new capabilities and does not need to violate positivity [89].

In difference to the Lindblad equations, the mathematical form of Bloch-Redfield equations does not guarantee *a priori* complete positivity of the density matrix, i.e. physicality. It is an underpinning consistent microscopic noise model that guarantees physical behaviour. This is however where the strength of the Bloch-Redfield formalism lies. It connects system behaviours to physical properties of the noise and the system-noise interaction type. Specifically the equations derive from the interaction Hamiltonian (eq. 2.3) with the system operators s_j and bath operators B_j and j runs over the spatial sites in the system. The spectral function $C_{jk}(\omega)$ of the noise environment defines both the noise spectrum and the strength of spatial correlations between sites j and k. To model a Markovian environment, the spectral function must be smooth on the scale set by the system evolution. This is a key point in correctly deriving physical master equations, which will be detailed further in section 6.2.3.

The system operators s_j define which part of the system couples to the noise environment. There can be noise on site-operators (e.g. site-energy-noise $\sigma_z^{(j)} = 2|j\rangle \langle j| - \mathbb{1}$, site recombination $\sigma_x^{(j)} = |j\rangle \langle G| + h.c.$) or there can be noise on the coupling operators between sites (e.g. transversal couplings $|j\rangle \langle k| + |k\rangle \langle j|$, longitudinal couplings $\sigma_z^j \sigma_z^k$) [68].

6.2.1 Measurement basis and oscillations

In light-harvesting complexes excitonic dynamics *between spatial sites* is of interest. Populations should therefore be taken in the site basis (aka bare basis, defined as

the eigenbasis of the Hamiltonian without couplings between sites). Then the populations correspond to the probability of finding an exciton at the corresponding site. If on the other hand the populations are taken in the eigenbasis of the Hamiltonian (with couplings), as for example done in [32], their physical meaning is unclear and oscillations in this basis *do not* correspond to excitonic movement any more. Secondly such oscillations are not caused by the system any more since it is the basis of stationary states in the coherent system dynamics.

6.2.2 The secular approximation for LHCs

As for most controlled quantum systems the Bloch-Redfield equations for LHCs can be simplified by means of the secular approximation based on the occurrence of two different frequency scales in the system. Although the frequencies in LHCs are typically three orders of magnitude larger (i.e. the time scales shorter) than in controlled quantum systems, the on-site energies are again much larger relative to the coupling energies. This is hugely advantageous in order to find analytical solutions to the equations and it helps to map the Bloch-Redfield equations to Lindblad form (sections 2.1.3 and 2.1.5), which can rid the equations of any physical inconsistencies should they arise from the underlying model. However, we emphasize that with the formalism presented throughout this thesis, this is in general unnecessary.

When the Bloch-Redfield equations are based on a consistent physical model, then the secular approximation does not alter the results. It merely makes it easier to find a solution to the equations by disregarding elements which don't change the solution significantly.

The secular approximation is based on different time scales. In section 2.1.3 we spoke in general terms of a short system time scale (large system frequencies) and long decoherence time scales (small decoherence rates). For LHCs the on-site energies are the large system frequencies but the inter-site couplings are typically much smaller and of the same order as the decoherence rates. Applying the secular approximation therefore requires a comparison of the elements of the superoperator (eq. 2.32) for each respective system individually. If the magnitude of two diagonal elements in the superoperator differ by more than their shared off-diagonal elements, then those off-diagonal elements can be replaced with zero. The secular approximation should be applied by a careful pairwise comparison of the elements. The full secular approximation, which sets all dependencies between coherences and populations to

zero is rarely justified. Although this extreme case is guaranteed to rid the equations of any non-physical inconsistencies, it usually also rids the system of physical coherent oscillations. The frequent use of this full secular approximation has lead to the misconception that Redfield theory can not reproduce oscillations [32].

We recommend only using a partial secular approximation, which sets only those elements to zero which are justified for the respective system. An example will be given in section 6.3. A consistent connection of the equations to an interaction Hamiltonian (eq. 2.3) and spectral function (eq. 2.30) as outlined in equations 2.27 to 2.29 should never lead to non-physical behaviour in the first place.

The occurrence of two separated energy scales is quite common in light-harvesting systems. This is because the excitonic (on-site) energy, which is typically of the order 10,000 cm^{-1}, is much larger than the coupling energies and the differences of the on-site energies, both are typically on the order of 1 cm^{-1} to 100 cm^{-1}. A secular approximation based on this difference leads to two very general results: Firstly, it decouples the one-exciton subspace from both the ground state and from states with two or more excitons, see appendix B. This means that in LHCs states with more than one exciton can generally be neglected in the time evolution. Secondly, it separates the bath of the longitudinal couplings (e.g. $s_j = \sigma_z^{(j)} = 2\left|j\right\rangle\left\langle j\right| - \mathbb{1}$) from the bath of the transversal couplings (e.g. $s_j = \sigma_+^{(j)}\sigma_-^{(j+1)} + h.c. = \left|j\right\rangle\left\langle j+1\right| + h.c.$), see appendix C. This simplifies modeling since correlations in the noise of these different types of coupling do not have any effects and can be neglected.

6.2.3 Detailed balance

In the equilibrium state, the populations of two sites are given by $\rho_{11}/\rho_{22} = e^{-\hbar\epsilon_{12}/k_BT}$, where ϵ_{12} is the energy difference of the two sites. This detailed balance condition translates in the Bloch-Redfield formalism to the property

$$C(-\omega) = e^{-\hbar\omega/k_BT}C(\omega) \tag{6.1}$$

of the spectral function. Spectral functions derived from a microscopic model such as the spin-boson or related models can have this property already, see [20, 38] or eqs. 3.49 and 3.51, where:

$$\langle n(|\omega|)\rangle = \frac{1}{e^{\hbar\omega/k_BT}-1} = e^{-\hbar\omega/k_BT}\frac{e^{\hbar\omega/k_BT}-1+1}{e^{\hbar\omega/k_BT}-1} = e^{-\hbar\omega/k_BT}(1+\langle n(|\omega|)\rangle) \tag{6.2}$$

Regarding the detailed balance condition, eq. 6.1, at low temperatures the spectral function for negative frequencies can be approximated by zero. This needs to be done in a manner consistent with the Markov approximation. The Markov approximation requires that the spectral function does not change on the scale relevant to the system dynamics (typically g_{jk}). Therefore one *must* obey $C(0 \pm g_{jk}) \approx const.$ This is one of the subtle details which can cause issues with non-positivity. If there are other larger scales (e.g. $\omega_j \gg g_{kl}$) the spectral function has no restrictions on this scale and can vary appreciably.

The detailed balance is consistent with the fact that excitons recombine but are not spontaneously created even at room temperature from the surrounding noise environment. This means once recombination is considered the long-time equilibrium will have almost all population in the ground state even at room temperature. Neglecting recombination the detailed balance can be applied to the single exciton subspace only [32], however this is somewhat artificial since the detailed balance is typically driven by energy-exchanging noise on each site, i.e. recombination noise.

6.2.4 Spatial correlations

Through the spectral function $C_{jk}(\omega)$ the option to model spatially correlated noise arises naturally in the formalism. As for other controlled quantum systems it allows for a spatially decaying correlation function in the LHC with a distinctive correlation length ξ, i.e. one can transition smoothly between infinite, finite and no spatial correlations. This is advantageous over Lindblad and other approaches, which have to assume several (common and individual) baths [68]. This advantage becomes most apparent for systems with several sites (e.g. the realistic 7-site FMO model, see section 6.5), where finite correlation length can be applied to the actual geometry of the LHCs.

6.3 Example of a dimer system

As an illustrative example, we consider a dimer system with Hamiltonian

$$H_s = \begin{pmatrix} \epsilon_H & g \\ g & \epsilon_B \end{pmatrix} \tag{6.3}$$

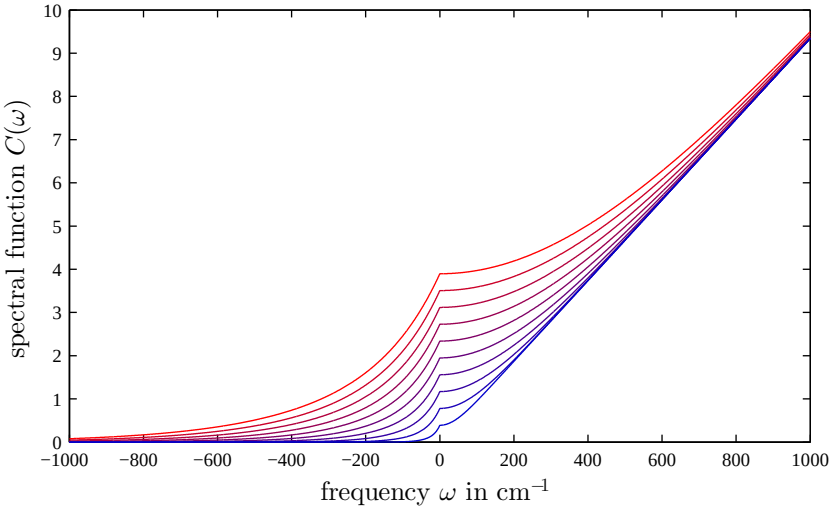

Figure 6.1: Ohmic spectral function for different temperatures T between 0 K (blue) and 300 K (red). The noise around zero frequency determines the dephasing strength and is strongly temperature dependent. The noise at higher frequencies determines the recombination and is largely unaffected by temperature. For negative frequencies the spectral function is exponentially damped, which leads to the detailed balance being preserved.

This system of two sites (labeled H and B) appears in many photosynthetic systems [32], e.g. in the reaction centre of the purple bacteria Rhodobacter sphaeroides [66,68] and serves as the most basic model of exciton transfer in light-harvesting complexes.

Neglecting all noise influences an exciton will oscillate between the sites with frequency $\hbar\omega = \sqrt{g^2 + (\epsilon_H - \epsilon_B)^2/4}$. The oscillation amplitude will be strongest for $\epsilon_H - \epsilon_B = 0$. In other words, the stronger g, the faster the oscillations, but increasing $|\epsilon_H - \epsilon_B|$ decouples the sites. This role of off-diagonal couplings and diagonal on-site-energies in the system Hamiltonian generalizes to more complex multiple-site systems.

6.3.1 Constructing the superoperator

Next we consider dephasing noise coupling to the site-energies by setting the system operators in the interaction Hamiltonian to $s_1 = v\ (2\,|H\rangle\langle H| - \mathbb{1})$, $s_2 = v\ (2\,|B\rangle\langle B| - \mathbb{1})$, where v is the coupling strength. First we model spatially uncorrelated noise and an Ohmic spectral function [17, 38, 70, 75, 77, 139] $C_{jk}(\omega) = \alpha\omega\coth(\hbar\omega/2k_BT)\,\delta_{jk}$, where α accounts for the noise strength (see figure 6.1). The oscillations then show an envelope exponential decay, due to the loss of phase coher-

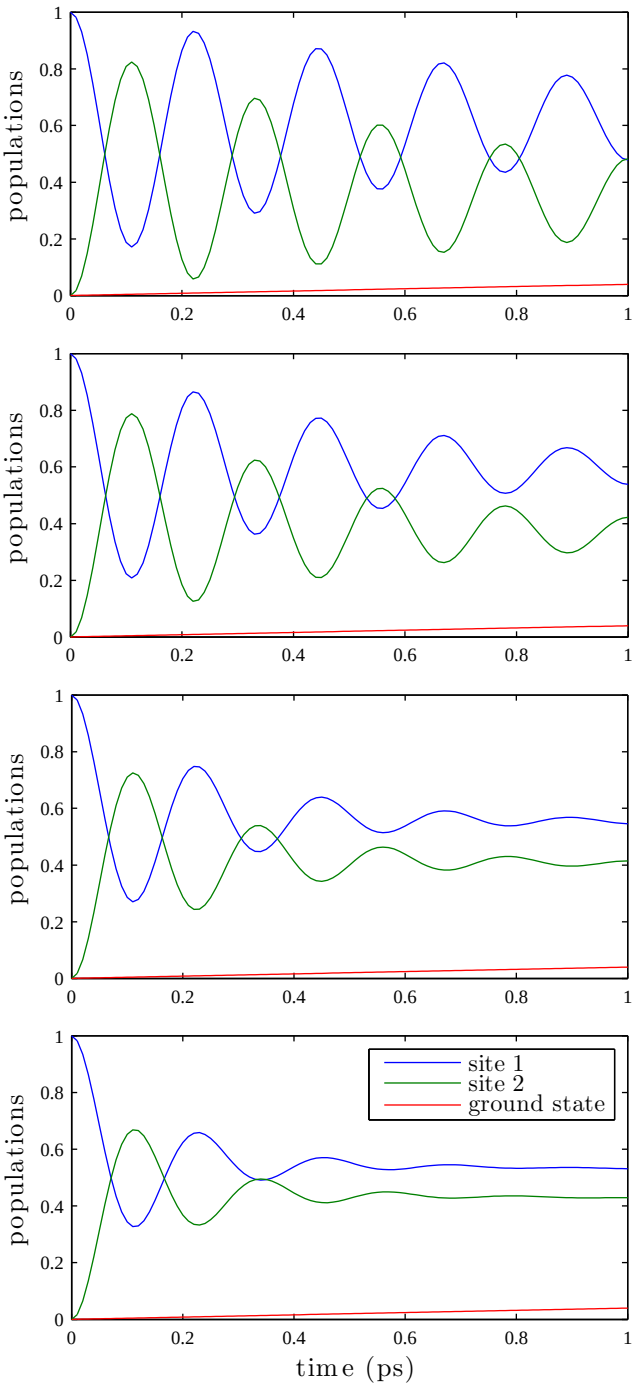

Figure 6.2: Dynamics of the dimer at different temperatures. From top to bottom: T=1K,100K, 200K, 298K. The oscillations decay due to dephasing. This is stronger at higher temperatures. Recombination makes the populations in the two sites slowly decay and the population of the ground state (red) rise. System-environment couplings are set to $v = 5\text{cm}^{-1}$ and $\nu = 0.1\text{cm}^{-1}$.

ence between the two sites. For sites with similar energy $|\epsilon_H - \epsilon_B| \ll g$ the decay rate is given by $\gamma_2 = v^2[C(2g) + C(-2g)]/2$. Since $C(\omega)$ is smooth on the scale of g one can approximate $C(\pm 2g) \approx C(0) \propto T$ for the given spectral function. In figure 6.2 we can see a few numerical examples for different temperatures. With decreasing temperature the environment fluctuates less, i.e. dephasing noise on the system is reduced and coherent oscillations last for longer times. The oscillation frequency is not affected by temperature since we have not considered a temperature dependency of the system Hamiltonian H_S.

We then add recombination noise into our considerations. To do so we need to add the ground state, in which the exciton has vanished from all sites to the system Hamiltonian.

$$H_s = \begin{pmatrix} \epsilon_H & g & 0 \\ g & \epsilon_B & 0 \\ 0 & 0 & \epsilon_0 \end{pmatrix} = \begin{pmatrix} 0 & 71.3 & 0 \\ 71.3 & 46.4 & 0 \\ 0 & 0 & -12210 \end{pmatrix} \tag{6.4}$$

The energy ϵ_0 of the ground state $|G\rangle$ is one excitonic energy lower than ϵ_H and ϵ_B. This difference is typically two orders of magnitude larger [139] than all other relevant parameters in H_S. Therefore any couplings between the ground state and states $|H\rangle$ and $|B\rangle$ would only have a negligible effect and are neglected entirely by employing the rotating wave approximation/ secular approximation. For simplicity we set them to zero in the first place. We then extend the system operators of each site $s_1 = v(2\,|H\rangle\langle H| - \mathbb{1}) + \nu\,|H\rangle\langle G| + \nu\,|G\rangle\langle H|$, $s_2 = v(2\,|B\rangle\langle B| - \mathbb{1}) + \nu\,|B\rangle\langle G| + \nu\,|G\rangle\langle B|$ and use the same spectral function as before. The excitonic energy is then lost from the system at a rate of $\gamma_1 = \nu^2 C(\epsilon_H - \epsilon_0)$, where the spectral function is again approximately constant around this frequency. While the dephasing rate is of about the same order as the inter-site couplings, the recombination rate is typically much slower and on the order of 1 ns [75, 152]. The recombination can be seen by a slow decay of the populations in H and B to the ground state in figure 6.2. As the ground state is considerably lower in energy almost all population is found in the ground state at thermal equilibrium, which is reached for very long times. This corresponds to the fact that the creation and existence of an exciton itself is a non-equilibrium process. However the recombination processes are typically much slower than dephasing processes due to a weaker noise coupling $\nu < v$. Therefore the system dephases first and then decays to the ground state on a longer time scale. In contrast to dephasing the recombination strength is almost temperature independent. In an Ohmic noise environment it is purely proportional to the excitonic energy.

6.3.2 Applying the secular approximation

The secular approximation is based on two largely different (i.e. 'secular') scales of parameters involved. Usually these two scales are the large excitonic energy on the one hand and the small couplings between sites and noise strength on the other. The approximation should never alter the solutions but merely simplify the process of finding a solution by setting those elements of the superoperator to zero, which only have a negligible effect on the solution. This is true for those off-diagonal superoperator elements, whose magnitude is much smaller than the difference of their corresponding diagonal elements.

We demonstrate this numerically for the dimer system. To write the superoperator as a matrix we first have to reorder the density matrix as a vector. We do so and put the diagonal density matrix elements first in the vector (eq. 6.5). The Bloch-Redfield equations are then given in eq. 6.5 without the secular approximation and in eq. 6.6 with the secular approximation. To transform from one to the other one needs to compare each pair of diagonal elements and if their difference is of the order $10,000$ then the two corresponding off-diagonal elements are set to zero. This detailed procedure yields what we call the partial secular approximation. The full secular approximation would set all off-diagonal elements which are outside the red rectangle in eq. 6.5 and 6.6 to zero and only leave behind those off-diagonal elements which link ρ_{11}, ρ_{22} and ρ_{33} (i.e. the elements inside the red rectangle). This full secular approximation would change the evolution of the system. It would neglect any coherent oscillations and only leave the transition rates un-altered (see figure 6.3).

The wide-spread usage of this full secular approximation has lead some to believe that the Bloch-Redfield formalism is not capable of modeling coherent oscillations at all. The partial secular approximation however leaves the non-negligible elements behind, which cause coherent oscillations. Ishizaki [76] discussed furthermore how the full secular approximation alters energy transfer rates between sites when the reorganisation energy becomes greater than the electronic couplings. Ishizaki further criticises [74, 76] that Bloch-Redfield equations in general are only second-order in the noise strength although the noise and the couplings are of similar order in light-harvesting systems. This criticism applies equally to Lindblad equations as typically the Lindblad rates are derived from a second-order perturbation theory calculation of the system-environment coupling.

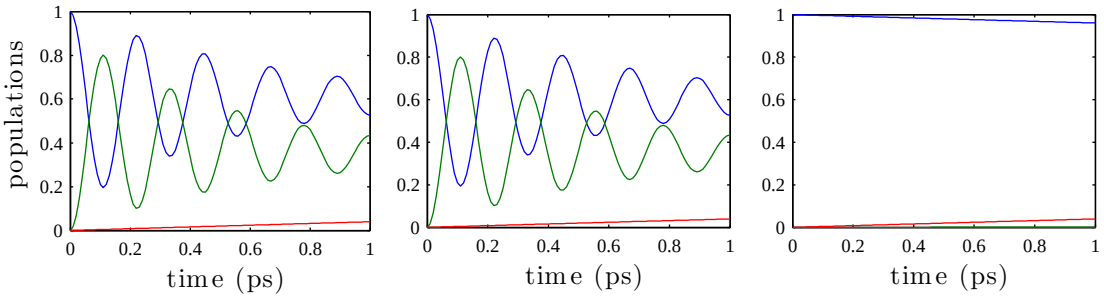

Figure 6.3: Time evolution of the dimer system. **Left:** No approximations are applied (eq. 6.5). **Middle:** The partial secular approximation is applied (eq. 6.6) **Right:** The illegitimate full secular approximation is applied, which sets all non-diagonal elements outside the red square in eq. 6.6 to zero. We can clearly see that the partial secular approximation does not alter the evolution and hence only sets negligible elements to zero. The full secular approximation however sets relevant elements to zero and hence the system's oscillations are lost.

$$\begin{pmatrix} \dot\rho_{11} \\ \dot\rho_{22} \\ \dot\rho_{33} \\ \dot\rho_{12} \\ \dot\rho_{13} \\ \dot\rho_{21} \\ \dot\rho_{23} \\ \dot\rho_{31} \\ \dot\rho_{32} \end{pmatrix} = \begin{pmatrix} -4 & 0 & 4 & 0-71i & 3 & 0+71i & 0 & 3 & 0 \\ 0 & -4 & 4 & 0+71i & 0 & 0-71i & 3 & 0 & 3 \\ 4 & 4 & -8 & 0 & -3 & 0 & -3 & -3 & -3 \\ -1-71i & 1+71i & 0 & -8-46i & -1 & 0 & 0 & 0 & -1 \\ 2 & 0 & -2 & -2 & -9+12210i & 0 & 0+71i & 4 & 0 \\ -1+71i & 1-71i & 0 & 0 & 0 & -8+46i & -1 & -1 & 0 \\ 0 & 2 & -2 & 0 & 0+71i & -2 & -9+12256i & 0 & 4 \\ 2 & 0 & -2 & 0 & 4 & -2 & 0 & -9-12210i & 0-71i \\ 0 & 2 & -2 & -2 & 0 & 0 & 4 & -0-71i & -9-12256i \end{pmatrix} \begin{pmatrix} \rho_{11} \\ \rho_{22} \\ \rho_{33} \\ \rho_{12} \\ \rho_{13} \\ \rho_{21} \\ \rho_{23} \\ \rho_{31} \\ \rho_{32} \end{pmatrix} \tag{6.5}$$

$$\begin{pmatrix} \dot\rho_{11} \\ \dot\rho_{22} \\ \dot\rho_{33} \\ \dot\rho_{12} \\ \dot\rho_{13} \\ \dot\rho_{21} \\ \dot\rho_{23} \\ \dot\rho_{31} \\ \dot\rho_{32} \end{pmatrix} = \begin{pmatrix} -4 & 0 & 4 & 0-71i & 0 & 0+71i & 0 & 0 & 0 \\ 0 & -4 & 4 & 0+71i & 0 & 0-71i & 0 & 0 & 0 \\ 4 & 4 & -8 & 0 & 0 & 0 & 0 & 0 & 0 \\ -1-71i & 1+71i & 0 & -8-46i & 0 & 0 & 0 & 0 & 0 \\ 0 & 0 & 0 & 0 & -9+12210i & 0 & 0+71i & 0 & 0 \\ -1+71i & 1-71i & 0 & 0 & 0 & -8+46i & 0 & 0 & 0 \\ 0 & 0 & 0 & 0 & -0+71i & 0 & -9+12256i & 0 & 0 \\ 0 & 0 & 0 & 0 & 0 & 0 & 0 & -9-12210i & 0-71i \\ 0 & 0 & 0 & 0 & 0 & 0 & 0 & -0-71i & -9-12256i \end{pmatrix} \begin{pmatrix} \rho_{11} \\ \rho_{22} \\ \rho_{33} \\ \rho_{12} \\ \rho_{13} \\ \rho_{21} \\ \rho_{23} \\ \rho_{31} \\ \rho_{32} \end{pmatrix} \tag{6.6}$$

6.4 Mapping to Lindblad equations

There are several ways by which one can map Bloch-Redfield equations to a Lindblad form. The correct approach depends on the level of modeling detail that one wants to transmit to Lindblad form. We can map the Bloch-Redfield equations to Lindblad equations by neglecting all time correlations (or taking the secular approximation) and neglecting all spatial correlations of the bath (or diagonalising the coefficient matrix). Neglecting all time correlations means assuming a strong form of Markovianity in that the bath correlations decay instantly and not just on a time scale shorter than the system dynamics. The spectral function must then be constant for all frequencies. This strong condition can however be replaced with the secular approximation combined with a piece-wise flat spectral function which only changes on the large scale of the secular approximation [84]. In section 2.1.3 we showed generally that the system operators can then be split up into the parts which are dependent on the same flat piece of the spectral function $s_j = \sum_\epsilon s_j(\epsilon)$ and the Bloch-Redfield equations 2.27 simplify to eq. 2.41.

Neglecting all spatial correlations in the noise sets all mixed terms involving $j \neq k$ to zero since the corresponding spectral functions $C_{jk}(\omega) = 0$. For correlated environments a diagonalisation of the coefficient matrix (C_{jk}) is necessary, see section 2.1.5. This however is a non-trivial step and will yield non-local Lindblad operators, eq. 2.53. The mapping is then merely a step to reassure physical behaviour of the master equation. However it shows that the Bloch-Redfield formalism can model more complex environments by considering different types of correlations.

If Lindblad equations are used without an underpinning Bloch-Redfield-like derivation the connection to a microscopic noise model is lost. This can lead to artificial effects like noise-induced oscillations whose physical cause is unclear. These can be misinterpreted as system oscillations [32] but a characteristic feature is that the strength of such oscillations is purely dependent on the noise strength and shows the same temperature dependency as the noise-induced decays.

6.5 Effects in large LHCs

The Fenna-Matthews-Olson (FMO) complex is a seven site light-harvesting complex, in which the Hamiltonian governing the excitonic dynamics can be estimated [140,

153], and which has therefore been studied by various groups [69, 73, 75, 137, 139, 150, 154]. In this section we demonstrate that the Bloch-Redfield equations are an excellent tool to investigate large LHCs such as the FMO complex. We use site-numbering that follows the original paper by Fenna et al [155]. The system operators which couple to the noise and the spectral function are chosen analogously to the dimer in the previous section, with an additional trapping rate of 1ps^{-1} from site 3 to the reaction centre (rc). We simulate the FMO complex at $T = 77\text{K}$ and set the recombination rate to $\gamma_1 = \nu^2 C(12210\text{cm}^{-1}) = 0.001\text{ps}^{-1}$. The time evolution for different dephasing rates $\gamma_2 = v^2 C(0)$ is shown in figure 6.4.

We find that even for strong noise the solution shows physical behaviour, ie. non-positivity is not an issue. The occurrence of an optimal dephasing rate is in agreement with other models [69, 137].

To demonstrate further the capabilities of the Bloch-Redfield equations we investigate the influence of temperature and spatial correlations on the transfer dynamics of the FMO. Recently Olbrich et al. did not find correlations within the *system* site energies in a classical molecular dynamics simulation of a truncated version of the FMO complex [156]. This can be seen as an indication of uncorrelated noise, however quantum simulations of the environmental space-time correlations of the full FMO complex have not yet been performed.

Temperature is modeled via the Ohmic spectral function, figure 6.1. The influence of spatial noise correlations is modelled via a homogeneous exponentially decaying function $C_{jk}(\omega) = \exp(-|\mathbf{r}_j - \mathbf{r}_k|/\xi)C(\omega)$, which we combine with the three-dimensional relative distances of the FMO chromophores [157, 158]. Figure 6.5 shows the time for a 90% probability of the exciton initially placed on site 1, to transfer to the reaction centre as a function of temperature and spatial correlation length ξ. For temperatures, which are not too close to zero we find that increasing the correlation length of the noise from zero enhances the exciton transport by reinstating the coherent transfer dynamics similar as in chapter 5. For $\gamma_2 = 20\text{ps}^{-1}$ the optimal correlation length is approximately $\xi = 100$ Å. Even longer correlation lengths are detrimental to the transfer, contrary to the spin chain in chapter 5. This is in agreement with the finding that a certain level of dephasing is advantageous to the transfer [137, 140, 150, 151] in the FMO complex as the coherent dynamics is not ideal in regards to exciton transfer.

We found in sections 2.2.2 and 5.2, that increasing noise correlation length leads to dephasing-reduced subspaces of states with equal excitation number. Transport

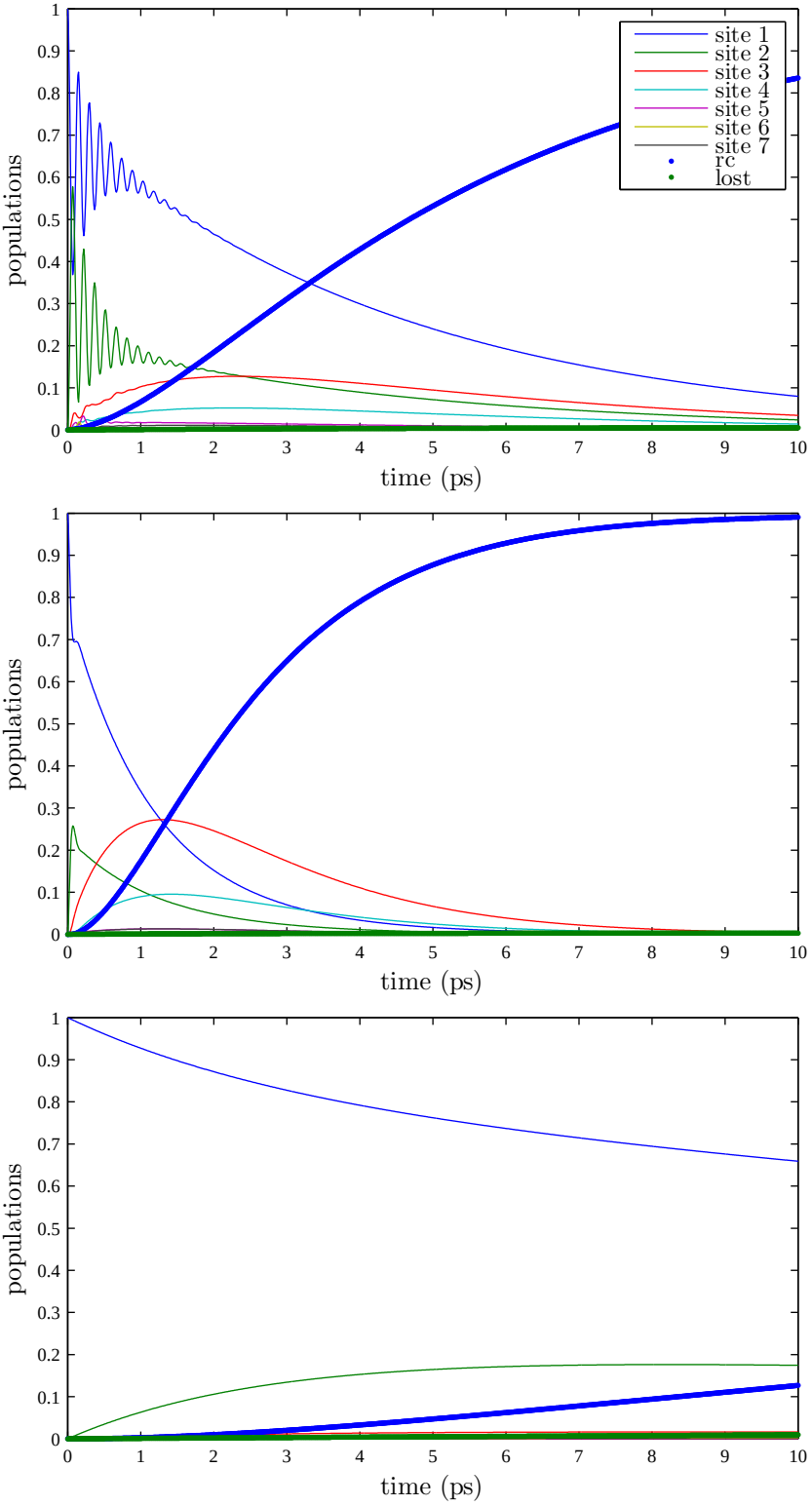

Figure 6.4: Time evolution of the FMO complex at three different dephasing rates: from top to bottom $\gamma_2 = 1\text{ps}^{-1}, 10\text{ps}^{-1}, 1000\text{ps}^{-1}$. Top: Within the coherence time there are several oscillations between site 1 and 2. Middle: Around the optimal dephasing rate the exciton is transferred very quickly. Bottom: Strong dephasing starts to "freeze" the system (quantum zeno effect), which slows down the transfer.

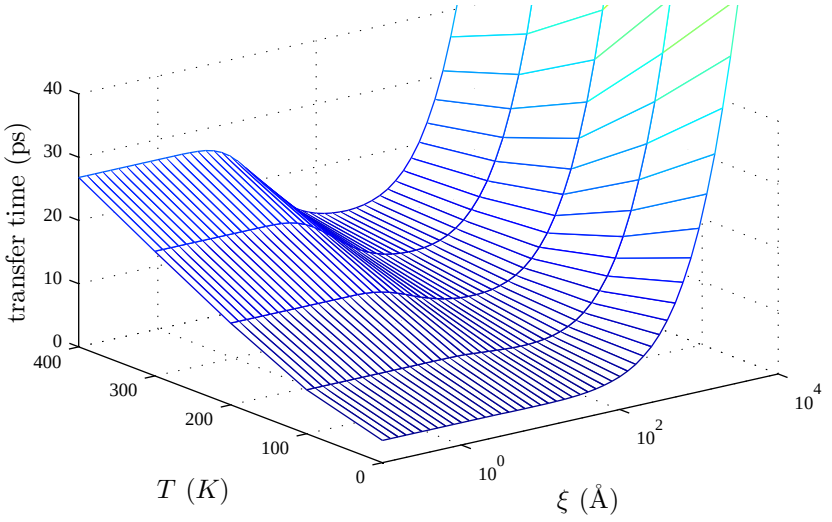

Figure 6.5: Transfer time as a function of temperature and spatial noise correlation length for a dephasing rate $\gamma_2 = 20$ ps^{-1}. We find an optimal region with short transfer times for finite correlation length $\xi \approx 100$ Å.

processes are limited to the single-excitation subspace, therefore the optimal correlation length is strongly dependent on the dephasing rate. We find in figure 6.5 that around the optimal correlation length the transfer time can be reduced to less than 20ps. We plot the probability of transfer after this time in figure 6.6 as a function of correlation length and dephasing rate. We find that the optimal correlation length, which is defined by the region of high transfer probability increases with the dephasing rate. The dependence of the optimal correlation length on the dephasing rate is consistent over many orders of magnitude. It shows that the effective reduction of dephasing caused by noise correlations can help to bring the system into the regime of optimal dephasing strength. This is in agreement with the findings in references [69, 73].

6.6 Conclusions

We have presented how the Bloch-Redfield equations can be utilised to model excitonic dynamics in chromophoric aggregates or light-harvesting complexes in a consistent manner. The equations link back generally to a physical model of system-environment interaction Hamiltonian and spatial-temporal correlations contained in the spectral function, giving more flexible and adaptable modeling options than a phenomenological Lindblad approach.

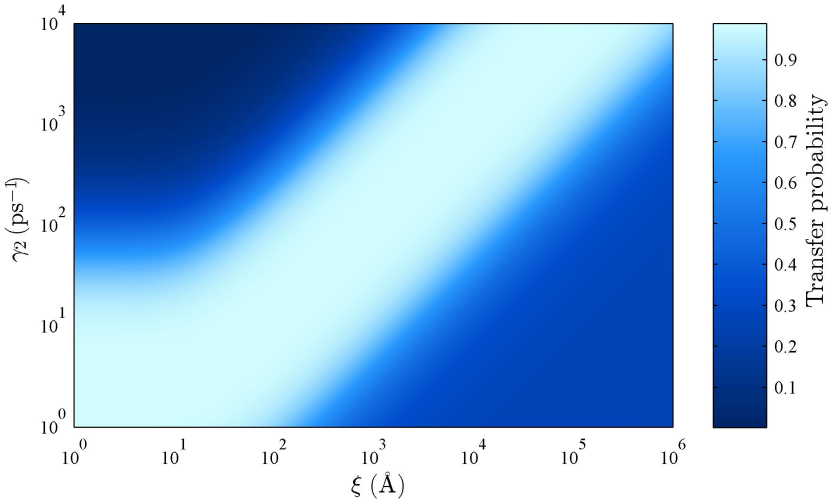

Figure 6.6: Probability of exciton transfer to the reaction centre after 20 ps^{-1}. Since correlation length reduces the dephasing noise effects, correlations can help to reach the optimal parameter regime and hence be advantageous to transport. Temperature was $T = 300K$ in this simulation.

We have shown how issues of non-positivity and non-physicality or the loss of coherent oscillations are not inherent to the Bloch-Redfield formalism, and can be ruled out by an underpinning consistent physical model. If the secular approximation is applied, it needs to be based on the occurrence of different scales and applied carefully for the respective system at hand. Given these conditions, the secular approximation will not change the equations but merely simplify them by setting negligible elements to zero.

For a dimer system we have shown how coherent oscillations between the sites arise from the coupling g and site-energy difference $|\epsilon_H - \epsilon_B|$. The oscillations are damped when the site-energies couple to the noise environment causing dephasing noise in the dimer and dissipation into the ground state arises from recombination noise. We have shown how dephasing noise is linked to thermal effects, while recombination is independent of temperature in an Ohmic noise environment.

In the FMO complex, we have combined a model with finite correlation length of the dephasing noise with the actual relative positions of the chromophores in the complex. We show the relative influences of correlation length, dephasing strength and temperature on the transfer time and probability. No issues of non-physicality arise, even for strong noise. We find an optimal noise correlation length, which is particularly relevant at higher temperatures, and strongly dependent on the dephasing rate. Our findings are both in agreement with and an extension of previous work

by other groups. In conclusion the Bloch-Redfield equations are an excellent tool to model Markovian noise in light-harvesting complexes.

Chapter 7

7 The quantum ferromagnet with correlated decoherence

The Heisenberg model for a quantum ferromagnet is extended to a master-equation approach in order to model the effects of a bath such as the phonons which interact with the spins in the ferromagnet. This enables us to study non-equilibrium dynamics of material properties such as the magnetisation. We focus on the influence of spatial noise correlations onto this dynamics and find analytical expressions for the decay rate of magnons to equilibrium dependent on the correlation length. Longer spatial noise correlations are found to prolong the out-of-equilibrium time of the magnetisation. The unique approach of calculating properties of solid-state systems with master equation techniques is based on collaborative work with Ángel Rivas [82].

7.1 Coherent spin wave theory for the quantum ferromagnet

First we revisit the coherent quantum model of a ferromagnet as given in text-books such as [118]. It is described by linear spin wave theory. In this section we show how the Hamiltonian for the Heisenberg model can be diagonalised by a Holstein-Primakoff transformation, combined with a linear spin wave approximation and followed by a Fourier lattice transform, which yields the Hamiltonian describing 'magnons', the elementary collective magnetic excitations. We start with a Heisenberg model for the spins in the quantum ferromagnet with only nearest-neighbour

interaction:

$$H = J \sum_{\langle \mathbf{r}, \mathbf{r}' \rangle} \mathbf{S}_\mathbf{r} \mathbf{S}_{\mathbf{r}'} \tag{7.1}$$

where $J < 0$ for a ferromagnet. Antiferromagnetic behaviour ($J > 0$) has been investigated similarly [82].

This Hamiltonian can be mapped to a system of interacting bosons via the Holstein-Primakoff transformation [118, 159] for spins $S \geq 1/2$:

$$\begin{aligned} S^z_\mathbf{r} &= S - n_\mathbf{r} \\ S^+_\mathbf{r} &= \sqrt{2S}\phi(n_\mathbf{r}) a_\mathbf{r} \\ S^-_\mathbf{r} &= \sqrt{2S} a^\dagger_\mathbf{r} \phi(n_\mathbf{r}) \end{aligned} \tag{7.2}$$

where $n_\mathbf{r} = a^\dagger_\mathbf{r} a_\mathbf{r}$ and

$$\phi = \sqrt{1 - \frac{n_\mathbf{r}}{2S}} \tag{7.3}$$

This function is then approximated by a series expansion to first order in the normal-ordered number operator [118]:

$$\phi \approx 1 - \left(1 - \sqrt{1 - 1/2S}\right) n_\mathbf{r} \qquad \text{for } \langle a^\dagger_\mathbf{r} a_\mathbf{r} \rangle \ll 2S \tag{7.4}$$

With this linear spin-wave approximation the Hamiltonian 7.1 becomes for a D-dimensional system:

$$H_{LSW} = JNDS^2 - 2JDS \sum_\mathbf{r} a^\dagger_\mathbf{r} a_\mathbf{r} + JS \sum_{\langle \mathbf{r}, \mathbf{r'} \rangle} \left(a^\dagger_\mathbf{r} a_{\mathbf{r}'} + a^\dagger_{\mathbf{r}'} a_\mathbf{r} \right) \tag{7.5}$$

This Hamiltonian is then diagonalized for $D = 3$ via a three-dimensional Fourier lattice transform :

$$\begin{aligned} a_\mathbf{r} = a_{x,y,z} &= \frac{1}{\sqrt{N}} \sum_\mathbf{k} e^{i\mathbf{kr}} a_\mathbf{k} = \frac{1}{\sqrt{N_x N_y N_z}} \sum_{k_x, k_y, k_z} e^{ik_x x} e^{ik_y y} e^{ik_z z} a_{k_x, k_y, k_z} \\ a^\dagger_\mathbf{r} &= \frac{1}{\sqrt{N}} \sum_\mathbf{k} e^{-i\mathbf{kr}} a^\dagger_\mathbf{k} \end{aligned} \tag{7.6}$$

We choose the nearest-neighbour parameterization $\mathbf{r}' = \mathbf{r} + \mathbf{d}$, where $\mathbf{d} = (d_x, d_y, d_z)$ is the vector containing the lattice constants in x-,y- and z-direction and $\sum_{\langle \mathbf{r}, \mathbf{r}' \rangle} =$

$\sum_{x,y,z}$. Analogous to the one-dimensional case (eqs. 3.9 to 3.12) one then diagonalises the Hamiltonian in k-space.

$$H_{LSW} = E_0 + \sum_{\mathbf{k},\mathbf{k}'} JS\frac{1}{N}\sum_{x,y,z} \exp\left[i(\mathbf{k}\text{-}\mathbf{k}')\mathbf{r}\right]\left(-2D\, a^\dagger_{\mathbf{k}} a_{\mathbf{k}'} + e^{i\mathbf{k}'\mathbf{d}} a^\dagger_{\mathbf{k}} a_{\mathbf{k}'} + e^{-i\mathbf{k}'\mathbf{d}} a^\dagger_{\mathbf{k}'} a_{\mathbf{k}}\right) \tag{7.7}$$

$$= E_0 + \sum_{\mathbf{k},\mathbf{k}'} JS\delta_{k_x,k'_x}\delta_{k_y,k'_y}\delta_{k_z,k'_z}\left(-2D\, a^\dagger_{\mathbf{k}} a_{\mathbf{k}'} + e^{i\mathbf{k}'\mathbf{d}} a^\dagger_{\mathbf{k}} a_{\mathbf{k}'} + e^{-i\mathbf{k}'\mathbf{d}} a^\dagger_{\mathbf{k}'} a_{\mathbf{k}}\right) \tag{7.8}$$

$$= E_0 + \sum_{\mathbf{k}} 2JS\left[-D + \cos(\mathbf{k}\mathbf{d})\right]\; a^\dagger_{\mathbf{k}} a_{\mathbf{k}} \tag{7.9}$$

$$= E_0 + \sum_{\mathbf{k}} \omega(\mathbf{k}) a^\dagger_{\mathbf{k}} a_{\mathbf{k}} \tag{7.10}$$

where $E_0 = JNDS^2$ is a constant energy shift.

This is the diagonal linear spin wave Hamiltonian. The excitations of these harmonic oscillators are called magnons as they represent the elementary magnetic excitation.

7.2 Magnon decay rates and spatial correlations

In this section we extend the coherent description of the quantum ferromagnet by adding a decoherent master equation part. Particularly our interest is to investigate how the magnon decay rate of a particular master equation, and thereby the decay rate of non-equilibrium magnetisation, can be linked to the spatial correlations of the noise. To do so we start with a master equation for the ferromagnetic spins in k-space, which we haven't yet linked to a particular environmental model. This master equation is of Lindblad form:

$$\dot{\rho} = -i[H_{LSW}, \rho] + \sum_{\mathbf{k}} \gamma_{\mathbf{k}}\left(a_{\mathbf{k}}\rho a^\dagger_{\mathbf{k}} - \frac{1}{2}\left\{a^\dagger_{\mathbf{k}} a_{\mathbf{k}}, \rho\right\}\right) \tag{7.11}$$

We then replace operators with their Fourier lattice transforms:

$$a_{\mathbf{k}} = \frac{1}{\sqrt{N}}\sum_{\mathbf{r}} e^{-i\mathbf{k}\mathbf{r}} a_{\mathbf{r}} \qquad a^\dagger_{\mathbf{k}} = \frac{1}{\sqrt{N}}\sum_{\mathbf{r}} e^{i\mathbf{k}\mathbf{r}} a^\dagger_{\mathbf{r}} \tag{7.12}$$

where d is the spatial distance between sites and find:

$$\dot{\rho} = -i[H_{LSW}, \rho] + \sum_{\mathbf{r},\mathbf{r'}} C_{\mathbf{r}-\mathbf{r}'} \left(a_{\mathbf{r}} \rho a_{\mathbf{r}'}^{\dagger} - \frac{1}{2} \left\{ a_{\mathbf{r}'}^{\dagger} a_{\mathbf{r}}, \rho \right\} \right) \tag{7.13}$$

$$\text{where } C_{\mathbf{r}-\mathbf{r}'} = \sum_{\mathbf{k}} \gamma_{\mathbf{k}} \frac{1}{N} e^{-i\mathbf{k}(\mathbf{r}-\mathbf{r}')} = \sum_{k_x=-\pi/d_x}^{\pi/d_x} \sum_{k_y=-\pi/d_y}^{\pi/d_y} \sum_{k_z=-\pi/d_y}^{\pi/d_y} \gamma_{\mathbf{k}} \frac{1}{N} e^{-i\mathbf{k}(\mathbf{r}-\mathbf{r}')} \tag{7.14}$$

The actual discrete summations in eq. 7.14 are over the N_μ different values ($\mu = x, y, z$) for $k_{\mu,n} = \frac{2\pi}{N_\mu d_\mu} n$ with the whole numbers $n \in \left\{ -\frac{N_\mu}{2}, \ldots, \frac{N_\mu}{2} - 1 \right\}$ where N_μ is the even number of sites in the μ-direction of the ferromagnetic crystal.

We find that the spatial correlation function $C_{\mathbf{r}-\mathbf{r}'}$ is the discrete Fourier transform of the magnon decay rate $\gamma_{\mathbf{k}}$. The correlation function only depends on the difference $\mathbf{r}-\mathbf{r}'$ (not on the position $\mathbf{r}$) because we assumed a $\mathbf{k}$-space master equation (eq. 7.11) with only one k-summation. The frequency dependence of the spectral function is here neglected in agreement with a strict Markov approximation.

This relationship between $C_{\mathbf{r}-\mathbf{r}'}$ and $\gamma_{\mathbf{k}}$ is analogous to the relationship between the coupling strength $g_{x-x'}$ in a bosonic system $H_{\text{bos}} = \sum_{x,x'} g_{x-x'} a_x^{\dagger} a'_x$ and the dispersion relation ω_k of that same system $H_{\text{bos}} = \sum_k \omega_k a_k^{\dagger} a_k$ (see eq. 3.13).

The inverse Fourier transform yields the magnon decay rate corresponding to a particular spatial correlation function. We substitute the relative distance $\mathbf{u} = \mathbf{r} - \mathbf{r}' = (u_x, u_y, u_z)$:

$$\gamma_{\mathbf{k}} = \sum_{\mathbf{u}} e^{i\mathbf{k}\mathbf{u}} C_{\mathbf{u}} \tag{7.15}$$

The actual discrete summation in each direction is carried out in steps of the lattice constants $\mathbf{d} = (d_x, d_y, d_z)$:

$$\sum_{u_\mu} e^{ik_\mu u_\mu} = \sum_{u_\mu=0}^{N-1} e^{ik_\mu d_\mu u_\mu} = \sum_{u_\mu=-N_\mu/2}^{N_\mu/2-1} e^{ik_\mu d_\mu u_\mu} = \sum_{u_\mu=-N_\mu+1}^{0} e^{ik_\mu d_\mu u_\mu} \tag{7.16}$$

where the periodicity of the exponential makes all three summations equivalent since

k_μ only takes on the discrete values $k_{\mu,n} = \frac{2\pi}{N_\mu d_\mu} n$. We therefore can also write:

$$\sum_{u_\mu=0}^{N-1} e^{ik_\mu d_\mu u_\mu} = \frac{1}{2} \sum_{u_\mu=-N_\mu+1}^{0} e^{ik_\mu d_\mu u_\mu} + \frac{1}{2} \sum_{u_\mu=0}^{N_\mu-1} e^{ik_\mu d_\mu u_\mu} = \frac{1}{2} \sum_{u_\mu=0}^{N_\mu-1} (e^{ik_\mu d_\mu u_\mu} + e^{-ik_\mu d_\mu u_\mu})$$
$$= \sum_{u_\mu=0}^{N_\mu-1} \cos(k_\mu d_\mu u_\mu) \tag{7.17}$$

Accordingly we can rewrite eq. 7.15:

$$\gamma_{\mathbf{k}} = \sum_{\mathbf{u}} \cos(\mathbf{ku}) C_{\mathbf{u}} \tag{7.18}$$

For this transformation to work a homogeneous spatial correlation function $C_{\mathbf{u}} = C_{-\mathbf{u}}$ must be assumed. We write out the three-dimensional discrete summation in detail in the following equation and insert for each dimension the discrete values for $k_{\mu,n} = \frac{2\pi}{N_\mu d_\mu} n$. For large N, smooth $C_{\mathbf{u}}$ and correlation functions which decay on a length shorter than the three edge lengths of the ferromagnet the discrete summation can be written as a continuous Fourier transform, which can be helpful to obtain analytical expressions:

$$\gamma_{\mathbf{k}} = \sum_{u_x=-N_x/2}^{N_x/2-1} \sum_{u_y=-N_y/2}^{N_y/2-1} \sum_{u_z=-N_z/2}^{N_z/2-1} \cos(k_x d_x u_x + k_y d_y u_y + k_z d_z u_z) C_{\mathbf{u}} \tag{7.19}$$

$$= \sum_{u_x=-N_x/2}^{N_x/2-1} \sum_{u_y=-N_y/2}^{N_y/2-1} \sum_{u_z=-N_z/2}^{N_z/2-1} \cos\left[2\pi \left(\frac{n_x u_x}{N_x} + \frac{n_y u_y}{N_y} + \frac{n_z u_z}{N_z}\right)\right] C_{\mathbf{u}} \quad \text{(discrete)} \tag{7.20}$$

$$\gamma_{\mathbf{k}} \approx \int_{-\infty}^{\infty} du_x \int_{-\infty}^{\infty} du_y \int_{-\infty}^{\infty} du_z \; e^{i(k_x d_x u_x + k_y d_y u_y + k_z d_z u_z)} C_{\mathbf{u}} \quad \text{(continuous)} \tag{7.21}$$

7.2.1 Magnon emission and magnon absorption

In the previous section we found how the magnon decay rate $\gamma_{\mathbf{k}}$ relates to the spatial correlation function $C_{\mathbf{u}}$ of the noise. In the master equation 7.11 only magnon emission was considered. We now consider both emission and absorption of magnons and their relative strengths, which defines the equilibrium. Both processes are due to the interaction of the quantum ferromagnet with its phonon environment. Note that in this 3D model of a quantum ferromagnet the system-environment interaction is

not limited to the edges of the crystal but every site in the crystal interacts with the noise environment because the noise is caused by phonon dynamics, which occurs inside the crystal.

The general master equation describing both emission and absorption of magnons is given by:

$$\dot{\rho} = -i[H_{LSW}, \rho] + \sum_{\mathbf{r},\mathbf{r}'} C^{\mathrm{em}}_{\mathbf{r}-\mathbf{r}'} \left(a_{\mathbf{r}} \rho a^{\dagger}_{\mathbf{r}'} - \frac{1}{2} \left\{ a^{\dagger}_{\mathbf{r}'} a_{\mathbf{r}}, \rho \right\} \right) + \sum_{\mathbf{r},\mathbf{r}'} C^{\mathrm{abs}}_{\mathbf{r}-\mathbf{r}'} \left(a^{\dagger}_{\mathbf{r}'} \rho a_{\mathbf{r}} - \frac{1}{2} \left\{ a_{\mathbf{r}} a^{\dagger}_{\mathbf{r}'}, \rho \right\} \right) \tag{7.22}$$

For a bosonic environment (phonons) where $\langle n(\omega) \rangle$ is the mean number of phonons in the bath at frequency ω one finds the relative strength of emission and absorption to be (cf. eq. 3.49 and 3.51):

$$C^{\mathrm{abs}}_{\mathbf{r}-\mathbf{r}'} = C_{\mathbf{r}-\mathbf{r}'} \langle n(\omega) \rangle \tag{7.23}$$

$$C^{\mathrm{em}}_{\mathbf{r}-\mathbf{r}'} = C_{\mathbf{r}-\mathbf{r}'} (1 + \langle n(\omega) \rangle) \tag{7.24}$$

In eq. 3.49 and 3.51 these functions depend on the spatial distance $\mathbf{u} = \mathbf{r} - \mathbf{r}'$ and on the probing frequency ω with a dependence which is set by the *environmental* dispersion relation ω^{env}_k. For the purpose of this chapter we assume in accordance with strong Markovianity that on the scale of the *system* energies the frequency dependence is negligible. Eq. 7.22 can be transformed into $\mathbf{k}$-space analogous to section 7.2:

$$\dot{\rho} = -i[H_{LSW}, \rho] + \sum_{\mathbf{k}} \gamma_{\mathbf{k}} (1 + \langle n(\omega) \rangle) \left(a_{\mathbf{k}} \rho a^{\dagger}_{\mathbf{k}} - \frac{1}{2} \left\{ a^{\dagger}_{\mathbf{k}} a_{\mathbf{k}}, \rho \right\} \right) + \sum_{\mathbf{k}} \gamma_{\mathbf{k}} \langle n(\omega) \rangle \left(a^{\dagger}_{\mathbf{k}} \rho a_{\mathbf{k}} - \frac{1}{2} \left\{ a_{\mathbf{k}} a^{\dagger}_{\mathbf{k}}, \rho \right\} \right) \tag{7.25}$$

This form is advantageous because H_{LSW} is diagonal in the Fock states of these operators (see eq. 7.10). The magnon decay rate is given by eq. 7.18:

$$\gamma_{\mathbf{k}} = \sum_{\mathbf{u}} e^{i\mathbf{k}\mathbf{u}} C_{\mathbf{u}} \tag{7.26}$$

In the next section we will investigate how different spatial correlation functions $C_{\mathbf{u}}$ influence the dynamics of the magnetisation of the ferromagnetic crystal that follows

the given master equation for magnon emission and absorption.

7.3 Influence of spatial noise correlations on the magnetisation

After constructing the master equation for the quantum ferromagnet we will now solve it and consider the time evolution of the magnetisation. We will sum over all sites and obtain the magnetisation of the entire ferromagnet rather than the microscopic expectation value of a single site. The dynamics of a macroscopic quantity is obtained from calculations of a microscopic quantum master equation. This application of the master-equation approach to a many-body problem shows the versatility of this approach which can be used beyond the usual applications of quantum optics or quantum chemistry.

The magnetisation $\langle m_z \rangle$ transforms via the Holstein-Primakoff transform:

$$\langle m_z \rangle = \frac{1}{N} \sum_{\mathbf{r}} \langle S^z_{\mathbf{r}} \rangle = S - \frac{1}{N} \sum_{\mathbf{r}} \langle a^\dagger_{\mathbf{r}} a_{\mathbf{r}} \rangle = S - \frac{1}{N} \sum_{\mathbf{k}} \langle a^\dagger_{\mathbf{k}} a_{\mathbf{k}} \rangle \tag{7.27}$$

We solve eq. 7.25 for the expectation value $\langle a^\dagger_{\mathbf{k}} a_{\mathbf{k}}(t) \rangle$ by using the adjoint master equation in the Heisenberg picture. The same technique was used in section 3.1.3 and an example for a single harmonic oscillator can be found in section 3.4.6.2 of reference [1]. The solution here is analogous once we keep in mind the bosonic commutation relation $[a_{\mathbf{k}}, a^\dagger_{\mathbf{k}'}] = \delta_{\mathbf{k}\mathbf{k}'}$. We therefore do not give the calculation in detail but give the solution, which is analogous to eq. 3.319 in [1] and eq. 40 in [82]:

$$\langle a^\dagger_{\mathbf{k}} a_{\mathbf{k}}(t) \rangle = \langle a^\dagger_{\mathbf{k}} a_{\mathbf{k}}(0) \rangle \, e^{-\gamma_{\mathbf{k}} t} + \langle n(\omega) \rangle (1 - e^{-\gamma_{\mathbf{k}} t}) \tag{7.28}$$

Accordingly the time-evolution of a non-equilibrium state of the magnetisation is given by:

$$\langle m_z(t) \rangle = S - \frac{1}{N} \sum_{\mathbf{k}} \left[e^{-\gamma_{\mathbf{k}} t} a^\dagger_{\mathbf{k}} a_{\mathbf{k}}(0) + \langle n(\omega) \rangle (1 - e^{-\gamma_{\mathbf{k}} t}) \right] \tag{7.29}$$

Assuming that we start from the ground state $\langle a_{\mathbf{k}}^{\dagger} a_{\mathbf{k}}(0)\rangle = 0$ it simplifies to:

$$\langle m_z(t)\rangle = S - \langle n(\omega)\rangle \left(1 - \frac{1}{N}\sum_{\mathbf{k}} e^{-\gamma_{\mathbf{k}} t}\right) \tag{7.30}$$

The discrete summations are explicitly given by a summation over the Brillouin zone, where each k_μ (where $\mu = x, y, z$) is discretised as $k_{\mu,n} = \frac{2\pi}{N_\mu d_\mu} n$ with the whole numbers $n \in \left\{-\frac{N_\mu}{2}, \ldots, \frac{N_\mu}{2} - 1\right\}$. For large enough N we can change the summation to an integral over the Brillouin zone volume:

$$\langle m_z(t)\rangle = S - \langle n(\omega)\rangle \left(1 - \frac{1}{N}\sum_{k_x=-\pi/d}^{\pi/d}\sum_{k_y=-\pi/d}^{\pi/d}\sum_{k_z=-\pi/d}^{\pi/d} e^{-\gamma_{\mathbf{k}} t}\right) \tag{7.31}$$

$$\langle m_z(t)\rangle \approx S - \langle n(\omega)\rangle \left(1 - \frac{d^3}{(2\pi)^3}\int_{-\pi/d}^{\pi/d} dk_x \int_{-\pi/d}^{\pi/d} dk_y \int_{-\pi/d}^{\pi/d} dk_z \, e^{-\gamma_{\mathbf{k}} t}\right) \tag{7.32}$$

Using the continuous limit for the calculation of the magnon decay rate (eq. 7.21) and the magnetisation (eq. 7.32) facilitates finding an analytical expression. However we need to keep in mind, that this is only valid for large N and a correlation length which is not too short (otherwise the correlation function is not smooth enough to change the sum to an integral) and not too long (otherwise the correlations do not decay over the length of the entire crystal and a finite summation cannot be changed to an infinite Fourier transform.

Next we will give several different cases of spatial correlation functions $C_{\mathbf{r}-\mathbf{r}'}$, the corresponding magnon decay rate $\gamma_{\mathbf{k}}$, eq. 7.20 or 7.21, and a numerical plot of the decay of the magnetisation to its equilibrium value where the parameters $S = 1/2$, $\langle n(\omega)\rangle = 0.3$ are chosen, which sets the starting and end point of the magnetisation decay. Note that most variables are dimensionless in this chapter and the plots hence make relative statements about the effects of spatial correlations. For those spatial correlation functions with a correlation length ξ this length is given in units of the spacing d between the system's (equally spaced $d = d_x = d_y = d_z$) sites, i.e. $\xi = 10$ means a correlation length of 10 spins. Figure 7.1 shows all types of correlation functions which will be discussed.

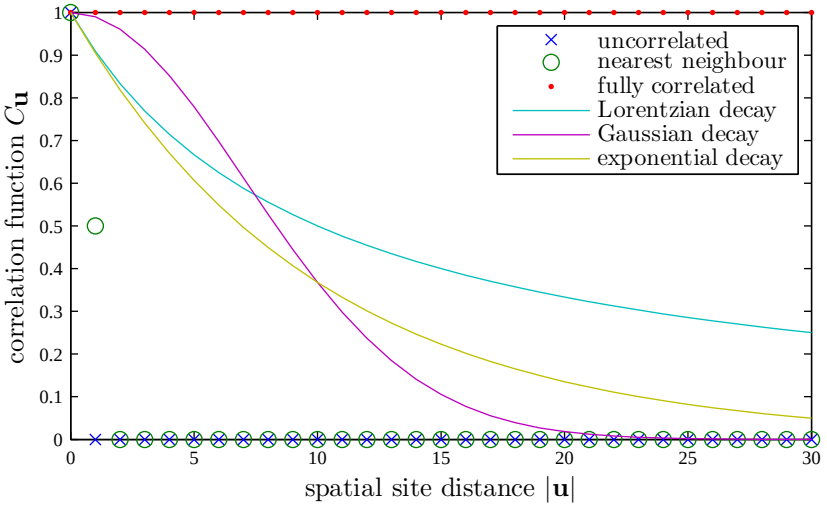

Figure 7.1: The different types of spatial correlation functions discussed in this chapter, plotted in units of the nearest-neighbour distance d. The correlation lengths here is set to $\xi = 10$.

Spatially uncorrelated decoherence

For spatially uncorrelated decoherence we have

$$C_{\mathbf{u}} = \gamma_0 \delta^{(3)}_{\mathbf{u},0} = \gamma_0 \; \delta_{u_x,0} \; \delta_{u_y,0} \; \delta_{u_z,0} \tag{7.33}$$

$$\gamma_{\mathbf{k}} = \gamma_0 \tag{7.34}$$

$$\langle m_z(t) \rangle = S - \langle n(\omega) \rangle (1 - e^{-\gamma_0 t}) \tag{7.35}$$

In this case the magnetisation decays exponentially. We will set the factor $\gamma_0 = 1$ from now on for simplicity and plotting.

Spatial nearest-neighbour correlations of the noise

We now assume nearest neighbour correlations, which are half as strong as the self-correlations:

$$C_{\mathbf{u}} = \delta^{(3)}_{\mathbf{u},0} + 0.5 \delta^{(3)}_{\mathbf{u},1} \tag{7.36}$$

$$\gamma_{\mathbf{k}} = 1 + 0.5 \cos(\mathbf{kd}) = 1 + 0.5 \cos(2\pi n_x/N_x + 2\pi n_y/N_y + 2\pi n_z/N_z) \tag{7.37}$$

$$\langle m_z(t) \rangle = S - \frac{\langle n(\omega) \rangle d^3}{8\pi^2} \int_{-\pi/d}^{\pi/d} d\mathbf{k} (1 - e^{-[1+0.5\cos(\mathbf{kd})]t}) = S - \langle n(\omega) \rangle [1 - e^{-t} I_0(0.5t)] \tag{7.38}$$

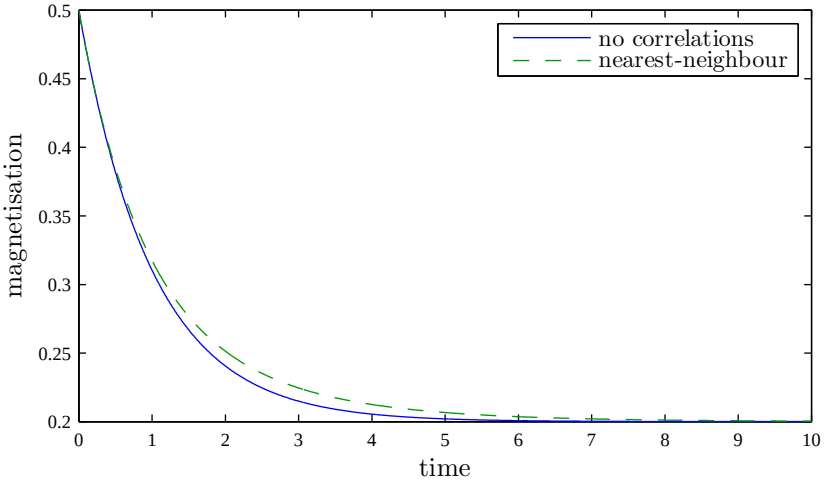

Figure 7.2: Magnetisation as a function of time for uncorrelated noise (blue) and nearest-neighbour correlations of the noise (green). The nearest-neighbour correlations slow down the decay to a non-exponential shape (cf. eq. 7.38). Starting and final point of the decay are set by the parameters $S = 1/2, \langle n(\omega) \rangle = 0.3$. Note that all plots in this chapter give only relative statements of correlation effects since we have used dimensionless units in our calculations.

where $I_0(0.5t)$ denotes the modified Bessel function of the first kind. Note that this Bessel function is the only difference to the previous case of uncorrelated noise. Figure 7.2 shows a plot of the magnetisation as a function of time for both cases. For the calculation of the magnon decay rate we have to use the discrete summation since the decay is not a smooth function of the sites. For the calculation of the magnetisation however we have used integration assuming large enough N. A discrete summation for $N_x = N_y = N_z = 100$ yields numerically the same plot.

Spatially fully correlated noise

We will now regard the extreme case that the noise is perfectly correlated over all sites of the ferromagnet. This is an idealized and arguably pathological case but is

discussed to understand the physical effects of spatial correlations.

$$C_{\mathbf{u}} = 1 \tag{7.39}$$

$$\gamma_{\mathbf{k}} = \sum_{u_x=0}^{N-1}\sum_{u_y=0}^{N-1}\sum_{u_z=0}^{N-1} \cos\left[2\pi\left(\frac{n_x u_x}{N_x} + \frac{n_y u_y}{N_y} + \frac{n_z u_z}{N_z}\right)\right] = \begin{cases} N & \text{if } \mathbf{k} = \mathbf{0} \\ 0 & \text{else} \end{cases} \tag{7.40}$$

$$\langle m_z(t)\rangle = S - \langle n(\omega)\rangle\left(1 - \frac{1}{N}e^{-Nt} - \frac{N-1}{N}\right) \tag{7.41}$$

$$\lim_{N\to\infty}\langle m_z(t)\rangle = S \tag{7.42}$$

In this extreme limit, the magnetisation does not decay to the equilibrium state anymore. Note that for finite N there is a fraction of $\frac{1}{N}$ that decays very fast, which is due to one fast-relaxing (or super-radiant) state in the single-excitation subspace (cf. section 2.2.3).

Furthermore the Holstein-Primakoff condition $S \gg a_r^\dagger a_r$ means that the system is close to the 'ground state'. For states which have many excitations (and do not fulfil this condition) the fraction of fast-relaxing states would be higher (cf. section 2.2.3).

Lorentzian spatial decay of noise correlations

We now assume spatial correlations of Lorentzian shape (i.e. Cauchy-Lorentz distribution). For a one-dimensional ferromagnet the magnetisation can be calculated analytically:

$$C_u = \frac{1}{\frac{|u|^2}{\xi^2} + 1} \tag{7.43}$$

$$\gamma_k = \pi\xi e^{-\xi|k|d} \tag{7.44}$$

$$\langle m_z(t)\rangle = S - \langle n(\omega)\rangle\left[1 - \frac{\mathrm{Ei}(-\pi\xi\mathrm{t}) - \mathrm{Ei}(-\mathrm{e}^{-\pi\xi}\pi\xi\mathrm{t})}{\pi\xi}\right] \tag{7.45}$$

where $\mathrm{Ei}(x)$ is the exponential integral function. Note that these results are obtained via Fourier transform and integration. This is only valid for not too short ξ (or else the decay is too steep to change the discrete sum to an integral) and not too long ξ (or else the correlations do not decay to zero over the length of the ferromagnet and the Fourier transform from $-\infty$ to ∞ does not agree with a finite ferromagnet). Numerical comparisons with $N = 1000$ show that for $3d < \xi < L/10$ discrete

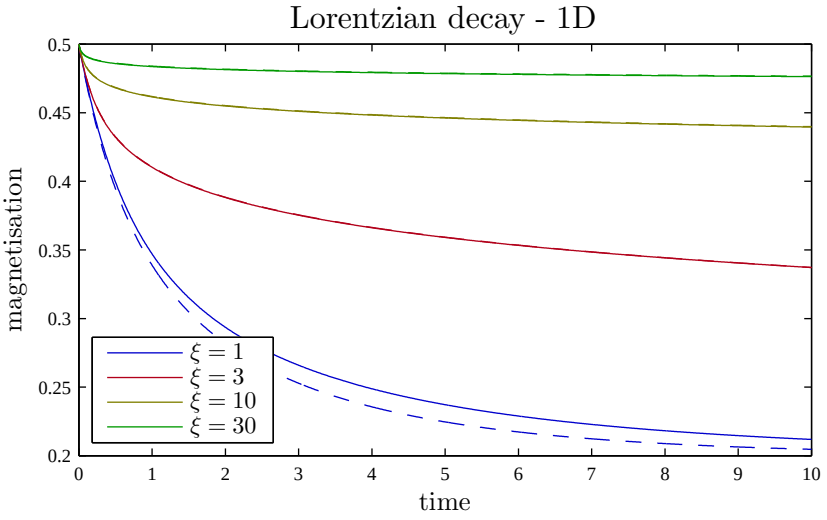

Figure 7.3: Magnetisation as a function of time for Lorentzian spatial decay of the noise correlations in a 1D ferromagnet. Four different correlation lengths ξ are shown for both continuous calculation (solid), eqs. 7.21 / 7.32, and discrete calculation (dashed), eqs. 7.20 / 7.31. We see a slight difference only for $\xi = 1$.

and continuous calculations agree very well. Figure 7.3 shows the decay of the magnetisation with time for several correlation lengths.

For a three-dimensional ferromagnet the magnon decay rate can be calculated with a three-dimensional Fourier transform for radial functions in spherical coordinates (also called a 3D Hankel transform or 3D Fourier-Bessel transform) [160,161]. For the calculation of the magnetisation however we need to resort to numerical integration.

$$C_{\mathbf{u}} = \frac{1}{\frac{|\mathbf{u}|^2}{\xi^2} + 1} \tag{7.46}$$

$$\gamma_{\mathbf{k}} = 4\pi \int_0^\infty \frac{\sin(kr)}{kr} \frac{1}{r^2/\xi^2 + 1} r^2 dr \tag{7.47}$$

$$= 2\pi^2 \xi^2 \frac{e^{-\xi|k|}}{|k|} \tag{7.48}$$

$$\langle m_z(t)\rangle = S - \langle n(\omega)\rangle \left[1 - \frac{d^3}{(2\pi)^3} \int_{-\pi/d}^{\pi/d} d\mathbf{k} \exp\left(-\frac{e^{-\xi\sqrt{k_x^2+k_y^2+k_z^2}}}{\sqrt{k_x^2+k_y^2+k_z^2}} 2\pi^2\xi^2 t\right)\right] \tag{7.49}$$

Figure 7.6 shows the numerical results for the 3D case for several correlation lengths.

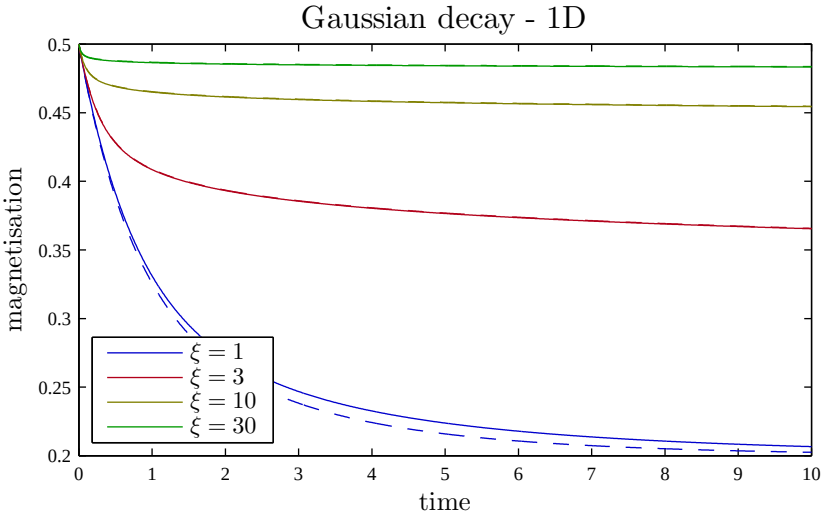

Figure 7.4: Magnetisation as a function of time for Gaussian spatial decay of the noise correlations and five correlation lengths. The solid lines are calculated via Fourier transform and numerical integration, the dashed lines via discrete summation. Again we find only a slight difference for $\xi = 1$.

Gaussian spatial decay of noise correlations

For Gaussian spatial decay of noise correlations we find qualitatively similar results. In a one-dimensional ferromagnetic chain the magnon decay rate is calculated easily:

$$C_u = \exp(-u^2/\xi^2) \tag{7.50}$$

$$\gamma_k = \sqrt{\pi}\xi \exp(-\xi^2 k^2/4) \tag{7.51}$$

The corresponding magnetisation is then calculated numerically and is displayed in figure 7.4.

For a three-dimensional ferromagnet we find the rate very similarly:

$$C_{\mathbf{u}} = \exp(-|\mathbf{u}|^2/\xi^2) \tag{7.52}$$

$$\gamma_{\mathbf{k}} = \pi^{3/2}\xi^3 \exp\left(-\frac{k_x^2 + k_y^2 + k_z^2}{4}\xi^2\right) \tag{7.53}$$

$$\langle m_z(t)\rangle = S - \langle n(\omega)\rangle \left\{1 - \frac{d^3}{(2\pi)^3}\int_{-\pi/d}^{\pi/d} d\mathbf{k} \exp\left[-t\pi^{3/2}\xi^3 \exp\left(-\frac{k_x^2 + k_y^2 + k_z^2}{4}\xi^2\right)\right]\right\} \tag{7.54}$$

Again the calculation of the magnetisation is only carried out numerically. Results can be found in figure 7.6.

Exponential spatial decay

For exponential spatial decay of the noise correlations we also find qualitatively similar results. The magnon decay rate in a one-dimensional ferromagnet is a Lorentzian in k-space. However we need to be aware that continuous and discrete calculations do not agree as well here because the Lorentzian decay in k-space is the slowest decay compared to the other cases. Therefore the differences between the discrete and continuous calculation of γ_k, which are typically the strongest for large k-values have a greater effect because γ_k does not decay to zero as quickly for large k values as in the other cases. The differences are strongest for large k values because the summands in eq. 7.20 are less smooth as a function of spatial distance $\mathbf{u}$ for large k values. Small differences are enhanced in the calculation of the magnetisation by the exponential in eq. 7.31.

In one dimension we find:

$$C_u = \exp(-|u|/\xi) \tag{7.55}$$

$$\gamma_k = \frac{2\xi}{1+k^2\xi^2} \tag{7.56}$$

$$\gamma_k = \sqrt{\pi}\xi \exp(-\xi^2 k^2/4) \tag{7.57}$$

The corresponding magnetisation can be found in figure 7.5.

For a three-dimensional ferromagnet we need to employ the three-dimensional Fourier transform in spherical coordinates again:

$$\gamma_{\mathbf{k}} = 4\pi \int_0^\infty \frac{\sin(kr)}{kr} \exp\left(\frac{r}{\xi}\right) r^2 dr \tag{7.58}$$

$$= \frac{8\pi\xi^3}{(k^2\xi^2+1)^2} \tag{7.59}$$

$$\langle m_z(t)\rangle = S - \langle n(\omega)\rangle \left\{ 1 - \frac{d^3}{(2\pi)^3} \int_{-\pi/d}^{\pi/d} d\mathbf{k} \exp\left[-t \frac{8\pi\xi^3}{(k_x^2\xi^2 + k_y^2\xi^2 + k_z^2\xi^2 + 1)^2} \right] \right\}$$

The magnetisation is calculated numerically and displayed in figure 7.6

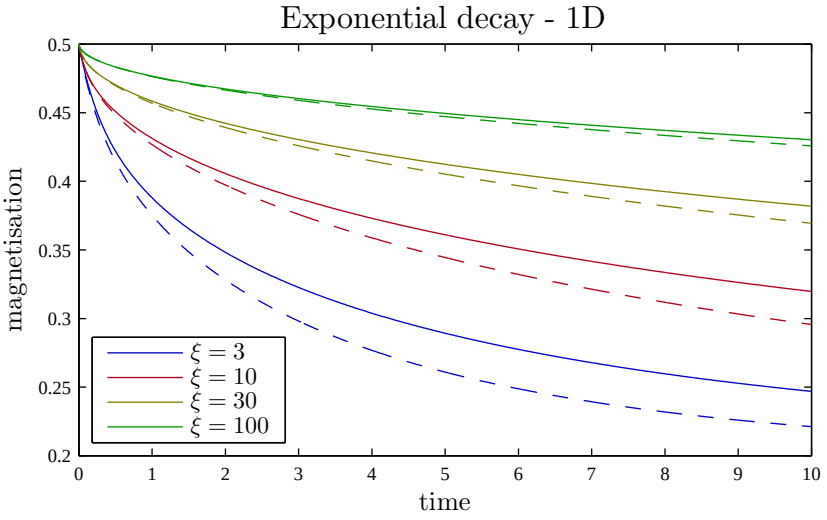

Figure 7.5: Magnetisation as a function of time for exponential spatial decay of the correlations and four correlation lengths. The solid lines are calculated via Fourier transform and numerical integration, the dashed lines via discrete summation. The two methods agree only roughly because of the slow decay of γ_k in k-space.

7.4 Chapter summary

We have investigated phonon-noise effects on the dynamics of a quantum ferromagnet by using master equation techniques on a Heisenberg model. We were able to derive analytical solutions by employing a Holstein-Primakoff transformation with a linear spin-wave approximation. This is valid for states of the ferromagnet with a low number of magnons.

Independent of the functional form we found that spatial correlations in the noise generally slow down the time-decay of the magnetisation to its equilibrium value, i.e. prolong the out-of-equilibrium time. The spatial correlations furthermore change the shape of the magnetisation decay from purely exponential to a slower non-exponential shape. For three-dimensional crystals a correlation length of just a few crystal sites slows down the time-decay considerably while in one-dimensional crystals the effect is not as immediate.

This effect of spatial noise correlations on the dynamics of ferromagnetic behaviour can be attributed to the same microscopic origins as the increased transfer efficiency found in chapter 5, namely the emergence of decoherence-reduced states with increasing noise correlation length as generally discussed in section 2.2. The relaxation-reduced states are of the form $(|n\rangle - |m\rangle)/\sqrt{2}$ where $|n\rangle$ refers to the state with the

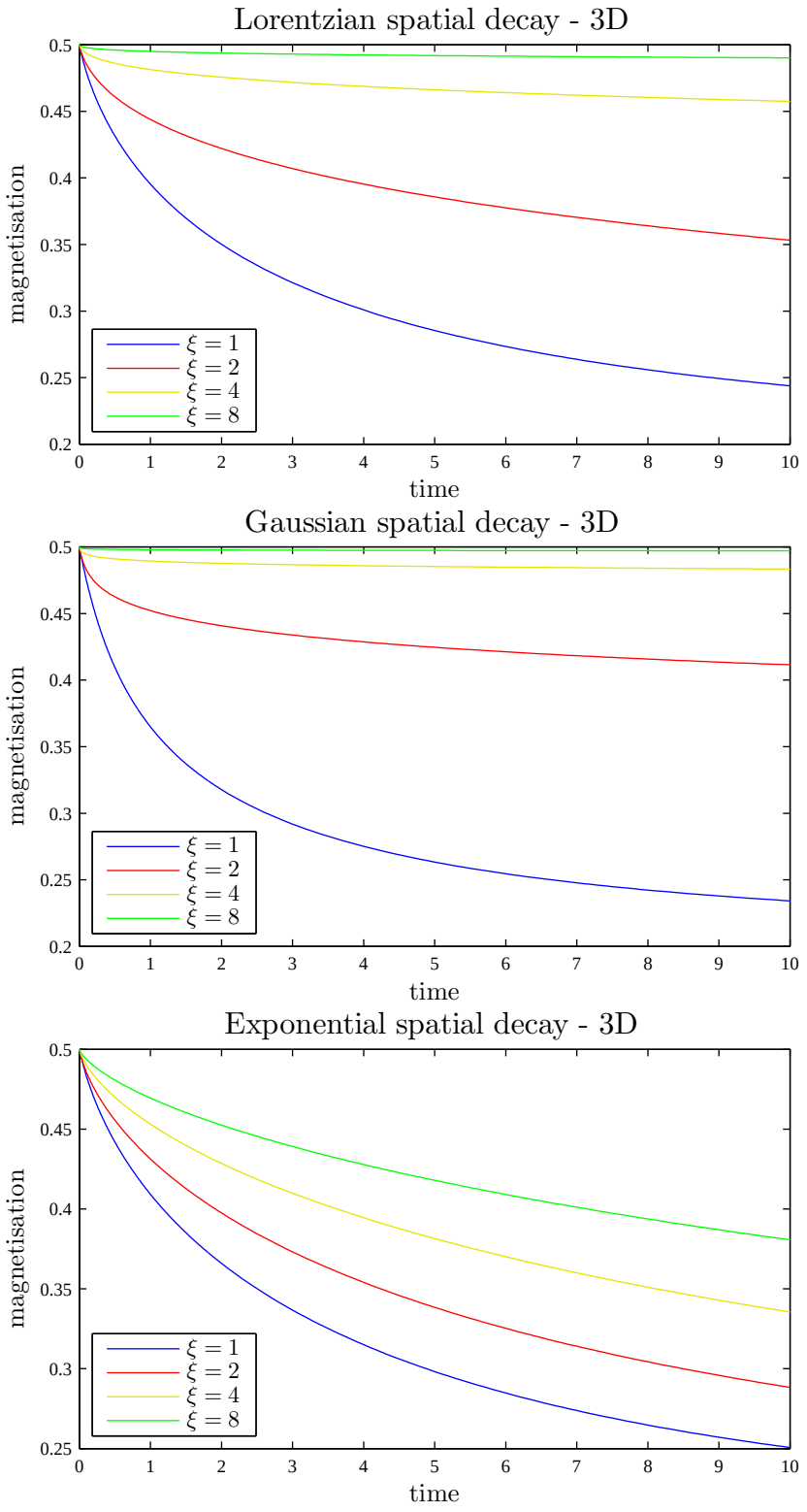

Figure 7.6: Magnetisation of a 3D ferromagnet as a function of time for Lorentzian, Gaussian and exponential spatial decay of the noise correlations and four different correlation lengths respectively. The effects are qualitatively the same but slightly less strong for exponential shape, which decays faster than the Lorentzian and does not have the plateau around zero of a Gaussian.

nth spin in the 'up state' (or second lowest state for $S > 1/2$) and all other spins in their 'down state'. In the limit of perfect correlations the emerging decoherence-free subspace equates (for large N) the single-excitation subspace. In this limit the phenomenon is also analogous to the effect of sub-radiance [7] in a radiating gas.

The analogy to quantum transport is most apparent for fully correlated decoherence, where the magnetisation does not decay anymore except for a fraction of $1/N$, which decays N times faster. This is analogous to the emergence of two different time scales in quantum transport for relaxation-reduced and relaxation-enhanced states. This also hints at the behaviour of the ferromagnet outside the spin-wave regime, i.e. for states with a high number of magnons: The fraction of the magnetisation that decays faster will probably be higher and the two time scales would become visible for the macroscopic magnetisation.

Chapter 8
8 Conclusions

We investigated the effects of spatial correlations in the environmental noise of quantum systems by comparing the effects of uncorrelated and fully correlated noise. More importantly we employed a formalism that allows us to model any spatial correlation of the environment. Particularly we focused on the intuitive situation of correlation functions which decay with increasing distance, which was supported by microscopic model calculations of the environment and proved to be a physically valid model for Markovian noise by general mathematical considerations.

We employed the comprehensive Bloch-Redfield formalism, which allows us to model both the noise spectra as well as the spatial correlations generally but efficiently via the spectral functions, which contain all environmental properties. With these spectral functions the Bloch-Redfield equations can be written down immediately for systems of any type and size. For the examples of an environment of coupled harmonic oscillators and an Ising model environment we have shown how to derive these spectral functions analytically. The Ising model shows that in a solid state environment the spatial extent of correlations is determined by the coupling strengths between environmental sites and is weakened by thermal effects for higher temperatures. The environment of coupled harmonic oscillators showed oscillating spatial correlations which have qualitatively different features because points with anticorrelated noise exist, which is of relevance to quantum metrology. We furthermore saw that the frequency of a noise mode is broadened by the respective coupling strength of that mode.

When the spectral function is chosen phenomenologically based on the desired environmental properties we have provided a mapping to the Lindblad form of a master

equation, which provides a test of physicality for Markovian spectral functions. The resulting non-local Lindblad operators show the capabilites and uniqueness of our equations since there is no intuition to find these operators from an ad-hoc Lindblad approach.

For the majority of controlled quantum systems, a secular approximation of the Bloch-Redfield equations can be made based on large on-site energies relative to the noise strength. This reduces the noise influences to longitudinal and transversal system-bath couplings, which induce dephasing and relaxation respectively. In terms of systems of spins the effects of spatial correlations can be discussed very generally. For uncorrelated dephasing it is well known that the dephasing rate between two states is proportional to the number of flipped spins between the two states. With increasing noise correlation length this configuration transitions to a dependence of the dephasing strength which is $\propto n_e^2$, where n_e is the difference in number of excitations between the two states. This can lead to a large increase of dephasing for pairs of states with large n_e but also leads to the emergence of dephasing-reduced subspaces of states with equal n_e. For relaxation we find similarly, that increasing correlations in the noise can both increase or decrease the transition rates between states. Pairs in the state $(|\uparrow\downarrow\rangle+|\downarrow\uparrow\rangle)/\sqrt{2}$ increase their transition rates up to a factor of two, whereas pairs in the state $(|\uparrow\downarrow\rangle - |\downarrow\uparrow\rangle)\sqrt{2}$ decrease their transition rates up to zero. For larger systems this can lead to complex dynamics, where the system evolves into intermediate relaxation-reduced states, and then slowly decays to the equilibrium. An important counter-intuitive effect is that the relaxation of a single spin can be reduced and even blocked when other uncoupled spins in their respective ground state are exposed to the same noise environment due to the emergence of a subspace of relaxation-reduced states.

For quantum metrology, high-precision measurements are typically carried out with trapped ions, which are subject to dephasing noise. This noise has been found to be strongly correlated. The dephasing-reduced subspace, which emerges from that can be utilised in the measurements of atomic electric quadrupole moments. For finite spatial noise correlations the order in which ions are placed within an ion trap becomes critically important to the dephasing rate. In order to reduce it it is necessary to minimize the distance between pairs in different states, making an alternating order of two types an optimised state. With this it is possible to beat the standard quantum limit and gain quantum advantage in the precision scaling with increasing number of measurements. This is in stark contrast to all metrology experiments which are exposed to uncorrelated decoherence, where quantum advantage has been

proven to be impossible. We have shown that even for partially correlated environments, it is possible to achieve the best possible quantum advantage, Heisenberg scaling, which reduces the experimental error as $1/n$ with the number of entangled ions n which is better by a factor of $1/\sqrt{n}$ than the standard quantum limit. Ordinary GHZ states however experience a stronger dephasing rate in the correlated environment of an ion trap. In an environment with oscillating spatial correlations however they can be arranged to be dephasing-reduced, i.e. also achieve Heisenberg scaling.

For quantum transport an increasing correlation length reinstates the transport dynamics. Particularly destructive effects of dephasing on the coherent transport dynamics of a single excitation vanish entirely with increasing noise correlation length. If relaxation is involved, two time scales arise: a fast decay into an intermediate entangled state, which decays on a longer time scale to the ground state. In the particular spin chain which we studied in detail the two end spins were entangled in this relaxation-reduced state. A critical noise correlation length scale exists in a transport process below which the transport dynamics is seriously affected. This critical correlation length linearly depends on the maximal spread or delocalisation of the excitation in the transport process. If the noise correlation length is longer than the critical length the coherent dynamics is hardly perturbed even for strong noise and the excitation is transported through the spin chain. This can again be linked to the dephasing reduced single-excitation subspace which is involved in the transport. However the phase coherence to the ground state is lost in a transport process with correlated noise even when the excitation is transported unperturbed. This is because the ground state has one excitation less than the dephasing-reduced subspace and changes a coherent perfect-state transfer into a classical bit transfer in the context of quantum information. This might be overcome with more sophisticated dynamical decoupling methods.

In photosynthetic light-harvesting complexes, where dephasing is the main noise source the effects of the previous paragraph apply similarly. Since the phase coherence to the ground state is irrelevant in this context and only the energy transfer matters, long noise correlations reinstate the coherent dynamics of the light-harvesting complex entirely. By weakening the perturbing influence of dephasing finite spatial correlations can be advantageous to the speed and efficiency of light-harvesting complexes. The noise correlations typically have an optimal correlation lengths beyond which the efficiency starts to decrease. The reason is that the purely coherent dynamics is actually not optimal for the transport and a certain level of dephas-

ing assists the transport process. We furthermore addressed the misconception in the formalism for modeling light-harvesting complexes, that Bloch-Redfield equations are not capable of modeling coherent oscillations or are a subset of Lindblad equations. In order to not lose the coherent dynamics in the modeling process one needs to apply the secular approximation by comparing the Redfield-tensor elements for each respective system individually, particularly because the noise is typically smaller than the exciton energy but of similar strength as the intersite coupling in light-harvesting complexes. Therefore only some level-splittings are large compared to the noise strength. If the secular approximation is applied consistently the Bloch-Redfield equations presented in this thesis are an excellent tool to model Markovian noise in light-harvesting systems.

The quantum ferromagnet is a solid-state system where macroscopic properties can be analytically calculated from a master equation approach, which takes the effects of phonon noise in the crystal into consideration. Using this as an example we showed the macroscopic influences of noise correlations on the non-equilibrium dynamics of the magnetisation. Longer correlation lengths prolong the out-of-equilibrium time of the magnetisation by slowing down the decay to equilibrium and changing the shape to a non-exponential decay. This is true in both the one-dimensional and three-dimensional case. The effect is stronger in the three-dimensional ferromagnet since there are more neighbouring correlated sites for the same correlation length.

Correlated noise perturbs the coherent dynamics in a very different manner than uncorrelated noise, which manifests in different ways in a variety of fields such as quantum compuatation, metrology, photosynthetic systems and solid-state physics. This thesis highlights the importance of modeling noise correlations, for which we provide a formalism. With growing system sizes of controlled quantum systems and continuing miniaturisation, noise correlations can be expected to be of increasing relevance.

Chapter 9
9 Appendix

A Spin-boson example

Here we replicate the spin-boson calculation in Zanardi [20] in our language of correlation functions. We find a close correspondence of our correlation function and Zanardi's given decoherence rates. This is one example, where the correlation function can be calculated from an explicit bath Hamiltonian instead of being just phenomenologically assumed.

Assume a bath Hamiltonian

$$H_B = \sum_k \omega_k b_k^\dagger b_k \qquad \text{with} \quad \forall\, k,k' : \quad [b_k, b_{k'}^\dagger] = \delta_{kk'} \\ \text{and} \quad \forall\, k,k' : \quad [b_k, b_{k'}] = [b_k^\dagger, b_{k'}^\dagger] = 0 \tag{9.1}$$

which defines b_k as a bosonic destruction operator. Assume an interaction Hamiltonian

$$H_{int} = \sum_i s_i B_i = \sum_{k\,j} g_{kj} b_k^\dagger A_j + g_{kj}^* b_k A_j^\dagger \tag{9.2}$$

where b_k is a bath operator,
A_j is a system operator with $[H_S, A_j] = -\epsilon A_j$ with $\epsilon \in \mathbb{R}_0^+$ and
g_{jk} is a coupling strength.

We assume that the index j in eq. 9.2 refers to different subsystems (e.g. qubits) in the system, the index k to bosonic modes in the environment. Notice that the commutator definition of A_j is one of a "destruction operator" if $\epsilon > 0$ (meaning

$A_j \rightarrow \epsilon\,\sigma_-$ for a qubit). For $\epsilon = 0$ on the other hand A_j commutes with H_S (meaning $A_j \rightarrow \sigma_z$ for a qubit in its eigenbasis). In other words ϵ defines longitudinal or transversal bath coupling. Going back to the notation of the first term in equation 9.2 the number of bath operators B_i is two times the number of subsystems. Instead of index i we label them:

$$B_{1j} = \sum_k g_{kj} b_k^\dagger \qquad\qquad B_2 j = g_{kj}^* b_k$$

Temporal part of the correlation function

As we want to calculate the correlation function in the interaction picture we first change the description to the interaction picture choosing the simple notation that all operators in the interaction picture are denoted as the Schrödinger picture operators with a tilde on top:

$$\begin{aligned}
\tilde{H}_{int} &= e^{-i(H_S+H_B)t} H_{int} e^{i(H_S+H_B)t} \\
&= \sum_i e^{-iH_S t} s_i e^{iH_S t}\; e^{-iH_B t} B_i e^{iH_B t} \\
&= \sum_i \tilde{s}_i(t) \tilde{B}_i(t)
\end{aligned}$$

This works because operators acting on the system and the environment (i.e. two different subspaces of the total Hilbert space) always commute. We can therefore transform our bath operators:

$$\begin{aligned}
\tilde{B}_{1j}(t) &= \exp\left(-i \sum_k \omega_k b_k^\dagger b_k t\right) \sum_{k'} g_{k'j} b_{k'}^\dagger \exp\left(i \sum_{k''} \omega_{k''} b_{k''}^\dagger b_{k''} t\right) \\
&= \prod_k \exp\left(-i\omega_k b_k^\dagger b_k t\right) \sum_{k'} g_{k'j} b_{k'}^\dagger \prod_{k''} \exp\left(i\omega_{k''} b_{k''}^\dagger b_{k''} t\right) \\
&= \sum_k \exp\left(-i\omega_k b_k^\dagger b_k t\right) g_{kj} b_k^\dagger \exp\left(i\omega_k b_k^\dagger b_k t\right) \qquad (9.3)
\end{aligned}$$

The last step is justified because any combination of creation and destruction operators for different modes commute (eq. 9.1). Next we use the series definition of the exponential function and the commutators (eq. 9.1) to manipulate the first part of

the expression:

$$\begin{aligned}\exp\left(-i\omega_k b_k^\dagger b_k t\right) g_{kj} b_k^\dagger &= \sum_n \frac{1}{n!}(-i\omega_k t)^n g_{kj}(b_k^\dagger b_k)^n b_k^\dagger \\ &= \sum_n \frac{1}{n!}(-i\omega_k t)^n g_{kj} b_k^\dagger (b_k b_k^\dagger)^n \\ &= g_{kj} b_k^\dagger \exp\left(-i\omega_k b_k b_k^\dagger t\right) \\ &= g_{kj} b_k^\dagger \exp\left(-i\omega_k (b_k^\dagger b_k + 1) t\right)\end{aligned}$$

Inserting this into eq. 9.3 we find:

$$\tilde{B}_{1j}(t) = \sum_k g_{kj} b_k^\dagger e^{-i\omega_k t}$$

We calculate $\tilde{B}_{2j}(t)$ analogously but bring the second exponential to the front using

$$b(b^\dagger b)^n = (bb^\dagger)^n b$$

and find:

$$\tilde{B}_{2j}(t) = \sum_k g_{kj}^* b_k e^{i\omega_k t} = B_{1j}^\dagger$$

We have now found a simple expression for the time-dependent bath operators in the interaction picture. Now we can calculate the various correlation functions for the bath operators. We start with the correlation functions for the same types of bath operators:

$$\begin{aligned}\langle \tilde{B}_{1j}(t)\tilde{B}_{1j'}(t')\rangle &= \mathrm{Tr}\left(\tilde{B}_{1j}(t)\tilde{B}_{1j'}(t')\rho_B\right) \\ &= \mathrm{Tr}\left(\sum_{k\,k'} g_{kj} g_{k'j'} b_k^\dagger b_{k'}^\dagger e^{-i\omega_k t} e^{-i\omega_{k'} t'} \rho_B\right) \\ &= \sum_{k\,k'} g_{kj} g_{k'j'} e^{-i(\omega_k t + \omega_{k'} t')} \mathrm{Tr}(b_k^\dagger b_{k'}^\dagger \rho_B) \\ &= 0\end{aligned}$$

where ρ_B is the density matrix of the bath. The trace in the expression is zero. This becomes obvious when we write the density matrix in the occupation number representation of the environmental k-states $|m_j\rangle = |n_{k=k_1}\rangle \otimes |n_{k=k_2}\rangle \otimes \cdots =$

$|n_{k=k_1}, n_{k=k_2}, \dots\rangle$ and assume that the environment is not in a superposition but in one particular occupation number state for each element in the ensemble. In other words we assume that the different bosonic modes of the environment are not interacting with each other. Then we can write the density matrix of the environment as $\rho_B = \sum_j |n_j\rangle\langle n_j| p_j$. Now $b_k^\dagger b_{k'}^\dagger$ increase the occupation number of modes k and k' by one and therefore we are left with a matrix which contains only off-diagonal elements which are non-zero and we find:

$$\mathrm{Tr}\left(\sum_j b_k^\dagger b_{k'}^\dagger |n_j\rangle\langle n_j|\right) = \mathrm{Tr}\left(\sum_j |\dots, n_k+1, \dots, n_{k'}+1, \dots\rangle\langle \dots, n_k, \dots, n_{k'}, \dots|\right) \tag{9.4}$$

$$= 0 \tag{9.5}$$

Analogously one finds:

$$\langle \tilde{B}_{2j}(t)\tilde{B}_{2j'}(t')\rangle = 0$$

Calculating a correlation function of different types of bath operators on the other hand, i.e. correlation functions which contain creation and destruction operators, we find

$$\begin{aligned}\langle \tilde{B}_{1j}(t)\tilde{B}_{2j'}(t')\rangle &= \mathrm{Tr}\left(\tilde{B}_{1j}(t)\tilde{B}_{2j'}(t')\rho_B\right) \\ &= \sum_{k\,k'} g_{kj} g_{k'j'}^* e^{i(\omega_{k'}t' - \omega_k t)} \mathrm{Tr}\left(b_k^\dagger b_{k'}\rho_B\right) \\ &= \sum_k g_{kj} g_{kj'}^* e^{-i\omega_k(t-t')}\langle n_k\rangle \end{aligned} \tag{9.6}$$

because $\mathrm{Tr}\left(b_k^\dagger b_{k'}\rho_B\right) = \delta_{kk'}\langle n_k\rangle$. As we have chosen independent bosons for the environment the mean occupation number should be chosen as the Bose-Einstein-distribution

$$\langle n_k\rangle = \left(e^{\frac{\hbar\omega}{kT}} - 1\right)^{-1}$$

The Fourier transform of that correlation function $C(\omega) := \frac{1}{2\pi}\int_{-\infty}^{\infty} e^{i\omega\tau}\langle \tilde{B}_{1j}\tilde{B}_{2j'}\rangle d\tau$ (i.e. the spectral function which is used in the B-R equations) is then given by

$$C(\omega) = \sum_k \delta(\omega - \omega_k) g_{kj} g_{kj'}^* \langle n_k(\omega)\rangle$$

because transforming this function back gives the correlation function:

$$\int e^{-i\omega\tau} C(\omega) d\omega = \sum_k g_{kj} g^*_{kj'} e^{-i\omega_k \tau} \langle n_k \rangle = \langle \tilde{B}_{1j}(t) \tilde{B}_{2j'}(t') \rangle$$

where $\tau := t - t'$

Analogously we find:

$$\begin{aligned} \langle \tilde{B}_{2j}(t) \tilde{B}_{1j'}(t') \rangle &= \sum_{k\,k'} g^*_{kj} g_{k'j'} e^{i(\omega_k t - \omega_{k'} t')} \mathrm{Tr}\left(b_k b^\dagger_{k'} \rho_B \right) \\ &= \sum_k g^*_{kj} g_{kj'} e^{i\omega_k \tau} \left(1 + \langle n_k \rangle\right) \end{aligned} \tag{9.7}$$

because: $\mathrm{Tr}\left(b_k b^\dagger_{k'} \rho_B \right) = \delta_{kk'} \mathrm{Tr}\left((1 + b^\dagger_{k'} b_k) \rho_B \right) = \delta_{kk'} \left(1 + \langle n_k \rangle\right)$

With that we have found all correlation functions and we could set up the Bloch-Redfield equations. Notice the correspondence between the two non-zero correlation functions eq. 9.6 and 9.7 on the one side and the decoherence rates directly calculated by Zanardi in equation 7 of reference [20].

Spatial part of the correlation function

So far we have only spoken about the temporal part of the correlation function. At the moment the only spatial dependence is hidden in the pairs of coupling strengths $g_{kj} g_{kj'}$ of the jth and j'th subsystem located at a certain position $\mathbf{r}_j$ and $\mathbf{r}_{j'}$. Instead of defining each coupling strength individually we can apply our continuous concept of a spatial correlation function $G(\omega, |\mathbf{r}_j - \mathbf{r}_{j'}|)$. This adds complexity to the model as we can now define a spatial correlation which depends on the distance instead of the basic model in which only the local coupling strength of the particular subsystem can be set. We extend our model accordingly and replace:

$$\begin{matrix} g^*_{kj} g_{kj} \\ g_{kj} g^*_{kj} \end{matrix} \longrightarrow G(\omega, 0) \qquad\qquad \begin{matrix} g^*_{kj} g_{kj'} \\ g_{kj} g^*_{kj'} \end{matrix} \longrightarrow G(\omega, |\mathbf{r}_j - \mathbf{r}_{j'}|)$$

Now any spatial correlation function can be chosen and the Bloch-Redfield equations can be derived from that in the usual manner.

B General coupling operator between two arbitrary two-level systems

In this section we discuss how a completely general coupling between two TLS can be rewritten as just longitudinal and transversal coupling if the coupling strength is small compared to the level splitting. Without loss of generality (w.l.o.g.) we assume the uncoupled Hamiltonian to be:

$$H_0 = \omega_q \sigma_z^1 + (\omega_q + \delta)\sigma_z^2$$

In terms of spin-1/2 this means we assume individual coordinate systems for each spin with the z-direction along the local magnetic field direction[1]. Since the operator set $\{\sigma_x, \sigma_y, \sigma_z, \mathbb{1}\}$ is a complete basis of the operator space for a two-level system, a completely general coupling between two TLS can be written as tensor products of all combinations of these operators, excluding the unity matrix since it does not define an actual coupling. The Hamiltonian reads

$$\begin{aligned} H = H_0 + H_c = H_0 &+ v_{xx}\sigma_x \otimes \sigma_x + v_{xy}\sigma_x \otimes \sigma_y + v_{xz}\sigma_x \otimes \sigma_z \\ &+ v_{yx}\sigma_y \otimes \sigma_x + v_{yy}\sigma_y \otimes \sigma_y + v_{yz}\sigma_y \otimes \sigma_z \\ &+ v_{zx}\sigma_z \otimes \sigma_x + v_{zy}\sigma_z \otimes \sigma_y + v_{zz}\sigma_z \otimes \sigma_z \end{aligned}$$

where v_{jk} are coupling strengths $\forall j, k = x, y, z$. Changing to an interaction picture $|\Psi_{int}\rangle = \exp(-iH_0 t)\,|\Psi\rangle$ the Hamiltonian becomes[2]:

$$H_{int} = \exp(iH_0 t) H_c \exp(-iH_0 t)$$

[1] This simplification means we can no longer w.l.o.g. assume a simple coupling of the form $v_{xx}\sigma_x^1\sigma_x^2 + v_{yy}\sigma_y^1\sigma_y^2 + v_{zz}\sigma_z^1\sigma_z^2$ since the two coordinate systems are not parallel.

[2] This is not to be confused with the interaction picture in the derivation of the Bloch-Redfield equations. Here, a closed system without environment is discussed.

Using the tensor product basis $|\uparrow\uparrow\rangle, |\uparrow\downarrow\rangle, |\downarrow\uparrow\rangle, |\downarrow\downarrow\rangle$ this Hamiltonian can be evaluated to the matrix:

$$H_{int} = \begin{pmatrix} v_{zz} & e^{i2(\omega_q+\delta)t}(v_{zx} - iv_{zy}) \\ e^{-i2(\omega_q+\delta)t}(v_{zx} + iv_{zy}) & -v_{zz} \\ e^{-i2\omega_q t}(v_{xz} + iv_{yz}) & e^{i2\delta t}(v_{xx} - iv_{xy} + iv_{yx} + v_{yy}) \\ e^{-i2(2\omega_q+\delta)t}(v_{xx} + i(v_{xy} + v_{yx} + iv_{yy})) & \end{pmatrix}$$

$$\begin{pmatrix} e^{i2\omega_q t}(v_{xz} - iv_{yz}) & e^{i2(2\omega_q+\delta)t}(v_{xx} - i(v_{xy} + v_{yx} - iv_{yy})) \\ e^{-i2\delta t}(v_{xx} + iv_{xy} - iv_{yx} + v_{yy}) & -e^{i2\omega_q t}(v_{xz} - iv_{yz}) \\ -v_{zz} & -e^{i2(\omega_q+\delta)t}(v_{zx} - iv_{zy}) \\ -e^{-i2(\omega_q+\delta)t}(v_{zx} + iv_{zy}) & v_{zz} \end{pmatrix}$$

The assumption $\omega_q \gg \delta, v_{jk}(\forall j,k = x,y,z)$ allows us to make the secular approximation i.e. neglect all terms with a fast oscillating factor $\exp(\pm i2\omega_q t)$ since their influence in the differential equation of the system averages to zero on the time scales of the system (section 2.1.3). In the interaction picture the similarity to the rotating wave approximation is very clear. With the secular approximation and the definitions $v_{\perp real} := v_{xx} + v_{yy}$ and $v_{\perp imag} := v_{xy} - v_{yx}$ the Hamiltonian becomes:

$$H_{int} = \begin{pmatrix} v_{zz} & 0 & 0 & 0 \\ 0 & -v_{zz} & e^{-i2\delta t}(v_{\perp real} + iv_{\perp imag}) & 0 \\ 0 & e^{i2\delta t}(v_{\perp real} - iv_{\perp imag}) & -v_{zz} & 0 \\ 0 & 0 & 0 & v_{zz} \end{pmatrix} \tag{9.8}$$

This matrix is equivalent to the interaction-picture Hamiltonian of only longitudinal and transversal coupling, i.e. a Schrödinger-picture Hamiltonian of the form

$$H_c = v_\perp \sigma_+^1 \sigma_-^2 + v_\perp^* \sigma_-^1 \sigma_+^2 + v_\parallel \sigma_z^1 \sigma_z^2 \tag{9.9}$$

will lead to the exact same matrix (eq. 9.8) when transformed to the interaction picture with the identification $v_\perp = v_{\perp real} + iv_{\perp imag}$. For symmetry reasons the imaginary part of the transversal coupling strength will often be zero $v_{\perp imag} = v_{xy} - v_{yx} = 0$. In that case the Hamiltonian can also be written in this form:

$$H_c = v_\perp \frac{1}{2}(\sigma_x^1 \sigma_x^2 + \sigma_y^1 \sigma_y^2) + v_\parallel \sigma_z^1 \sigma_z^2 \tag{9.10}$$

To model a general coupling, these simple forms (eq. 9.9 and 9.10) can therefore be used. For systems of several TLSs the same argument applies in the subspace of each pair of TLSs.

C Separate baths for transversal and longitudinal bath couplings of TLSs

In this section it is shown that for systems of TLSs all decoherence effects due to correlations between a transversal and a longitudinal bath coupling operator can be neglected if the level splitting is large compared to all coupling strengths. This statement is true for the case of two coupling operators of the same TLS as well as the case of two coupling operators acting on different TLSs.

Operators acting on the same TLS

The Bloch-Redfield equations in column-ordered superoperator form (eq. 2.32) for a single TLS with the two system operators coupling to the bath

$$s_1 = v_\perp \sigma_x; \qquad s_2 = v_\parallel \sigma_z$$

where $v_\perp, v_\parallel$ are coupling strengths, read in the eigenbasis $|\uparrow\rangle, |\downarrow\rangle$ of the Hamiltonian $H = (\omega_q/2)\sigma_z$:

$$\dot{\vec{\rho}} = \mathfrak{R}\vec{\rho} \tag{9.11}$$

with:

$$\mathfrak{R} = \begin{pmatrix} -v_\perp^2 C_{1,1}(-\omega_q) & v_\parallel v_\perp C_{1,2}(0) & v_\parallel v_\perp C_{1,2}(0) & v_\perp^2 C_{1,1}(\omega_q) \\ v_\parallel v_\perp C_{2,1}(-\omega_q) & i\omega_q - \frac{1}{2}v_\perp^2 C_{1,1}(-\omega_q) - \frac{1}{2}v_\perp^2 C_{1,1}(\omega_q) - 2v_\parallel^2 C_{2,2}(0) & \frac{1}{2}v_\perp^2 C_{1,1}(-\omega_q) + \frac{1}{2}v_\perp^2 C_{1,1}(\omega_q) & -v_\parallel v_\perp C_{2,1}(\omega_q) \\ v_\parallel v_\perp C_{2,1}(-\omega_q) & -i\omega_q - \frac{1}{2}v_\perp^2 C_{1,1}(-\omega_q) - \frac{1}{2}v_\perp^2 C_{1,1}(\omega_q) - 2v_\parallel^2 C_{2,2}(0) & -v_\parallel v_\perp C_{2,1}(\omega_q) & -v_\parallel v_\perp C_{2,1}(\omega_q) \\ v_\perp^2 C_{1,1}(-\omega_q) & -v_\parallel v_\perp C_{1,2}(0) & -v_\parallel v_\perp C_{1,2}(0) & -v_\perp^2 C_{1,1}(\omega_q) \end{pmatrix}$$

With the assumption of large level splitting compared to the bath coupling $\omega_q \gg v_\perp, v_\parallel$ the secular approximation can be applied (section 2.1.3), i.e. off-diagonal elements of $\mathfrak{R}$ can be set to zero if their corresponding diagonal elements have a difference of the order ω_q or larger. The resulting Redfield tensor no longer contains

any terms which arose from mixed correlations of B_1 and B_2:

$$\mathfrak{R} = \begin{pmatrix} -v_\perp^2 C_{1,1}(-\omega_q) & 0 & 0 & v_\perp^2 C_{1,1}(\omega_q) \\ 0 & \frac{1}{2}\left(2i\omega_q - v_\perp^2 C_{1,1}(-\omega_q) - v_\perp^2 C_{1,1}(\omega_q) - 4v_\parallel^2 C_{2,2}(0)\right) & 0 & 0 \\ 0 & 0 & \frac{1}{2}\left(-2i\omega_q - v_\perp^2 C_{1,1}(-\omega_q) - v_\perp^2 C_{1,1}(\omega_q) - 4v_\parallel^2 C_{2,2}(0)\right) & 0 \\ v_\perp^2 C_{1,1}(-\omega_q) & 0 & 0 & -v_\perp^2 C_{1,1}(\omega_q) \end{pmatrix}$$

For systems comprised of more than one TLS the same argument applies in the respective subspace of each TLS and correlations between transversal and longitudinal bath couplings of the same TLS can in general be neglected in the secular approximation.

Operators acting on different TLS

Consider two TLSs

$$H_0 = \frac{\omega_q}{2}\sigma_z^1 + \frac{\omega_q + \delta}{2}\sigma_z^2$$

with the general coupling term (eq. 9.10)

$$H_c = \frac{g_\perp}{2}(\sigma_x^1\sigma_x^2 + \sigma_y^1\sigma_y^2) + g_\parallel \sigma_z^1\sigma_z^2$$

We use the tensor product basis, i.e. the four states $|\uparrow\uparrow\rangle, |\uparrow\downarrow\rangle, |\downarrow\uparrow\rangle, |\downarrow\downarrow\rangle$. The Bloch-Redfield equations in column-ordered superoperator form(eq. 2.32) with the two system operators which couple to the bath

$$s_1 = v_\perp \sigma_z^1; \qquad s_2 = v_\parallel \sigma_x^2$$

result in a 16x16 superoperator matrix $\mathfrak{R}$. Assuming a large level splitting $\omega_q \gg g_\perp, g_\parallel, v_\perp, v_\parallel, \delta$ the secular approximation can be applied, i.e. off-diagonal elements in $\mathfrak{R}$ can be neglected when the difference of the corresponding diagonal elements are of the order of ω_q or larger. The contribution of H_0 determines these differences of the diagonal elements because ω_q only appears in this contribution. The contribution of

H_0 is given by the diagonal matrix:

$$i \operatorname{diag}(0, \delta + \omega_q, \omega_q, \delta + 2\omega_q, -\delta - \omega_q, 0, -\delta, \omega_q, -\omega_q, \delta, 0, \delta + \omega_q, -\delta - 2\omega_q, -\omega_q, -\delta - \omega_q, 0)$$

With the secular approximation all terms due to mixed correlations of B_1 and B_2 vanish from the Redfield tensor $\mathfrak{R}$. For several TLSs the argument is valid in the subspace of each pair of TLSs.

The calculation was performed in Mathematica. The mixed correlation terms were identified with the Mathematica function 'Coefficient[$v_\perp v_\parallel$]'.

In conclusion, correlations between transversal and longitudinal coupling operators can be neglected for systems of TLSs in the secular approximation based on large level splittings compared to all coupling strengths. Formally this is equivalent to two independent baths for all transversal coupling operators and all longitudinal coupling operators respectively.

D Spatially correlated dephasing rates in qubit systems

In this appendix we calculate the effects of spatially correlated dephasing in qubit systems and compare it to uncorrelated dephasing. In particular we give the detailed derivation of the general result, stated in section 2.2.2, that in fully correlated environments the dephasing rate between two states is proportional to n_e^2, where n_e is the difference in the number of excitations between the two states, while for uncorrelated environments the dephasing rate is proportional to the number n_f of flipped spins between the two states. For this derivation we take only the dephasing part of eq. 2.54 and rewrite it slightly:

$$\dot{\rho} = \frac{i}{\hbar}[\rho, H_s] + \frac{1}{2\hbar^2}\sum_{j,k} C(0, \mathbf{r}_j, \mathbf{r}_k)\left(\sigma_z^{(j)}\rho\sigma_z^{(k)} + \sigma_z^{(k)}\rho\sigma_z^{(j)} - \sigma_z^{(j)}\sigma_z^{(k)}\rho - \rho\sigma_z^{(j)}\sigma_z^{(k)}\right) \tag{9.12}$$

We use the Fock states of the qubit's eigenbasis $\{|\uparrow\rangle, |\downarrow\rangle\}$, and write use the short notation $|\uparrow\downarrow\downarrow\rangle = |\uparrow\rangle \otimes |\downarrow\rangle \otimes |\downarrow\rangle$. The $\sigma_z^{(j)}$ operators doesn't change the state:

$$\sigma_z |\uparrow\rangle = |\uparrow\rangle; \qquad \langle\uparrow| \sigma_z = \langle\uparrow| \tag{9.13}$$

$$\sigma_z |\downarrow\rangle = -|\downarrow\rangle; \qquad \langle\downarrow| \sigma_z = -\langle\downarrow| \tag{9.14}$$

and we can regard eq. 9.12 for each element of the density matrix separately. Since dephasing affects only the off-diagonal elements, the *coherences*, we only regard them. By calculating their time-derivative we immediately find the dephasing rate between the two corresponding states.

Self-contributions The self-contributions ($j = k$) for a particular qubit j in eq. 9.12 are:

$$\sigma_z^{(j)}\rho\sigma_z^{(j)} + \sigma_z^{(j)}\rho\sigma_z^{(j)} - \sigma_z^{(j)}\sigma_z^{(j)}\rho - \rho\sigma_z^{(j)}\sigma_z^{(j)} \tag{9.15}$$

$$= 2\sigma_z^{(j)}\rho\sigma_z^{(j)} - 2\rho \tag{9.16}$$

For coherences where the jth qubit is in the same state $|\ldots\uparrow\ldots\rangle\langle\ldots\uparrow\ldots|$ the contributions are zero:

$$2\sigma_z\,|\ldots\uparrow\ldots\rangle\langle\ldots\uparrow\ldots|\,\sigma_z - 2\,|\ldots\uparrow\ldots\rangle\langle\ldots\uparrow\ldots| = 0 \tag{9.17}$$

$$2\sigma_z\,|\ldots\downarrow\ldots\rangle\langle\ldots\downarrow\ldots|\,\sigma_z - 2\,|\ldots\downarrow\ldots\rangle\langle\ldots\downarrow\ldots| = 0 \tag{9.18}$$

For coherences where the jth qubit is flipped the contribution is:

$$2\sigma_z\,|\ldots\uparrow\ldots\rangle\langle\ldots\downarrow\ldots|\,\sigma_z - 2\,|\ldots\uparrow\ldots\rangle\langle\ldots\downarrow\ldots| = -4\,|\ldots\uparrow\ldots\rangle\langle\ldots\downarrow\ldots|$$

$$2\sigma_z\,|\ldots\downarrow\ldots\rangle\langle\ldots\uparrow\ldots|\,\sigma_z - 2\,|\ldots\downarrow\ldots\rangle\langle\ldots\uparrow\ldots| = -4\,|\ldots\downarrow\ldots\rangle\langle\ldots\uparrow\ldots|$$

We summarise: For any off-diagonal density matrix element we find $\dot{\rho}_{\mathrm{el}} = f\rho_{\mathrm{el}}$. The factor f is a sum of many contributions. We find the

$$\text{self contributions of } \begin{cases} \text{spins that are the same} = 0 \\ \text{spins that are flipped} = -4 \end{cases} \tag{9.19}$$

Mixed contributions The mixed contributions for a particular pair $j \neq k$, where we choose w.l.o.g. $j = 1, k = 2$ in eq. 9.12 are:

$$\sigma_z^{(1)}\rho\sigma_z^{(2)} + \sigma_z^{(2)}\rho\sigma_z^{(1)} - \sigma_z^{(1)}\sigma_z^{(2)}\rho - \rho\sigma_z^{(1)}\sigma_z^{(2)} \tag{9.20}$$

Again we regard single elements of the density matrix but we now omit the 'dots' for the other qubits and write each element just in the subspace of the qubit pair.

We calculate the contributions to the factor f in all three cases:

$$\text{1) both spins are the same in both states} \begin{cases} |\downarrow\downarrow\rangle\langle\downarrow\downarrow| : 1+1-1-1=0 \\ |\uparrow\uparrow\rangle\langle\uparrow\uparrow| : 1+1-1-1=0 \\ |\downarrow\uparrow\rangle\langle\downarrow\uparrow| : -1-1+1+1=0 \\ |\uparrow\downarrow\rangle\langle\uparrow\downarrow| : -1-1+1+1=0 \end{cases}$$

$$\text{2) one is flipped, one is the same} \begin{cases} |\downarrow\downarrow\rangle\langle\downarrow\uparrow| : +1-1+1-1=0 \\ |\downarrow\uparrow\rangle\langle\downarrow\downarrow| : -1+1-1+1=0 \\ |\uparrow\downarrow\rangle\langle\uparrow\uparrow| : -1+1-1+1=0 \\ |\uparrow\uparrow\rangle\langle\uparrow\downarrow| : +1-1+1-1=0 \end{cases}$$

$$\text{3) both spins are flipped} \begin{cases} \text{equally} \begin{cases} |\downarrow\downarrow\rangle\langle\uparrow\uparrow| : -1-1-1-1=-4 \\ |\uparrow\uparrow\rangle\langle\downarrow\downarrow| : -1-1-1-1=-4 \end{cases} \\ \text{differently} \begin{cases} |\downarrow\uparrow\rangle\langle\uparrow\downarrow| : 1+1+1+1=4 \\ |\uparrow\downarrow\rangle\langle\downarrow\uparrow| : 1+1+1+1=4 \end{cases} \end{cases}$$

In case 2 it was assumed w.l.o.g. that it is the second spin which is flipped.

We find that the only mixed contributions come from pairs, which are both flipped. Having calculated all possible contributions we can now add them up and find the factor f.

For uncorrelated decoherence $\xi \to 0 \Leftrightarrow C(0, \mathbf{r}_j, \mathbf{r}_k) \to \delta_{jk}$ all mixed contributions are zero. The only contributions are self-contributions of spins, which are flipped. The uncorrelated dephasing rate between two states is therefore proportional to the number n_f of spins that are flipped between the states.

For perfectly correlated decoherence $\xi \to \infty$ the spatial correlation function is equal for all contributions $C(0, \mathbf{r}_j, \mathbf{r}_k) \to 1$. We name n_e the difference in the number of excitations of the two states which are linked by the off-diagonal element ρ_{el} and calculate f for this element. We note that:

- We have to add all self-contributions of spins that are flipped and all mixed contributions of all pairs where both spins are flipped. Mixed contributions have a factor of 2 relative to self-contributions since $j = 1, k = 2$ and $j = 2, k = 1$ both appear in the summation.
- There must be at least n_e spins flipped between the two states.
- If there are more spins flipped, the additional ones must occur in pairs which are flipped differently.

- For such pairs their mixed contributions cancel their self-contributions. For any other spins that are flipped one in the pair flips equally and one flips differently, which cancels each other. Therefore the net contribution of these pairs is zero and they can be ignored.
- Ignoring such pairs we are left with n_e spins which all flip equally. These n_e spins form $\binom{n_e}{2} = \frac{n_e(n_e-1)}{2}$ pairs which all give a contribution of $2(-4) = -8$. Their self-contributions sum up to $-4n_e$. Summing self-contributions and mixed contributions we find $f = \frac{n_e(n_e-1)}{2}(-8) - 4n_e = n_e^2$.

We found that for spatially uncorrelated noise the dephasing rate between two states is proportional to the number n_f of spins which are flipped between the two states. For spatially fully correlated noise environments the dephasing rate is proportional to n_e^2, where n_e is the difference in the number of excitations between the two states.

E Dephasing rates for n ions

We now present the calculation of the two dephasing rates given in eq. 4.27 and 4.29 for the two different initial states of the system (eq. 4.3 and 4.4). Starting from the master equation (eq. 4.20) with the system operator $s_j = J_z^{(j)}$

$$\dot{r} = i[r, H_s] + \frac{1}{2}\sum_{j,k} \exp\left(-\frac{|j-k|}{\xi}\right)(-s_j s_k r + s_k r s_j - r s_k s_j + s_j r s_k) \tag{9.21}$$

for the respective density matrix element of interest (eq. 4.21 and 4.22):

$$r = |m_-, m_-, ..., m_-, m_+, m_+, ..., m_+\rangle \langle m_1, m_1, m_1, ..., m_1| \tag{9.22}$$

$$r_2 = |m_-, m_+, m_-, m_+, ...\rangle \langle m_1, m_1, m_1, ..., m_1| \tag{9.23}$$

These two elements only differ in the order of the ions. The coherent part is the same for both and easily calculated:

$$i(rH_s - H_s r) = i(\omega_0 n m_1 + \alpha n m_1^2 - \omega_0 n m_1 - \alpha n(m_1^2 + m_2^2)r = -in\alpha m_2^2 r \tag{9.24}$$

Dephasing rate for element r

To calculate the decoherent part we remember how s_j acts from the left and from the right onto element r

$$s_j r = \begin{cases} (m_1 - m_2)r & \text{if } j \leq n/2 \\ (m_1 + m_2)r & \text{if } j > n/2 \end{cases} \tag{9.25}$$

$$r s_j = m_1 r \tag{9.26}$$

The outcome of this calculation is going to be a sum over exponentials. We now calculate the coefficients of $\exp\left(-\frac{|j-k|}{\xi}\right)$ for a fixed distance of ions $|j-k| = x$. Regarding figure E.1 we can see that there are $n - x$ pairs of ions with the distance x between them.

We now calculate the four terms in eq. 4.20 for a fixed x. We have to distinguish between three cases:

case 1) $x > n/2$ All pairs will have one ion in the left half and one ion in the right half. We need to count each pair twice since j will be each ion once in the

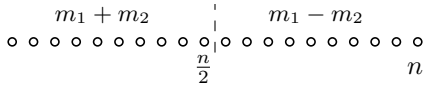

Figure E.1: A chain of n ions. The operator $s_j = J_z^{(j)}$ acting from the left onto our element (eq. 4.21 to 4.24) gives m_1+m_2 for j in the left half and m_1-m_2 for j in the right half.

summation. Note that the contributions from $s_j r s_k$ and $s_k r s_j$ must always be the same because the two indices are equivalent.

$$\sum_{|j-k|=x} s_j s_k r = 2(n-x)(m_1+m_2)(m_1-m_2)r = 2(n-x)(m_1^2-m_2^2)r \tag{9.27}$$

$$\sum_{|j-k|=x} r s_j s_k = 2(n-x)m_1^2 r \tag{9.28}$$

$$\sum_{|j-k|=x} s_j r s_k = m_1[(n-x)(m_1+m_2)+(n-x)(m_1-m_2)]r = 2(n-x)m_1^2 r \tag{9.29}$$

$$\sum_{|j-k|=x} s_k r s_j = 2(n-x)m_1^2 r \tag{9.30}$$

$$\frac{1}{2}\sum_{|j-k|=x} \exp\left(-\frac{|j-k|}{\xi}\right)(-s_j s_k r + s_k r s_j - r s_k s_j + s_j r s_k) = (n-x)m_2^2\, e^{x/\xi} r \tag{9.31}$$

case 2) $0 < x \leq n/2$ There will now be $n/2-x$ pairs which have both ions in the left half. Equivalently $n/2-x$ pairs will have both ions in the right half. In between there are x pairs which have one ion in the left and one in the right half.

$$\begin{aligned}\sum_{|j-k|=x} s_j s_k r &= 2\left(\frac{n}{2}-x\right)[(m_1+m_2)^2+(m_1-m_2)^2]r + 2x(m_1+m_2)(m_1-m_2)r \\ &= (n-2x)(2m_1^2+2m_2^2)r + 2x(m_1^2-m_2^2)r \qquad (9.32)\\ &= 2(n-x)m_1^2 r + 2(n-3x)m_2^2 r \qquad (9.33)\end{aligned}$$

$$\sum_{|j-k|=x} r s_j s_k = 2(n-x)m_1^2 r \tag{9.34}$$

$$\sum_{|j-k|=x} s_j r s_k = m_1 \left[\frac{n}{2}(m_1+m_2) + \left(\frac{n}{2}-x\right)(m_1-m_2) + \left(\frac{n}{2}-x\right)(m_1+m_2) + \frac{n}{2}(m_1-m_2)\right] r \quad (9.35)$$

$$= m_1 \left[(n-x)(m_1+m_2+m_1-m_2)\right] r = 2(n-x)m_1^2 r \quad (9.36)$$

$$\sum_{|j-k|=x} s_k r s_j = 2(n-x)m_1^2 r \quad (9.37)$$

$$\frac{1}{2}\sum_{|j-k|=x} \exp\left(-\frac{|j-k|}{\xi}\right)(-s_j s_k r + s_k r s_j - r s_k s_j + s_j r s_k) = -(n-3x)m_2^2\, e^{x/\xi} r \quad (9.38)$$

case 3) $x = 0$ For $x = 0 \Leftrightarrow j = k$ there are n such cases in the summation (which should not have the factor of 2 from the other cases).

$$\sum_{|j-k|=x} s_j s_k r = \frac{n}{2}(m_1+m_2)^2 r + \frac{n}{2}(m_1-m_2)^2 r = n(m_1^2+m_2^2)r \quad (9.39)$$

$$\sum_{|j-k|=x} r s_j s_k = m_1 \left[\frac{n}{2}(m_1+m_2) + \frac{n}{2}(m_1-m_2)\right] r = n m_1^2 r \quad (9.40)$$

$$\sum_{|j-k|=x} s_j r s_k = n m_1^2 r \quad (9.41)$$

$$\sum_{|j-k|=x} s_k r s_j = n m_1^2 r \quad (9.42)$$

$$\frac{1}{2}\sum_{|j-k|=x} \exp\left(-\frac{|j-k|}{\xi}\right)(-s_j s_k r + s_k r s_j - r s_k s_j + s_j r s_k) = -\frac{n}{2} m_2^2 r \quad (9.43)$$

We have now calculated all coefficients for the exponentials $\exp(x/\xi)$ in the decoherent part of the master equation and can now write it down in the form:

$$\dot{r} = -in\alpha m_2^2 r + \Gamma(n,\xi) r \quad (9.44)$$

$$r(t) = r(0)\exp\left(-in\alpha m_2^2 t + \Gamma(n,\xi)t\right) \quad (9.45)$$

$$(9.46)$$

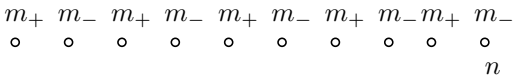

Figure E.2: A chain of n ions. The operator s_j acting from the left onto our element (eq. 4.22 to 4.24) gives $m_+ = m_1 + m_2$ for j odd and $m_- = m_1 - m_2$ for j even.

The dephasing rate $\Gamma(n, \xi)$ is given by:

$$\Gamma(n,\xi) = \left(-\frac{n}{2} + \sum_{x=1}^{n/2} -(n-3x)e^{x/\xi} + \sum_{x=n/2+1}^{n} (n-x)e^{x/\xi} \right) m_2^2 \tag{9.47}$$

$$= \frac{6e^{\frac{1}{\xi}} + 2e^{\frac{1-n}{\xi}} - 8e^{-\frac{-2+n}{2\xi}} + n - e^{2/\xi}n}{2\left(-1 + e^{\frac{1}{\xi}}\right)^2} \tag{9.48}$$

Dephasing rate for element r_2

To calculate the decoherent part of eq. 9.21 for the element r_2 we regard how $s_j = J_z^{(j)}$ acts from the left and from the right onto element r_2 (figure E.2):

$$s_j r_2 = \begin{cases} m_- r_2 = (m_1 - m_2) r_2 & \text{if } j \text{ is odd} \\ m_+ r_2 = (m_1 + m_2) r_2 & \text{if } j \text{ is even} \end{cases} \tag{9.49}$$

$$r_2 s_j = m_1 r_2 \tag{9.50}$$

From that we find that the four terms for a given pair of j and k in the master equation 9.21 have an alternating sign depending on whether $|j-k|$ is odd or even:

$$\begin{aligned} &- s_j s_k r_2 + s_k r_2 s_j - r_2 s_k s_j + s_j r_2 s_k \\ &\quad = \begin{cases} r_2[-(m_1^2 + m_2^2) + m_1^2 - m_1^2 + m_1^2] = -m_1^2 r_2 & \text{if } |j-k| \text{ is even} \\ r_2[-(m_1^2 - m_2^2) + m_1^2 - m_1^2 + m_1^2] = m_1^2 r_2 & \text{if } |j-k| \text{ is odd} \end{cases} \end{aligned} \tag{9.51}$$

This alternation is the key to a better scaling because cancelling terms now have similar values of $x = |j-k|$ with similar values of the correlation function. We now discuss this in mathematical detail.

Next we calculate the sum over each of the four terms in eq. 9.21 for a fixed distance of ions $|j-k| = x$ and then regard the coefficients of $\exp\left(-\frac{x}{\xi}\right)$. The two terms $\sum_{|j-k|=x} s_j r_2 s_k$ and $\sum_{|j-k|=x} s_k r_2 s_j$ must always be the same. Again there are $(n-x)$

pairs of ions with a distance x between them. Again for $x > 0$ each pair is counted twice because j will be the right one and the left one once. We distinguish three cases:

case 1) x is odd In each pair there is one spin in state m_+ and one in state m_-.

$$\sum_{|j-k|=x} s_j s_k r_2 = 2(n-x)(m_1^2 - m_2^2) r_2 \tag{9.52}$$

$$\sum_{|j-k|=x} r_2 s_j s_k = 2(n-x) m_1^2 r_2 \tag{9.53}$$

$$\sum_{|j-k|=x} s_j r_2 s_k = m_1^2 (n-x) 2 r_2 \tag{9.54}$$

For the last equation, note that j is each ion in the pair once and therefore give once m_+ and once m_-. Furthermore $m_+ + m_- = 2m_1$ for each pair.

$$\frac{1}{2} \sum_{|j-k|=x} \exp\left(-\frac{|j-k|}{\xi}\right) (-s_j s_k r_2 + s_k r_2 s_j - r_2 s_k s_j + s_j r_2 s_k) = +(n-x) m_2^2 \, e^{x/\xi} r_2 \tag{9.55}$$

case 2) x is even In each pair the ions are in the same state. There is an equal number of (m_+, m_+) pairs and (m_-, m_-) pairs because (moving along the chain) the pairs start with one type and finish with the other (n is even).

$$\sum_{|j-k|=x} s_j s_k r_2 = 2(n-x)(m_1^2 + m_2^2) r_2 \tag{9.56}$$

$$\sum_{|j-k|=x} r_2 s_j s_k = 2(n-x) m_1^2 r_2 \tag{9.57}$$

$$\sum_{|j-k|=x} s_j r_2 s_k = 2(n-x) m_1^2 r_2 \tag{9.58}$$

$$\frac{1}{2} \sum_{|j-k|=x} \exp\left(-\frac{|j-k|}{\xi}\right) (-s_j s_k r_2 + s_k r_2 s_j - r_2 s_k s_j + s_j r_2 s_k) = -(n-x) m_2^2 \, e^{x/\xi} r_2 \tag{9.59}$$

case 3) $x = 0$ Analogous to eq. 9.43 one finds:

$$\frac{1}{2}\sum_{|j-k|=x} \exp\left(-\frac{|j-k|}{\xi}\right)(-s_j s_k r_2 + s_k r_2 s_j - r_2 s_k s_j + s_j r_2 s_k) = -\frac{n}{2}m_2^2 r_2 \quad (9.60)$$

We have now calculated all coefficients for the exponentials $\exp(x/\xi)$ in the decoherent part of the master equation and can now write it down in the form:

$$\dot{r}_2 = -in\alpha m_2^2 r_2 + \Gamma_2(n,\xi) r_2 \quad (9.61)$$

$$r_2(t) = r_2(0)\exp\left(-in\alpha m_2^2 t + \Gamma_2(n,\xi)t\right) \quad (9.62)$$

$$(9.63)$$

The dephasing rate $\Gamma_2(n,\xi)$ is given by:

$$\Gamma_2(n,\xi) = \left(-\frac{n}{2} + \sum_{x_c=1}^{n/2}(n-2x_c+1)e^{(2x_c-1)/\xi} + \sum_{x_c=1}^{n/2}(2x_c-n)e^{2x_c/\xi}\right)m_2^2 \quad (9.64)$$

$$= \frac{-2e^{\frac{1}{\xi}} + 2e^{\frac{1-n}{\xi}} + n - e^{2/\xi}n}{2\left(1+e^{\frac{1}{\xi}}\right)^2}m_2^2 \quad (9.65)$$

Different functional forms

One can easily generalise eq. 9.47 and 9.64 for a different functional form than exponential decay by replacing $\exp(x/\xi) \to C_{|j-k|=x}(\omega = 0)$. As an example we can replace the exponential decay with Gaußian decay $\exp(x/\xi) \to \exp(x^2/\xi^2)$ in eq. 9.47, however the sum is not easily evaluated any more:

$$\Gamma_{\text{Gaussian}}(x,\xi) = \left(-\frac{n}{2} + \sum_{x=1}^{n/2} -(n-3x)\exp(x^2/\xi^2) + \sum_{x=n/2+1}^{n}(n-x)\exp(x^2/\xi^2)\right)m_2^2 \quad (9.66)$$

F The von-Neumann equation in the Schrödinger, interaction and Heisenberg pictures

In this appendix we will present the density matrix and operators in the three different pictures and their respective differential equation, i.e. the von-Neumann equation (also called Liouville equation) for the time evolution of the density matrix ρ and the differential equation for the evolution of any operator A. The idea of using different pictures is based on the fact that only expectation values of observables are actual, physical and measurable. The state, operators and time evolution are merely part of the theoretical description, which can be grouped in different ways:

$$\begin{aligned}
\langle A\rangle &= \langle\Psi_S(t)|\, A_S\, |\Psi_S(t)\rangle && \text{Schrödinger picture} && (9.67)\\
&= \langle\Psi_H|\, U^\dagger(t) A_S U(t)\, |\Psi_H\rangle && && (9.68)\\
&= \langle\Psi_H|\, A_H(t)\, |\Psi_H\rangle && \text{Heisenberg picture} && (9.69)
\end{aligned}$$

We assume that the Hamiltonian consists of two time-independent parts

$$H = H_0 + W$$

where H_0 is the bare uncoupled Hamiltonian and W contains the couplings.

Schrödinger picture The most common way to understand quantum mechanics is the Schrödinger picture, where the states evolve in time and the observables are represented by time-independent operators. The states follow the Schrödinger equation, from which we find the von-Neumann equation by Hermitian conjugation and the product rule:

$$\begin{aligned}
i\hbar d_t\, |\Psi\rangle &= H\, |\Psi\rangle && (9.70)\\
\langle\Psi|\, \overleftarrow{d_t}(-i\hbar) &= \langle\Psi|\, H && (9.71)\\
i\hbar d_t\, |\Psi\rangle\, \langle\Psi| &= H\, |\Psi\rangle\, \langle\Psi| - |\Psi\rangle\, \langle\Psi|\, H && (9.72)\\
i\hbar d_t\rho &= [H,\rho] \qquad \text{von-Neumann equation} && (9.73)
\end{aligned}$$

Eq. 9.70 is a description with a state. Eq. 9.73 is a description with a density matrix. In the Schrödinger picture all time evolution is in the density matrix and operators are time independent except for the rare case of an explicitly time-dependent oper-

ator:

$$i\hbar\dot{\rho}_S = [H, \rho_S] \qquad \dot{A}_S = \frac{\partial}{\partial t} A_S \tag{9.74}$$

interaction picture In the interaction picture we define a new state vector, which only describes the time evolution of the interaction. We define a time evolution operator U_0, which contains only the evolution due to H_0, apply a backwards evolution to the Schrödinger state vector and define this as the new state vector $|\Psi_I\rangle$ in the interaction picture.

$$|\Psi_I\rangle = U_0^\dagger |\Psi\rangle \qquad \text{with } U_0 = e^{-\frac{i}{\hbar}H_0 t} \tag{9.75}$$

$$A_I = U_0^\dagger A U_0 \tag{9.76}$$

$$\rho_I = |\Psi_I\rangle \langle\Psi_I| = U_0^\dagger |\Psi\rangle \langle\Psi| U_0 = U_0^\dagger \rho_S U_0 \tag{9.77}$$

$$\frac{d}{dt}\rho_I = \frac{i}{\hbar} H_0 \rho_I + U_0^\dagger \left(\frac{d}{dt}\rho_S\right) U_0 - \frac{i}{\hbar} U_0^\dagger \rho_S H_0 U_0 \tag{9.78}$$

$$= U_0^\dagger \frac{1}{i\hbar} [H, \rho_S] U_0 + \frac{1}{i\hbar}\left(-U_0^\dagger H_0 U_0 U_0^\dagger \rho_S U_0 + U_0^\dagger \rho_S U_0 U_0^\dagger H_0 U_0\right) \tag{9.79}$$

$$= \frac{1}{i\hbar}\left(\left[\tilde{H}, \rho_I\right] - \left[\tilde{H}_0, \rho_I\right]\right) = \frac{1}{i\hbar}\left[\tilde{W}, \rho_I\right] \tag{9.80}$$

where the tilde over an operator means the operator transformed into the interaction picture $\tilde{A} = A_I = U_0^\dagger A U_0$. In the interaction picture the time evolution due to the interaction is in the state/density matrix and the time evolution due to H_0 in the operators:

$$i\hbar\dot{\rho}_I = \left[\tilde{W}, \rho_I\right] \qquad i\hbar\dot{A}_I = \left[A_I, \tilde{H}_0\right] + U_0^\dagger \frac{\partial A}{\partial t} U_0 \tag{9.81}$$

Heisenberg picture In the Heisenberg picture the state at time $t = 0$ is used as the only state/density matrix. All time evolution is in the operators:

$$|\Psi_H\rangle = |\Psi_S(t=0)\rangle = U^\dagger |\Psi_S\rangle \qquad \text{with } U = e^{-\frac{i}{\hbar}Ht} \tag{9.82}$$

$$A_H = U^\dagger A_S U \tag{9.83}$$

The subscript index means the operator transformed to the Heisenberg picture $A_H = U^\dagger A_S U$. The equations of motion are:

$$i\hbar\dot{\rho}_H = 0 \qquad i\hbar\dot{A}_H = [A_H, H_H] + i\hbar U^\dagger(\partial_t A_S)U \tag{9.84}$$

G Fourier transformation and Fourier series

Since both analytical as well as numerical Fourier transforms are used in several places throughout this thesis for both discrete and continuous functions we give an overview of consistent formulas in this appendix.

Non-periodic functions can be Fourier transformed into a continuous function. Periodic functions can be developed into a Fourier series, with discrete frequencies ω_k. Functions over a finite interval can be interpreted as periodic. For periodic functions the integral needs to go over the entire length of the periodicity but one is free to choose the starting point for the integration. Mathematically the equations are:

Analytically

Fourier transform	Fourier series
$F(\omega) = \int_{-\infty}^{\infty} dt f(t) \exp(-i\omega t)$	$F_k = \frac{1}{T}\int_{-T/2}^{T/2} dt f(t) \exp\left(-i \overbrace{\frac{2\pi}{T}}^{\omega_k} k\, t\right)$
$f(t) = \frac{1}{2\pi}\int_{-\infty}^{\infty} d\omega F(\omega) \exp(i\omega t)$	$f(t) = \sum_{k=-\infty}^{\infty} F_k \exp\left(i\frac{2\pi}{T}kt\right)$

The normalisations $1/(2\pi)$ and $1/N$ can be chosen to be in either of the transform. It is only important, that after applying both transformations the normalisation factor has been acquired. The equations give general rules for a function and its Fourier complement: Finiteness (or periodicity) of the interval of a function corresponds to discreteness in Fourier space. Infinity of the interval corresponds to continuity (i.e. non-discreteness) in Fourier space. Discreteness of a function corresponds to finiteness of the function interval in Fourier space. Non-discreteness corresponds to an infinite function interval. The larger the interval T of a function the closer together the frequencies $\omega_k = 2\pi k/T$ in Fourier space. In other words, the better the resolution in one domain, the larger the interval in the other and vice versa.

When considering measured signals they will always be only over a finite interval and have discrete values although they usually represent a smooth, continuous function. The finite interval can sometimes be interpreted as periodic (Fourier series applicable) or as a function over an infinite interval (Fourier transform applicable) where the rest of the function is zero. We discretize time and frequency in the Fourier

transform and we discretize time in the Fourier series and find the same equations. Discretization with step-size $\Delta\omega = 2\pi/T$ directly results in limiting the time interval to T. Discretization with step-size $\Delta t = 2\pi/\Omega$ results in limiting the frequency interval to Ω.

Numerically

Fourier transform	Fourier series
Discretize t :	Discretize t with $T = N\Delta t$
$F(\omega) = \Delta t \sum_j f_j e^{-i\omega j \Delta t}$	$t \to j\Delta t$
Discretize ω :	$\int dt \to \Delta t \sum_j$
$F_k = \Delta t \sum_{j=0}^{N-1} f_j \exp\left(-i \overbrace{\frac{2\pi}{N\Delta t}}^{\omega_k} k\, j\Delta t\right)$	$F_k = \frac{1}{N\Delta t}\Delta t \sum_{j=0}^{N-1} f_j \exp\left(-i\frac{2\pi}{N\Delta t} kj\Delta t\right)$
$\frac{1}{2\pi}\int d\omega \to \frac{1}{2\pi}\Delta\omega \sum_k = \frac{1}{N\Delta t}\sum_k$	
$\Delta\omega = \frac{2\pi}{T} = \frac{2\pi}{N\Delta t}$	
$f_j = \frac{1}{N}\sum_{k=0}^{N-1} \frac{F_k}{\Delta t} \exp\left(i\frac{2\pi}{N\Delta t} kj\Delta t\right)$	$f_j = \sum_{k=0}^{N-1} F_k \exp\left(i\frac{2\pi}{N} kj\right)$

We find that the equations are the same except that the normalisation factor $1/N$ is at a different position, which is purely conventional and that in the Fourier transform the F_k have an additional factor of Δt, which is cancelled divided out in the transformation to f_j.

These are the equations for numerical Fourier transformation as they are used e.g. in Matlab. If the result is to be compared to an analytical Fourier transform of a function the left convention should be used. If the result is to be compared to an analytical Fourier series the right-hand convention should be used.

If the values f_j are replaced by quantum mechanical operators, which correspond a lattice structure the same transformation is usually called *Fourier lattice transform*. See references [111, 112].

References

[1] Heinz-Peter Breuer and Francesco Petruccione. *The theory of open quantum systems*. Oxford University Press, 2003.

[2] Barbara M. Terhal and Guido Burkard. Fault-tolerant quantum computation for local non-markovian noise. *Phys. Rev. A*, 71:012336, Jan 2005.

[3] Roland Doll, Martijn Wubs, Peter Hänggi, and Sigmund Kohler. Incomplete pure dephasing of n-qubit entangled w states. *Phys. Rev. B*, 76:045317, Jul 2007.

[4] L. D. Contreras-Pulido and R. Aguado. Entanglement between charge qubits induced by a common dissipative environment. *Phys. Rev. B*, 77:155420, Apr 2008.

[5] D. P. S. McCutcheon, A. Nazir, S. Bose, and A. J. Fisher. Long-lived spin entanglement induced by a spatially correlated thermal bath. *Phys. Rev. A*, 80:022337, Aug 2009.

[6] Jan Jeske, Jared H Cole, Clemens Müller, Michael Marthaler, and Gerd Schön. Dual-probe decoherence microscopy: probing pockets of coherence in a decohering environment. *New Journal of Physics*, 14(2):023013, February 2012.

[7] R. H. Dicke. Coherence in spontaneous radiation processes. *Phys. Rev.*, 93:99–110, Jan 1954.

[8] A Crubellier, S Liberman, D Pavolini, and P Pillet. Superradiance and subradiance. i. interatomic interference and symmetry properties in three-level systems. *Journal of Physics B*, 18(18):3811, 1985.

[9] T. Ojanen, A. O. Niskanen, Y. Nakamura, and A. A. Abdumalikov. Global relaxation of superconducting qubits. *Phys. Rev. B*, 76:100505, Sep 2007.

[10] D. A. Lidar, I. L. Chuang, and K. B. Whaley. Decoherence-free subspaces for quantum computation. *Phys Rev Lett*, 81:2594–2597, Sep 1998.

[11] Daniel A. Lidar, Dave Bacon, Julia Kempe, and K. B. Whaley. Decoherence-free subspaces for multiple-qubit errors. i. characterization. *Phys. Rev. A*, 63:022306, Jan 2001.

[12] Daniel A. Lidar, Dave Bacon, Julia Kempe, and K. B. Whaley. Decoherence-free subspaces for multiple-qubit errors. ii. universal, fault-tolerant quantum computation. *Phys. Rev. A*, 63:022307, Jan 2001.

[13] Daniel A. Lidar and K. Birgitta Whaley. Decoherence-free subspaces and subsystems. In F. Benatti and R. Floreanini, editors, *Irreversible Quantum Dynamics*, volume 622 of *Lecture Notes in Physics*, pages 83–120. Springer Berlin, 2003.

[14] Robin Blume-Kohout, Hui Khoon Ng, David Poulin, and Lorenza Viola. Characterizing the structure of preserved information in quantum processes. *Phys. Rev. Lett.*, 100:030501, Jan 2008.

[15] R. Doll, M. Wubs, P. Hänggi, and S. Kohler. Limitation of entanglement due to spatial qubit separation. *EPL (Europhysics Letters)*, 76(4):547, 2006.

[16] GM Palma, KA Suominen, and AK Ekert. Quantum computers and dissipation. *Proceedings of the Royal Society a-Mathematical Physical and Engineering Sciences*, 452(1946):567–584, 1996. contains mistake, claimed in Reina2002, PRA 65, 032326.

[17] J.H. Reina, L. Quiroga, and N.F. Johnson. Decoherence of quantum registers. *Physical Review A*, 65(3):032326, 2002.

[18] Lu-Ming Duan and Guang-Can Guo. Reducing decoherence in quantum-computer memory with all quantum bits coupling to the same environment. *Phys. Rev. A*, 57:737–741, Feb 1998.

[19] P. Zanardi and M. Rasetti. Noiseless quantum codes. *Phys. Rev. Lett.*, 79:3306–3309, Oct 1997.

[20] Paolo Zanardi. Dissipation and decoherence in a quantum register. *Physical Review A*, 57(5):3276–3284, May 1998.

[21] F. K. Wilhelm, M. J. Storcz, U. Hartman, and M. R. Geller. *Manipulating Quantum Coherence in Solid State Systems*, chapter Superconducting qubits II: Decoherence, pages 195–232. NATO Science Series. Spri, 2007.

[22] Robert Alicki, Michał Horodecki, Paweł Horodecki, and Ryszard Horodecki. Dynamical description of quantum computing: Generic nonlocality of quantum noise. *Physical Review A*, 65:062101, May 2002.

[23] D. V. Averin and R. Fazio. Active suppression of dephasing in josephson-junction qubits. *JETP Lett.*, 78:664, Nov 2003.

[24] James P. Clemens, Shabnam Siddiqui, and Julio Gea-Banacloche. Quantum error correction against correlated noise. *Phys. Rev. A*, 69:062313, Jun 2004.

[25] Dorit Aharonov, Alexei Kitaev, and John Preskill. Fault-tolerant quantum computation with long-range correlated noise. *Phys. Rev. Lett.*, 96:050504, Feb 2006.

[26] Panos Aliferis, Daniel Gottesman, and John Preskill. Quantum accuracy threshold for concatenated distance-3 code. *Quantum Inf. Comput.*, 6(2):97, March 2006.

[27] E. Novais and Harold U. Baranger. Decoherence by correlated noise and quantum error correction. *Phys. Rev. Lett.*, 97:040501, Jul 2006.

[28] P. Jouzdani, E. Novais, and E. R. Mucciolo. Fidelity of the surface code in the presence of a bosonic bath. *Phys. Rev. A*, 88:012336, Jul 2013.

[29] F. Caruso, A. W. Chin, A. Datta, S. F. Huelga, and M. B. Plenio. Highly efficient energy excitation transfer in light-harvesting complexes: The fundamental role of noise-assisted transport. *Journal of Chemical Physics*, 131(10):105106, 2009.

[30] Gregory D. Scholes, Tihana Mirkovic, Daniel B. Turner, Francesca Fassioli, and Andreas Buchleitner. Solar light harvesting by energy transfer: from ecology to coherence. *Energy Environ. Sci.*, 5:9374–9393, 2012.

[31] Mino Yang and Graham R. Fleming. Influence of phonons on exciton transfer dynamics: comparison of the redfield, förster, and modified redfield equations. *Chemical Physics*, 282(1):163 – 180, 2002.

[32] Benoit Palmieri, Darius Abramavicius, and Shaul Mukamel. Lindblad equations for strongly coupled populations and coherences in photosynthetic complexes. *J. Chem. Phys.*, 130:204512, 2009.

[33] A. K. Ringsmuth, G. J. Milburn, and T. M. Stace. Multiscale photosynthetic and biomimetic excitation energy transfer. *Nature Physics*, 8:562, 2012.

[34] A. Safavi-Naini, P. Rabl, P. F. Weck, and H. R. Sadeghpour. Microscopic model of electric-field-noise heating in ion traps. *Phys. Rev. A*, 84:023412, Aug 2011.

[35] Thomas Monz, Philipp Schindler, Julio T. Barreiro, Michael Chwalla, Daniel Nigg, William A. Coish, Maximilian Harlander, Wolfgang Hänsel, Markus Hennrich, and Rainer Blatt. 14-qubit entanglement: Creation and coherence. *Phys. Rev. Lett.*, 106:130506, Mar 2011.

[36] L. Deslauriers, S. Olmschenk, D. Stick, W. K. Hensinger, J. Sterk, and C. Monroe. Scaling and suppression of anomalous heating in ion traps. *Phys. Rev. Lett.*, 97:103007, Sep 2006.

[37] C. Schroll, W. Belzig, and C. Bruder. Decoherence of cold atomic gases in magnetic microtraps. *Phys. Rev. A*, 68:043618, Oct 2003.

[38] A. J. Leggett, S. Chakravarty, A. T. Dorsey, Matthew P. A. Fisher, Anupam Garg, and W. Zwerger. Dynamics of the dissipative two-state system. *Rev. Mod. Phys.*, 59:1–85, Jan 1987.

[39] W. G. Unruh. Maintaining coherence in quantum computers. *Phys. Rev. A*, 51:992–997, Feb 1995.

[40] David P. DiVincenzo. Two-bit gates are universal for quantum computation. *Phys. Rev. A*, 51:1015–1022, Feb 1995.

[41] Ulrich Weiss. *Quantum Dissipative Systems (Series in Modern Condensed Matter Physics)*. World Scientific Publishing Company, 3 edition, mar 2008.

[42] G. Lindblad. On the generators of quantum dynamical semigroups. *Communications in Mathematical Physics*, 48:119–130, 1976.

[43] Vittorio Gorini, Andrzej Kossakowski, and E. C. G. Sudarshan. Completely positive dynamical semigroups of n-level systems. *Journal of Mathematical Physics*, 17:821, 1976.

[44] H. J. Carmichael. *Statistical methods in quantum optics 1*. Springer, 1999.

[45] M. Chwalla, K. Kim, T. Monz, P. Schindler, M. Riebe, C.F. Roos, and R. Blatt. Precision spectroscopy with two correlated atoms. *Applied Physics B*, 89(4):483–488, 2007.

[46] S. F. Huelga, C. Macchiavello, T. Pellizzari, A. K. Ekert, M. B. Plenio, and J. I. Cirac. Improvement of frequency standards with quantum entanglement. *Phys. Rev. Lett.*, 79:3865–3868, Nov 1997.

[47] D. Leibfried, M. D. Barrett, T. Schaetz, J. Britton, J. Chiaverini, W. M. Itano, J. D. Jost, C. Langer, and D. J. Wineland. Toward heisenberg-limited spectroscopy with multiparticle entangled states. *Science*, 304(5676):1476–1478, 2004.

[48] C. F. Roos, M. Chwalla, K. Kim, M. Riebe, and R. Blatt. 'designer atoms' for quantum metrology. *Nature*, 443:316–9, September 2006.

[49] Sougato Bose. Quantum communication through spin chain dynamics: an introductory overview. *Contemporary Physics*, 48(1):13–30, 2007.

[50] Sougato Bose. Quantum communication through an unmodulated spin chain. *Phys. Rev. Lett.*, 91:207901, Nov 2003.

[51] Tobias J. Osborne and Noah Linden. Propagation of quantum information through a spin system. *Phys. Rev. A*, 69:052315, May 2004.

[52] Claudio Albanese, Matthias Christandl, Nilanjana Datta, and Artur Ekert. Mirror inversion of quantum states in linear registers. *Phys. Rev. Lett.*, 93:230502, Nov 2004.

[53] Matthias Christandl, Nilanjana Datta, Artur Ekert, and Andrew J. Landahl. Perfect state transfer in quantum spin networks. *Phys. Rev. Lett.*, 92,:187902, 2004.

[54] Matthias Christandl, Nilanjana Datta, Tony C. Dorlas, Artur Ekert, Alastair Kay, and Andrew J. Landahl. Perfect transfer of arbitrary states in quantum spin networks. *Phys. Rev. A*, 71:032312, Mar 2005.

[55] Ying Li, Tao Shi, Bing Chen, Zhi Song, and Chang-Pu Sun. Quantum-state transmission via a spin ladder as a robust data bus. *Phys. Rev. A*, 71:022301, Feb 2005.

[56] Tao Shi, Ying Li, Zhi Song, and Chang-Pu Sun. Quantum-state transfer via the ferromagnetic chain in a spatially modulated field. *Phys. Rev. A*, 71:032309, Mar 2005.

[57] Man-Hong Yung and Sougato Bose. Perfect state transfer, effective gates, and entanglement generation in engineered bosonic and fermionic networks. *Phys. Rev. A*, 71:032310, Mar 2005.

[58] Daniel Burgarth and Sougato Bose. Conclusive and arbitrarily perfect quantum-state transfer using parallel spin-chain channels. *Phys. Rev. A*, 71:052315, May 2005.

[59] Daniel Burgarth and Sougato Bose. Perfect quantum state transfer with randomly coupled quantum chains. *New Journal of Physics*, 7(1):135, 2005.

[60] Antoni Wójcik, Tomasz Łuczak, Paweł Kurzyński, Andrzej Grudka, Tomasz Gdala, and Małgorzata Bednarska. Unmodulated spin chains as universal quantum wires. *Phys. Rev. A*, 72:034303, Sep 2005.

[61] Joseph Fitzsimons and Jason Twamley. Globally controlled quantum wires for perfect qubit transport, mirroring, and computing. *Phys. Rev. Lett.*, 97:090502, Sep 2006.

[62] Andrew D. Greentree, Simon J. Devitt, and Lloyd C. L. Hollenberg. Quantum-information transport to multiple receivers. *Phys. Rev. A*, 73:032319, Mar 2006.

[63] V. Kostak, G. M. Nikolopoulos, and I. Jex. Perfect state transfer in networks of arbitrary topology and coupling configuration. *Phys. Rev. A*, 75:042319, Apr 2007.

[64] M. A. Jafarizadeh and R. Sufiani. Perfect state transfer over distance-regular spin networks. *Phys. Rev. A*, 77:022315, Feb 2008.

[65] Giulia Gualdi, Vojtech Kostak, Irene Marzoli, and Paolo Tombesi. Perfect state transfer in long-range interacting spin chains. *Phys. Rev. A*, 78:022325, Aug 2008.

[66] Hohjai Lee, Yuan-Chung Cheng, and Graham R. Fleming. Coherence dynamics in photosynthesis: Protein protection of excitonic coherence. *Science*, 316(5830):1462–1465, 2007.

[67] Gregory S. Engel, Tessa R. Calhoun, Elizabeth L. Read, Tae-Kyu Ahn, Tomas Mancal, Yuan-Chung Cheng, Robert E. Blankenship, and Graham R. Fleming. Evidence for wavelike energy transfer through quantum coherence in photosynthetic systems. *Nature*, 446(7137):782–786, April 2007.

[68] P. Huo and D.F. Coker. Influence of environment induced correlated fluctuations in electronic coupling on coherent excitation energy transfer dynamics in model photosynthetic systems. *Journal of Chemical Physics*, 136(11):115102, 2012.

[69] Jianlan Wu, Fan Liu, Young Shen, Jianshu Cao, and Robert J Silbey. Efficient energy transfer in light-harvesting systems, i: optimal temperature, reorga-

nization energy and spatial-temporal correlations. *New Journal of Physics*, 12(10):105012, 2010.

[70] P Nalbach, J Eckel, and M Thorwart. Quantum coherent biomolecular energy transfer with spatially correlated fluctuations. *New Journal of Physics*, 12(6):065043, 2010.

[71] Francesca Fassioli, Ahsan Nazir, and Alexandra Olaya-Castro. Quantum state tuning of energy transfer in a correlated environment. *The Journal of Physical Chemistry Letters*, 1(14):2139–2143, 2010.

[72] D. Abramavicius and S. Mukamel. Exciton dynamics in chromophore aggregates with correlated environment fluctuations. *Journal of Chemical Physics*, 134(17):174504, 2011.

[73] Mohan Sarovar, Yuan-Chung Cheng, and K. Birgitta Whaley. Environmental correlation effects on excitation energy transfer in photosynthetic light harvesting. *Phys. Rev. E*, 83:011906, Jan 2011.

[74] A. Shabani, M. Mohseni, H. Rabitz, and S. Lloyd. Efficient estimation of energy transfer efficiency in light-harvesting complexes. *Phys. Rev. E*, 86:011915, Jul 2012.

[75] Patrick Rebentrost, Masoud Mohseni, and Alan Aspuru-Guzik. Role of quantum coherence and environmental fluctuations in chromophoric energy transport. *The Journal of Physical Chemistry B*, 113(29):9942–9947, 2009.

[76] Akihito Ishizaki and Graham R. Fleming. On the adequacy of the redfield equation and related approaches to the study of quantum dynamics in electronic energy transfer. *The Journal of Chemical Physics*, 130(23):234110, 2009.

[77] Akihito Ishizaki and Yoshitaka Tanimura. Nonperturbative non-markovian quantum master equation: Validity and limitation to calculate nonlinear response functions. *Chemical Physics*, 347:185 – 193, 2008.

[78] Akihito Ishizaki and Graham R. Fleming. Unified treatment of quantum coherent and incoherent hopping dynamics in electronic energy transfer: Reduced hierarchy equation approach. *The Journal of Chemical Physics*, 130(23):234111, 2009.

[79] P. Huo and D. F. Coker. Iterative linearized density matrix propagation for modeling coherent excitation energy transfer in photosynthetic light harvesting. *The Journal of Chemical Physics*, 133(18):184108, 2010.

[80] Pengfei Huo and David F. Coker. Communication: Partial linearized density matrix dynamics for dissipative, non-adiabatic quantum evolution. *The Journal of Chemical Physics*, 135(20):201101, 2011.

[81] Jian Xu, Hou-Dao Zhang, Rui-Xue Xu, and YiJing Yan. Correlated driving and dissipation in two-dimensional spectroscopy. *The Journal of Chemical Physics*, 138:024106, 2013.

[82] Ángel Rivas and Miguel A. Martin-Delgado. Dynamics of thermal effects in the spin-wave theory of quantum antiferromagnets. *Annals of Physics*, 331(0):9 – 23, 2013.

[83] Jan Jeske and Jared H. Cole. Derivation of markovian master equations for spatially correlated decoherence. *Phys. Rev. A*, 87:052138, May 2013.

[84] Nicolas Vogt, Jan Jeske, and Jared H. Cole. Stochastic bloch-redfield theory: Quantum jumps in a solid-state environment. *Phys. Rev. B*, 88:174514, Nov 2013.

[85] R. K. Wangsness and F. Bloch. The dynamical theory of nuclear induction. *Physical Review*, 89:728–739, Feb 1953.

[86] F. Bloch. Dynamical theory of nuclear induction. ii. *Physical Review*, 102:104–135, Apr 1956.

[87] F. Bloch. Generalized theory of relaxation. *Physical Review*, 105(4):1206–1222, Feb 1957.

[88] A. G. Redfield. On the theory of relaxation processes. *IBM Journal of Research and Development*, 1(1):19 –31, jan 1957.

[89] Robert S Whitney. Staying positive: going beyond lindblad with perturbative master equations. *Journal of Physics A: Mathematical and Theoretical*, 41(17):175304, 2008.

[90] Charles P. Slichter. *Principles of Magnetic Resonance*. Springer, 1990. includes discussion about Bloch-Redfield theory.

[91] Joseph Schriefl. *Decoherence in Josephson Qubits*. PhD thesis, Institut für theoretische Festkörperphysik, Karlsruhe Institute of Technology, 2005. Index mistake in the Bloch-Redfield equations. Correct in Jeske et al. N J Phys 2011.

[92] Clemens Müller. *Coherent Defects in Superconducting Circuits*. PhD thesis, Institut für Theorie der kondensierten Materie, Karlsruhe Institute of Technology, May 2011.

[93] Michael Marthaler. *Study of Quantum Electrodynamics in Superconducting Devices*. PhD thesis, Institut für theoretische Festkörperphysik, Karlsruhe Institute of Technology, June 2009.

[94] Stephen Barnett. *Matrices: Methods and Applications*. Oxford University Press, 1990. Chapter 5 contains tensor identity for superoperator form.

[95] F. W. Byron Jr. and R. W. Fuller. *Mathematics of Classical and Quantum Physics*. Dover Publications, New York, 1992. Chapter 3 contains vector identity for superoperator form.

[96] Léon Van Hove. Correlations in space and time and born approximation scattering in systems of interacting particles. *Physical Review*, 95:249–262, Jul 1954.

[97] Jan Jeske. Two qubits as a decoherence probe of the environment. Master's thesis, Institut für theoretische Festkörperphysik, Karlsruhe Institute of Technology, 2011.

[98] Stephen M. Barnett and Paul M. Radmore. *Methods in theoretical quantum optics*. Clarendon Press, 2002.

[99] G. Scheja and U. Storch. *Lehrbuch der Algebra*. Stuttgart : Teubner, 1988.

[100] Robert M. Gray. *Toeplitz and Circulant Matrices: A review*, volume 2 of *Foundations and Trends in Communications and Information Theory*. now Publishers Inc., 2006.

[101] E. T. Whittaker and G. N. Watson. *A Course of Modern Analysis*. Cambridge University Press, fourth edition, 1963.

[102] Malcolm Pemberton and Nicholas Rau. *Mathematics For Economists*. Manchester University Press, 2001. Chapter 13.4, "Quadratic Forms"p. 241 in second edition.

[103] U Dorner. Quantum frequency estimation with trapped ions and atoms. *New Journal of Physics*, 14(4):043011, 2012.

[104] Jan Jeske, Nicolas Vogt, and Jared H. Cole. Excitation and state transfer through spin chains in the presence of spatially correlated noise. *Phys. Rev. A*, 88:062333, Dec 2013.

[105] Y. Saad. Analysis of some krylov subspace approximations to the matrix exponential operator. *SIAM J. Numer. Anal*, 29:209–228, 1992.

[106] Kurt Busch, Jens Niegemann, Martin Pototschnig, and Lasha Tkeshelashvili. A krylov-subspace based solver for the linear and nonlinear maxwell equations. *Physica Status Solidi B*, 244(10):3479–3496, 2007.

[107] John W. Harris and Horst Stocker. *Handbook of Mathematics and CoComputation Science*. Springer, 1998. table 18.1 on page 684.

[108] J. R. Dormand and P. J. Prince. A family of embedded Runge–Kutta formulae. *J. Comp. Appl. Math.*, 6:19–26, 1980. Explains ode45 solver etc in Matlab.

[109] Roy J. Glauber. Time-dependent statistics of the ising model. *Journal of Mathematical Physics*, 4(2):294, Feb 1963.

[110] M. A. de Ponte, S. S. Mizrahi, and M. H. Y. Moussa. Networks of dissipative quantum harmonic oscillators: A general treatment. *Physical Review A*, 76:032101, Sep 2007.

[111] Wolfgang Nolting. *Fundamentals of Many-body Physics*. Springer Berlin Heidelberg, 2009.

[112] Paolo Longo. *Waveguide Quantum Optics: A Wave-Function Based Approach*. PhD thesis, Institut für theoretische Festkörperphysik, Karlsruhe Institute of Technology, 2012.

[113] Melvin Lax. Formal theory of quantum fluctuations from a driven state. *Phys. Rev.*, 129:2342–2348, Mar 1963.

[114] Melvin Lax. Quantum noise. xi. multitime correspondence between quantum and classical stochastic processes. *Phys. Rev.*, 172:350–361, Aug 1968.

[115] Eric W. Weisstein. Delta function. From MathWorld–A Wolfram Web Resource.

[116] Ernst Ising. Beitrag zur theorie des ferromagnetismus. *Zeitschrift für Physik*, 31(1):253–258, 1925.

[117] Lars Onsager. Crystal statistics. i. a two-dimensional model with an order-disorder transition. *Phys. Rev.*, 65:117–149, Feb 1944.

[118] Wolfgang Nolting and Anupuru Ramakanth. *Quantum Theory of Magnetism*. Springer Berlin Heidelberg, 2009.

[119] Eric W. Weisstein. Bessel function of the first kind. From MathWorld–A Wolfram Web Resource.

[120] Vittorio Giovannetti, Seth Lloyd, and Lorenzo Maccone. Quantum-enhanced measurements: Beating the standard quantum limit. *Science*, 306(5700):1330–1336, 2004.

[121] Norman F. Ramsey. A molecular beam resonance method with separated oscillating fields. *Phys. Rev.*, 78:695–699, Jun 1950.

[122] W. M. Itano, J. C. Bergquist, J. J. Bollinger, J. M. Gilligan, D. J. Heinzen, F. L. Moore, M. G. Raizen, and D. J. Wineland. Quantum projection noise: Population fluctuations in two-level systems. *Phys. Rev. A*, 47:3554–3570, May 1993.

[123] D. J. Wineland, J. J. Bollinger, W. M. Itano, F. L. Moore, and D. J. Heinzen. Spin squeezing and reduced quantum noise in spectroscopy. *Phys. Rev. A*, 46:R6797–R6800, Dec 1992.

[124] D. J. Wineland, J. J. Bollinger, W. M. Itano, and D. J. Heinzen. Squeezed atomic states and projection noise in spectroscopy. *Phys. Rev. A*, 50:67–88, Jul 1994.

[125] J. J . Bollinger, Wayne M. Itano, D. J. Wineland, and D. J. Heinzen. Optimal frequency measurements with maximally correlated states. *Phys. Rev. A*, 54:R4649–R4652, Dec 1996.

[126] B. M. Escher, R. L. de Matos Filho, and L. Davidovich. General framework for estimating the ultimate precision limit in noisy quantum-enhanced metrology. *Nature Physics*, 7(5):406–411, mar 2011.

[127] Rafal Demkowicz-Dobrzanski, Jan Kolodynski, and Guta Madalin. The elusive heisenberg limit in quantum-enhanced metrology. *Nature communications*, 03:1063, 2012.

[128] Wayne M. Itano. Quadrupole moments and hyperfine constants of metastable states of Ca^+, Sr^+, Ba^+, Yb^+, Hg^+, and Au. *Phys. Rev. A*, 73:022510, Feb 2006.

[129] Wayne M. Itano. External-field shifts of the $^{199}Hg^+$ optical frequency standard. *J. Res. Natl. Inst. Stand. Technol.*, 105(6):829–837, Nov 2000.

[130] Samuel L. Braunstein and Carlton M. Caves. Statistical distance and the geometry of quantum states. *Phys. Rev. Lett.*, 72:3439–3443, May 1994.

[131] Alex W. Chin, Susana F. Huelga, and Martin B. Plenio. Quantum metrology in non-markovian environments. *Phys. Rev. Lett.*, 109:233601, Dec 2012.

[132] D. Kielpinski, C Monroe, and D. J. Wineland. Architecture for a large-scale ion-trap quantum computer. *Nature*, 417:709, 2002.

[133] Yuichiro Matsuzaki, Simon C. Benjamin, and Joseph Fitzsimons. Magnetic field sensing beyond the standard quantum limit under the effect of decoherence. *Phys. Rev. A*, 84:012103, Jul 2011.

[134] Olaf Mandel, Markus Greiner, Artur Widera, Tim Rom, Theodor W. Hansch, and Immanuel Bloch. Controlled collisions for multi-particle entanglement of optically trapped atoms. *Nature*, 425(6961):937–940, Oct 2003.

[135] BE Kane. A silicon-based nuclear spin quantum computer. *Nature*, 393(6681):133–137, MAY 14 1998.

[136] Daniel Loss and David P. DiVincenzo. Quantum computation with quantum dots. *Phys. Rev. A*, 57:120–126, Jan 1998.

[137] M B Plenio and S F Huelga. Dephasing-assisted transport: quantum networks and biomolecules. *New Journal of Physics*, 10(11):113019, 2008.

[138] Patrick Rebentrost, Masoud Mohseni, Ivan Kassal, Seth Lloyd, and Alán Aspuru-Guzik. Environment-assisted quantum transport. *New Journal of Physics*, 11(3):033003, 2009.

[139] Stephan Hoyer, Mohan Sarovar, and K Birgitta Whaley. Limits of quantum speedup in photosynthetic light harvesting. *New Journal of Physics*, 12(6):065041, 2010.

[140] Adriana Marais, Ilya Sinayskiy, Alastair Kay, Francesco Petruccione, and Artur Ekert. Decoherence-assisted transport in quantum networks. *New Journal of Physics*, 15(1):013038, 2013.

[141] Daniel Burgarth and Sougato Bose. Universal destabilization and slowing of spin-transfer functions by a bath of spins. *Phys. Rev. A*, 73:062321, Jun 2006.

[142] Jian-Ming Cai, Zheng-Wei Zhou, and Guang-Can Guo. Decoherence effects on the quantum spin channels. *Phys. Rev. A*, 74:022328, Aug 2006.

[143] M. L. Hu and H. L. Lian. State transfer in intrinsic decoherence spin channels. *The European Physical Journal D*, 55(3):711–721, 2009.

[144] M. L. Hu. State transfer in dissipative and dephasing environments. *The European Physical Journal D*, 59(3):497–507, 2010.

[145] Chiara Macchiavello and G. Massimo Palma. Entanglement-enhanced information transmission over a quantum channel with correlated noise. *Phys. Rev. A*, 65:050301, Apr 2002.

[146] Nigum Arshed and A. H. Toor. Entanglement-assisted classical capacity of quantum channels with correlated noise. *Phys. Rev. A*, 73:014304, Jan 2006.

[147] Abolfazl Bayat, Daniel Burgarth, Stefano Mancini, and Sougato Bose. Memory effects in spin-chain channels for information transmission. *Phys. Rev. A*, 77:050306, May 2008.

[148] Giuliano Benenti, Antonio D'Arrigo, and Giuseppe Falci. Enhancement of transmission rates in quantum memory channels with damping. *Phys. Rev. Lett.*, 103:020502, Jul 2009.

[149] A. D'Arrigo, G. Benenti, and G. Falci. Transmission of classical and quantum information through a quantum memory channel with damping. *The European Physical Journal D*, 66(6):1–15, 2012.

[150] M.a Mohseni, P.a Rebentrost, S.b Lloyd, and A.a Aspuru-Guzik. Environment-assisted quantum walks in photosynthetic energy transfer. *Journal of Chemical Physics*, 129(17):174106, 2008.

[151] I. Sinayskiy, A. Marais, F. Petruccione, and A. Ekert. Decoherence-assisted transport in a dimer system. *Phys. Rev. Lett.*, 108:020602, Jan 2012.

[152] T G Owens, S P Webb, L Mets, R S Alberte, and G R Fleming. Antenna size dependence of fluorescence decay in the core antenna of photosystem i: estimates of charge separation and energy transfer rates. *Proceedings of the National Academy of Sciences*, 84(6):1532–1536, 1987.

[153] Julia Adolphs and Thomas Renger. How proteins trigger excitation energy transfer in the FMO complex of green sulfur bacteria. *Biophysical Journal*, 91(8):2778 – 2797, 2006.

[154] Ana Camara-Artigas, RobertE. Blankenship, and JamesP. Allen. The structure of the fmo protein from chlorobium tepidum at 2.2 åresolution. *Photosynthesis Research*, 75(1):49–55, 2003.

[155] R. E. Fenna and B. W. Matthews. Chlorophyll arrangement in a bacteriochlorophyll protein from chlorobium limicola. *Nature*, 258:573–577, 1975.

[156] C Olbrich, J Strümpfer, K Schulten, and U Kleinekathöfer. The quest for spatially correlated fluctuations in the fmo light-harvesting complex. *J Phys Chem B*, 115(4):758–764, 2011.

[157] Adam Ben-Shem, Felix Frolow, and Nathan Nelson. Evolution of photosystem i from symmetry through pseudosymmetry to asymmetry. *FEBS Letters*, 564(3):274 – 280, 2004. Structure, Dynamics and Function of Proteins in Biological Membranes.

[158] Protein ID '3bsd'. RSCB Protein Data Bank (rcsb.org).

[159] T. Holstein and H. Primakoff. Field dependence of the intrinsic domain magnetization of a ferromagnet. *Phys. Rev.*, 58:1098–1113, Dec 1940.

[160] William G. Faris. Radial functions and the fourier transform - notes for math 583a. http://math.arizona.edu/ faris/methodsweb/hankel.pdf, Dec 2008.

[161] pyOZ project. Theory: Fourier, fourier-bessel, and sine transformations. http://pyoz.vrbka.net/theory/fourier-transformation.